



OMAR YESID DURAN TRIANA

**DEVELOPMENT OF A SURROGATE MULTISCALE RESERVOIR  
SIMULATOR COUPLED WITH GEOMECHANICS**

*DESENVOLVIMENTO DE UM SIMULADOR SUBSTITUTO DE  
RESERVATÓRIO MULTIESCALA ACOPLADO COM GEOMECÂNICA*

CAMPINAS  
2017





## UNIVERSIDADE ESTADUAL DE CAMPINAS

Faculdade de Engenharia Mecânica e Instituto de Geociências

**OMAR YESID DURAN TRIANA**

### **DEVELOPMENT OF A SURROGATE MULTISCALE RESERVOIR SIMULATOR COUPLED WITH GEOMECHANICS**

*DESENVOLVIMENTO DE UM SIMULADOR SUBSTITUTO DE  
RESERVATÓRIO MULTIESCALA ACOPLADO COM GEOMECÂNICA*

Thesis presented to the Petroleum Engineering Department of the State University of Campinas in partial fulfillment of the requirements for the degree of Doctor in Science and Petroleum Engineering.

*Tese apresentada ao Departamento de Engenharia de Petróleo da Universidade Estadual de Campinas como parte dos requisitos exigidos para a obtenção do título de Doutor em Ciências e Engenharia de Petróleo.*

**Orientador: Philippe Remy Bernard Devloo**

ESTE EXEMPLAR CORRESPONDE À VERSÃO FINAL DA  
TESE DEFENDIDA PELO ALUNO OMAR YESID DURAN  
TRIANA ORIENTADO PELO PROF. DR. PHILIPPE REMY  
BERNARD DEVLOO.

**Assinatura do Orientador**

---

CAMPINAS  
2017

## Abstract

Reservoir simulation softwares are used as a tool to understand the behavior of petroleum reservoirs and, eventually, to diagnose operating anomalies. The increased computational power allows reservoir engineers to develop more realistic geological models, that are very refined and have a large amount of input data. As an example, multi-physics models couple geomechanical, thermal, geochemical effects and include multiple scales inherent to full field models. These models are generally costly, because the direct calculation of a refined geocellular model, generates a huge linear systems of equations. When coupling the geomechanical deformation with fluid flow through porous media, a very large system of equations associated with elasticity, is coupled to an equally large system of equations, which is associated with fluid flow and mass transport. Therefore, most simulations are performed without considering the geomechanical coupling. These simulations ignore physical phenomena that can have serious environmental impacts such as fault activation, land subsidence and others. In this work an innovative multiscale method is developed, allowing the direct simulation of a fine geocellular model in a cost-effective way. A surrogate model has also been developed for simulating the geomechanical deformation coupled to the fluid model. The goal is obtain approximations for the nonlinear multiphysic problem described by the multiphase poroelastic equations. In order to attain this goal, different finite element technologies are integrated within a reservoir simulator, solving problems that include a geocellular model with different scales, coupled with a surrogate model of geomechanical deformation. The mathematical model is written in a form suitable for the NeoPZ finite element framework. At each timestep, the approximation is obtained as a sequence of elastic, Darcy's and transport problems. Each component in this sequence is treated by a different numerical scheme and/or approximation space; first, a surrogate model, inspired on the theory of poroelastic inclusions, is used for the calculation of the geomechanical deformation of rocks; second, a multiscale method based on mixed approximation of multiphasic equations is used; third, for the convection of the phases, a mixed multiscale approximation of the Darcy's velocity field is used together with a first-order upwind scheme. The potential of the numerical approach is demonstrated through several bi-dimensional and three-dimensional examples, in which reservoirs are simulated using unstructured meshes. All simulations have been executed using low cost computational structures.

**Keywords:** Finite elements; Reservoir Simulator; Poroelasticity; Reduced Base Modeling; Multiscale Modeling.

## Resumo

Os softwares de simulação de reservatórios são utilizados como ferramentas para o entendimento dos reservatórios de petróleo e eventualmente, para diagnosticar anomalias operacionais. O aumento da potência computacional permite aos engenheiros de reservatórios desenvolver modelos geológicos mais realistas, refinados e com uma grande quantidade de dados de entrada. Alguns exemplos são os modelos multi-físicos que acoplam efeitos geomecânicos, térmicos, geoquímicos e modelos que incluem múltiplas escalas inerentes aos modelos de campo completo. Estes modelos são geralmente caros, porque o cálculo direto de um modelo geocelular refinado gera enormes sistemas lineares de equações. Quando é considerado o efeito da deformação geomecânica com o fluxo de fluido através de meios porosos, um sistema muito grande de equações associado com a elasticidade é acoplado a um sistema igualmente grande de equações, associadas ao fluxo de fluido e ao transporte de massa. Portanto, a maioria das simulações são realizadas sem considerar o acoplamento geomecânico. Essas simulações ignoram fenômenos físicos que podem ter sérios impactos ambientais, como ativação de falhas, subsidência e outros. Neste trabalho desenvolve-se um inovador método multiescala que permite diretamente simular um modelo geocelular fino em uma maneira econômica. Um modelo substituto também foi desenvolvido para simular a deformação geomecânica acoplada ao modelo de fluido. O objetivo é obter aproximações do problema multifísico não linear descrito pelas equações multifásicas poroelásticas. Para atingir esse objetivo, diferentes tecnologias de elementos finitos são integradas dentro de um simulador de reservatórios, resolvendo problemas que incluem um modelo geocelular com diferentes escalas, acoplado a um modelo substituto de deformação geomecânica. O modelo matemático é escrito em uma forma adequada para a estrutura de elementos finitos do NeoPZ. Em cada passo de tempo, a aproximação é obtida como uma sequência de problemas elásticos, de Darcy e de transporte. Cada componente nesta sequência é tratado por um esquema numérico diferente e / ou espaço de aproximação; em primeiro lugar, um modelo substituto, inspirado na teoria das inclusões poroelásticas, é usado para o cálculo da deformação geomecânica das rochas; em segundo lugar, utiliza-se um método multiescala baseado na aproximação mista de equações multifásicas; em terceiro lugar, para a convecção das fases, uma aproximação mista multi-escala do campo de velocidade de Darcy é usada, em conjunto com um esquema de upwind de primeira ordem. O potencial da abordagem numérica é demonstrado através de vários exemplos bidimensionais e tridimensionais, em que os reservatórios são simulados usando malhas não estruturadas. Todas as simulações foram executadas usando estruturas computacionais de baixo custo.

**Keywords:** Elementos Finitos, Simulador de Reservatórios, Poroelasticidade, Modelagem por Bases Reduzidas, Modelagem Multi-escala.

# Contents

<b>Dedication</b>	<b>ix</b>
<b>Acknowledgement</b>	<b>x</b>
<b>1 Literature review</b>	<b>7</b>
1.1 Reservoir simulation . . . . .	8
1.1.1 Advances in reservoir simulation . . . . .	10
1.2 Multiscale modelling . . . . .	13
1.2.1 Multiscale heterogeneous modeling . . . . .	15
1.2.2 Homogeneous multiscale modeling . . . . .	16
1.3 Reduced base modeling . . . . .	20
1.3.1 Applications of reduced base modeling . . . . .	20
1.3.2 Base reduction and surrogate modeling . . . . .	22
1.4 Conclusions . . . . .	23
<b>I Numerical Tools</b>	<b>24</b>
<b>2 Finite element method</b>	<b>25</b>
2.1 $L^2(\Omega)$ approximation space . . . . .	29
2.2 $H^1(\Omega)$ -conforming approximation space . . . . .	30
2.2.1 $H^1(\Omega)$ scalar shape functions . . . . .	30
2.3 $H(\text{div}, \Omega)$ -conforming approximation space . . . . .	31
2.3.1 Neopz: the construction of $H(\text{div}, \Omega)$ -conforming spaces . . . . .	32
2.3.2 Application to finite element formulations . . . . .	37
2.3.3 Numerical example - Curved mesh: . . . . .	39
2.3.4 Numerical example - Linear mesh: . . . . .	42
2.4 Conclusions . . . . .	46
<b>3 Reduced order Modeling</b>	<b>47</b>
3.1 The general picture . . . . .	48
3.1.1 Reduced basis approximation . . . . .	49
3.1.2 Affine decomposition . . . . .	49
3.2 Monophasic poromechanics . . . . .	50

3.2.1	About Sequential methods . . . . .	54
3.2.2	Implementation for the Fixed Stress Split . . . . .	58
3.2.3	Consolidation benchmark problem . . . . .	58
3.2.4	Footing problem . . . . .	63
3.2.5	Empirical reduction strategy . . . . .	67
3.2.6	RB approximation for consolidation problem . . . . .	70
3.2.7	RB approximation for the footing problem . . . . .	74
<b>4</b>	<b>A Multiscale Method</b>	<b>76</b>
4.1	A mixed multiscale method . . . . .	77
4.1.1	Reinterpreting MHM . . . . .	78
4.1.2	Multiscale Process . . . . .	80
4.1.3	Downscaling operator . . . . .	83
4.1.4	Upscaling operator . . . . .	83
4.1.5	MHM- $H$ ( $\text{div}$ ) implementation . . . . .	85
4.2	Application of the multiscale method . . . . .	86
4.2.1	Examples of MHM- $H$ ( $\text{div}$ ) approximations . . . . .	86
4.3	Conclusions . . . . .	92
<b>II</b>	<b>Geomechanics multi-phase reservoir modelling</b>	<b>94</b>
<b>5</b>	<b>Strong Formulation</b>	<b>95</b>
5.1	Historical Note on Linear Poroelasticity . . . . .	96
5.2	Linear Poroelasticity . . . . .	96
5.2.1	Equilibrium Equation . . . . .	96
5.2.2	Constitutive Model for Rock Deformation . . . . .	96
5.3	Conservation of Mass for Fluid Flow in a Deformable Medium . . . . .	97
5.3.1	Mass conservation for multiphase flow . . . . .	98
5.3.2	Mass conservation considering the deformation of the solid phase . . . . .	98
5.3.3	Summary of the mathematical model . . . . .	99
5.4	Constitutive laws of the blackoil model . . . . .	100
5.5	Poroelasticity in a multiphase context . . . . .	101
5.6	Weighted pressure formulation . . . . .	102
5.7	Condensed form of the conservation laws and constitutive equations . . . . .	102
5.7.1	Three phase model: water oil gas system . . . . .	103
5.7.2	Two phase model: water oil system . . . . .	104
5.8	Conclusions . . . . .	105
<b>6</b>	<b>Finite Element Reservoir Modelling</b>	<b>106</b>
6.1	Weak Formulation . . . . .	106
6.2	Nested sequencial method (NSM) . . . . .	109
6.2.1	Sequential method for multiphase equations . . . . .	110

6.2.2	Solving the multiphase equations . . . . .	110
6.2.3	Solving the geomechanical coupling . . . . .	111
6.2.4	Transfer Interfaces . . . . .	112
6.3	Conclusions . . . . .	113
<b>III</b>	<b>An advance reservoir simulator</b>	<b>114</b>
<b>7</b>	<b>Advanced Reservoir Simulator</b>	<b>115</b>
7.1	A multiscale geomechanic reservoir simulator . . . . .	116
7.1.1	Geometry description . . . . .	116
7.1.2	Spatial properties . . . . .	117
7.1.3	Well Model . . . . .	118
7.1.4	Something about the implementation . . . . .	119
7.2	Numerical verification . . . . .	121
7.2.1	Homogeneous pressure change of a poroelastic inclusion . . . . .	121
7.2.2	Single phase water injection . . . . .	126
7.2.3	Injection of a passive tracer . . . . .	131
7.2.4	Water injection in an oil-water system . . . . .	134
7.3	Reservoir simulations . . . . .	139
7.3.1	Injection of linear tracer in 3D reservoir . . . . .	139
7.3.2	Reduced geomechanic 3D simulation . . . . .	147
7.3.3	Water injection in an oil water system in 3D . . . . .	152
7.4	Conclusions . . . . .	154
<b>8</b>	<b>Conclusions and outlook</b>	<b>155</b>
8.1	Conclusions . . . . .	155
8.2	Outlook . . . . .	157
<b>Bibliography</b>		<b>159</b>
<b>A</b>	<b>Derivation of poroelastic black-oil equations</b>	<b>159</b>
<b>Index</b>		<b>163</b>

*From my mother I have learned love and memory, from my father strong character and integrity,  
this work is dedicated to my Parents.*

“You have to learn the rules of the game. And then you have to play better than anyone else” -  
Albert Einstein.

# Acknowledgement

My sincere thanks to my supervisor Philippe, for taking me out of the Plato's cavern for a few seconds. It was when I stopped seeing shadows and started seeing what is science.

Special thanks to Sonia, because your advices generated an awakening inside of me, and I discovered the beauty of mathematics in the area of numerical analysis.

Special thanks to my friends Nathan, Tiago Forti and Francisco, for sharing time with me and for the scientific discussions. In many aspects I grew up through their friendship.

A thank to the LabMeC, it has been a great place to work. The collaboration with the different lab members all these years has been a real pleasure.

A thank to the Petrobras and ANP for the financing support during the first two years of the doctoral process.

A special thank to Tiago Forti, Cesar Rylo and Gustavo Longhin for the opportunity to grow up working in Simworx R&D. It was crucial to successfully finish my doctorate.

# List of Figures

1.1	Stages in the development of a reservoir simulator. source: <b>Odeh1982</b>	9
1.2	Different ways of geomechanical coupling.	12
1.3	Hierarchy of scales in geological structures. Source: <b>Mohan2002</b>	14
2.1	Geometrical transformation on a triangle.	28
2.2	Illustration of curved hexahedral elements of the spherical region in Problem 1: black lines indicate the edges of one curved element at the coarsest level; blue and red curves refer to the next two subsequent refinements, respectively.	40
2.3	$L^2$ -error curves in terms of $h$ for $\sigma$ (left) and for $u$ (right), using the mixed formulations with $\mathbf{P}_k^* P_k$ and $\mathbf{P}_k^{**} P_{k+1}$ space configurations based on curved hexahedral (up) and tetrahedral (bottom) uniform meshes $\Gamma_h$ , for $k = \{1, 2, 3, 4\}$ .	41
2.4	Percentage of condensed degrees of freedom in the discrete mixed method, using $\mathbf{P}_k^* P_k$ and $\mathbf{P}_k^{**} P_{k+1}$ space configurations at the finest refinement level of hexhedral (left) and tetrahedra (right) meshes.	42
2.5	Steady-state flow to a well in a bounded reservoir with constant pressure.	43
2.6	Finite element tetrahedra, prism and hexahedra meshes. A Visualization of wellbore region is rendered with red color by each case. In the adapted case red region has order $k = 2$ and blue region $k = 1$	44
2.7	Comparison error and solution profiles for different mixed approximations settings.	45
3.1	Boundary conditions for the column problem (left). Analytical solution at $t = 10$ [s] (right), with $n = 1000$ terms.	60
3.2	$L^2(\Omega)$ error plots for $k = \{1, 2\}$ , left correspond for operator 3.41, right for operator 3.43. Analytical solution at $t = 10$ [s], with $n = 1000$ terms.	61
3.3	Snapshot for approximations with $k = 1$ (blue dots Continuous Galerkin) and (black dots Mixed formulation of Type I). Plot over line $l = \{\{0, 0.5\}, \{0, -0.5\}\}$ .	63
3.4	Boundary conditions for the footing problem.	64
3.5	Snapshot for approximations of displacements associated to discretization of flow equation (blue Continuous Galerkin) and (red dots Mixed formulation of Type I). Right top partition, Right bottom color map of $\sigma_{yy}$ . Profiles rendered over line $l = \{\{-4.5, 0\}, \{-4.5, -5\}\}$ .	65
3.6	Snapshot for approximations (blue Continuous Galerkin) and (red Mixed formulation of Type I). Plot over line $l = \{\{-4.5, 0\}, \{-4.5, -5\}\}$ .	66
3.7	Reservoir $\Omega_r$ and side-burden $\Omega_s$ regions for a typical deformation.	67

3.8	Process for selecction of elements where the pressure field $p_i$ is applied.	69
3.9	Snapshot for RB approximations with $k = 1$ and $\mathcal{M} = 40$ , (blue dots Continuous Galerkin) and (black dots Mixed formulation of Type I). Plot over line $l = \{\{0, 0.5\}, \{0, -0.5\}\}$ .	72
3.10	Error ratio for flow equation left (CG) and right (MF Tipe I). $\mathbf{u}_{\mathcal{N}}$ is replaced by the RB approximation $\mathbf{u}_{\mathcal{M}}$ .	73
3.11	Snapshot for RB approximations with $\mathcal{M} = \{26, 101, 785\}$ . Plot over line $l = \{\{0, 0\}, \{0, -5\}\}$ .	75
4.1	MHM- $H$ ( $\text{div}$ ) partition and subpartitions defined over $\Omega$ .	79
4.2	Downscaling and upscaling multiscale operators and MHM- $H$ ( $\text{div}$ ) variables separation.	81
4.3	Downscaling and upscaling multiscale operators and MHM- $H$ ( $\text{div}$ ) variables separation.	82
4.4	Fine fluxes restricted to coarse fluxes.	85
4.5	Multiscale approximations of Thiem solution, with different levels $l = \{0, 1, 2\}$ . Left top geometric mesh with linear mappings, left bottom zoom on the wellbore region. Right plots over $line = \{\{-50, -50, 0\}, \{50, 50, 0\}\}$ .	88
4.6	Error plots for MHM- $H$ ( $\text{div}$ ) approximations of global mixed Thiem-Dupuit solution.	88
4.7	Multiscale approximations of Thiem setting with oscillatory permeability, and different levels $l = \{0, 1, 2\}$ . Left top geometric mesh with linear mappings (skeleton mesh in $\zeta_{\text{skeleton}}$ for $l = 0$ ), left bottom zoom on the wellbore region with skeleton mesh $\zeta_{\text{skeleton}}$ black wireframe for $l = 0$ ). Right plots over $line = \{\{-50, -50, 0\}, \{50, 50, 0\}\}$ of the pressure and flux respectively.	90
4.8	Multiscale approximations over Thiem problem setting with oscillatory permeability at $l = 0$ .	91
4.9	Multiscale approximations over Thiem problem setting with oscillatory permeability at $l = 1$ .	91
4.10	Multiscale approximations over Thiem problem setting with oscillatory permeability at $l = 2$ .	92
4.11	Color maps of 4.7 for $k_x$ and $k_y$ , the functions are rendered in log scale over the partition with resolution level $l = 0$ .	92
7.1	2D reservoir, wellbore, wellbore region, side-burden, and boundaries representation.	116
7.2	3D reservoir, wellbore, wellbore region, side-burden, and boundaries representation.	117
7.3	Discretization of finite elements embedded within a rasterization of a section of the SPE case. Properties transferred to the geometric representation after the use of the algorithm 7.1.	118
7.4	Physical setting of an oil-water reservoir under injection and side burden boundary conditions.	123
7.5	Geometric partition $\Gamma_h$ . The blue region represent the rectangular reservoir.	124
7.6	Sample of two RB funcions for the case of $\mathcal{M} = 6$ .	125

7.7	Contours and plots for RB approximation of the homogeneous pressure change. Top left shows contours of $u_x$ for $\mathcal{M} = 21$ . Bottom left shows contours of $u_y$ for $\mathcal{M} = 21$ . Top right shows plots over line $\{\{-1000, 0\}, \{1000, 0\}\}$ of $\ \mathbf{u}\ $ for $\mathcal{M} = \{6, 21\}$ and <b>Segall1985</b> solution. Bottom right shows plots over line $\{\{0, -100\}, \{0, 100\}\}$ of $\ \mathbf{u}\ $ for $\mathcal{M} = \{6, 21\}$ and <b>Segall1985</b> solution (Green line). . . . .	126
7.8	Approximation of reservoir pressure by iMRS and IMEX. The pressure profiles are rendered over the line $\{\{-500, 0\}, \{500, 0\}\}$ . . . . .	127
7.9	MHM- $H$ ( <i>div</i> ) partition mesh with $l = 0$ . Color maps of pressure and saturations at $t = 500$ [d]. . . . .	128
7.10	Natural logarithm of a field of permeability and 2D porosity, this field was extracted from the top layer of the 3D model of the SPE 10. The variance of log-permeability is $\sigma_{\ln k}^2 = 5.49$ , which corresponds to a coefficient of variation $CV = 2.97$ . . . . .	129
7.11	Examples of porosity transferred to MHM- $H$ ( <i>div</i> ) meshes at three different levels. The white wire frame represents the skeleton mesh. Properties transmitted with the algorithm 7.1. . . . .	130
7.12	Plot over line $l = \{\{-500, 0\}, \{500, 0\}\}$ of porosity transferred to the MHM- $H$ ( <i>div</i> ) meshes at level 2 and 3. The black line represents the SPE porosity. . . . .	131
7.13	Approximation of reservoir pressure by iMRS and IMEX. The pressure profiles are rendered over the line $\{\{-500, 0\}, \{500, 0\}\}$ . . . . .	132
7.14	Approximation of reservoir pressure and saturations with SPE10 properties. The profiles are rendered over the line $\{\{-500, 0\}, \{500, 0\}\}$ . . . . .	132
7.15	MHM- $H$ ( <i>div</i> ) wellbore pressure approximations with SPE10 properties. . . . .	133
7.16	MHM- $H$ ( <i>div</i> ) velocity on reservoir domain $\Omega_r$ . Approximations with SPE10 properties. . . . .	134
7.17	. Partition used in the STARS simulations. . . . .	136
7.18	Comparison of variables $(\mathbf{u}_\mathcal{M}, p_{\mathcal{N}_l}, s_{w\mathcal{N}})$ at $t = 250$ [d], the plot is rendered over the line $l = \{\{-500, 0\}, \{500, 0\}\}$ . . . . .	137
7.19	Color maps of variables $\mathbf{u}_{x\mathcal{M}}, s_{w\mathcal{N}}$ at $t = 250$ [d]. The black wire fram represents the multiscale mesh. . . . .	138
7.20	Comparison of variables $(\mathbf{u}_\mathcal{M}, p_{\mathcal{N}_l}, s_{w\mathcal{N}})$ at $t = 250$ [d], The plot is rendered over the line $l = \{\{-500, 0\}, \{500, 0\}\}$ . . . . .	138
7.21	Partition of a rectangular 3D reservoir $\Omega_r$ , ellipsoidal wellbore region $\Omega_w$ and cylindrical wells $\partial\Omega_w$ . The blue wellbore region is the producer. . . . .	140
7.22	Stream lines from the velocity colored with pressure. . . . .	142
7.23	Stream lines from the velocity colored with vorticity magnitude (right). The blue wellbore region is the producer well. . . . .	142
7.24	MHM- $H$ ( <i>div</i> ) skeleton mesh and comparison of $p_{\mathcal{N}_l}$ approximation of $p_{\mathcal{N}}$ , plot over line $l = \{\{-100, -100, 0\}, \{100, 100, 0\}\}$ . . . . .	143
7.25	Tracer saturation at $t = 100$ [d], transported with $\mathbf{q}_\mathcal{N}$ (top) and computed with $\mathbf{q}_{\mathcal{N}_l}$ (bottom). . . . .	144
7.26	Multiscale mesh surrounded by the external cartesian mesh of properties, the cartesian mesh represented by blue outline (left). External mesh with used with rasterized porosity (right). . . . .	145

7.27 Stream lines from the velocity colored with pressure (left) and $p_{\mathcal{N}_l}$ approximation of $p_{\mathcal{N}}$ , plot over line $l = \{\{-100, -100, 0\}, \{100, 100, 0\}\}$ (right). The blue wellbore region is the producer.	146
7.28 Water saturations at $t = 100$ [d], computed with $\mathbf{q}_{\mathcal{N}_l}$ .	146
7.29 Saturation states at $t = 200$ [d]. Left transport with $\mathbf{q}_{\mathcal{N}_l}$ at $l = 1$ , and right transport with $\mathbf{q}_{\mathcal{N}_l}$ at $l = 0$ .	147
7.30 Partition of a rectangular 3D sideburden $\Omega_s$ , reservoir $\Omega_r$ , ellipsoidal wellbore region $\Omega_w$ and cylindrical wells $\partial\Omega_w$ . The blue wellbore region is the producer. For visualization purposes just the surface mesh is rendered.	148
7.31 Memory consumption during the offline phase with $\mathcal{N} = 218547$ , $\mathcal{M} = 108$ .	148
7.32 RB functions samples when $\mathcal{M} = 9$ . Left $\mathbf{u}_{1\mathcal{N}}$ , right $\mathbf{u}_{2\mathcal{N}}$ .	149
7.33 Memory consume for: Top online RB with $\mathcal{M} = 63$ (Left), Top online RB with $\mathcal{M} = 108$ (Right), and below rigid problem (not geomechanic effect). phase with $\mathcal{N} = 218547$ .	150
7.34 Color maps for displacements $u_x$ and $u_z$ with $\mathcal{M} = 108$ .	151
7.35 Reservoir expansion due to injection and saturations profile at $t = 100$ [d]. Reservoir top plot over line $l = \{\{-100, -100, 10\}, \{100, 100, 10\}\}$ and reservoir bottom plot over line $l = \{\{-100, -100, -10\}, \{100, 100, -10\}\}$ .	151
7.36 Vertical displacements at reservoir top and bottom, at $t = 10$ [d]. Plot over line $l = \{\{-100, -100, 0\}, \{100, 100, 0\}\}$ .	152
7.37 MHM- $H$ ( <i>div</i> ) with $l = 0$ . Left $p_{\mathcal{N}_l}$ evolution at $t = 200$ [d] and $t = 1000$ [d], plot over line $l = \{\{-100, -100, 0\}, \{100, 100, 0\}\}$ . Right gravity effect on saturations at $t = 200$ [d].	153

# List of Tables

1.1	Description of some multiscale methods found in the literature.	18
2.1	Number of scalar shape functions $B_k^{\hat{K}}$ of $P(\hat{K})$ .	31
2.2	Input data for mixed approximation of the steady-state radial flow.	44
3.1	Input data for the column problem. Quase-incompressible solid-fluid structure response $tr(\boldsymbol{\sigma}^*) = -p_0$ is forced by setting ( $\nu = 0.4999$ ) .	60
3.2	Input data for the footing problem. Quase-incompressible solid-fluid structure response $tr(\boldsymbol{\sigma}^*) = -p_0$ is forced by setting ( $\nu = 0.4999$ ) .	64
3.3	Input data for the column problem. Quase-incompressible solid-fluid structure response $tr(\boldsymbol{\sigma}^*) = -p_0$ is forced by setting ( $\nu = 0.4999$ ) .	71
4.1	Input data for MHM- $H(\text{div})$ approximation of the steady-state radial flow.	87
4.2	DoF data for MHM- $H(\text{div})$ approximation of the steady-state radial flow.	87
5.1	Phase interaction matrix for three-phase flow. $m$ means fluid mass.	98
5.2	Phase interaction matrix for two-phase flow. $m$ means fluid mass	98
5.3	Closure relationships for the operators 5.33, 5.34 and 5.35. The subscript $sdt$ means standard or surface conditions, and $\beta = \{w, o, g\}$ .	104
5.4	Closure relationships for the operators 5.36, 5.37 and 5.38. The subscript $sdt$ means standard or surface conditions, and $\beta = \{o, w\}$ .	105
6.1	Matrix relation for the transfer interfaces.	112
7.1	Input data for the homogeneous pressure change problem.	124
7.2	Input data for the homogeneous pressure change problem.	127
7.3	Condensed linear system of equations after MHM- $H(\text{div})$ .	128
7.4	Input data for the two phase no homogeneous pressure change problem.	135
7.5	Input data for the linear trace on 3D reservoir.	141
7.6	Input data for the water injection on 3D reservoir.	153

# List of Symbols

## Geometry and Mesh

$d$  : Euclidean dimension  $d = [d]$

$\Gamma_h$  : Mesh of characteristic size  $h$  [ $\text{m}^3$ ]

$K$  : Geometrical element domain  $K \in \Gamma_h$  [ $\text{m}^3$ ]

$\hat{K}$  : Geometrical reference element domain [ $\text{m}^3$ ]

$T_K^{geo}$  : Geometrical transformation  $T_K^{geo} : \hat{K} \rightarrow K$

$\mathbf{n}$  : Unit outward normal

## Approximation spaces

$\Omega$  : Euclidean domain [ $\text{m}^3$ ]

$\partial\Omega$  : Euclidean boundary [ $\text{m}^2$ ]

$X(\Omega)$  : Functional space

$(\cdot, \cdot)_X$  : inner product associated with function space  $X(\Omega)$

$L^2(\Omega) : \left\{ f \mid \int_{\Omega} f^2 d\Omega < \inf \right\}$

$H^1(\Omega) : \left\{ f \in L^2(\Omega) \mid \nabla f \in [L^2(\Omega)]^d \right\}$

$H(div, \Omega) : \left\{ \mathbf{f} \in [L^2(\Omega)]^d \mid \nabla \cdot \mathbf{f} \in L^2(\Omega) \right\}$

$H(curl, \Omega) : \left\{ \mathbf{f} \in [L^2(\Omega)]^d \mid \nabla \times \mathbf{f} \in L^2(\Omega) \right\}$

## **Finite element method**

$\mathcal{N}$  : Finite approximation space dimension

$u_{\mathcal{N}}$  : Finite element approximation

$\alpha_{\mathcal{N}}$  : Degree of freedom or multipliers values

## **Reduce order modelling**

$\mathcal{M}$  : Reduced base space dimension

$u_{\mathcal{M}}$  : Reduced base approximation

$\alpha_{\mathcal{M}}$  : Degree of freedom or multipliers values of the reduced base

## **Reservoir modelling**

$p$  : Pressure [Pa]

$c$  : Compressibility [Pa $^{-1}$ ]

$\mathbf{g}$  : Gravity vector field [m s $^{-2}$ ]

$\mathbf{K}$  : Rock absolute permeability function [m]

$\phi$  : Rock porosity function

$\rho$  : Mass density [kg m $^{-3}$ ]

$\eta$  : Dynamic viscosity [Pa s]

## **subscripts**

$e$  : Designate equivalent

$t$  : Designate total

$b$  : Designate bulk

$ph$  : Designate phase  $p = o, w, g$

# Geomechanic modelling

$M$  : Maurice Biot poroelastic modulus [Pa]

$S_e$  : specific storage coefficient at constant strain [ $\text{Pa}^{-1}$ ]

$\mathbf{v}$  : Darcy velocity [ $\text{m s}^{-1}$ ]

$\mathbf{q}$  : Mass flux [ $\text{kg s}^{-2} \text{m}^{-1}$ ]

$\mathbf{u}$  : Displacement [m]

$\boldsymbol{\sigma}$  : Stress tensor [Pa]

$\boldsymbol{\sigma}^*$  : Effective Stress tensor [Pa]

$\boldsymbol{\epsilon}$  : Strain tensor

$\lambda$  : First Lamé parameter [Pa]

$\mu$  : Second Lamé parameter [Pa]

$\alpha$  : Maurice Biot poroelastic coefficient

## subscripts

$f$  : Designate fluid

$r$  : Designate rock

$dr$  : Designate drained

# Introduction

## Motivation

[U.S. Geological Survey](#) has realized studies related to subsidence ever since the 1950's; some studies are: San Joaquin Valley, Coachella Valley, Mojave Desert, Sacramento-San Joaquin Delta, and Santa Clara Valley. These studies integrate a series of tools that involve space and terrestrial infrastructures, in order to report high quality scientific information, subsidence status, trend and possible predictions. In 1991, more than 125 million USD was invested in repairing structural damage associated with subsidence, according to the [National Research Council](#) of US.

It is well known that subsidence due to the exploitation of oil causes damage to the surface infrastructure and environmental impacts. A good example of the effect of oil exploitation is reported by the U.S. Geological Survey in Long Beach California. about 3.75 trillion barrels were extracted from the Wilmington oil field. This production induced a bowl-shaped subsidence, that reached as low as 8.8392 [m] (29 feet) around Long Beach Harbor and the coastline of the city. About 51.7998 [ $\text{km}^2$ ] (20 square miles) were affected. At the beginning of 1940's water extraction began and contributed to the continued sinking of the city; this subsidence was attributed to the oil and gas extraction. Public and private patrimony were damaged, and the reconstruction of the facilities of city and the port cost billions in current dollars. In the 1950's, the reservoir conditions, oil properties and the development of new technologies allowed for the starting of a water injection project, that repressed the reservoir and eliminated the rock compaction, and stopped the subsidence. This water injection improved the oil recovery and induced uplift. Uplift is the opposite process of subsidence, where the rock undergoes volumetric dilatation. It is mainly driven by fluid injection, either water or CO<sub>2</sub>.

The extraction of petroleum is a process that involves different stages: exploration, development, production and abandonment of wells. This sequence of processes occur in a dynamic form, where the information collected, during each stage is assimilated using a computational infrastructure with the objective of predicting the behavior and planning the development of an oil field. Thus, reservoir simulation is a tool that allows to guide this dynamic process of the extraction of oil. Simulation models are constructed with  $10^5$  to  $10^6$  cells. Additionally, many efforts in numerical simulation applied to petroleum engineering, such as history matching, optimization and uncertainty evaluation, require to perform of many simulations. For such computational demand, the robustness and efficiency of a simulator is a crucial factor. The correct evaluation of the development of an oil field defines guidelines to increase recovery of oil, resulting in a minimum environmental impact. As mentioned before, the geomechanical coupling to large subsidence.

The numerical simulation of this coupling can be essential to obtain reliable results, justifying the inconvenience that it increases the computational cost of each reservoir simulation.

## Justification

The direct consideration of finer geocellular scales in the computational models is an unfeasible task. In order to turn the finer scale problem solvable, one can apply degree of freedom reduction, either by an upscaling or homogenization process. These procedures rely on computing material properties or functions on coarse domain partitions **Kyte1975; Guzman1996**. However, such procedures are not well accepted by the scientific community. The second alternative is to include finer geocellular scales directly changing the computational model, leading to numerical schemes capable of incorporating these scales in a complete way. These numerical approaches are called multiscale methods. There are a large number of publications dedicated to multiscale problems and advances have been made in the simulation of large problems with highly heterogeneous rocks. However, there are some limitations associated with existing multiscale models, corresponding to the need to extend them to complex mechanisms such as compressibility, gravity and capillarity.

Multiscale methods can be embedded within all families of numerical schemes such as finite differences, finite volumes and finite elements. In terms of geometric representation finite volumes and finite elements offer a mathematical infrastructure for the treatment of complex geometries. In the case of finite volumes and finite element approximations the conservation laws can be modeled using two very different approaches. In the case of Darcy's law, the velocity and pressure can be modeled either by a second order problem (primal form) or by a system of two first order equations (dual or mixed form).

The term mixed was introduced in the 1960's to describe finite element methods where both stress and displacements are approximated as state variables. **Arnold1990** outlines several reasons for the use of mixed formulations instead of primary or second order formulations. The reasons range from limits defined by the corresponding equations, as in the case of linear elasticity, in which the use of mixed formulations facilitates the resolution of the incompressible limit, whereas the primal (e.g. displacements based) formulation is not suitable for this purpose. In the case of simulation of porous media exists several publications (**Arbogast2000; Wheeler2002; Aarnes2006; Castro20163D**) advocate the use of mixed formulations, where improved pressure approximations are reported. This pressure fields satisfy the second order problem (primal formulation) arising from Darcy's law. More interestingly, in the multiphase case the mixed approximations generate conservative velocity fields that are suitable for solving transport equations associated with each phase.

In conclusion, the most appropriate multiscale method is based on mixed approximations, is applicable to the multiphase case, includes the finest scales in the reservoir simulation, and nonlinear effects such as compressibility, gravity and capillarity. Also, the multiscale method must be coupled with geomechanical deformations where the material properties are defined at finer geocellular scales.

# Problem Statement

There is a growing trend to integrate technologies in reservoir simulations. These technologies incorporate geological models, porous flow and heat transfer modeling with or without chemical reactions, 4D time-lapse seismic analysis, all of them coupled with poromechanical modeling (**Wheeler2002**). The benefits of such complex multiphysics simulations are:

- Better understanding of the dynamic fluid-structure interaction.
- Accurately predicting underground deformation and surface subsidence, due to the over-exploitation of underground natural resources and/or underground storage of energy residues.
- Effectively monitoring small changes in land surface elevation with an unprecedented level of spatial detail.
- Providing cost effective damage prevention or control.

Whereas integrated geomechanical modeling has many energy and environmental applications, the numerical modeling of such coupled physical processes has been, historically, considered extremely complex and unfeasible due to limited computing resources. Currently, assumptions about part of the interaction process, which are not of primary interest, are made. For instance, in a 3D coupled problem the geomechanical deformation is approximated by a 1D or 2D model. For example, in conventional reservoir simulation the effects of rock compaction and porosity changes are only partially accounted for by adding a rock compressibility term to the pressure equation. This leads to a porous flow modeling that is completely decoupled from solid mechanics calculations. Another example is groundwater modeling in which porous flow is modeled in 3D, but compaction is typically simulated as a 1D process. Even though the poroelastic theory developed by **Biot1941a**; **Biot1941b** provides the fundamental basis for 3D consolidation analysis, scientists and engineers commonly use the one-dimensional consolidation theory of **Terzaghi1943**

The above simplified models, either through decoupling or dimensional reduction, are only appropriate and reasonably accurate under certain circumstances (e.g. as competent rocks). However, these circumstances are sometimes unacceptable because the underlying physics, involves a strong coupling of fluid flow and solid deformation. In stress-sensitive reservoirs, rock deformation, porosity and permeability changes, as well as rock failures cannot be fully represented by the rock compressibility term alone. Moreover, the common assumption of 1D consolidation in groundwater modeling is motivated that most aquifer-system compaction or reservoir compaction take places in the vertical dimension. Nevertheless, the widespread occurrence of earth fissures indicates that horizontal deformation may be locally significant.

Since the advent of inexpensive high-speed digital computers, scientists and engineers have the ability to simultaneously solve multiple field equations, such as thermoporoelastoplasticity, single phase or multiphase flow and heat transfer problems. The integrated analysis can be carried out in a loosely coupled fashion or with a fully coupled scheme.

Challenges still exist in large scale, full-field 3D applications with a spatial size similar to the one in 3D seismic models. These challenges lie in the intensive demands for computational time and memory storage, which are attributed to:

- Considering large scales in rocks imply in considering several scales that are represented by fine geocellular models, and they impact the accuracy of approximated solutions.
- Large coupled systems which include mass conservation equations for flow, and force balance equations for elasticity; In the case of the black-oil model coupled with 3D poroelasticity. Thus, effective linear solvers and numerical schemes need to be applied for solving the system efficiently and robustly.
- The complex nonlinear behaviors of coupling multiphase flow and rock mechanics can result in slow nonlinear convergence.
- Several coupling techniques have been proposed and widely used for solving multiphysics equations with different time scales for each model. However, judging the trade-offs between accuracy and efficiency is difficult.
- Field observations suggest that, while pressure depletion is a local process that only occurs inside aquifers or reservoirs, it triggers a redistribution of effective stress in a more extensive domain. In order to get a accurate numerical solution, the computational domain needs to be as large as possible.

In summary, the problem amounts to solving a coupled system in a large physical domain on a full-field scale with a considerable vertical depth. Such a coupled analysis involves a large linear system with millions of unknowns and different rocks scales, whose solution need to be computed iteratively.

This research is an investigation focused on the coupling of subsurface flow (single phase and multiphase) with 3D poroelasticity. It emphasizes seeking an accurate numerical sequential scheme for solving the coupled system, reducing the equivalent linear system of equations and using a multiscale method that deals with several reservoir scales. To turn the geomechanic problem solvable, a reduce order modelling is addressed on the elastic counter part.

## Objectives

The goal of this work is to approximate the 3D geomechanical reservoir response, considering highly heterogeneous rocks and side burden rocks deformation. An iterative coupling technique is adopted to solve the single phase and the multiphase (water, oil) flow equations coupled to a deformable porous media. The method is implemented using a surrogate multi-scale reservoir simulator coupled with geomechanics that generates such desired approximations.

To reach this goal following mile-stones are established:

1. To develop and verify  $H_{div}(\Omega)$ -conforming approximation spaces in Neopz, as a contribution to the framework.
2. To develop a reduced order model to approximate the geomechanic coupling.
3. To develop a multi-scale method that is able to model a fine-scale solution and ensure local mass conservation.

4. To rewrite the poroelastic multiphase equations in a suitable mathematical kernel for sequential methods.
5. To apply all these technologies to model reservoir 2D/3D simulation cases.

## Outline of the thesis

The document is divided in three main parts, that are associated to: 1) the numerical tools used; 2) the mathematical model and its discretization; and 3) the application of all these ingredients to a reservoir simulator. In this way, all the discussions in this thesis are organized as follows:

- Chapter 1: Presents the literature review.
- Chapter 2: Introduces the finite element method (FEM) as the basis of all developments of this research. The chapter gives a general description of the finite element method, and presents the approximation spaces used for this research and outlines the main contributions to the Neopz framework.
- Chapter 3: Gives a description for the proposed reduced basis approximation. The chapter outlines the reduced form of the elasticity operator, which is generated from a Galerkin projection on an approximation space of global displacement functions. The reduced basis shape functions are obtained for the Biot's poroelasticity and used to account for the poroleastic effect in a surrogate way for two types of formulations.
- Chapter 4: Describes the multiscale approach adopted in this work. A mixed method is applied with precision being controlled through the resolution of the multiscale mesh, solving the elliptic problem with variable coefficients that comes from any porous medium. The accuracy of the method is demonstrated through 3D simulations applied to a monophasic problem.
- Chapter 5: Describes the mathematical model for multiphase fluid flow description coupled with geomechanics; several comments and remarks are given, as well as a summary of the equations for the triphasic and biphasic case.
- Chapter 6: Describes the sequential scheme adopted for the solution of the elliptic, parabolic and hyperbolic components of the multiphase equations. The discussion is described in terms of: the base reduction technique of chapter 3, the multiscale technique of chapter 4 and a first order upwind scheme for the saturation equations.
- Chapter 7: Describes how all the finite element technologies have been incorporated into a home-made reservoir simulator with coupled geomechanics, called iMRS (innovative Multiscale Reservoir Simulator). Some numerical examples on the simulation of water injection on different model settings and their surrogate approximations.
- Chapter 8: Gives a short discussion on the conclusions and several points for future research.

## Publications

- The mixed finite element formulation for elliptic problems is characterized by simultaneous calculations of the potential (primal variable) and of the flux field (dual variable). This work focuses on new  $H(\text{div})$ -conforming finite element spaces, which are suitable for flux approximations, based on curved meshes of a planar region or a manifold domain embedded in  $\mathcal{R}^3$  (**Castro20162D**).
- There are different possibilities of choosing balanced pairs of approximation spaces for dual (flux) and primal (pressure) variables to be used in discrete versions of the mixed finite element method for elliptic problems arising in fluid simulations. Three cases shall be studied and compared for discretized three dimensional formulations based on tetrahedral, hexahedral and prismatic meshes (**Castro20163D**).
- Two stable approximation space configurations are treated for discrete versions of the mixed finite element method for elliptic problems. The construction of these approximation spaces are based on curved 3D meshes composed of different topologies (tetrahedral, hexahedral or prismatic elements). Furthermore, their choices are guided by the property that, in the master element, the image of the flux space by the divergence operator coincides with the primal space. Additionally, using static condensation, the global condensed matrices sizes, which are proportional to the dimension of border fluxes (plus one) are reduced. High order finite element bases for  $H_{\text{div}}$  spaces based on 3D adaptive curved meshes (Submitted).
- In this paper, it a mathematical model is proposed to describe the functioning of a bioreactor landfill, that is a waste management facility in which biodegradable waste is used to generate methane. A framework for the approximation of the model is implemented using Feel++, a C++ open-source library to solve Partial Differential Equations. Some heuristic considerations on the quantitative values of the parameters in the model are discussed and preliminary numerical simulations are presented (**Dolle2016**).

## Oral presentations

- A conservative mixed finite element - finite volume method for two-phase considering gravity and capillary effects in heterogeneous media was presented on the Fifth Chilean Workshop on Numerical Analysis of Partial Differential Equations. January 15, 2016. Title: Conservative high order coupled mixed finite element- finite volume method for two-phase flows in heterogeneous media. O. Duran, J. Villegas, S. Gomes, P. Devloo.

## Scientific events

- Participant in the summer school and the long research session of CEMRACS 2015 Coupling Multi-Physics Models involving Fluids. The CEMRACS is a scientific event of the SMAI (the french Society of Applied and Industrial Mathematics). July 20 - August 28 2015, CIRM, Marseille.

# Chapter 1

## Literature review

A problem in the field of computational physics is a problem that can be modeled by a system of partial differential equations. This system of equations can then be approximated by a closed form mathematical expression or by a numerical technique. Many problems in the field of computation physics have not been completely explored. This is the case of multiscale problems associated to reservoir engineering.

Several commercial softwares applied to reservoir engineering, use technologies developed more than 50 years ago, to approximate multiphase flow in heterogeneous porous media. The last 10 years many research projects have been devoted to multiscale simulation, in an attempt to incorporate high resolution geological models directly as data of the fine scale problem (**Aarnes2004**; **Wheeler2002**). The research in this area is mainly motivated by:

- (i) The complexity and inherent multiscale nature of the rocks.
- (ii) The rapid growth of computational power.
- (iii) The need/desire to approximate detailed multiscale, multi-physics problems accurately and efficiently.

A different approach to multiscale simulations, that is not very well explored, is the use of surrogate models that allow to reduce substantially the computational costs, allowing to approximate large problems in a reasonable computational time.

This revision deals with these two numerical approaches in the field of reservoir simulations coupled with geomechanics.

## Contents

---

1.1	Reservoir simulation	8
1.1.1	Advances in reservoir simulation	10
1.2	Multiscale modelling	13
1.2.1	Multiscale heterogeneous modeling	15

1.2.2	Homogeneous multiscale modeling . . . . .	16
1.3	Reduced base modeling . . . . .	20
1.3.1	Applications of reduced base modeling . . . . .	20
1.3.2	Base reduction and surrogate modeling . . . . .	22
1.4	Conclusions . . . . .	23

---

## 1.1 Reservoir simulation

Most aspects of reservoir engineering can be approximated with existing reservoir simulators, which have different applications ranging from pressure tests to enhanced oil recovery. Many research groups and companies have developed simulators for years, but each simulation study is still a unique process (**Peaceman1977**; **Odeh1982**; **Ertekin2001**). Starting from the description of the reservoir, its geology, petrophysics, geomechanics and formation evaluations, to the simulation of the reservoir and results analysis, each study of a reservoir is different.

Traditionally, **Odeh1982**; **Ertekin2001**; **Fanchi2005** show, that developing a reservoir simulator follows the stages being shown in the figure 1.1. Each step in the approximation means:

- (i) Formulation: This the first step and involves several simplifications that lead to a mathematical description. A good formulation incorporates the essential characteristics of the physical processes that determine the behavior of the oil reservoir and describes the flow of fluids through the porous medium (**Ertekin2001**).
- (ii) Partial Differential Equations: As a final result of the formulation process, a system of conservation laws and constitutive equations are explicitly written.
- (iii) Discretization: By the discretization a system of nonlinear differential equations is transformed into a system of nonlinear equations. At this stage the numerical scheme is chosen. The numerical scheme completely defines the computational framework, necessary for the development of the simulator.
- (iv) Nonlinear system of equations: Once, discretized by a numerical method, the nonlinearities of the constitutive equations result in a nonlinear algebraic system of equations.
- (v) Linearization: The nonlinear system of equations is solved by a sequence of inversions (or approximate inversions) of linear system of equations. A common approach is to use gradient-based optimization methods. A possibility is to use the Newton method which relies on the computation of the tangent matrix of the residual vector.
- (vi) Wells representation: It is a necessary step that represents the extraction/production of fluids. Very often, the representation of the well is very crude.

- (vii) Solution: The results from the simulator are used to compute quantities of interest such as pressures, velocities and saturations.
- (viii) Verification and application: During this process, the simulator is used to approximate known analytical solutions. The properties (convergence rates, accuracy etc.) of the numerical scheme are tested with the purpose of debugging and evaluating the quality of the simulator. This task is accomplished by computing error graphs in each state variable, verifying the execution times and flexibility of the approach. These criteria determine if the implemented numerical scheme can be efficiently applied to the simulation of real problems in reservoir engineering.
- (ix) Simulation: This process represents the use of the simulator in a real environment, where a series of simulations are carried out to optimize the production of fluids and mitigate possible economic risks during the execution of the development plan.

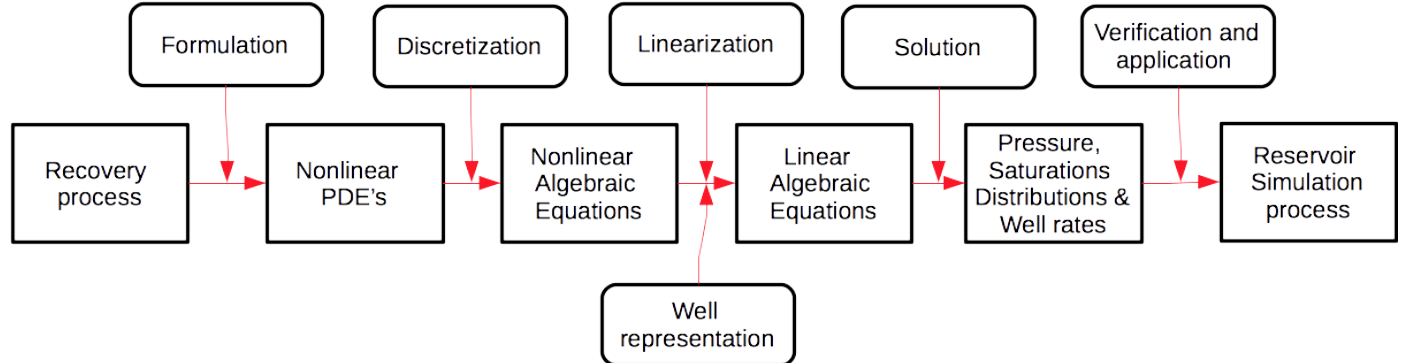


Figure 1.1: Stages in the development of a reservoir simulator. source: **Odeh1982**

Most commercial softwares applied to reservoir simulation use the finite difference method (**Peaceman1977**; **Young1980**; **Liu1994**; **Das1994**; **Ertekin2001**; **Fanchi2005**). More recently finite volume approximation brought increased flexibility in mesh generating (**Forsyth1990**; **Fung1992**; **Aavatsmark1998**; **Marcondes2010**; **Panchadhara2013**). Finite element approximations, promoted by the pioneering work of **Chavent1982** and then **Wheeler2002**; **Aarnes2006**; **Matringe2007**; **Efendiev2009** have found increasing acceptance over the last years due to advances in understanding the convergence properties of  $H(\text{div}, \Omega)$  approximations and their even larger flexibility in choice of approximation spaces and adaptivity. In reservoir simulation with geomechanics coupling. The geomechanical response of the rock is generally simulated with finite elements. In this research, following this line, the other mathematical components of reservoir modelling are approximated by mixed finite elements and discontinuous finite elements.

### 1.1.1 Advances in reservoir simulation

#### New formulations

There are several fronts of active research in reservoir modeling. One area consists in mastering the complexity and computational cost of compositional models, topic that is left open for future researches. Incorporating natural fractures networks into reservoir simulations is another area of active research. Motivated by experimental observations, double permeability, double porosity models have been proposed by **Tidwell1995; Saghir2001 Choi1997** has shown that the conventional use of Darcy's law for both matrix and fracture are not adequate even in single-phase flows. He proposed to use a nonlinear Forchheimer model in the fracture, maintaining Darcy's law in the rock matrix. He showed good agreement with experimental data. However, to obtain a robust and efficient modelling, the extension of the methodology developed by **Choi1997** to multiphase flows have not been sufficiently explored. In the meantime, other publications use conventional approach to create discrete models of discrete fracture networks (DFN) (**Formaggia2014; Chen2016**). In a different approach authors such as in **Popov2007; Abdelazim2016** that explores mechanical properties of DFN's and their influence on multiphasic flow. With the above mentioned, the use of complex nonlinear formulations lead to the need of increase the accuracy and velocity of the numerical schemes.

#### Accuracy and speed

The accuracy of a numerical model measures the error between the numerical approximation and the mathematical model. Its value is measured by the norm of the difference between the approximation and the exact solution (which is often unknown). Current simulation techniques used by most industries use numerical schemes of low order approximation, which means that in order to obtain accurate solutions (pressures and saturations) billions of degrees of freedom need to be used. It is also noted that, in order to circumvent the limitations imposed by finite difference and/or finite volume approximations, numerical tricks are often applied that diminish even more their accuracy. For literature on finite-difference approximations, the reader is referred to (**Young1980; Liu1994**), and on finite volume schemes, to (**Aavatsmark1998; Panchadhara2013**). Relevant reference on mixed finite element schemes applied to reservoir modeling are **Masud2002; Matringe2007**

High order approximations are more accurate but require larger computer resources than lower order models. Availability of such computer resources can be challenging, especially if the model contains relevant solution features of different scales or different geometric dimensions. Many numerical simulation are unfit to include dimensional coupling (e.g. coupling 1D well flow, 2D fractures flow and a 3D reservoir flow). Trying to model problems with different scales with a non-adapted code leads high resolution in the discretization, i.e.  $10^7 - 10^8$  elements or simulation blocks (**Durlofsky1991**). Having such large meshes lead to numerical schemes of difficult convergence, rendering the simulation unfeasible. In this work, is proposed the simulation of problems with multiple scales/resolutions, using a method specifically developed for this purpose. The MHM (multiscale hybrid method), developed by **Paredes2013** is briefly described in the chapter 4, this research use a variation of the MHM method called here of MHM-*H* (*div*) which is also detailed and analyzed in chapter 4.

## Geomechanical coupling

The coupling of the reservoir deformation with the fluid flow is a current challenge in the multi-physics simulation of reservoirs. **Pedrosa1986** introduced a computational framework with hybrid meshes, in order to couple cylindrical meshes with Cartesian meshes. His work was later used as the basis for implementing different geomechanics coupling schemes with fluid flow (**Islam1990**).

The geomechanical state of stress is important quantity of interest in any production simulator. In a case of massive fluid extractions, due to the geomechanical stress state, the formations can partially disintegrate and release very fine sands near the producing wells, decreasing the oil extraction. In the last years, several studies have been carried out in the study of geomechanics coupling with fluid flow near the wellbore. In the research of **Nouri2002; Nouri2006** a finite element analysis with a Mohr-Coulomb fault criteria was implemented to simulate the induced stresses, near to the producing wellbores, the coupled model was useful in the quantification of sand production near the wells. More recent work on the develop of a simplified methodology, which is proposed for elastoplastic calculations holding for associative models (**Cecilio2015**). This methodology was developed at the Universidade Estadual de Campinas (Brazil) and applied on the simulation of the elasoplastic simulation of breakouts by the research group under the leadership of the Professor Philippe Remy Bernard Devloo at the Laboratory of Computational mechanics LabMeC.

**Settari2008** applied numerical techniques to calculate the subsidence induced by gas production in the Northern Adriatic. Other authors **Lewis1993; Settari1998; Settari2001; Thomas2002; Li2005** focus more on applications such as: well failure, stress-dependent permeability or permeability coupling, as well as tar-sand and heavy-oil production.

Due to the relevance of the coupling of the fluid flow in the reservoir and compaction mechanisms, he combined the results of the fluid flow simulator and geomechanical simulators in an iterative way for the prediction of subsidence. Different types of coupling between the simulators are graphically represented in Figure 1.2:

- (i) One way: Transfers pressures to the geomechanical model.
- (ii) Two ways: Transfers pressures and stress/strain in a reciprocating way.
- (iii) Iterative: Transfers pressures and stress/strain in a iterative way until a desired convergence tolerance is reached.
- (iv) Fully coupled: Strong coupling of both models at the level of algebraic system of equations.  
This is the most robust method but also the most expensive one.

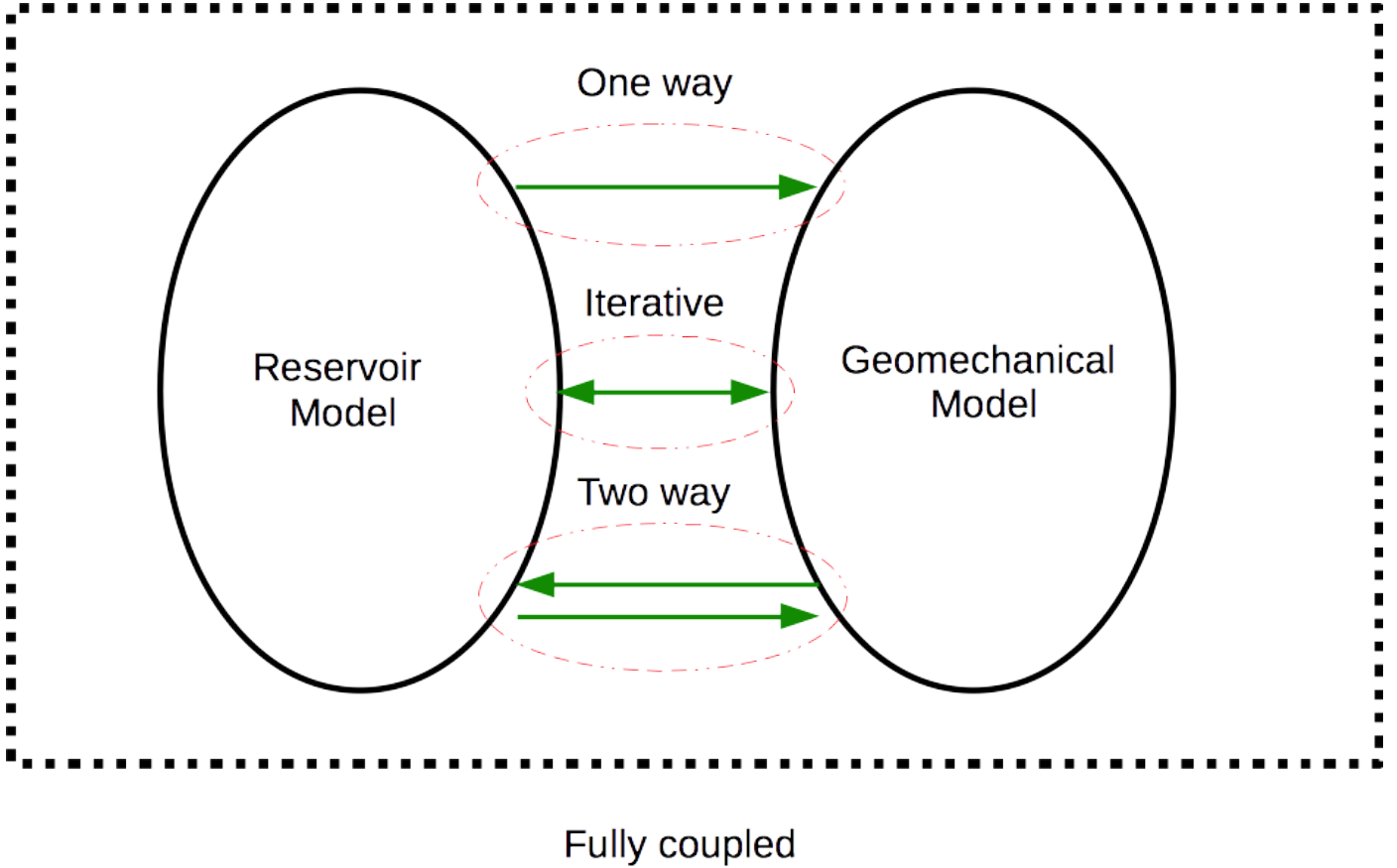


Figure 1.2: Different ways of geomechanical coupling.

Recently a new methodology for the modeling geomechanical coupling was proposed and analysed (**Kim2011a**; **Kim2011b**; **Kim2011c**). The novel method is called "fixed-stress split", which can be applied for all coupling flavours described in Figure 1.2. The underlying idea of different split schemes including the "fixed-stress split" for the monophasic poroelasticity case is detailed in chapter 3, extended for the mixed multiphase case in chapter 6, and applied on chapter 7.

The stability and convergence analyses has shown that "fixed-stress split" is unconditionally stable, for both linear or nonlinear in single phase problems. The fixed-stress split methodology also shows excellent approximation properties, even for the quasi-incompressible case. **Coussy2005**; **Kim2013** also have shown, that the stability and convergence can be extended to multiphase problems, through the correct definition of the pore pressure variable.

The main challenge in the solution of a coupled geomechanical problem is the computation of the deformations in an efficient way. In this research we propose a reduced base method for the geomechanical deformation in conjunction with a fixed-stress split approach. This reduced base method can be used in all coupling schemes mentioned in the figure 1.2.

## 1.2 Multiscale modelling

Recently, there is a growing interest in solving multiphysics problems involving multiple scales. This renewed interest is motivated by the fact that most problems of interest are multiscale in nature and because of the large computer resources available. There are many different approaches to analysing multiscale problems, for example, using fourier series and wavelet transformations (**Engquist2007**). Many problems which are inherently multiscale in nature, have been reduced to macroscale problems using classical mechanics, homogenization, statistical mechanics and/or turbulence models. Recently, the modeling of problems in the microscale level has gained considerable popularity, mainly motivated by nanoscience, molecular dynamics simulation, pore-scale simulation, hemoflux in capillary vessels simulation, among others. Multiscale simulations try to solve the macroscopic problem taking the microscale behaviour into consideration through numerical simulation.

Many real problems have different characteristic lengths. In many cases the physics of the macroscale and the microscale are described by different types of equations. The most traditional approach to solve a problem that has different scales, is to approximate it at the level of the macroscale, to obtain an analytical or numerical solution of the variables in the space-time scale of interest, incorporating the contributions of the missing scales through constitutive laws. The Darcy's law for fluid flow in a porous medium, the Fick's law for mass diffusion, and the Fourier's law for thermal conduction are examples of constitutive laws that approximated physical problems that inherently have different scales. Using these constitutive laws combined with the corresponding conservation laws, it is possible to obtain a good description of homogenized system. When the systems become more complex, e.g. composite materials with complicated internal stresses, fracture dynamics, plasticity, of fluid flow simulation with different turbulent flow regimes (**Engquist2007**), the traditional numerical schemes suffer from serious deficiencies.

An important example of a relevant multiscale simulation, is the transport of fluids inside an (highly heterogeneous) oil reservoir. In a typical oil reservoir, heterogeneities occur at different scales. In most cases, empirical curves and mean permeability values are used to represent heterogeneities of the smallest (i.e. missing) scales. In terms of geologic structures, the figure 1.3 shows the hierarchy of different scales, ranging from pore scale to tectonic plate structures that have tens of millions of meters in length. In reservoir engineering, the scales of interest are the microscale and the mesoscale, i.e. pore scale and full oil field simulations, where different types of heterogeneities can be found. Within the mesoscale, the heterogeneities are the result of a depositional, diagenetic and structural deformation process of the rocks that compose the reservoir (**Mohan2002**). The permeability of the reservoirs can vary within different orders of magnitude, from impermeable flow barriers to highly permeable channels. Different rocks and layers can compose the same reservoir, exhibiting different hydraulic and deformation properties. There are different techniques for the characterization of a reservoir: gravimetry readings, seismic images, nuclear magnetic resonance imaging, exploratory drilling, etc. These techniques allow to obtain descriptions of the petrophysical properties of rocks at a high resolution level, but the limitations of the current simulation capabilities, impose a bottleneck to use this information in a complete and integrated way (**islam2010advanced**).

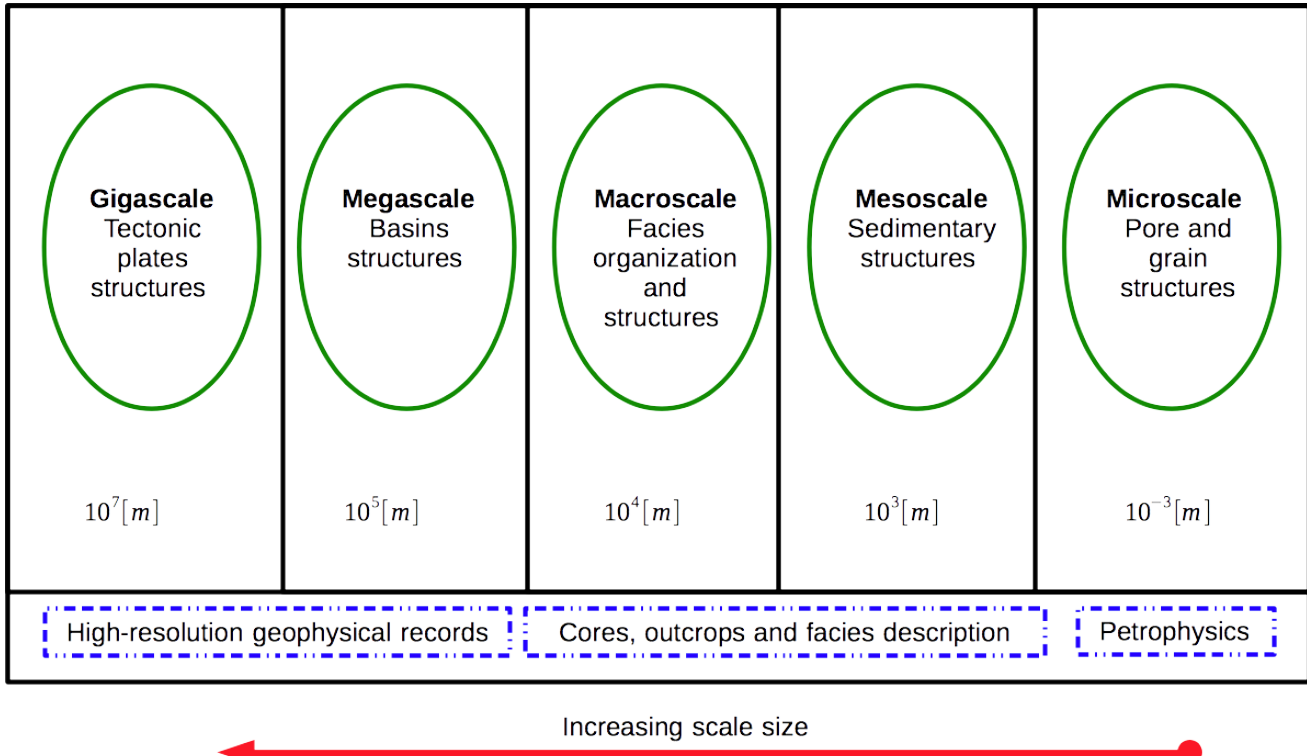


Figure 1.3: Hierarchy of scales in geological structures. Source: **Mohan2002**

Modern reservoir discretizations in practical applications can only solve a few million of blocks (**Aarnes2006**). As a result of this limitation, different techniques of upscaling have been proposed (**Durlofsky1991; Farmer2002; Chen2006; Qi2009**), where an approximation of the homogenized representation of the problem is extended to model the microscale behaviour. However, upscaling is a technique that is not quite robust and not very well accepted by the scientific community. Thus, multiscale modeling enters as an alternative solution to the upscaling techniques.

The multiscale modeling is one of the methodologies that allows the approximation of a high resolution model. According to **Wheeler2002** it is expected that in the 21st century, the implementation of software and programming tools will be fully integrated in commercial software for approximating multiphysics - multiscale problems. **Engquist2007** has classified the existing multiscale methods into two main categories, heterogeneous and homogeneous methods, this separation is motivated by two main problems that appear in the context of multiscale modeling:

- (i) Type A: The macroscopic description is known, but its validity is limited to localized regions of space-time. The smaller scale approximations of interest can be directly modeled when determining the fields in the larger scales. Coarse to fine approaches (**Efendiev2009**).
- (ii) Type B: The macroscopic description is known implicitly and its calculation is required. There is a set of microscopic models that together obey the macroscopic model, and this fact is used to obtain the approximation of the mentioned macroscopic model.

Examples of type A problems are crystal defects, turbulent flame front, chemical systems with localized reactions. Examples of type B are problems such as multiphasic transport within an petroleum (oil and gas) reservoir.

Recently, there has been an interest in the development of multiscale methods with limited information, which opens a new and an active field of research (**Efendiev2009**).

In simulations of porous media, "multiscale" methods are presented as methods that use the same governing equations to model a unique physical process in different macroscopic resolutions. These multiscale methods, such as multigrid and mesh adaptations, are called multi-scale homogeneous methods. These methods are typically applied in situations where the fine scale is computationally prohibitive at the global level. Considering as an example, the simulation of fluid flow in heterogeneous porous media.

$$\nabla \cdot (\lambda(\mathbf{x}) \nabla p(\mathbf{x})) = f(\mathbf{x}) \text{ in } \Omega \quad (1.1)$$

Where  $\lambda(\mathbf{x})$  is the mobility, (i.e. the permeability tensor divided by the viscosity of the fluid),  $p$  is the pressure,  $f$  is the source term and  $\Omega$  is the domain of interest. In this case the parameter  $\lambda(\mathbf{x})$  can be obtained from a simple volumetric mean, to a complex function of its spatial distribution. In this sense, the homogenization methods are techniques designed to merge the information of the fine scale in solutions of the coarse scale at different resolutions. The numerical solutions are an equally coarse approximating and improve as the resolution of the coarse scale becomes finer. In addition the empirical nature of the model remains the same, e.g. Darcy's law, and therefore the governing equations are the same in the coarse and fine scales. Another issue in homogeneous multiscale methods, is that they need the information of the fine scale, and in practice estimating the information of the fine scale is a complex problem by itself (**islam2010advanced**).

In a different approach, the heterogeneous multiscale methods recognize that the problems are governed by different physical and mathematical models, that are motivated by the so-called "first principle" (**Wdowik2008; Qin2015**). Examples of this approach are homogenization applied to molecular dynamics, quantum mechanics based on Boltzmann's kinetic equations where at the fine scale the interaction of particles at the microscale are modeled. The results of the microscale are subsequently used to compute the data necessary for the macroscopic model. As a consequence, the approximation obtained by this approach in general, is more precise because it eliminates the inherent error of the constitutive laws.

Most of the existing multiscale methods for reservoir simulations fit into the context of homogeneous multiscale methods. Only a few studies have been carried out in the heterogeneous multiscale category method (**Kang2002; Kang2006**).

### 1.2.1 Multiscale heterogeneous modeling

There are two essential parts in the framework of a multiscale heterogeneous method:

- (i) A macroscopic scheme for calculating state variables, using either volumes or finite elements.
- (ii) The solution of a restricted microscopic model, for the estimation of the missing data of the macroscopic mode.

The macroscopic and microscopic variables are related by operators of "compression" and "expansion" (**Engquist2007**), which are problem-dependent.

As an example a scheme for gas kinetics. The microscopic model in this case is the equation:

$$\frac{\partial f}{\partial t} + \mathbf{v} \cdot \nabla f = \frac{1}{\epsilon} B(f) \quad (1.2)$$

Where the microscopic variable  $f$  is the phase-space distribution function of a particle,  $B(f)$  is the collision kernel,  $\epsilon$  is the free path between two collisions. The macroscopic variables are the hydrodynamic variables, density  $\rho$ , velocity  $\mathbf{v}$  and energy density  $E$ , which are related to  $f$  as:

$$\rho = \int f dV, \mathbf{u} = \frac{1}{\rho} \int f \mathbf{v} dV, \text{ and } E = \int f \frac{|\mathbf{v}|^2}{2} dV \quad (1.3)$$

Where  $V$  is the integration volume. The equations 1.2 and 1.3 define the compression operator. If a finite volume scheme is chosen as the macroscopic scheme, the macroscopic fluxes at the boundaries of the cells, become the necessary data to calculate the microscopic model 1.2, subject to certain restrictions.

In the last two decades, the lattice method Boltzmann has gained popularity in the pore-scale area. Linking the Lattice Boltzman's method to a macroscopic flow in a heterogeneous environment is still an active area of research. It is well known that the lattice Boltzmann method can recover the continuity of the Navier-Stokes equations. (**Kang2002**) proposed a unified theory using the lattice Boltzmann method for fluid flow in heterogeneous media. In this work, the microscopic model uses the discrete lattice Boltzmann equation of 1.2 to model the particle velocity distribution function. The key in this work was to include an external force within the macroscopic model alternating between local and instantaneous velocities during the calculation of collisions. However, the marcoscopic permeability is a necessary data to calculate the external forces. The lattice Boltzmann scheme has also been applied to several synthetic problems with a field of random permeability and a system of fractures. The lattice Boltzmann method has shown good performance and is not just restricted to low Reynolds numbers, which makes it suited to model Darcy's law and Forchheimer's laws.

However, there are potential limitations to the lattice Boltzmann method, and other heterogeneous multiscale methods applied to the simulation of macroscopic flow in porous media:

- (i) The knowledge of the permeability is required, but in practice have stochastic behaviour. This has a big impact on the capacity of these multiphysics models of generating meaningful quantities of interest, reducing the usefulness of this family of multiscale method.
- (ii) Numerical results have been presented only for regular grid.
- (iii) The subject is relatively new with few applications.

### 1.2.2 Homogeneous multiscale modeling

The homogeneous multiscale methods are related to multigrid methods, domain decomposition methods, wavelet-based methods and mesh adaptation (**Engquist2007**). These methods embed

a fine discretization in a coarse discretization. In other words, multigrid methods and mesh adaptation methods can be grouped into schemes to solve EPDs using a hierarchical discretization, in which different submodels coexist in a computational infrastructure. The methods of domain decomposition divide the computational domain into subdomains such that the solution of each subdomain, can be efficiently obtained via parallel programming. The domain decomposition methods can also be used in combination with multigrid methods in infrastructures for parallel computing. The wavelet methods apply a transformation, to divide a given function into different components of frequencies, dedicated to solving certain resolutions that matches a given scale. This research uses a homogeneous multiscale method approach that is suited for the areas of hydrology and reservoir simulation. The table 1.1 summarizes some homogeneous multiscale methods found in the literature.

Method	Comments	Conservative	
Multiscale Finite Element method ( <b>Hou1997</b> )	It constructs basis functions to represent the effects of fine scales within the coarse scale incorporating sub-grid features. Localization of the effects of the fine scale is obtained through the boundary conditions on the coarse scale elements.	not	3D
Mixed Multiscale Finite Element method ( <b>Chen2003</b> )	Similar to <b>Hou1997</b> conservative velocity fields at both, the fine mesh and the coarse mesh level in the absence of source terms.	yes	2D
Subgrid Multiscale Finite Elements ( <b>Arbogast2006</b> )	The effects of the fine scale are modeled by considering, Green's functions at the boundary conditions at the coarse level using .	yes	2D
Mimetic Multiscale Finite Elements in corner point ( <b>Aarnes2008</b> )	This is a variant of <b>Chen2003</b> which generates conservative fields in the fine and coarse scales. The method is applied on corner point meshes, which are of common use in the simulation of reservoirs	yes	3D
Multiscale Finite Volumes ( <b>Jenny2003</b> )	This scheme of finite volumes, is easy to implement in any finite volume code.	yes	2D
Variational Multiscale Finite Element method ( <b>BadriNarayanan2005</b> )	This multiscale stochastic model uses a Galerkin approach through polynomial chaos expansion, for input and output of uncertainty representation.	not	2D
Multiblock Finite Element method ( <b>Arbogast2000; Wheeler2002</b> )	It uses mortar elements to connect meshed blocks with different geometries, while ensuring the preservation of local mass inside and between the entangled blocks. This method is easy to combine with domain decomposition.	yes	2D
Multiscale Hybrid-Mixed method ( <b>Paredes2013; Harder2013; Harder2015</b> )	This new family of multiscale methods, allows the solution of a pressure field and through a hybridization process, it obtains conservation at the coarse scale. This method is in theory equivalent to solving a global mixed problem. It is a technique with high parallel content.	yes	2D
Multiscale Hybrid-Mixed $H(\text{div})$ method (this research)	It is a variant of ( <b>Harder2013; Harder2015</b> ) that the subproblems are model with mixed higher order elements and the hybridization step is dropped out.	yes	3D

Table 1.1: Description of some multiscale methods found in the literature.

All methods mentioned in table 1.1, with the exception of 1 and 6, are varieties of mixed finite element formulations. For elliptic problems the mixed formulation involves solving a scalar variable and a vector variable simultaneously. The main features of mixed finite element approximations are: local conservation, continuous streamlines, and the same order of convergence between flux and pressure variable (**Wheeler2002**) or higher convergence order for the pressure (**Castro20163D**).

Following the contents of the table 1.1, many methods are essentially related to the calculation of the base functions. Associated with the interface between the blocks (skeleton) in the coarse scale

model, a corresponding base function  $\Pi_{ij}$  is used to incorporate the effect of fine scale permeability. These fine scale fluxes are related to a unknown potential  $\Phi_{ij}$ , but in the case of porous media and under the simplification of low Reynolds numbers, this potential is defined by Darcy's law.

$$\Pi_{ij} = -\mathbf{K}\nabla\Phi_{ij} \quad (1.4)$$

The functions  $\Pi_{ij}$  and  $\Phi_{ij}$  are obtained by solving a fine scale problem associated with each macro-domain subject to Neumann boundary conditions. The imposed boundary fluxes are piecewise polynomials, and ensure compatibility of boundary fluxes between each element at the coarse scale. These boundary fluxes are approximations of the true fluxes of the finer scale problem. Forcing unit flow conditions through the interfaces of the coarse blocks, generate better results than those obtained with schemes with constant or linear pressure functions (**Jenny2003**; **Aarnes2006**), and produce even richer solutions when adaptive meshes are used in the interior (**Devloo2016**). An important advantage of the use of mixed element approximations is that they generate conservative vector fields at both, the fine scale and coarse scale approximation.

There is a physical modelling limitation, which is associated to the volume of the elements used in the fine scale, since in many cases constitutive laws (e.g. 1.4) are derived from an analysis on a representative volume, in which is assumed that the law is valid (**Kang2002**). Thus, if the elements are smaller than the representative volume of the problem, it approximation generates discrepancies and reduces the relevance of the model.

A minimum requirements that a multiscale solver method must satisfy according to **Engquist2007** is that the performance ratio  $r_{per}$  satisfies:

$$r_{per} = \frac{\text{cost multiscale solver}}{\text{cost fine problem}} \ll 1 \quad (1.5)$$

The complexity of several of the mixed methods in table 1.1, tend to have a performance  $r_{per} \approx 1$ , which means that several of the schemes cited are equivalent to solving a global mixed problem in the fine scale, due to the fact that the bulk of the computational cost is associated with the computation of the basis functions.

At this point a relevant question arises, why do we use a homogeneous multiscale method, if the performance ratio  $r_{per} \approx 1$ ? The answer lies in parallelism and the answer is outlined in the following statements:

- (i) Applying the methods in table 1.1 in a parallel computing frameworks is often straight forward, because each problem of fine resolution is independent of the other. This results in solvers that can handle large problems with the requirement of local conservation subject to  $r_{per} \ll 1$ . Domain decomposition methods are generally used to handle large problems, but they introduce errors in the balance of the amount of interest.
- (ii) These multiscale methods offer significant savings in computational time for stochastic analysis of permeabilities or boundary conditions, because the shape functions can be calculated once or precomputed in a preprocessing strategies.

The main advantage of mixed finite element / multiscale finite volume methods is the facility for representing complex geometries, which in geological applications such as reservoir simulations

are important. They can represent geological units of great geometric irregularity. The use of these techniques surpasses the upscaling stage in reservoir engineering workflows, because the finer scale can be the geological model generated during the characterization of the reservoir, eliminating the uncertainties associated with the coarse scales and maintaining local conservation of mass. For this reason in this work a multiscale approach is adopted and is described in chapter 4.

## 1.3 Reduced base modeling

Numerical simulations associated with the coupling of deformations and fluid flow through porous media lead to very large systems of equations. The need for simulating these coupled problems justify the acquisition of large parallel computers, even more so when multiple evaluations of a large problem are necessary: either by the nonlinearity of the equations (iterative methods for non-linear systems) or by the solution of multiple realizations (e.g. Stochastic problems). Reducing the computational cost of these equation systems is the main objective of a reduced base model (RB) (Prudhomme2002; Prudhomme2004; Quarteroni2015). The field of study on base reduction is framed in a wide set of mathematical methods dedicated to the generation and evaluation of reduced models.

Reduced base modeling is applicable to a wide class of problems, in which the equations represent a physical system that is characterized by a finite number of parameters and where the objective is to obtain a high resolution approximation. An example of this type of systems is the simulation of the geomechanics response of a petroleum reservoir, where the coupling of the pressure associated with a flow system is coupled with the deformation of rocks. The parameter space associated with reduction, can be often related to material properties, but can also be associated with boundary conditions, initial conditions, source terms and/or the geometry of the problem. This appropriate choice of parametric dependence represents one of the main challenges for the construction of a reduced model. In the following subsection, it is presented a brief overview of the literature dedicated to development of reduced base models.

### 1.3.1 Applications of reduced base modeling

What is the importance and necessity of a reduction? In the design, control, optimization and quantification of uncertainty, there is a need to evaluate a model which can depend on a wide range of parameter values. Performing the full simulation for each of the parameters is prohibitive in terms of computational effort. For many reduced base models it is possible to define a strategy in which the total cost of the approximation can be divided into an offline step, in order to obtain a reduced base, that later allows the simulation of the large scale model at a substantially lower computational cost (Quarteroni2015).

**In design applications** Reduced base modeling is applied to a problem, when it is necessary to simulate the performance of a system over a range of values that represent certain critical design conditions. For example, a parametric reduced model captures the dynamic behavior between the fluid - structure interaction of an airplane, providing a rapid evaluation of the aeroelastic

behavior in a wide range of operating conditions (**Prudhomme2004; Lieu2006; Lieu2007**). The rapid assessment and characterization of the aircraft’s flight envelope is achieved using reduced base models. Calculating flight envelope without using a base reduction would require weeks of computational time. Reduced parametric models are also applied to the synthesis and design of semiconductors (**WHess2014**), as well as in electrochemical and electro-thermal applications.

**In controller design applications** Reduced base models are applied when it is necessary to characterize the dynamics of the system through the variation of parameters. For example, when controlling a numerical experiment in the fluid flow simulation, where the Reynolds number or the shape of the geometry are varied (**Hay2009; Mathelin2009**). Redesigning a new controller require obtaining a very fast response for a given set of parameters. The full simulation can not be computed fast enough for an online controller. Instead of designing a controller for each set of parameters, it is possible to use a reduced base model that can be used to adjust the controller for the full range of parameters using a minimal computational effort. In summary, predictive control models can be implemented, using a computationally fast approximated model to control the system of interest. Reduction of predictive models have been developed and applied for the control of a variety of systems, either parametrized (**Amsallem2013**) or not parametrized (**Hovland2008**).

**In uncertainties quantification** When the computation model depend on parameters with stochastic distributions, the repeated evaluation of models, often thousands millions, are computed to sample the space of uncertainty, e.g. using Monte Carlo sampling. In **BuiThanh2008** the definition of the most likely realizations in a complex CDF model are achieved at reasonable computation cost for a design purposes, using reduced base models. In **Elman2013** a parametric reduced base model is applied to the approximation of a PDE governed by coefficients that vary randomly, and without an essential loss of accuracy. In **Wang2005; Galbally2009; Lieberman2010; Druskin2013** a reduced parametric model is used to significantly reduce the computational time in the approximation of large inverse problems. The solution of a reverse statistical problem using Monte Carlo sampling, applied to the full scale model becomes intractable for two reasons: it requires excessive amount of CPU time and/or the parameter space becomes so large, that it can not be explored by the traditional sampling methods.

**In reservoir simulation** According to **Ghasemi2014** high-resolution simulation models are still a challenging task, despite the introduction of high-performance computing and improved solvers. High resolution models requires the solution of nonlinear systems of equations using the computational resources available. The computational efficiency of the models is essential, because they will be applied to the optimization or evaluation of uncertainty quantification. In order to optimize the simulation process, several reduced base models have been proposed for the simulation of fluid flow in porous media (**Cardoso2010; Efendiev2012; Ghasemi2014; Afra2014**). However, all of these applications introduce errors in the mass balance, a property that is fundamental in reservoir simulation (**Chen2000**). The development of reduced base models that maintain local conservation still remains a challenge.

The solution of geological models coupled with geomechanics poses a challenge, since the computational cost associated with the coupling is large or prohibitive. When performing the literature review, there is not direct applications of the reduced base approximations to reservoir geomechanics. In **Rumpler2013** a base reduction is applied to the poroacoustic simulation of the biot poroelasticity problem. In this research 2D / 3D simulations were performed to approximate the response modes of an acoustic cavity. Their work generate a reduced base model for the fluid flow that is not conservative.

In this research a novel reduction strategy is proposed, where the reduced base is applied only to the elastic contribution of the geomechanical coupling. This approach allows to obtain a locally conservative scheme for the flow equations, without an essential overall loss of accuracy in the approximation.

### 1.3.2 Base reduction and surrogate modeling

Base reduction is an approach in numerical simulation, that can be associated with the more general category of surrogate models. Surrogate models are applied to the reduction of the computational time in applications of design, control, optimization and uncertainty. According to **Eldred2006** surrogate models fall into three different categories:

- (i) Data-fit models: They involve the interpolation or regression of the response surface obtained from the simulation data. This interpolation is used to adjust the system responses as a function of the parameters of the system. In **Kennedy2001** surrogate models are applied to statistical analysis of different mathematical models. Bayesian calibration is used as a fitting process to obtain the response surface. In **Kaufman1996; Venter1998; Eldred2004** polynomials are used to obtain response surface, in **Wild2008** radial functions are used, and in **Simpson2001** for kriging models.
- (ii) Projection-based models: The basic idea is to perform a series of projections of the operators onto a reduced subspace, which has a smaller dimension (**Prudhomme2002; Prudhomme2004; Quarteroni2015**).
- (iii) Hierarchical models: These methods include approximations such as simplifications of the physical model, reduction of resolution processes (amalgamate elements), alternative expansions of the base functions, and approaches subject to large residues. Examples in the literature, that use a simplified physics in reservoir simulation are (**Havlena1963; Siddiqui2010; Shams2016**) or in the design (**Alexandrov2001; March2012**), multigrid approaches for PDE's and mesh amalgamation for the solution of inverse problems (**Arridge2006**) or direct problems (**Durlofsky1991**).

Each of the three classes of surrogate models have their field of application. Models with simplified physics are typically used when their application has an engineering interest. Generally data fit and projection base reduction are derived mathematically and aim high fidelity simulations.

A significant advantage of the data fit models, is these approaches have an offline phase, that does not affect the structure of the original model. The substitute model is evaluated as a black

box, where the only difficulty is to feed the model with a set of parameters to predict the behavior of the system.

The offline process of a reduced base model has a large impact on the implementation because it requires the projection of the associated PDE on a subspace of smaller dimension. An advantage of a projection-based reduction is that the reduced model maintains the mathematical structure of the model. This feature is important in the modeling of dynamical systems, having the benefit of allowing to reconstruct the full system state. Dynamic problems modeled using a data fit approach represent a challenge and typically lead to a loss of flexibility which is an essential characteristic of a surrogate models. Another advantage of a projection-based reduction is that this approach allows a rigorous infrastructure, for the definition of theoretical error limits, and even error estimates (**Arridge2006**).

In summary, the reduction by projections keeps the mathematical structures intact and can be applied to dynamic problems. In this research, reduced base model is proposed for the modeling of geomechanical coupling. This technique of reduction is presented in chapter [3](#).

## 1.4 Conclusions

From this bibliographic review is possible to conclude:

- (i) In reservoir simulation, there still exists interest in the development of algorithms for high resolution models or using the geological model directly.
- (ii) Where no references found, on base reduction applied to geomechanical coupling. This research, proposes a novel solution to the use of a reduction base method, determined by projections.
- (iii) Multiscale heterogeneous methods required microscopic models, that are used to simulate physics at a microscopic level, they are used to generate the approximated data, needed in physics describing the macroscopic scale. Multiscale heterogeneous methods is still an active area of research, and it is necessary to investigate the applicability of this technique.
- (iv) Homogeneous multiscale methods include a wide range of different theoretical and numerical approaches, with the following characteristics:
  - (i) These methods generally assume that the set of differential equations are applicable in different resolutions within the macroscopic scale. The method turns out inconsistent, when the discrete volumes become smaller than the representative volume, where the constitutive law prevails and is developed for.
  - (ii) The multiscale mixed finite element methods are flexible in terms of geometric representation and are applicable to real applications. They offer advantages in relation to current upscaling techniques, because the fine scale characteristics of the solution are immediately reconstructed. The reconstruction of the fine scales (i.e. the deformation of the geological solid) is needed at each step in the modeling of a reservoir. These methods can be easily implemented in parallel computers.

# **Part I**

## **Numerical Tools**

# Chapter 2

## Finite element method

From the mathematical point of view, most of physical phenomena are governed by Partial Differential Equations (PDE). This general statement applies to the case of the physics related to multiphase flow in a deformable porous media, which is the focus of this study. Many numerical methods have been applied to the numerical simulation of reservoir engineering, among which are finite difference methods (**Das1994; Ertekin2001; Fanchi2005**), finite volume method (**Forsyth1990; Fung1992; Marcondes2010**) and also finite elements (**Chavent1986mathematical; Chen2003; Arbogast2006; Aarnes2006; Efendiev2009**). Especially recognized for its versatile properties, the Finite Element Method (FEM) is particularly suitable for complex geometries, such as the ones encountered in models of oil reservoirs, aquifers and geologic structures.

A general description of the finite element method is given by (**BrezziFortin1991; Ciarlet2002**). In this section FEM is presented as the basis of all further developments of this work. All implementations are codified in the **Neopz** environment. The first part of this section is dedicated to review of the definitions and the characteristics of the standard finite elements namely the  $L^2$  discontinuous spaces,  $H^1$ -conforming,  $H_{div}$ -conforming and multiphysics approximation spaces already incorporated in Neopz. A description of them can be found in the following references:

- (i)  $L^2$  discontinuous spaces (**Forti2010**)
- (ii)  $H^1$ -conforming hierarchical finite elements (**Devloo2009**)
- (iii)  $H(div)$ -conforming hierarchical finite elements (**DeSiqueira2013; Devloo2016**)
- (iv)  $H(div)$ -conforming finite elements using piola transformations in (**Castro20162D; Castro20163D**)
- (v) A multiphysics combination of all theses approximation spaces (**Farias2014**)

The approximation spaces above are used in the considered examples and models. Excluding  $H(div)$ -conforming space using piola transformations, the development of the approximation spaces above do not represent a codified contribution of this investigation, since they were already fully available. However, verifying the consistency through examples and convergence rates of all this assessment allows to take the next step, which focuses on other finite element types as essential ingredients of the multi-physics model described in the part [II](#). The main requirement for

the development of the MHM- $H$  ( $div$ ) method in this study, is composed of several approximation space implementations and applying them to the water-oil reservoir equations (**Chen2000**) coupled with linear Biot's poroelasticity. The implementation of the multiscale methodology within Neopz as well as its verification represents an important contribution of this research.

## Contents

---

2.1	$L^2(\Omega)$ approximation space	29
2.2	$H^1(\Omega)$ -conforming approximation space	30
2.2.1	$H^1(\Omega)$ scalar shape functions	30
2.3	$H(div, \Omega)$ -conforming approximation space	31
2.3.1	Neopz: the construction of $H(div, \Omega)$ -conforming spaces	32
2.3.2	Application to finite element formulations	37
2.3.3	Numerical example - Curved mesh:	39
2.3.4	Numerical example - Linear mesh:	42
2.4	Conclusions	46

---

One of the first formal descriptions of **Ciarlet2002** states the equivalence of the solution of a PDE's and its weak formulation. The solution  $u$  defined on an arbitrary domain  $\Omega$  can be found as follows:

$$Find u \in X(\Omega) \mid a(u, v) = f(v) \quad \forall v \in X(\Omega) \quad (2.1)$$

where  $X(\Omega)$  represents and Hilbert space,  $a : X(\Omega) \times X(\Omega) \rightarrow \mathbb{R}$  is a continuous form, and  $f : X(\Omega) \rightarrow \mathbb{R}$  is a continuous linear form.

**Galerkin method** The importance of the above weak statement is that it forms the basis of an approximation method that converts the continuous problem (2.1), into an algebraic problem associated with a finite dimensional space:

$$Find u_N \in X_N(\Omega) \mid a(u_N, v_N) = f(v_N) \quad \forall v_N \in X_N(\Omega) \quad (2.2)$$

the solution  $u_N$  is a linear combination of basis functions  $\{\phi_i\}_{1 \leq i \leq N}$  in  $X_N$ :

$$u_N = \sum_{j=1}^N u_N^j \phi_j \text{ with } X_N(\Omega) = \langle \phi_i \rangle_{i=1}^N \quad (2.3)$$

When applying the methodology of the weak statement associated with a conservation law to nonlinear problem, the bilinear form  $a(u, v)$  remains linear in  $v$ , but is nonlinear in  $u$ . Taking the jacobian of the  $a(u_N, v_N)$  with respect to  $u_N$  a tangent matrix is obtained (often called the stiffness matrix)  $A_N \in \mathbb{R}^{N \times N}$  and the associated vector  $B_N = f(\phi_i)$ . The vector  $\alpha_N = (u_N^0, \dots, u_N^N)$  as

the solution of the system can then be used to update the solution of the nonlinear system of equations.

$$A_{\mathcal{N}} \alpha_{\mathcal{N}} = B_{\mathcal{N}} \quad (2.4)$$

**Finite element definition** The Galerkin approximation (2.2) is based on the knowledge of the discrete subspace  $X_{\mathcal{N}}(\Omega)$  and the weak statement associated with the system of partial differential equations. The definition of this approximation space is determined by the definition of the weak statement. Thus, a FEM approximation defines the  $X_{\mathcal{N}}(\Omega)$  and it has three main components (**Ciarlet2002**):

- (i)  $K$  is a geometrical element of the partition  $\Gamma_h$  on a the domain  $\Omega$ .
- (ii)  $P(K)$  is a piecewise polynomial space of finite dimension which forms the basis  $\{\phi_i\}_{1 \leq i \leq N}$ .
- (iii)  $\Sigma_K$  Set of functionals which consist of degress of freedom  $\alpha_{\mathcal{N}}$ .

Thus, FEM method provides a systematic way to define the discrete subspace  $X_{\mathcal{N}}$  required to solve (2.4).

Some contributions of this research has been dedicated to the definition and implementation of two and three dimensional  $H(\text{div}, \Omega)$  approximation spaces, which are particularly suited to model parabolic conservation laws.

**Geometrical transformation** The partition of  $\Omega$  is a set  $\Gamma_h = \{K\}$  of non-empty elements (i.e. geometric elements)  $K \in \Gamma_h$ . In **Neopz** the geometric elements are either, points (0D), lines (1D), triangles (2D), quadrangles (2D), tetrahedrons (3D), prims (3D) or pyramids (3D), and can be curved or not (**Lucci2009**).

The finite element approximation space combines each geometric element  $K$  with its approximation space  $P(K)$ , and multiplying coefficients  $\alpha_{\mathcal{N}}$ , defining an element wise basis functions. In order to compute a finite element integral, is necessary to associate a reference element  $\hat{K}$  with  $P(\hat{K})$ . Each real element  $K \in \Gamma_h$  is a image of  $\hat{K}$  under a transformation  $T_K^{geo}$  as is shown in the figure 2.1

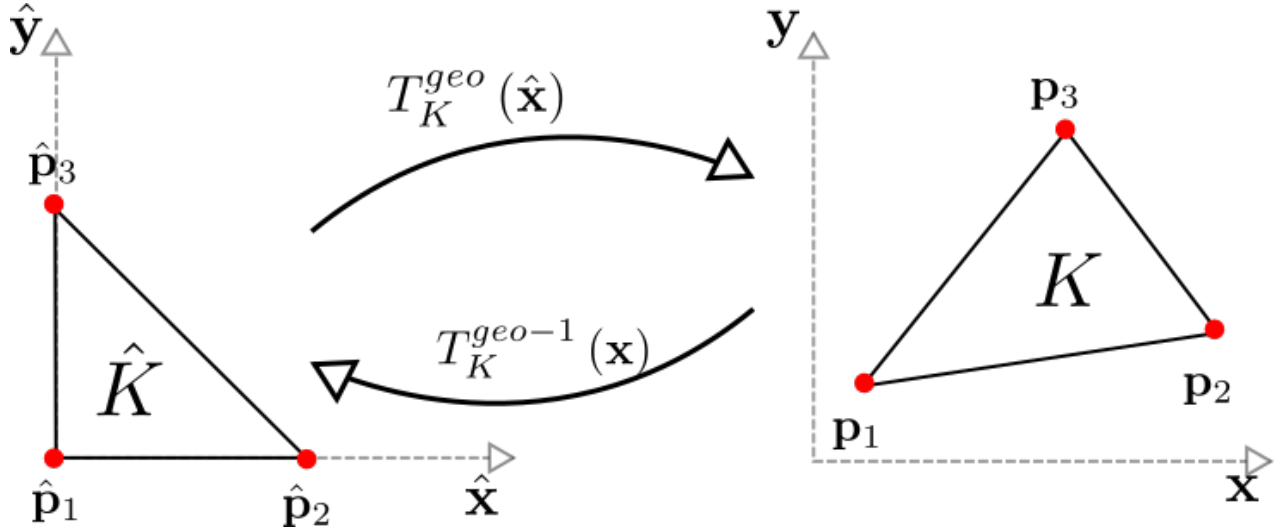


Figure 2.1: Geometrical transformation on a triangle.

Using the transformation  $T_K^{geo}$  and its inverse, all integrals performed on  $K$  elementary computations can be transformed into integrals on the reference element, which induces the knowledge Jacobian of the transformation. In this context, let denote  $J_K^{geo}$  the jacobian matrix of  $T_K^{geo}$ , and  $\det(J_K^{geo})$  its determinant. The shape functions of the element  $\{\phi_i\}_{i=1}^N$  (2.5) are deduced from the definition of shape functions on the reference basis  $B_k^{\hat{K}} = \{\hat{\phi}_i\}_{i=1}^N$  by combination of the geometric transformation  $T_K^{geo}$ .

$$\phi_i(T_K^{geo}(\hat{x})) = \hat{\phi}_i(\hat{x}) \quad (2.5)$$

**The DeRham complex diagram** Specifically, when using mixed formulations for the weak statement, the approximation space  $X(\Omega)$  has to be carefully chosen to such that the divergence of its elements can be represented by a member of its corresponding space of Lagrange multipliers. As mentioned in **Boffi2013** the so-called De Rham complex diagram (2.7) establishes a sequence relating spaces from the main differential operators. If the projection operators, between the continuous and discrete spaces can be defined, such projections commute then, and it can be shown that the vector space (flux) and the scalar (potencial) space are compatible.

Introducing the standard differential form spaces, where  $d$  is the dimension of  $\Omega$

$$\begin{aligned} L^2(\Omega) &= \left\{ f \mid \int_{\Omega} f^2 d\Omega < \inf \right\} \\ H^1(\Omega) &= \left\{ f \in L^2(\Omega) \mid \nabla f \in [L^2(\Omega)]^d \right\} \\ H(div, \Omega) &= \left\{ \mathbf{f} \in [L^2(\Omega)]^d \mid \nabla \cdot \mathbf{f} \in L^2(\Omega) \right\} \\ H(curl, \Omega) &= \left\{ \mathbf{f} \in [L^2(\Omega)]^d \mid \nabla \times \mathbf{f} \in L^2(\Omega) \right\} \end{aligned} \quad (2.6)$$

The De Rham complex diagram is expressed as the following sequence:

$$\mathbb{R} \rightarrow H^1(\Omega) \xrightarrow{\text{grad}} H(\text{curl}, \Omega) \xrightarrow{\text{curl}} H(\text{div}, \Omega) \xrightarrow{\text{div}} L^2(\Omega) \rightarrow \{0\} \quad (2.7)$$

The range of each operator relating two spaces in (2.7), coincides with the null space of the next operator.

The discrete compactness property of the De Rham complex diagram, makes it valuable for the selection of discrete finite element space  $X_N \subset X$ . Denoting  $\pi_N : X \rightarrow X_N$  the galerkin interpolation operator resulting in discrete spaces  $V_N = \pi_N^U(H^1(\Omega))$ ,  $U_N = \pi_N^V(H(\text{curl}, \Omega))$ ,  $W_N = \pi_N^W(H(\text{div}, \Omega))$  and  $Z_N = \pi_N^Z(L^2(\Omega))$ , the De Rham complex (2.7) turns out:

$$\begin{array}{ccccccccc} \mathbb{R} & \rightarrow & H^1(\Omega) & \xrightarrow{\text{grad}} & H(\text{curl}, \Omega) & \xrightarrow{\text{curl}} & H(\text{div}, \Omega) & \xrightarrow{\text{div}} & L^2(\Omega) & \rightarrow & \{0\} \\ & & \downarrow \pi_N^V & & \downarrow \pi_N^U & & \downarrow \pi_N^W & & \downarrow \pi_N^Z & & \\ \mathbb{R} & \rightarrow & V_N & \xrightarrow{\text{grad}} & U_N & \xrightarrow{\text{curl}} & W_N & \xrightarrow{\text{div}} & Z_N & \rightarrow & \{0\} \end{array} \quad (2.8)$$

As was stated in the previous section, this chapter describes the finite element spaces used in the development of the 3D multi-physics model for mutliphasic flow in oil reservoirs. Especially, the De Rham diagram (2.8) compatibility was checked for the  $H(\text{div}, \Omega)$  approximation spaces for fluxes, and corresponding  $L^2(\Omega)$  approximation spaces for pressures. In this research, a special contribution is on the development and verification of  $H(\text{div}, \Omega)$  approximation spaces for three dimensional topologies. Their implementation within the library is detailed in section 2.3, it represents a key contribution for the framework.

## 2.1 $L^2(\Omega)$ approximation space

From the implementation point of view, this is the most simple finite element space and it is suitable when the solution resides in  $L^2(\Omega)$  Hilbert space (2.6)

$$L^2(\Omega) = \left\{ f \mid \int_{\Omega} f^2 d\Omega < \inf \right\} \quad (2.9)$$

The Hilbert space  $L^2(\Omega)$  (2.14) has inner product:

$$(u, v) \equiv (u, v)_{L^2} := \int_{\Omega} u \cdot v d\Omega \quad (2.10)$$

which defines the  $L^2$  norm

$$\|\cdot\|_{L^2} := \sqrt{(\cdot, \cdot)_{L^2}} \quad (2.11)$$

and the projection operator  $\Pi_{L^2}$  which defines the projection  $\Pi_{L^2}f$  of any function  $f \in X$  into  $Y \subset L^2(\Omega)$

$$(\Pi_{L^2}f, v)_{L^2} = (f, v)_{L^2} \quad \forall v \in Y \quad (2.12)$$

From the definitions above, the Galerkin continuous and finite subspace for  $L^2(\Omega)$  turns out

$$Z = \{z \in L^2(\Omega)\} \quad (2.13)$$

$$Z_N = \left\{ z \in L^2(\Omega) : T_K^{geo-1}(z|_K) \in P(\hat{K}) \right\} \quad (2.14)$$

As a hierarchical basis  $B_k^{\hat{K}}$  of  $P(\hat{K})$ , a scaled Chebyshev polynomials of first kind with arbitrary order  $0 \leq k$ . Further details about the implementation of these spaces can be found in **Forti2010; Farias2014**

## 2.2 $H^1(\Omega)$ -conforming approximation space

The basis functions of  $H^1(\Omega)$  are based on a hierarchical approximation space (**Devloo2009; DeSiqueira2013**). This class of basis is suitable for problems whose solution resides in  $H^1(\Omega)$  Hilbert space (2.6), it is defined as:

$$H^1(\Omega) = \left\{ f \in L^2(\Omega) \mid \nabla f \in [L^2(\Omega)]^d \right\} \quad (2.15)$$

The Hilbert space  $H^1(\Omega)$  (2.15) is associated with the standard inner product:

$$(u, v)_{H^1} := (u, v)_{L^2} + (\nabla u, \nabla v)_{L^2} \quad (2.16)$$

which defines  $H^1$  norm:

$$\|\cdot\|_{H^1} := \sqrt{(\cdot, \cdot)_{H^1}} = \sqrt{\|\cdot\|_{L^2}^2 + \|\nabla(\cdot)\|_{L^2}^2} \quad (2.17)$$

and the projection operator  $\Pi_{H^1}$  which defines the projection  $\Pi_{H^1}f$  of any function  $f \in X$  into  $Y \subset H^1(\Omega)$

$$(\Pi_{H^1}f, v)_{H^1} = (f, v)_{H^1} \forall v \in Y \quad (2.18)$$

From the definitions above, the finite subspace for  $H^1(\Omega)$  in this case is:

$$V_N = \left\{ v \in H^1(\Omega) : T_K^{geo-1}(v|_K) \in P(\hat{K}) \right\} \quad (2.19)$$

For the sake of clarity of the next development, the description of these functions is outlined for  $K_T$  (Tetrahedron),  $K_P$  (Prism) and  $K_H$  (Hexahedron), but noting that all these functions apply for lines, triangles, quadrangle, and pyramids.

### 2.2.1 $H^1(\Omega)$ scalar shape functions

The scalar shape functions  $\hat{\phi}$  are associated with one of the sides of  $\hat{K}$ , namely, vertex, edge, face or the volume  $\hat{K}$  itself, and are characterized by the following main properties:

- Vertex functions  $\hat{\phi} = \phi^{\hat{a}}(\hat{\mathbf{x}})$ : traditional Lagrangian first order basis functions, such that  $\phi^{\hat{a}}(\hat{a}) = 1$ , vanish in all vertices different from  $\hat{a}$ , edges and faces not sharing the vertex  $\hat{a}$ .
- Edge functions  $\hat{\phi} = \hat{\phi}^{\hat{e},n}(\hat{\mathbf{x}})$ : they vanish in all edges different from  $\hat{e}$ , and in all faces not sharing  $\hat{e}$ .
- Face functions  $\hat{\phi} = \hat{\phi}^{\hat{f},n_1,n_2}(\hat{\mathbf{x}})$ : they vanish in all edges, vertices, and faces, other than  $\hat{f}$ .
- Internal functions  $\hat{\phi} = \hat{\phi}^{\hat{K},n_1,n_2,n_3}(\hat{\mathbf{x}})$ : they vanish in all faces, edges and vertices of  $\hat{K}$ .

	Vertex $\hat{a}$	Edge $\hat{e}$	Face $\hat{f}$	Internal $\hat{K}$	Total
$K_T$	4	$6(k-1)$	$\frac{1}{2}(k-1)(k-2)$	$\frac{1}{6}(k-1)(k-2)(k-3)$	$\frac{1}{6}(k+1)(k+2)(k+3)$
$K_P$	6	$9(k-1)$	$(k-1)(4k-5)$	$\frac{1}{2}(k-1)^2(k-2)$	$\frac{1}{2}(k+1)^2(k+2)$
$K_H$	8	$12(k-1)$	$6(k-1)^2$	$(k-1)^3$	$(k+1)^3$

Table 2.1: Number of scalar shape functions  $B_k^{\hat{K}}$  of  $P(\hat{K})$ .

The shape functions associated with edge, face and internal sides are formed by the product of two functions. The first function, called blending function, is a specific combination of products of vertex functions. There is one blending function for each edge, face and volume of an element; and its role is to enforce the corresponding vanishing property on the other sides. In order to increase the degrees of the shape functions, the blending functions are multiplied by a second function formed by the product of Chebyshev polynomials (of degree  $n$  or  $n_i$ ), which vary according to a particular geometry. These Chebyshev polynomials are evaluated in parameters determined by appropriate affine transformations of the reference element coordinates  $\hat{\mathbf{x}}$ .

The resulting set of functions:

$$B_k^{\hat{K}} = \left\{ \phi^{\hat{a}}, \hat{\phi}^{\hat{e},n}, \hat{\phi}^{\hat{f},n_1,n_2}, \hat{\phi}^{\hat{K},n_1,n_2,n_3} \right\} \quad (2.20)$$

$B_k^{\hat{K}}$  is linear independent, spanning a subspace of  $H_1(\hat{K})$ . The total numbers of each type of shape functions in  $B_k^{\hat{K}}$  are indicated in table 2.1. **Devloo2009** provides further details of the functions (2.20) for all topologies available in **Neopz**

## 2.3 $H(\text{div}, \Omega)$ -conforming approximation space

$H(\text{div}, \Omega)$ -conforming basis are important for the approximation of conservation laws, when local mass conservation is crucial (**Chavent1982**; **Chavent1986mathematical**; **Chen2000**).

$H(\text{div}, \Omega)$  Hilbert space (2.6) is defined as:

$$H(\text{div}, \Omega) = \left\{ \mathbf{f} \in [L^2(\Omega)]^d \mid \nabla \cdot \mathbf{f} \in L^2(\Omega) \right\} \quad (2.21)$$

The Hilbert space  $H(\text{div}, \Omega)$  (2.21) is associated with the standard inner product

$$(\mathbf{u}, \mathbf{v})_{H(\text{div})} := (\mathbf{u}, \mathbf{v}) + (\nabla \cdot \mathbf{u}, \nabla \cdot \mathbf{v}) \quad (2.22)$$

which defines the  $H(\text{div}, \Omega)$  norm:

$$\|\cdot\|_{H(\text{div})} := \sqrt{(\cdot, \cdot)_{H(\text{div})}} = \sqrt{\|\cdot\|_{L^2}^2 + \|\nabla \cdot (\cdot)\|_{L^2}^2} \quad (2.23)$$

and the projection operator  $\Pi_{H(\text{div})}$  which defines the projection  $\Pi_{H(\text{div})}\mathbf{f}$  of any function  $\mathbf{f} \in Y \subset H(\text{div})$  such that:

$$(\Pi_{H(\text{div})}\mathbf{f}, \mathbf{v})_{H(\text{div})} := (\mathbf{f}, \mathbf{v})_{H(\text{div})} \quad \forall \mathbf{f} \in Y \quad (2.24)$$

Find the solution  $\mathbf{u}_N \in X_N \subset H(\text{div}, \Omega)$  using finite element method, requires approximation spaces which meet  $H(\text{div})$  conditions. Especially, it is necessary to ensure the continuity of the normal component  $\mathbf{u}_N \cdot \mathbf{n}$  of the solution  $\mathbf{u}_N$ , along the interfaces between elements of the mesh  $\Gamma_h$ .

### 2.3.1 Neopz: the construction of $H(\text{div}, \Omega)$ -conforming spaces

This section focuses on the development of  $H(\text{div}, \Omega)$ -conforming finite element spaces for flux approximations, which can be applied to curved/linear 3D elements of different topologies (tetrahedral, hexahedral or prismatic). The development of 3D approximations are an extension of 2D dimensional elements, which are documented in **Castro20162D** for regular meshes and in **Devloo2016** for hp-adaptative meshes. Alternative construction of  $H(\text{div}, \Omega)$  space is documented in **DeSiqueira2013**. The vectorial shape functions for these spaces, use appropriate constant vector fields, defined on the geometry of the master elements multiplied by a set of  $H^1(\Omega)$ -conforming hierarchical scalar basis of any degree  $k$ .

There are two families of shape functions in this methodology: Interior functions, with vanishing normal components over all element faces; Face functions that have normal component on the face associated with them coinciding with the restriction of the corresponding scalar shape function used in their definition, and vanishing over the other faces. The shape functions defined on the master element are then mapped to the actual geometrical elements, by the Piola transformation, and assembled in order to get continuous normal components.

Following the developments by **Castro20162D** for affine elements, two stable configurations for approximation spaces are considered for curved meshes, that produce different orders of accuracy for the primal variable ( $k+1$ ) of ( $k+2$ ), while maintaining the order of accuracy ( $k+1$ ) for the flux variable. The stabilization is obtained by increasing the polynomial order of the flux spaces, associated with the internal shape functions, while keeping the polynomial order of the border fluxes of degree  $k$ . In all the cases, the choices of approximation spaces are guided by the property: at the level of the reference element  $\hat{K}$ , the image of the dual space by the divergence operator coincides with the primal space.

The methodology used for the construction of approximation spaces, follows a sequence of steps described below. This research is concerned with hexahedral, tetrahedral or prismatic meshes. Pyramids are left for future works.

- (i) Associated with each  $K$ , an isomorphism  $\mathbb{F}: \hat{\phi} \rightarrow \phi$  mapping  $H^1(\hat{K})$  to scalar functions  $H^1(K)$  (2.5), is induced by the transformation  $T_K^{geo}$ . It also induces a contravariant Piola transformation  $\mathbb{F}_{div}: \hat{\phi} \rightarrow \phi$ , that is a isomorphism mapping vector fields  $\hat{\phi} \in H(div, \hat{K})$  to vector fields  $\phi \in H(div, \Omega)$  in the actual geometry.
- (ii) Polynomial spaces  $P(\hat{K})$  and hierarchical basis  $B_k^{\hat{K}}$  on  $P(\hat{K})$  are provided. For the tetrahedra, the polynomials in  $P(\hat{K})$  have a total degree  $k$ , for hexahedra. They have maximum degree  $k$  in each coordinate and for prismatic elements,  $P(\hat{K})$  is formed by polynomials of total degree  $k$  ( $\hat{x}_0, \hat{x}_1$ ) and of maximum degree  $k$  in  $\hat{x}_2$ .
- (iii) Constant vectors fields  $\hat{\mathbf{v}}$  are defined over  $\hat{K}$ . These fields are classified as being of face or internal functions. A field associated with a given face has nonzero normal component on the face, and zero normal component on all other faces. The internal fields are associated with the interior of  $\hat{K}$  and have zero normal component on all faces.
- (iv) A family of hierarchical vectorial bases  $\mathbf{B}_k^{\hat{K}} = \{\hat{\phi}_i\}_{i=1}^N$  is obtained. The principle in their construction is to multiply a scalar basic function  $\hat{\phi} \in B_k^{\hat{K}}$  by a vector field  $\hat{\mathbf{v}}$ , in order to get  $\hat{\phi} = \hat{\phi}\hat{\mathbf{v}}$ . The shape functions of interior type, have vanishing normal components over all element faces. Otherwise,  $\hat{\phi}$  has nonzero normal component only on one face that is associated with itself.
- (v) A vectorial basis  $\mathbf{B}_k^{\hat{K}}$  is defined over  $K$  by the Piola transformation  $\phi = \mathbb{F}_{div}(\hat{\phi})$ .
- (vi) Construction of approximation spaces  $W_N \in H(div, \Omega)$  formed by functions  $\mathbf{q} \in [L_2(\Omega)]^d$ , which are defined piecewise over the elements of  $\Gamma_h$  by local functions  $\mathbf{w} = \mathbf{w}|_K \in \mathbf{B}_k^{\hat{K}} \subset H(div, \Omega)$ . They can be assembled to get continuous normal components on the elements interfaces. This property is obtained as a consequence of the particular properties verified by the proposed vectorial shape functions, and of the continuity of the scalar shape functions used in their construction.

A detailed description of these steps are given in the next subsections. The case of two-dimensional geometries have already been discussed in **DeSiqueira2013** for uniform affine partitions, and in **Devloo2016** for hp-adaptive affine meshes. A detailed explanation is given in **Castro20163D** for 3D affine elements. Preliminary results in uniform curved meshes in 2D regions or manifolds immersed in R3 are presented in **Castro20162D**. The description here applies to 3D curved hp-adaptive partitions, without limitation on hanging faces and/or distribution of polynomial degrees.

## Vector fields

Connected to each basic geometric side of  $\hat{K}$ , (vertex, edge, face or volume), three linearly independent constant vector fields are defined using the following guidelines:

- (i) For each vertex  $\hat{a}$ , there are three fields  $\mathbf{v} = \mathbf{v}^{\hat{f}, \hat{a}}$ , each one associated with a face  $\hat{f}$  having  $\hat{a}$  as one of its vertices. The vector  $\mathbf{v}^{\hat{f}, \hat{a}}$  should be aligned to the edge adjacent to  $\hat{f}$  by the vertex  $\hat{a}$ . Furthermore, the vectors have constant normal component over  $\hat{f}$ .
- (ii) For each edge  $\hat{e}$ , there is a vector  $\mathbf{v} = \mathbf{v}^{\hat{e}, \parallel}$ , aligned to  $\hat{e}$  and there are two vectors  $\mathbf{v} = \mathbf{v}^{\hat{f}, \hat{e}}$ , which are incident to  $\hat{e}$  and parallel to the face adjacent to  $\hat{f}$  by  $\hat{e}$ .
- (iii) For each face  $\hat{f}$ , there is an outward normal  $\mathbf{v} = \mathbf{v}^{\hat{f}, \perp}$  vector and two linearly independent vectors  $\mathbf{v} = \mathbf{v}_j^{\hat{f}, \parallel}$ ,  $j = \{1, 2\}$  tangent to  $\hat{f}$ .
- (iv) With the volume  $\hat{K}$  itself, three orthonormal vector fields  $\mathbf{v} = \mathbf{v}_j^{\hat{K}} = \mathbf{e}_j$ ,  $j = \{1, 2, 3\}$  are associated. They can be defined by the canonical orthonormal vectors  $\mathbf{e}_1 = (1, 0, 0)$ ,  $\mathbf{e}_2 = (0, 1, 0)$  and  $\mathbf{e}_3 = (0, 0, 1)$ .

The vector fields are grouped into two categories:

1. Face vector fields, which are all vectors that have nonzero normal component over a face  $\hat{f}$ :
  - (a)  $\mathbf{v} = \mathbf{v}^{\hat{f}, \hat{a}}$ , vectors associated with the vertices  $\hat{a}$  of  $\hat{f}$ .
  - (b)  $\mathbf{v} = \mathbf{v}^{\hat{f}, \hat{e}}$ , vectors associated with the edges  $\hat{e}$  of  $\hat{f}$ .
  - (c)  $\mathbf{v} = \mathbf{v}^{\hat{f}, \perp}$ , vectors associated with the face  $\hat{f}$  itself (normal ones).
2. Internal vector fields, which have zero normal component over all faces:
  - (a)  $\mathbf{v} = \mathbf{v}^{\hat{e}, \parallel}$ , vector aligned to the edges  $\hat{e}$ .
  - (b)  $\mathbf{v} = \mathbf{v}_j^{\hat{f}, \parallel}$ ,  $j = \{1, 2\}$  vectors tangent to the faces  $\hat{f}$ .
  - (c)  $\mathbf{v} = \mathbf{v}_j^{\hat{K}} = \mathbf{e}_j$ ,  $j = \{1, 2, 3\}$  associated with the volume  $\hat{K}$ .

## Vector basis functions in $H_{div}(\hat{K})$

The purpose is to construct vector bases  $\mathbf{B}_k^{\hat{K}}$  formed by the product of functions  $\hat{\phi} \in H_{div}(\hat{K})$  defined on the element  $\hat{K}$  with a vector field:

$$\hat{\phi} = \hat{\phi} \mathbf{v} \quad (2.25)$$

where  $\mathbf{v}$  is previously defined as constant vector field on  $\hat{K}$ , and  $\hat{\phi}$  is the scalar basis functions (2.20) defined in the subsection (2.2.1). On the master element the following property hold:  $\nabla \cdot (\hat{\phi}) = \mathbf{v} \cdot \nabla (\hat{\phi})$ , which implies that  $\hat{\phi} \in H_{div}(\hat{K})$ . These vectorial shape functions shall be classified as face or internal functions, verifying the following properties:

## Face functions:

- Face functions  $\hat{\phi}^{\hat{f}, \hat{a}} = \hat{\phi}^{\hat{a}} \mathbf{v}^{\hat{f}, \hat{a}}$  vanish on the face that do not have  $\hat{a}$  as one of its vertices because the scalar functions  $\hat{\phi}^{\hat{a}}$  verify this property. If  $\hat{a}$  is a vertex of another face adjacent to  $\hat{f}$  by  $\hat{a}$ , then the normal component of  $\hat{\phi}^{\hat{f}, \hat{a}}$  restricted to itself also vanishes, because  $\mathbf{v}^{\hat{f}, \hat{a}}$  is parallel to the adjacent faces. The normal component  $\hat{\phi}^{\hat{f}, \hat{a}} \cdot \mathbf{n}^{\hat{K}}|_{\hat{f}} = \hat{\phi}^{\hat{a}}|_{\hat{f}}$ , having in mind that the normal component of  $\mathbf{v}^{\hat{f}, \hat{a}}$  is unitary over  $\hat{f}$ .
- Face functions  $\hat{\phi}^{\hat{f}, \hat{e}, n} = \hat{\phi}^{\hat{e}, n} \mathbf{v}^{\hat{f}, \hat{e}}$  vanish on the faces that do not have  $\hat{e}$  as one of its edges, because the scalar functions  $\phi^{\hat{e}, n}$  verify this property. Otherwise, the normal component of  $\hat{\phi}^{\hat{f}, \hat{e}, n}$  restricted to a face adjacent to  $\hat{f}$  by  $\hat{e}$  vanishes, because  $\mathbf{v}^{\hat{f}, \hat{e}}$  is parallel to it. Taking into account that the normal component of  $\mathbf{v}^{\hat{f}, \hat{e}}$  is unitary over  $\hat{f}$ , it follows that  $\hat{\phi}^{\hat{f}, \hat{e}, n} \cdot \mathbf{n}^{\hat{K}}|_{\hat{f}} = \hat{\phi}^{\hat{e}, n}|_{\hat{f}}$ .
- Face functions  $\hat{\phi}^{\hat{f}, n_1, n_2} = \hat{\phi}^{\hat{f}, n_1, n_2} \mathbf{v}^{\hat{f}, \perp}$  vanish on the faces different from  $\hat{f}$ , because the scalar functions  $\phi^{\hat{f}, n}$  have this property. Over  $\hat{f}$ , the normal component  $\hat{\phi}^{\hat{f}, n_1, n_2} \cdot \mathbf{n}^{\hat{K}}|_{\hat{f}} = \hat{\phi}^{\hat{f}, n_1, n_2}|_{\hat{f}}$ , considering that  $\mathbf{v}^{\hat{f}, \perp}$  coincides with outward unit normal to  $\hat{f}$ .

## Internal functions

- The internal functions  $\hat{\phi}^{\hat{K}, \hat{e}, n} = \phi^{\hat{e}, n} \mathbf{v}^{\hat{e}, \parallel}$  vanish on all faces not sharing  $\hat{e}$ , since the scalar function  $\phi^{\hat{e}, n}$  satisfy this property. Otherwise, the normal component of  $\hat{\phi}^{\hat{K}, \hat{e}, n}$  restricted to a face sharing  $\hat{e}$ , also vanishes and taking into account that  $\mathbf{v}^{\hat{e}, \parallel}$  is tangent to the face.
- The internal functions  $\hat{\phi}_j^{\hat{K}, n_1, n_2, n_3} = \phi^{\hat{K}, n_1, n_2, n_3} \mathbf{v}_j^{\hat{K}, \parallel}$  vanish on all faces, since the internal functions  $\phi^{\hat{K}, n_1, n_2, n_3}$  satisfy this property.

Let  $\mathbf{B}_k^{\hat{K}}$  be the set formed by face and internal vector basis functions:

$$\begin{aligned} \mathbf{B}_k^{\hat{K}} &= \left\{ \hat{\phi}^{\hat{f}, \hat{a}}, \hat{\phi}^{\hat{f}, \hat{e}, n}, \hat{\phi}^{\hat{f}, n_1, n_2} \right\} \\ &\cup \left\{ \hat{\phi}^{\hat{K}, \hat{e}, n}, \hat{\phi}_1^{\hat{K}, \hat{f}, n_1, n_2}, \hat{\phi}_2^{\hat{K}, \hat{f}, n_1, n_2}, \hat{\phi}_1^{\hat{K}, n_1, n_2, n_3}, \hat{\phi}_2^{\hat{K}, n_1, n_2, n_3}, \hat{\phi}_3^{\hat{K}, n_1, n_2, n_3} \right\} \end{aligned} \quad (2.26)$$

The functions are linearly independent, and  $\text{span } \mathbf{B}_k^{\hat{K}} \subset H_{div}(\hat{K})$ .

## Piola transformation $\phi = \mathbb{F}_{div} \hat{\phi}$

Let  $\mathbb{F}: \hat{K} \rightarrow K$  define a regular geometric mapping. Using standard finite element technology, the scalar functions defined in the reference element  $\hat{K}$ , are mapped to functions defined in  $K$  by the operator  $\phi = \mathbb{F}\hat{\phi}$ , as documented in (2.5). This map, which can be extended for vector functions is not suitable for mapping vectors fields in  $H(div, \hat{K})$ . The reason for it, is because the operator  $\mathbb{F}$  does not preserve the normal value of the vector field. The contravariant Piola transformation  $\mathbb{F}_{div}: \hat{\phi} \rightarrow \phi$  (Gabrio Piola (15 July 1794 – 1850)), associated with the geometric

mapping  $T_K^{geo}$  relates vector functions  $\hat{\phi}$  defined in the reference element  $\hat{K}$  with vector functions  $\phi$  defined in the deformed configuration by the formula:

$$\phi = \mathbb{F}_{div} \left[ \frac{1}{\det(J_K^{geo})} J_K^{geo} \hat{\phi} \right] \quad (2.27)$$

As reported in **BrezziFortin1991** divergence of vector functions given by the Piola contravariant transformation, verifies the expression

$$\nabla \cdot (\phi) = \mathbb{F}_{div} \left[ \frac{1}{\det(J_K^{geo})} \hat{\nabla} \cdot (\hat{\phi}) \right] \quad (2.28)$$

Furthermore, if  $\phi = \mathbb{F}\hat{\phi}$ , the following identities are valid:

$$\begin{aligned} \int_K \phi \cdot \nabla(\phi) d\mathbf{x} &= \int_{\hat{K}} \hat{\phi} \cdot \hat{\nabla}(\hat{\phi}) d\mathbf{x} \\ \int_K \phi \nabla \cdot (\phi) d\mathbf{x} &= \int_{\hat{K}} \hat{\phi} \hat{\nabla} \cdot (\hat{\phi}) d\mathbf{x} \\ \int_{\partial K} \phi \cdot \mathbf{n} \phi ds &= \int_{\partial \hat{K}} \hat{\phi} \cdot \hat{\mathbf{n}} \hat{\phi} d\hat{s} \end{aligned} \quad (2.29)$$

As a result,  $\mathbb{F}_{div}$  is an isomorphism between  $H_{div}(\hat{K})$  and  $H_{div}(K)$ , preserving normal components in the  $H^{\frac{1}{2}}$  sense.

## Approximation spaces in $H(div, K)$

The construction of vector shape functions  $\phi \in H(div, K)$  form a basis  $\mathbf{B}_k^K$  on the mapped element  $K$ , is based on the definition of shape functions of type  $\hat{\phi} = \hat{\phi}\hat{\mathbf{v}}$  in  $\mathbf{B}_{\hat{k}}^{\hat{K}}$ , defined in the master element. The Piola transformation  $\phi = \mathbb{F}_{div}\hat{\phi}$  is applied to the shape functions defined on the master element, resulting in:

$$\phi = \mathbb{F}_{div} \left( \frac{1}{\det(J_K^{geo})} J_K^{geo} \hat{\phi} \right) = \mathbb{F}_{div} \left( \hat{\phi} \frac{1}{\det(J_K^{geo})} J_K^{geo} \hat{\mathbf{v}} \right) = \phi \mathbf{b} \quad (2.30)$$

where  $\phi = \mathbb{F}\hat{\phi}$ , and  $\mathbf{b} = \mathbb{F}_{div} \left( \frac{1}{\det(J_K^{geo})} J_K^{geo} \hat{\mathbf{v}} \right) = \mathbb{F}_{div} \hat{\mathbf{v}}$ .

The set of functions  $\mathbf{B}_k^K$  associated with edge and internal functions, are constructed as documented in equation 2.26:

$$\begin{aligned} \mathbf{B}_k^K &= \left\{ \phi^{f,a}, \phi^{f,e,n}, \phi^{f,n_1,n_2} \right\} \\ &\cup \left\{ \phi^{K,e,n}, \phi_1^{K,f,n_1,n_2}, \phi_2^{K,f,n_1,n_2}, \phi_1^{K,n_1,n_2,n_3}, \phi_2^{K,n_1,n_2,n_3}, \phi_3^{K,n_1,n_2,n_3} \right\} \end{aligned} \quad (2.31)$$

It follows that  $\text{span } \mathbf{B}_k^K \subset H(div, K)$ .

Departing from a mesh  $\Gamma_h$  formed for elements  $K$ , and using the Neopz data structures, consistent approximation spaces can be generated without limitation on hanging faces and/or degree of polynomial order distribution  $\mathbf{k} = k_K$  over the elements.

Consistent approximation spaces are generated that are subspaces  $W \subset H(\text{div}, \Omega)$ , formed by functions  $\mathbf{w}$  defined piecewise, over the elements of  $\Gamma_h$  by local functions  $\mathbf{w}_K = \mathbf{w}|_K \in \text{span } \mathbf{B}_k^K$ . A necessary condition for a function to be in  $H(\text{div}, \Omega)$  is that normal components of  $\mathbf{w}$  across the interfaces  $f = K^i \cap K^j$  are continuous. This means that the jump on the normal component of  $\mathbf{w}$  across  $f$  should vanish (2.32).

$$[\mathbf{w}_{K^i} \cdot \mathbf{n}_{K^i} + \mathbf{w}_{K^j} \cdot \mathbf{n}_{K^j}]_f = 0 \quad (2.32)$$

This property is obtained as a consequence of the properties of the proposed vector shape functions, the properties of the contravariant Piola transformation, and the continuity of the scalar shape functions across the interfaces used in their construction.

Since the contravariant Piola transformation preserves zero normal components, mapping tangent vectors in  $\hat{f}$  to tangent vectors in  $f$ , the non-zero contributions to the normal component of  $\mathbf{w}_{K^i}$  on the face  $f$ , result exclusively from the face functions  $\phi^{f,a}$ ,  $\phi^{f,e,n}$  and  $\phi^{f,n_1,n_2}$  associated with its vertices, edges and to the face  $f$  itself.

In **Castro20162D** a procedure was described for creating vector functions, which have unit normal components over the element interface. In that context, assuming the continuity of the scalar basis functions across the interface  $f$ , and recalling that  $\mathbf{n}_{K^i} = -\mathbf{n}_{K^j}$ , the jump on the normal component of  $\mathbf{w}$  over  $f$  vanishes, if and only if, in the expansions of  $\mathbf{w}_{K^i}$  and  $\mathbf{w}_{K^j}$  the sum of the two coefficients, that multiply each of the face functions associated with the vertices, edges and face of the interface  $f$ , is zero. However, the vector functions used in this contribution differ from the functions define in **Castro20162D** by the determinant of the Jacobian associated with the interface and therefore ensures continuity of the normal component as well. The procedure to ensure continuity of the scalar basis, based on hp-adaptive meshes is described in **Calle2015**. The combination of the continuity of the scalar shape functions and vector functions ensures the continuity of the normal component of the shape functions.

From the developments above, finite subspaces for  $H(\text{div}, \Omega)$  are composed of:

$$W_{\mathcal{N}} = \left\{ \mathbf{w} \in W : \mathbb{F}_{\text{div}}^{-1}(\mathbf{w}|_K) \in [P(\hat{K})]^d \right\} \quad (2.33)$$

### 2.3.2 Application to finite element formulations

Considered the classical mixed formulation for the elliptic Poisson problem: find  $u \in Z$  and  $\boldsymbol{\sigma} \in W$  such that

$$\begin{aligned} \nabla \cdot (\boldsymbol{\sigma}) &= f \text{ in } \Omega \\ \boldsymbol{\sigma} &= -\nabla(u) \text{ in } \Omega \\ u &= u_D \text{ on } \partial\Omega_D \\ \boldsymbol{\sigma} &= \boldsymbol{\sigma}_N \text{ on } \partial\Omega_N \end{aligned} \quad (2.34)$$

As studied in **BrezziFortin1991** the variational mixed formulation of problem (2.34) is:

find  $u \in Z$  and  $\boldsymbol{\sigma} \in W$ , with  $\boldsymbol{\sigma} = \boldsymbol{\sigma}_N$  on  $\partial\Omega_N$ , such that:

$$\begin{aligned}\int_{\Omega} \boldsymbol{\sigma} \cdot \mathbf{w} \, d\Omega - \int_{\Omega} u \nabla \cdot (\mathbf{w}) \, d\Omega + \int_{\partial\Omega_D} u_D \mathbf{w} \cdot \mathbf{n} \, ds &= 0 \\ \int_{\Omega} z \nabla \cdot (\boldsymbol{\sigma}) \, d\Omega + \int_{\Omega} f z \, d\Omega &= 0\end{aligned}\tag{2.35}$$

for all  $\mathbf{w} \in W$ , and  $z \in Z$ .

A finite element approximation of 2.43 is the finite dimensional approximation of the weak statement using the approximation spaces  $\boldsymbol{\sigma} \in W_N$  and  $u \in Z_N$ .

This research contributed to the development of  $H(\text{div}, \Omega)$  conforming approximation spaces on curved meshes and/or h-p adaptive meshes, which extend the work developed for  $H^1$  conforming meshes (**Calle2015; Devloo2016**) to 3D topologies.

Convergence results for  $H(\text{div}, \Omega)$  conforming spaces applied to curved geometries as illustrated in 2.3.3, are documented in the following sections. Convergence studies of  $H(\text{div}, \Omega)$  approximations on three dimensional manifolds, have been published in **Castro20162D**

Recalling that the discrete functions  $u_N \in Z_N$  and  $\mathbf{w}_N \in W_N$  are defined in polynomial approximation spaces  $(Z_N^{\hat{K}}, W_N^{\hat{K}})$  on  $\hat{K}$  that, in the context of the NeoPZ library, can have non-uniform degree distribution over the elements  $K$ . It is well known that in order to produce stable and convergent approximations the exact De Rham property (2.8) is a necessary condition:

$$\hat{\nabla} \cdot (W_N^{\hat{K}}) \equiv Z_N^{\hat{K}}\tag{2.36}$$

In **Castro20163D** it was demonstrate this property is satisfied essentially by balancing the approximation order of the pressure space, and the polynomial order of the internal flux functions. Motivated by (2.36) two variants of balanced pairs of approximation spaces are:

## Approximation spaces of type I: $\mathbf{P}_k^* P_k$

The flux approximations in  $W_N^K$  are said to be of  $P_k^*$  type, if for each element  $K$  in  $\Gamma_h$ , the corresponding polynomial spaces  $W_N^{\hat{K}}$  in the  $\hat{K}$  is spanned by the face functions of  $P_{l, l \leq k}$  type, and by the internal shape functions defined by vector polynomials of degree  $k+1$  whose divergence are included in the scalar approximation space  $Z_N^{\hat{K}}$  of type  $P_k$ . Since the flux approximation space of type  $\mathbf{P}_k^*$  only involves the complete vector valued polynomials of degree  $k$ , in simulations using  $\mathbf{P}_k^* P_k$  configurations with uniform meshes  $h_K = h$ , and polynomial degree distributions  $k_K = k \forall K$ , the expected  $L^2$  convergence rates for the error are of order  $k+1$  for both,  $\boldsymbol{\sigma}$  and  $u$  variables. These pairs of polynomials correspond to the  $RT_K$  space configuration for rectangular (**RaviarT1977**) and hexahedral geometries (**Nedelec1980**), and to  $BDFM_{k+1}$  elements for triangular (**Brezzi1987**) and tetrahedral elements (**BrezziFortin1991**).

## Approximation spaces of type II: $\mathbf{P}_k^{**} P_{k+1}$

This space configuration was introduced by **Castro20163D** for affine meshes. The idea for the construction of flux approximation spaces of type  $\mathbf{P}_k^{**}$ , consist in adding to the vector valued spaces of  $\mathbf{P}_k$  interior shape functions of  $\mathbf{P}_{k+1}^*$  defined in  $\hat{K}$ , that are vector polynomials of degree  $k+2$

whose divergence is included in the scalar approximation space of type  $P_{k+1}$ . Therefore, in  $\mathbf{P}_k^{**}$  the face shape functions still correspond to polynomials of degree  $k_K$ , but the internal shape functions include polynomials of degree up to  $k_K + 2$ . As in the previous case, the De Rham property (2.36) is satisfied. In simulations using  $\mathbf{P}_k^{**}P_{k+1}$  configurations with uniform mesh spacing  $h_K = h$ , and polynomial degree distributions  $k_K = K \forall K$ , the  $L^2$  convergence rate for the error norm of the flux variable is of order  $k+1$ . However, for the primal variable  $u$  a higher order  $k+2$  of convergence is obtained.

## Static condensation

It was observed that the number of internal functions in mixed finite element approximations, constitutes a considerable percentage of the total number of degrees of freedom. This means that the size of the linear system of equations, can be reduced significantly by applying static condensation at the element level. The discrete mixed formulations are implemented using a static condensation technique, by organizing the degrees of freedom of each element in a particular sequence. The degrees of freedom of the flux are organized in the form  $\{\boldsymbol{\sigma}_i, \dots, \boldsymbol{\sigma}_e\}$  where  $\boldsymbol{\sigma}_i$  and  $\boldsymbol{\sigma}_e$  refer to internal and edge components of the flux, respectively. For the variable  $u$ , let  $u_0$  is a scalar value and  $u_i$  denote the remaining degrees of freedom except  $u_0$ . Thus, the matrix representation of the discrete mixed formulation is expressed in the form:

$$\left( \begin{array}{cc|cc} A_{ii} & B_{iu}^T & B_{ie}^T & A_{ie} \\ B_{ii} & 0 & 0 & B_{ie} \\ \hline B_{ie} & 0 & 0 & B_{ee} \\ A_{ei} & B_{ie}^T & B_{ee}^T & A_{ee} \end{array} \right) \begin{pmatrix} \boldsymbol{\sigma}_i \\ u_i \\ u_0 \\ \boldsymbol{\sigma}_e \end{pmatrix} = \begin{pmatrix} -u_D \\ -f_i \\ -f_0 \\ 0 \end{pmatrix} \quad (2.37)$$

Static condensation is applied by eliminating the internal degrees of freedom  $\boldsymbol{\sigma}_i$  and  $u_i$ , to get a condensed system in terms of  $\boldsymbol{\sigma}_e$  and  $u_0$ .

It should be observed that, for each kind of element geometry, the dimension of the static condensed matrix is determined by the number of degrees of freedom of the face components plus one, and that this number of equations is the same for both approximations spaces of types  $\mathbf{P}_k^*P_k$  and  $\mathbf{P}_k^{**}P_{k+1}$ .

### 2.3.3 Numerical example - Curved mesh:

In this section, convergence rates are computed for the mixed finite element approximations using the space configurations  $\mathbf{P}_k^*P_k$  and  $\mathbf{P}_k^{**}P_{k+1}$ . The domain composed of curved elements is a spherical region with a spherical cavity in the middle, having a known smooth solution 2.39. In the plots documenting the convergence (see figure 2.3), the two function pairs will be referred to by the acronyms  $MF^*$  and  $MF^{**}$ , respectively.

In this example, the domain  $\Omega = \left\{ \mathbf{x} \in \mathbb{R}^3; \frac{1}{4} \leq \| \mathbf{x} \| \leq 1 \right\}$ , and the analytic solution is given by the formula:

$$u = \frac{\pi}{2} - \tan^{-1} \left( d \left( \sqrt{(x-a)^2 + (y-b)^2 + (z-c)^2} - \frac{\pi}{3} \right) \right) \quad (2.38)$$

$$\boldsymbol{\sigma} = -\nabla u = \begin{cases} \frac{d(x-a)}{\sqrt{(a-x)^2 + (b-y)^2 + (c-z)^2} \left( d^2 \left( \sqrt{(a-x)^2 + (b-y)^2 + (c-z)^2} - \frac{\pi}{3} \right)^2 + 1 \right)} \\ \frac{d(y-b)}{\sqrt{(a-x)^2 + (b-y)^2 + (c-z)^2} \left( d^2 \left( \sqrt{(a-x)^2 + (b-y)^2 + (c-z)^2} - \frac{\pi}{3} \right)^2 + 1 \right)} \\ \frac{d(z-c)}{\sqrt{(a-x)^2 + (b-y)^2 + (c-z)^2} \left( d^2 \left( \sqrt{(a-x)^2 + (b-y)^2 + (c-z)^2} - \frac{\pi}{3} \right)^2 + 1 \right)} \end{cases} \quad (2.39)$$

where the coefficients are  $a = \frac{5}{4}$ ,  $b = c = -\frac{1}{4}$  and  $d = 5$ . Dirichlet boundary conditions are enforced in  $\partial\Omega_D = \partial\Omega$ .

For this problem, regular meshes  $\Gamma_h$  formed by curved tetrahedral and hexahedral elements are used. The curved hexahedral meshes are obtained by the projection of square meshes on the faces of a cube, onto the internal and external spherical surfaces of radius  $1/4$  and  $1$ . Then, these two curved quadrilateral surfaces are blended (**Lucci2009**) to form a grid on the entire 3D region  $\Omega$  using transfinite interpolation. In figure 2.2 this process is illustrated for one element at the coarsest level (left side) and its two subsequent refinements. The tetrahedral meshes are obtained from curved prismatic elements, with uniformly distributed curved triangular faces over the spherical surfaces. The edges of the triangular spherical surfaces are obtained by quadratic interpolation. Each of the prismatic elements are subdivided into 3 tetrahedral elements, to form a tetrahedral mesh for the domain  $\Omega$ .

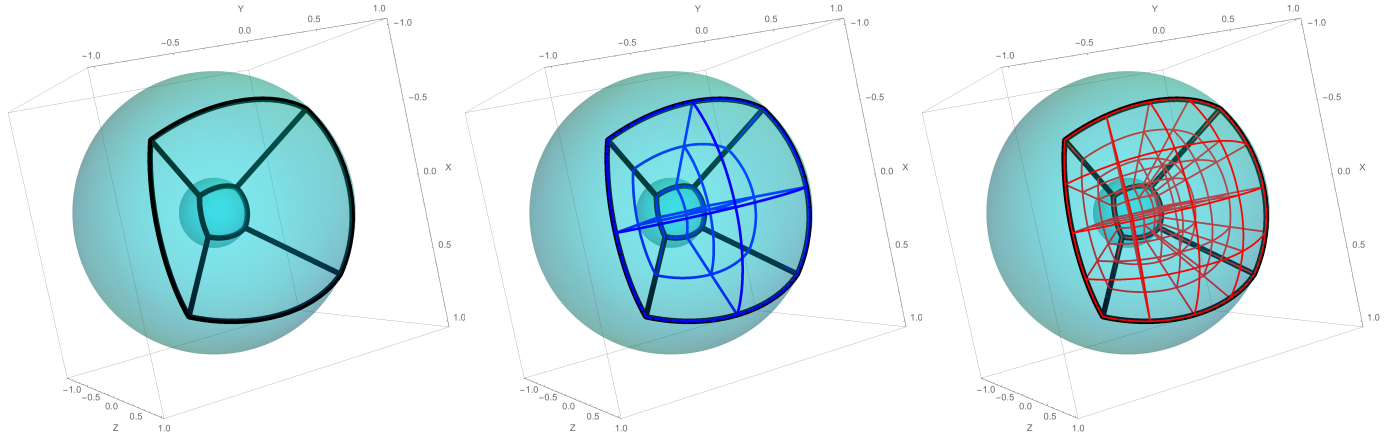


Figure 2.2: Illustration of curved hexahedral elements of the spherical region in Problem 1: black lines indicate the edges of one curved element at the coarsest level; blue and red curves refer to the next two subsequent refinements, respectively.

Figure 2.3 presents  $L^2$ -error curves for  $u$  and for the flux  $\boldsymbol{\sigma}$ , obtained with the two space configurations under consideration, for uniform polynomial degree distribution  $k = \{1, 2, 3, 4\}$ . For the  $MF^*$  configuration in hexahedral and tetrahedral meshes, corresponding to the classic  $RT_k$  and

$BDMF_{k+1}$  spaces,  $u$  and  $\sigma$  are approximated with accuracy of order  $k+1$ . For the approximation space  $MF^{**}$ ,  $\sigma$  is approximated with accuracy of order  $k+1$ , and enhanced approximation order of  $k+2$  is verified for the primal variable  $u$  in both geometries.

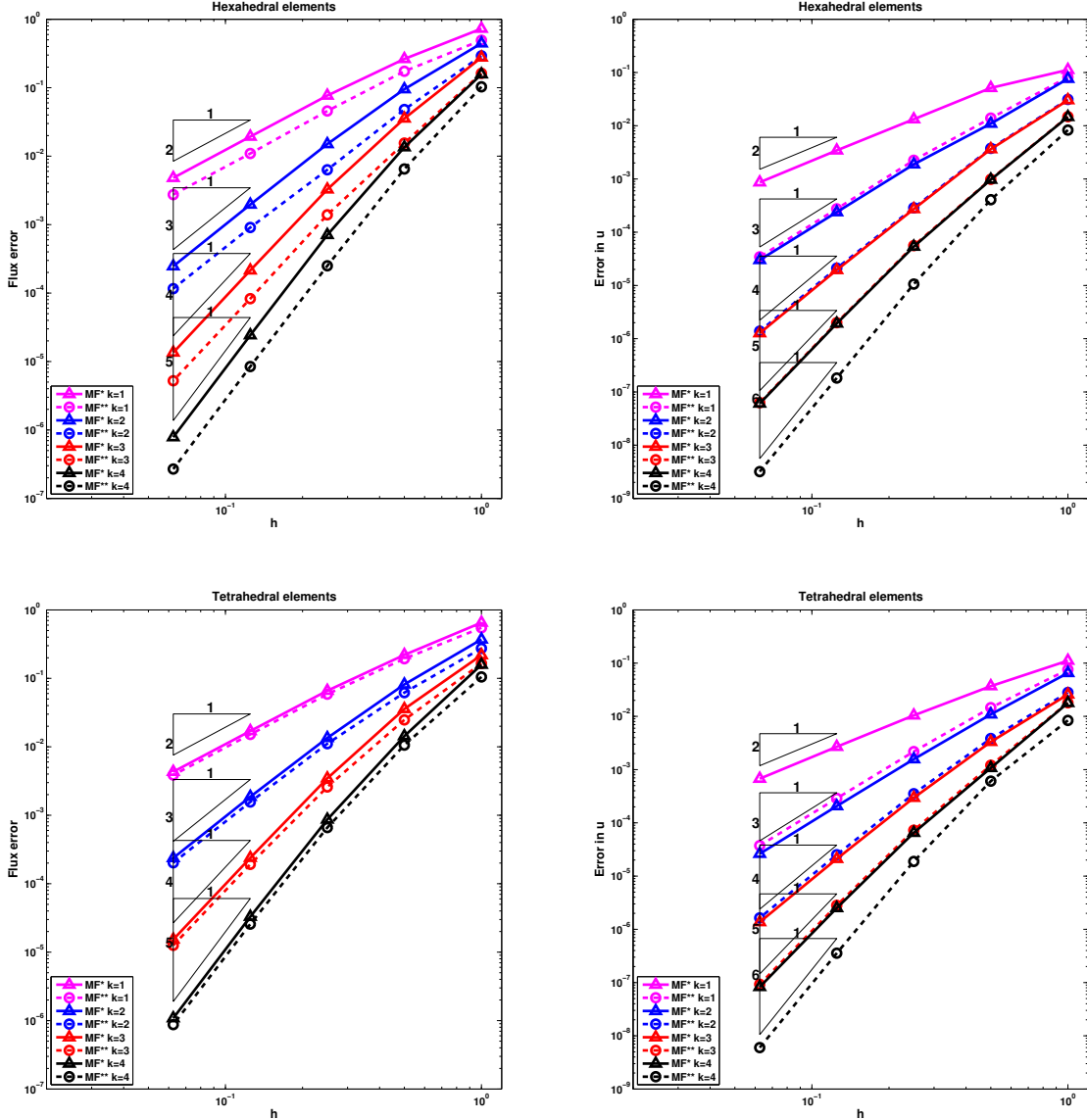


Figure 2.3:  $L^2$ -error curves in terms of  $h$  for  $\sigma$  (left) and for  $u$  (right), using the mixed formulations with  $\mathbf{P}_k^* P_k$  and  $\mathbf{P}_k^{**} P_{k+1}$  space configurations based on curved hexahedral (up) and tetrahedral (bottom) uniform meshes  $\Gamma_h$ , for  $k = \{1, 2, 3, 4\}$ .

Figure 2.4 illustrates the effectiveness of static condensation, in the reduction of degrees of freedom at the finest level of refinement. More degrees of freedom can be condensed when increasing the polynomial order. Hexahedral elements have a larger number of condensable degrees of freedom

than tetrahedrons. For instance, for  $k = 4$ , and using the  $\mathbf{P}_k^* P_k$  space configuration, about 87% of the total number of degrees of freedom are condensed when using hexahedral elements, and about 81% for tetrahedral elements. Using the  $\mathbf{P}_k^{**} P_{k+1}$  space configuration, about 92% of the total number of degrees of freedom are condensed using hexahedral elements, and about 87% for tetrahedral elements. Both space configurations share the same number face shape functions, but the  $\mathbf{P}_k^{**} P_{k+1}$  case uses more internal flux shape functions and scalar shape functions with  $k$  degree augmented by one, making the effect of static condensation more significant for the richer space configuration.

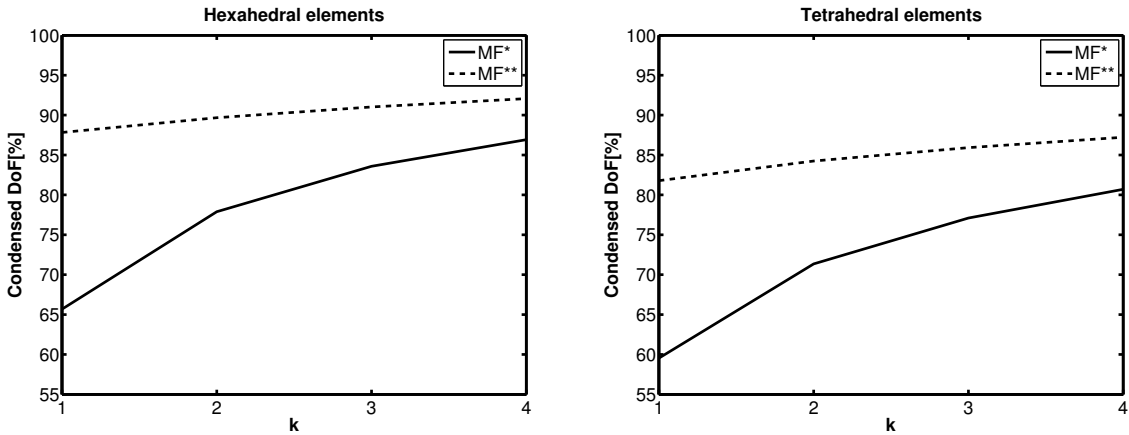


Figure 2.4: Percentage of condensed degrees of freedom in the discrete mixed method, using  $\mathbf{P}_k^* P_k$  and  $\mathbf{P}_k^{**} P_{k+1}$  space configurations at the finest refinement level of hexahedral (left) and tetrahedra (right) meshes.

### 2.3.4 Numerical example - Linear mesh:

Before proceeding with complex multiphase formulations, in this application of the mixed formulation, a simple, but sufficiently illustrative problem is examined, to demonstrate the approximation potential of the approximation spaces defined above.

The physical description of the problem is framed with a vertical well within a circular reservoir, having a constant pressure at the external boundary. Considering a reservoir of thickness  $h$ , permeability constant and equal to  $\kappa$ , which is completely penetrated and perforated by a vertical well of radius  $r_w$ . Assuming a radius  $r_o$ , where the pressure remains unchanged at a value  $p_o$ . If a fluid with constant viscosity  $\eta$  is produced at a constant rate  $Q$ , the pressure distribution is an immaterial solution, which depends only on the radius as shown below:

$$p = p_o - \frac{Q\eta}{2\pi\kappa h} \ln\left(\frac{r}{r_0}\right) \quad (2.40)$$

The Darcy's velocity is a function of the inverse of the radius:

$$\mathbf{q} = -\frac{\kappa}{\mu} \nabla p = \begin{cases} \frac{Q}{2\pi h r} \frac{x}{r} \\ \frac{Q}{2\pi h r} \frac{y}{r} \\ 0 \end{cases} \quad (2.41)$$

The expression 2.40 is the famous Dupuit-Thiem equation (**Dupuit1857**), which shows that the pressure under the above considerations varies logarithmically and most of the pressure drop occurs in the wellbore region, a plot of the solution is presented in the figure 2.5. This logarithmic dependence also appears in transient cases in which it is interesting to show the potency of mixed approximations.

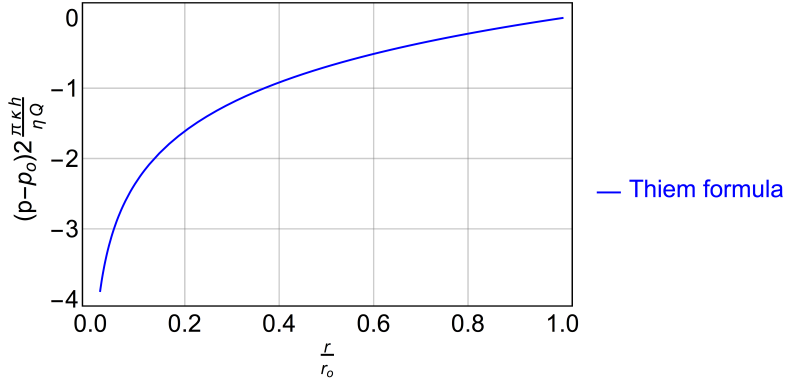


Figure 2.5: Steady-state flow to a well in a bounded reservoir with constant pressure.

The mixed formulation for the this elliptic problem: find  $p \in Z$  and  $\mathbf{q} \in W$  such that

$$\begin{aligned} \nabla \cdot (\mathbf{q}) &= 0 \text{ in } \Omega \\ \mathbf{q} &= -\frac{\kappa}{\eta} \nabla(p) \text{ in } \Omega \\ p &= p_o \text{ on } \partial\Omega_{D\text{external}} \\ \mathbf{q} \cdot \mathbf{n} &= Q \text{ on } \partial\Omega_{N\text{well}} \\ \mathbf{q} \cdot \mathbf{n} &= 0 \text{ on } \partial\Omega_{N\text{seal}} \end{aligned} \quad (2.42)$$

the variational mixed formulation of problem (2.42) is:  
find  $p \in Z$  and  $\mathbf{q} \in W$ , with  $\mathbf{q} = \mathbf{q}_N$  on  $\partial\Omega_N$ , such that:

$$\begin{aligned} \int_{\Omega} \frac{\eta}{\kappa} \mathbf{q} \cdot \mathbf{w} d\Omega - \int_{\Omega} p \nabla \cdot (\mathbf{w}) d\Omega + \int_{\partial\Omega_D} p_o \mathbf{w} \cdot \mathbf{n} ds &= 0 \\ \int_{\Omega} z \nabla \cdot (\mathbf{q}) d\Omega &= 0 \end{aligned} \quad (2.43)$$

for all  $\mathbf{w} \in W$ , and  $z \in Z$ .

Property	Value
Reservoir dimensions	$h = 10 \text{ m}$ ; $r_w = 0.3 \text{ m}$ ; $r_o = 50 \text{ m}$
Permeability	$\kappa = 1 \times 10^{-13} \text{ m}$
Viscosity	$\eta = 0.01 \text{ Pa s}$
External pressure	$p_o = 25 \times 10^6 \text{ Pa}$
Flow rate	$Q = 0.01 \text{ m}^3 \text{ s}^{-1}$

Table 2.2: Input data for mixed approximation of the steady-state radial flow.

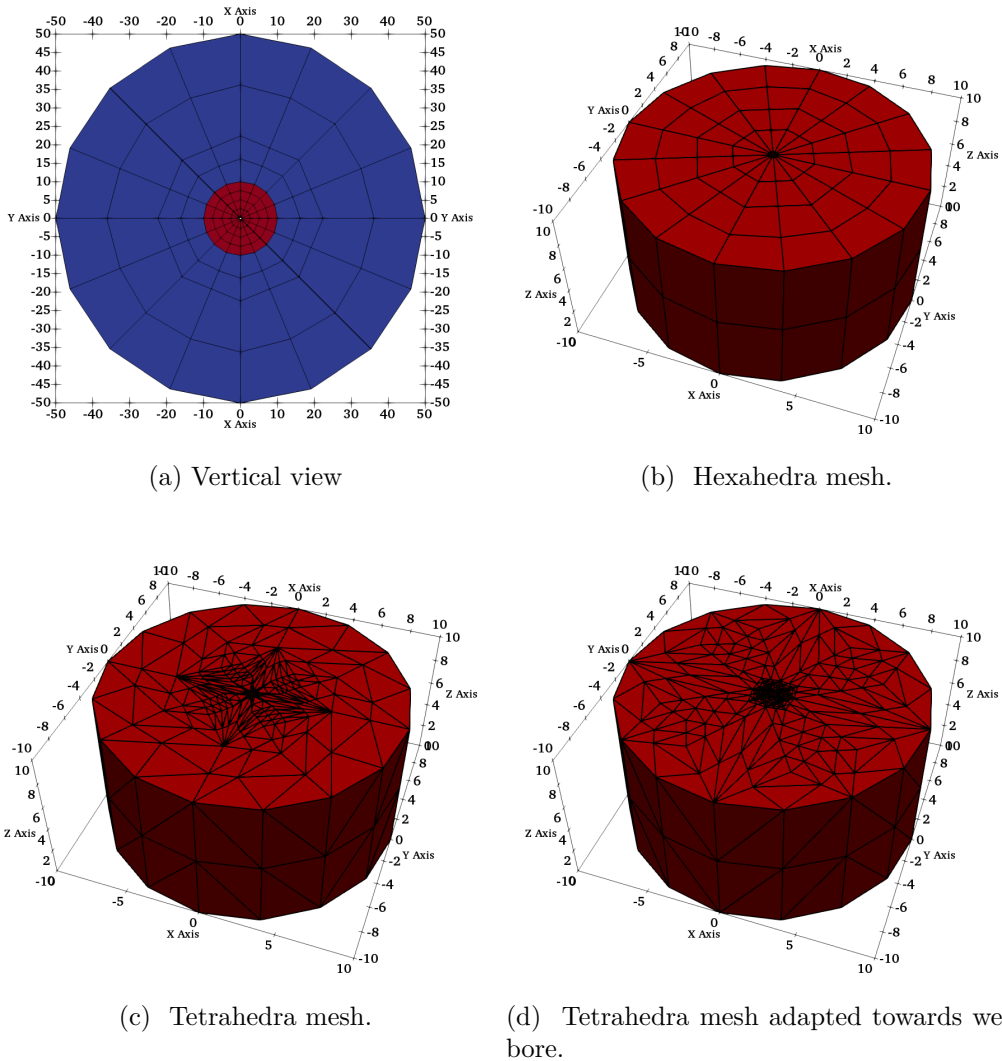


Figure 2.6: Finite element tetrahedra, prism and hexahedra meshes. A Visualization of wellbore region is rendered with red color by each case. In the adapted case red region has order  $k = 2$  and blue region  $k = 1$

Figure 2.6a shows an aerial view of the discretization for hexahedra mesh. A zoom on the wellbore region marked with red for different discretizations, it is presented, respectively in figures 2.6c, 2.6d, 2.6b for hexahedra, tetrahedra and tetrahedra adapted towards wellbore and respectively.

Figure 2.7a shows the convergence curves for approximation of type I and type II in meshes with tetrahedra, prisms and hexahedra. It is also shown the expected properties of the appoximation over non-stuctured meshes with engineering data and domain dimensions provided by table 2.2.

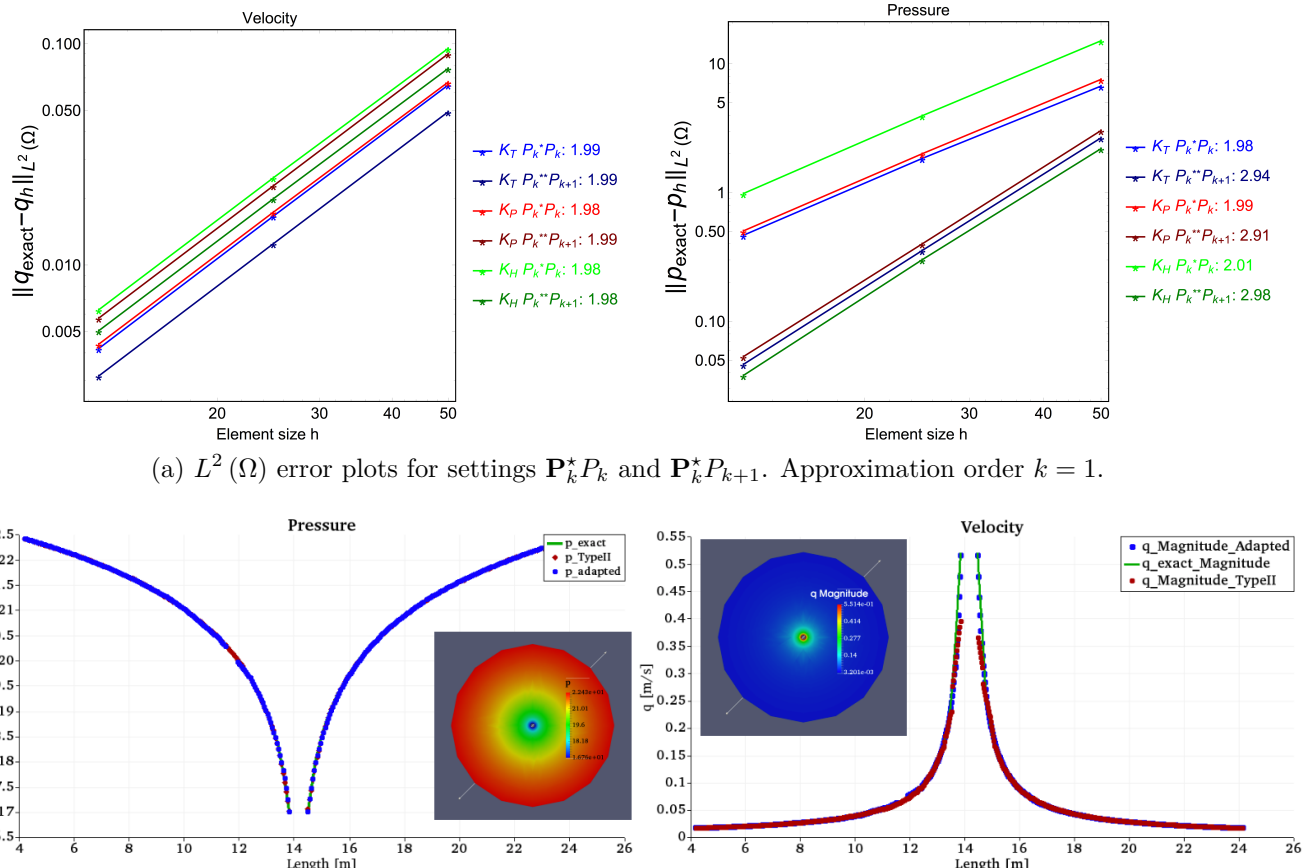


Figure 2.7: Comparison error and solution profiles for different mixed approximations settings.

The figure 2.7b shows the comparison inside wellbore region for pressure and velocity approximations using tetrahedra mesh. In this figure, an simple mesh adaptation is shown in fig 2.6c by refine the elements toward the wellbore, and increasing the order inside the wellbore region to  $k = 2$ . By comparing the solution analytical with an approximation of type II, an approximation of type I upgraded with an adaptation hp, the approximation of the pressure in the region shows, that using an adaptation, results on satisfactory pressure profiles, but with better results for velocity on unstructured meshes.

## 2.4 Conclusions

From the numerical experiments it is possible to conclude:

- (i) The numerical examples 2.3.3 and 2.3.4 were used to illustrate the approximation spaces detailed in sections 2.1, 2.2, and 2.3. The  $H(\text{div}, \Omega)$  approximation spaces applied to two (domain boundaries) and three dimensional element topologies are now fully operational in Neopz.
- (ii) The use of static condensation, makes the mixed formulation competitive in terms of error versus size of the associated linear system, even when compared with  $H_1$  approximations: For a given computational cost, it is possible to obtain more precise approximations with mixed finite element approximations.
- (iii) The two sets of approximation spaces  $\mathbf{P}_k^* P_k$  and  $\mathbf{P}_k^* P_{k+1}$ , are implemented and tested on linear and curved meshes, for partitions composed of a single element topology.

# Chapter 3

## Reduced order Modeling

In scientific computing reduction strategies, such as reduced order modeling (ROM) or reduced basis (RB) methods, have gained renewed interest in applications of increasing complexity (**Prudhomme2002; Prudhomme2004; Quarteroni2015**). The RB methods (built upon a high-fidelity (Full-order) finite element approximation) can be used as a fast and reliable approximation method of parametric partial differential equations. These approximations may be suited for realtime simulation, simulating specific physics inside a big multi-physics problems, and in other contexts it may form the basis for optimization, control and data assimilation. **Quarteroni2015** describe a model order reduction for non-affine depending of parameters on PDE coefficients, pointing to the possibilities for the reduction of non linear reservoir simulations.

The RB method used in this research is described as:

- (i) Properly selected Galerkin projections generating a low-dimensional space of basis functions.
- (ii) An affine parametric dependence enabling to perform a competitive Offline-Online splitting of the computational procedure.
- (iii) A posteriori error calculations used for the basis selection and the verification (certification) of the solution.

The combination of these three factors yields substantial computational savings and are the basis of an efficient reduced order model. This section is dedicated to the description of a reduced order model, applied to an affine linear elliptic quasi-static problem, describing the poroelastic coupling in single phase flow poromechanics.

## Contents

---

3.1	The general picture . . . . .	48
3.1.1	Reduced basis approximation . . . . .	49
3.1.2	Affine decomposition . . . . .	49
3.2	Monophasic poromechanics . . . . .	50

3.2.1	About Sequential methods . . . . .	54
3.2.2	Implementation for the Fixed Stress Split . . . . .	58
3.2.3	Consolidation benchmark problem . . . . .	58
3.2.4	Footing problem . . . . .	63
3.2.5	Empirical reduction strategy . . . . .	67
3.2.6	RB approximation for consolidation problem . . . . .	70
3.2.7	RB approximation for the footing problem . . . . .	74

---

### 3.1 The general picture

The reduced basis approximation described in this section, is a Galerkin projection on an  $\mathcal{N}$ -dimensional approximation space, that corresponds to a parametrically induced manifold or parameter space  $\mathcal{D}$ . The reduced basis shape functions in  $H^1(\Omega)$  are obtained by FEM solutions of the PDE, using a fine mesh and corresponding to certain parameter values, associated with the forcing function or boundary condition. Each simulation that computes a basis function for the reduced order model is computed and its result is stored. There is no need to orthogonalize the basis functions.

Similarly as mentioned in **Quarteroni2015** a set of parameters  $\mathbf{p}$  defined as  $\mathbf{p} = \{p_1, \dots, p_M\} \in \mathbb{R}^M$ , are associated with the reduced order model. The PDE (2.1) representing the physical phenomenon allows to relates the input parameter  $\mathbf{p}$ , with the investigated quantity of interest denoted as output. Then let to consider the parametrized PDE which consists in finding the parameter dependent solution  $u(\mathbf{p}) \in X(\Omega)$

$$a(u(\mathbf{p}), v; \mathbf{p}) = f(v; \mathbf{p}) \quad \forall v \in X(\Omega) \quad (3.1)$$

where  $a: X(\Omega) \times X(\Omega) \times \mathcal{D} \rightarrow \mathbb{R}$  is a continuous form, and  $f: X(\Omega) \rightarrow \mathbb{R}$  is a continuous linear form.

The outputs denoted as  $s(\mathbf{p})$  are expressed as linear functionals  $l: X \rightarrow \mathbb{R}$  of  $u(\mathbf{p})$  related with 3.1 as

$$s(\mathbf{p}) = l(u(\mathbf{p})) \quad (3.2)$$

Considering a set of inputs, the problem consists in finding  $s(\mathbf{p}) \in \mathbb{R}$ , from the solution  $u(\mathbf{p})$  of 3.1 for each given  $\mathbf{p}$ . Optimization methods as well as uncertainty quantification require a large amount of realizations, with a potentially large number of degree of freedom, considering the growing complexity of engineering problems. The cost of such simulations can become prohibitive very fast. The ROM methodology consists in a fast but reliable approximation, based on the projection on a low-dimensional space, combined with an offline/online strategy that is applied to the elasticity equations as documented in what follows.

### 3.1.1 Reduced basis approximation

As introduced in the chapter on finite element approximations (Chapter 2), the finite element method allows to compute a discrete approximation of  $u(\mathbf{p})$ . This approximation  $u_{\mathcal{N}}(\mathbf{p})$  is based on the Galerkin projection of partial differential equations solution, on a subspace  $X_{\mathcal{N}} \subset X_{\mathcal{N}}(\Omega)$  of size  $\mathcal{N}$ . It requires the resolution of an  $\mathcal{N} \times \mathcal{N}$  system

$$a(u_{\mathcal{N}}(\mathbf{p}), v; \mathbf{p}) = f(v; \mathbf{p}) \quad \forall v \in X_{\mathcal{N}}(\Omega) \quad (3.3)$$

The fast simulation response is obtained by the reduced basis method, that relies on a Galerkin projections on the low-dimensional subspace  $W_{\mathcal{M}}$  of size  $\mathcal{M} \ll \mathcal{N}$ , whose basis functions are computed from a set of finite element approximations. Typically, the size  $\mathcal{M}$  (number of modes or Galerkin projections) of the reduced system is small (e.g. it does not exceed 100).

By introducing the sample  $S_{\mathcal{M}} = \{\mathbf{p}_1, \dots, \mathbf{p}_{\mathcal{M}}\} \in \mathcal{D}$  and its associated set of finite element solutions  $S_{\mathcal{M}}^u = \{u_{\mathcal{N}}(\mathbf{p}_i)\}_{i=1}^{\mathcal{M}}$  obtained from 3.3, the parameters of  $S_{\mathcal{M}}$  can be selected in various ways, ranging from a random selection process to more advanced methods directed by physical considerations. In this research, instead use the Proper Orthogonal Decomposition (POD) method or the Greedy algorithms that are commonly used to optimize the building of this sample (**Quarteroni2015**), the selection of the lower dimensional basis is motivated by the physics of the fluid structure coupling. The choice of problems that generate the basis are detailed in subsection 3.2.5.

An additional optimization, could be achieved by the orthonormalization of the  $S_{\mathcal{M}}^u$  components, through a Gram-Schmidt process with respect to the  $(\cdot, \cdot)_X$  inner product associated with  $X$ . Each global function results in the definition of  $W_{\mathcal{M}} = \text{span}\{\xi_i \equiv u_{\mathcal{N}}(\mathbf{p}_i), 1 \leq i \leq \mathcal{M}\}$ . By analogy with 2.3, the reduced basis approximation  $u_{\mathcal{M}}(\mathbf{p}_i) \in W_{\mathcal{M}}$  of  $u(\mathbf{p}) \in X$  then follows as the linear combination

$$u_{\mathcal{M}}(\mathbf{p}) = \sum_{i=1}^{\mathcal{M}} u_{\mathcal{M},i}(\mathbf{p}) \xi_i \quad (3.4)$$

If the reduced basis is used to approximated a *stand alone* problem, the finite element approximation resides in the resolution of the  $\mathcal{M} \times \mathcal{M}$  reduced system

$$\sum_{i=1}^{\mathcal{M}} a(\xi_i, \xi_j; \mathbf{p}) u_{\mathcal{M},i}(\mathbf{p}) = f(\xi_j; \mathbf{p}) \quad \forall j \in \{1, \dots, \mathcal{M}\} \quad (3.5)$$

### 3.1.2 Affine decomposition

When the problem is affinely parametrized, the forms  $a$  and  $f$  depend affinely on the parameters (**Quarteroni2015**), then is possible to decouple the terms of 3.5 which do not depend on the input

from the others. Therefore  $a(u, v; \mathbf{p})$  and  $f(v; \mathbf{p})$  can be written as (  $\mathcal{Q}_a$  and  $\mathcal{Q}_f$  are finite integers)

$$\begin{aligned} a(u, v; \mathbf{p}) &= \sum_{q=1}^{\mathcal{Q}_a} \theta_a^q(\mathbf{p}) a^q(u, v) \quad \forall u, v \in X, \forall \mathbf{p} \in \mathcal{D} \\ f(v; \mathbf{p}) &= \sum_{q=1}^{\mathcal{Q}_f} \theta_f^q(\mathbf{p}) f^q(v) \quad \forall v \in X, \forall \mathbf{p} \in \mathcal{D} \end{aligned} \quad (3.6)$$

In an offline stage, the basis functions will be computed as a function of the parameter space. This allows the online simulations which consist in the assembly and the resolution of 3.5 to be even faster.

The affine decomposition 3.6 is an essential ingredient for the offline/online strategy. Such decomposition is not necessarily available, in particular for non-affine or non-linear problems, but this is out of the scope of this study and is left for future work.

## 3.2 Monophasic poromechanics

The main ingredient in poromechanical simulation is the strong coupling between pore pressure and deformation. Any change in pore pressure will affect the deformation of the solid and vice versa. **Biot1941** developed the first poroelastic three dimensional coupled system, to describe the dynamics of the flow in porous medium under deformation. Biot's formulation considers an isothermal process, inside a porous medium completely saturated with a single fluid that crosses the porous matrix, it also considers a linear stress deformation relation as well as a linear relation between pressure and velocity through the Darcy's law.

For a slightly compressible fluid inside a poroelastic material and ignoring the permeability stress dependency, the mass conservation is reduced to:

$$\frac{\partial (\phi^* B_f^{-1})}{\partial t} + \operatorname{div}(\mathbf{q}) = 0 \quad (3.7)$$

where  $\mathbf{q}$  [ $\text{m s}^{-1}$ ] is the fluid velocity provided by the Darcy's law:

$$\mathbf{q} = B_f^{-1} \mathbf{v}_f = -\mathbf{K} \frac{1}{\eta B_f} (\nabla p - \rho_f \mathbf{g}) \quad (3.8)$$

In 3.7 and 3.8  $B_f$  is the fluid formation volume factor,  $\mathbf{K}$  [ $\text{m}^2$ ] is the absolute permeability,  $\rho_f$  [ $\text{kg m}^{-3}$ ] is the fluid density,  $\eta$  [Pa s] is the dynamic fluid viscosity,  $p$  [Pa] is the fluid pressure,  $\mathbf{g}$  [ $\text{m s}^{-2}$ ] is the gravity constant vector field and  $\phi^*$  is the true porosity or total fluid increment (**Rudnicki1986**):

$$\phi^* = \Phi(\mathbf{u}, p) = \phi_0 + \alpha (\operatorname{div}(\mathbf{u}) - \operatorname{div}(\mathbf{u}_0)) + S_e(p - p_0) \quad (3.9)$$

Using the relation between volumetric strain and volumetric stress:

$$(\sigma_v - \sigma_{v0}) + \alpha(p - p_0) = K_{dr} \epsilon_v \quad (3.10)$$

Inserting 3.10 inside 3.9, is obtained an alternative expression for total fluid content:

$$\phi^* = \phi^0 + \left( S_e + \frac{\alpha^2}{K_{dr}} \right) (p - p^0) + \frac{\alpha}{K_{dr}} (\sigma_v - \sigma_v^0) \quad (3.11)$$

where  $S_e = \frac{1}{M} [\text{Pa}^{-1}]$  is the inverse of Biot's modulus  $M$  [Pa],  $\alpha$  is the Biot's coefficient,  $K_{dr}$  [Pa] is the rock bulk modulus in drained conditions,  $\epsilon_v = \text{div}(\mathbf{u})$  is the volumetric strain,  $\mathbf{u}$  [m] is the displacement vector and  $\sigma_v$  [Pa] is the volumetric stress. Superscript 0 represents the initial state.

Neglecting inertial forces, the deformation process is governed by the equilibrium equations:

$$\text{div}(\boldsymbol{\sigma} - \boldsymbol{\sigma}_0 - \alpha(p - p_0)\mathbf{I}) - \rho_r\mathbf{g} = 0 \quad (3.12)$$

in terms of total stress tensor:

$$\text{div}(\boldsymbol{\sigma}^* - \boldsymbol{\sigma}_0^*) - \rho_r\mathbf{g} = 0 \quad (3.13)$$

where  $\boldsymbol{\sigma}^* = \boldsymbol{\sigma} - \alpha p \mathbf{I}$ , represents the terzaghi decomposition in the effective stress  $\boldsymbol{\sigma}$  and the hydrostatic counterpart  $\alpha p \mathbf{I}$ .

Rock deformation is determined by the elastic stress-strain relationship:

$$\boldsymbol{\sigma} = 2\mu\boldsymbol{\epsilon}(\mathbf{u}) + \lambda \text{tr}(\boldsymbol{\epsilon}(\mathbf{u}))\mathbf{I} \quad (3.14)$$

With initial and boundary conditions:

$$\begin{aligned} \mathbf{u} &= \mathbf{u}_0 && \text{on } \Omega \\ p &= p_0 && \text{on } \Omega \end{aligned} \quad (3.15)$$

$$\begin{aligned} p &= p_D && \text{on } \partial\Omega_D^{\text{porous}} \\ q \cdot \mathbf{n} &= q_n && \text{on } \partial\Omega_N^{\text{porous}} \end{aligned} \quad (3.16)$$

$$\begin{aligned} \mathbf{u} &= \mathbf{u}_D && \text{on } \partial\Omega_D^{\text{elastic}} \\ \boldsymbol{\sigma}^* \cdot \mathbf{n} &= \mathbf{t} && \text{on } \partial\Omega_N^{\text{elastic}} \end{aligned} \quad (3.17)$$

## Strong form I

Assuming infinitesimal deformations and replacing 3.14 in 3.13 and 3.8 in 3.7, the strong form is find  $(\mathbf{u}, p)$  such that:

$$\begin{aligned} \text{div}(2\mu\boldsymbol{\epsilon}(\mathbf{u}) + \lambda \text{tr}(\boldsymbol{\epsilon}(\mathbf{u}))\mathbf{I} - \boldsymbol{\sigma}_0 - \alpha(p - p_0)\mathbf{I}) - \rho_r\mathbf{g} &= 0 \\ \frac{\partial(\phi^* B_f^{-1})}{\partial t} + \text{div}\left(-\mathbf{K} \frac{1}{\eta B_f} (\nabla p - \rho_f \mathbf{g})\right) &= 0 \end{aligned} \quad (3.18)$$

subjet to 3.15, 3.16 and, 3.17.

## Strong Form II

The second strong form used in this section is the mixed form of the second equation of 3.18

$$\begin{aligned} \operatorname{div}(2\mu\boldsymbol{\epsilon}(\mathbf{u}) + \lambda \operatorname{tr}(\boldsymbol{\epsilon}(\mathbf{u}))\mathbf{I} - \boldsymbol{\sigma}_0 - \alpha(p - p_0)\mathbf{I}) - \rho_r\mathbf{g} &= 0 \\ \mathbf{K}^{-1}\eta B_f\mathbf{q} + \nabla p - \rho_f\mathbf{g} &= 0 \\ \frac{\partial(\phi^*B_f^{-1})}{\partial t} + \operatorname{div}(\mathbf{q}) &= 0 \end{aligned} \quad (3.19)$$

subject to 3.15, 3.16 and 3.17

## Discretization

Temporal derivatives are approximated by the Implicit Euler method. Regarding the space a finite element discretization is used. Then, the requirement of second order derivatives is dropped by the use of Gauss theorem of divergence, applied to each conservation law of 3.2 and to the second equation of 3.2, to obtain the following weak forms:

### Weak form I: Continuous Galerkin

$$\begin{aligned} \int_{\Omega}(2\mu\boldsymbol{\epsilon} + \lambda \operatorname{tr}(\boldsymbol{\epsilon})\mathbf{I}) \cdot \nabla(\boldsymbol{\phi}_u) dV - \int_{\partial\Omega_N} \mathbf{t} \cdot \boldsymbol{\phi}_u dS - \int_{\Omega} (\alpha p\mathbf{I}) \cdot \nabla(\boldsymbol{\phi}_u) dV + \int_{\Omega} \rho_r\mathbf{g} \cdot \boldsymbol{\phi}_u dV &= 0 \\ \int_{\Omega} \frac{(\phi^*B_f^{-1})^{n+1} - (\phi^*B_f^{-1})^n}{\Delta t} \phi_p dV - \int_{\partial\Omega_N} q_n \phi_p dS + \int_{\Omega} \mathbf{K} \frac{1}{B_f} (\nabla(p) - \rho_f\mathbf{g}) \cdot \nabla \phi_p dV &= 0 \end{aligned} \quad (3.20)$$

In terms of forms, the continuous Galerkin (GC) problem is find  $(\mathbf{u}, p) \in H^1(\Omega)^d \times H^1(\Omega)$  such that:

$$\begin{aligned} a_u(\mathbf{u}, \boldsymbol{\phi}_u) - b_u(p, \boldsymbol{\phi}_u) + c_u(\boldsymbol{\phi}_u) - f_u(\boldsymbol{\phi}_u) &= 0 \\ a_p(p, \phi_p) + b_p(\mathbf{u}, \phi_p) + c_p(p, \phi_p) - f_p(\phi_p) &= 0 \end{aligned} \quad (3.21)$$

for all  $\boldsymbol{\phi}_u \in H^1(\Omega)^d$ , and  $\phi_p \in H^1(\Omega)$ . Where the forms have the following integral expressions:

$$\begin{aligned} a_u(\mathbf{u}, \boldsymbol{\phi}_u) &= \int_{\Omega} (2\mu\boldsymbol{\epsilon} + \lambda \operatorname{tr}(\boldsymbol{\epsilon})\mathbf{I}) \cdot \nabla(\boldsymbol{\phi}_u) dV \\ b_u(p, \boldsymbol{\phi}_u) &= \int_{\Omega} (\alpha p\mathbf{I}) \cdot \nabla(\boldsymbol{\phi}_u) dV \\ c_u(\boldsymbol{\phi}_u) &= \int_{\Omega} \rho_r\mathbf{g} \cdot \boldsymbol{\phi}_u dV \\ f_u(\boldsymbol{\phi}_u) &= \int_{\partial\Omega_N} \mathbf{t} \cdot \boldsymbol{\phi}_u dS \end{aligned} \quad (3.22)$$

$$\begin{aligned}
a_p(p, \phi_p) &= \int_{\Omega} \mathbf{K} \frac{1}{B_f} (\nabla(p) - \rho_f \mathbf{g}) \cdot \nabla \phi_p \, dV \\
b_p(\mathbf{u}, \phi_p) &= \int_{\Omega} \frac{\alpha}{K_{dr}} \frac{(\sigma_v B_f^{-1})^{n+1} - (\sigma_v^0 B_f^{-1})^n}{\Delta t} \phi_p \, dV \\
c_p(p, \phi_p) &= \int_{\Omega} \left( S_e + \frac{\alpha^2}{K_{dr}} \right) \frac{(p B_f^{-1})^{n+1} - (p^0 B_f^{-1})^n}{\Delta t} \phi_p \, dV \\
f_p(\phi_p) &= \int_{\partial\Omega_N} q_n \phi_p \, dS
\end{aligned} \tag{3.23}$$

The discrete form is given  $(\mathbf{u}_N^n, p_N^n)$  find  $(\mathbf{u}_N^{n+1}, p_N^{n+1})$  such that:

$$\begin{aligned}
a_u(\mathbf{u}_N^{n+1}, \phi_{Nu}) - b_u(p_N^{n+1}, \phi_{Nu}) + c_u(\phi_{Nu}) - f_u(\phi_{Nu}) &= 0 \\
a_p(p_N^{n+1}, \phi_{Np}) + b_p(\mathbf{u}_N^{n+1}, \phi_{Np}) + c_p(p_N^{n+1}, \phi_{Np}) - f_p(\phi_{Np}) &= 0
\end{aligned} \tag{3.24}$$

for all  $\phi_{Nu} \in V_N^d$ , and  $\phi_{Np} \in V_N$ .

## Weak form II: Mixed Formulation for fluid equation

$$\begin{aligned}
\int_{\Omega} (2\mu\epsilon + \lambda \text{tr}(\epsilon) \mathbf{I}) \cdot \nabla(\phi_u) \, dV - \int_{\partial\Omega_N} \mathbf{t} \cdot \phi_u \, dS - \int_{\Omega} (\alpha p \mathbf{I}) \cdot \nabla(\phi_u) \, dV + \int_{\Omega} \rho_r \mathbf{g} \cdot \phi_u \, dV &= 0 \\
\int_{\Omega} \mathbf{K}^{-1} \eta B_f \mathbf{q} \cdot \phi_q \, dV + \int_{\partial\Omega_D} p_D \phi_q \cdot \mathbf{n} \, dS - \int_{\Omega} p \, \text{div}(\phi_q) \, dV - \int_{\Omega} \rho_f \mathbf{g} \cdot \phi_q \, dV &= 0 \\
- \int_{\Omega} \frac{(\phi^* B_f^{-1})^{n+1} - (\phi^* B_f^{-1})^n}{\Delta t} \phi_p \, dV - \int_{\Omega} \text{div}(\mathbf{q}) \phi_p \, dV &= 0
\end{aligned} \tag{3.25}$$

In terms of forms, the mixed formulation (for fluid equation) and GC (for deformation) problem is find  $(\mathbf{u}, \mathbf{q}, p) \in H^1(\Omega)^d \times H(\text{div}, \Omega) \times L^2(\Omega)$  such that:

$$\begin{aligned}
a_u(\mathbf{u}, \phi_u) - b_u(p, \phi_u) + c_u(\phi_u) - f_u(\phi_u) &= 0 \\
a_q(\mathbf{q}, \phi_q) - b_q(p, \phi_q) - c_q(\phi_q) + f_q(\phi_q) &= 0 \\
- b_p(\mathbf{q}, \phi_p) - c_p(p, \phi_p) - c_u(\mathbf{u}, \phi_p) &= 0
\end{aligned} \tag{3.26}$$

for all  $\phi_u \in H^1(\Omega)^d$ ,  $\phi_q \in H(\text{div}, \Omega)$  and  $\phi_p \in L^2(\Omega)$ . Where the forms have the following integral expressions:

$$\begin{aligned}
a_u(\mathbf{u}, \phi_u) &= \int_{\Omega} (2\mu\epsilon + \lambda \text{tr}(\epsilon) \mathbf{I}) \cdot \nabla(\phi_u) \, dV \\
b_u(p, \phi_u) &= \int_{\Omega} (\alpha p \mathbf{I}) \cdot \nabla(\phi_u) \, dV \\
c_u(\phi_u) &= \int_{\Omega} \rho_r \mathbf{g} \cdot \phi_u \, dV \\
f_u(\phi_u) &= \int_{\partial\Omega_N} \mathbf{t} \cdot \phi_u \, dS
\end{aligned} \tag{3.27}$$

$$\begin{aligned}
a_q(\mathbf{q}, \phi_q) &= \int_{\Omega} \mathbf{K}^{-1} \eta B_f \mathbf{q} \cdot \phi_q \, dV \\
b_q(p, \phi_q) &= \int_{\Omega} p \operatorname{div}(\phi_q) \, dV \\
c_q(\phi_q) &= \int_{\Omega} \rho_f \mathbf{g} \cdot \phi_q \, dV \\
f_q(\phi_q) &= \int_{\partial\Omega_D} p_D \phi_q \cdot \mathbf{n} \, dS \\
b_p(\mathbf{q}, \phi_p) &= \int_{\Omega} \operatorname{div}(\mathbf{q}) \phi_p \, dV \\
c_u(\mathbf{u}, \phi_p) &= \int_{\Omega} \frac{\alpha}{K_{dr}} \frac{(\sigma_v B_f^{-1})^{n+1} - (\sigma_v^0 B_f^{-1})^n}{\Delta t} \phi_p \, dV \\
c_p(p, \phi_p) &= \int_{\Omega} \left( S_e + \frac{\alpha^2}{K_{dr}} \right) \frac{(p B_f^{-1})^{n+1} - (p^0 B_f^{-1})^n}{\Delta t} \phi_p \, dV
\end{aligned} \tag{3.28}$$

The discrete form is given  $(\mathbf{u}_{\mathcal{N}}^n, p_{\mathcal{N}}^n)$  find  $(\mathbf{u}_{\mathcal{N}}^{n+1}, \mathbf{q}_{\mathcal{N}}^{n+1}, p_{\mathcal{N}}^{n+1})$  such that:

$$\begin{aligned}
a_u(\mathbf{u}_{\mathcal{N}}^{n+1}, \phi_{\mathcal{N}u}) - b_u(p_{\mathcal{N}}^{n+1}, \phi_{\mathcal{N}u}) + c_u(\phi_{\mathcal{N}u}) - f_u(\phi_{\mathcal{N}u}) &= 0 \\
a_q(\mathbf{q}_{\mathcal{N}}^{n+1}, \phi_{\mathcal{N}q}) - b_q(p_{\mathcal{N}}^{n+1}, \phi_{\mathcal{N}q}) - c_q(\phi_{\mathcal{N}q}) + f_q(\phi_{\mathcal{N}q}) &= 0 \\
-b_p(\mathbf{q}_{\mathcal{N}}^{n+1}, \phi_p) - c_p(p_{\mathcal{N}}^{n+1}, \phi_{\mathcal{N}p}) - c_p(\mathbf{u}_{\mathcal{N}}^{n+1}, \phi_{\mathcal{N}p}) &= 0
\end{aligned} \tag{3.29}$$

for all  $\phi_{\mathcal{N}u} \in V_{\mathcal{N}}$ ,  $\phi_{\mathcal{N}q} \in W_{\mathcal{N}}$  and  $\phi_{\mathcal{N}p} \in Z_{\mathcal{N}}$ .

### 3.2.1 About Sequential methods

For reasons of high computational cost associated with the fully coupled model, and with the aim of obtaining the best efficiency, it is desirable to develop and implement sequential methods that can be competitive in terms of numerical stability and computational efficiency, when they are compared to fully coupled approach. Sequential methods offer a great flexibility from the implementation point of view, and facilitate the use of specialized numerical methods to solve the mechanical and fluid flow problems (**Kim2011a**).

The discretization given by 3.24 is used for the description of the following sequential methods, that approximates the solution of the problem 3.18 and 3.19. It is important to note that the following solution strategies are implemented on the structure of iterative methods (see figure 1.2).

**Kim2011c** presents 4 different types of implicit sequential methods called: drained, undrained, fixed strain, and fixed stress split. They are summarized in the following subsections. One of the contributions of the following sections is the introduction of fixed stress for the mixed case. Naturally, the fully coupled scheme is used as a reference and therefore is detailed first.

## Fully coupled method

Denoting  $\mathcal{A}$  an operator representing the strong form of 3.18. The discrete approximation 3.24 can be expressed by the corresponding fully coupled operator as:

$$\mathcal{A}_{fc} : \begin{cases} \begin{bmatrix} \mathbf{u}_N^n \\ p_N^n \end{bmatrix} \xrightarrow{\mathcal{A}_{fc}} \begin{bmatrix} \mathbf{u}_N^{n+1} \\ p_N^{n+1} \end{bmatrix} \\ a_u(\mathbf{u}_N^{n+1}, \phi_{Nu}) - b_u(p_N^{n+1}, \phi_{Nu}) + c_u(\phi_{Nu}) - f_u(\phi_{Nu}) = 0 \\ a_p(p_N^{n+1}, \phi_{Np}) + b_p(\mathbf{u}_N^{n+1}, \phi_{Np}) + c_p(p_N^{n+1}, \phi_{Np}) - f_p(\phi_{Np}) = 0 \end{cases} \quad (3.30)$$

Using the operator 3.30 is defined the following residual forms for the elliptic component:

$$R^e = a_u(\mathbf{u}_N^{n+1}, \phi_{Nu}) - b_u(p_N^{n+1}, \phi_{Nu}) + c_u(\phi_{Nu}) - f_u(\phi_{Nu}) \quad (3.31)$$

and for the parabolic component:

$$R^p = a_p(p_N^{n+1}, \phi_{Np}) + b_p(\mathbf{u}_N^{n+1}, \phi_{Np}) + c_p(p_N^{n+1}, \phi_{Np}) - f_p(\phi_{Np}) \quad (3.32)$$

In this sense, for a given approximation of the temporal solution  $\begin{bmatrix} \mathbf{u}_N^{n+1} & p_N^{n+1} \end{bmatrix}^{T^i}$ , the superscript  $i$  means an iteration of the newton process. Thus is obtained the following system of equations for a newton correction  $\begin{bmatrix} \delta\mathbf{u}_N^{n+1} & \delta p_N^{n+1} \end{bmatrix}^{T^i}$  as follows :

$$\underbrace{\begin{bmatrix} A & -B^T \\ B & F \end{bmatrix}}_J \begin{bmatrix} \delta\mathbf{u}_N^{n+1} \\ \delta p_N^{n+1} \end{bmatrix}^i = - \begin{bmatrix} R^e \\ R^p \end{bmatrix}^i \quad (3.33)$$

Where  $J$  is the Jacobian matrix,  $A$  is the stiffness matrix associated to the elastic material,  $B$  is the coupling matrix,  $F = Q + \Delta t T$  is the flux matrix,  $Q$  is the compressibility matrix and,  $T$  is the transmissibility matrix.

In this way, the full coupled method simultaneously solve the system 3.33, obtaining  $\begin{bmatrix} \mathbf{u}_N^{n+1} & p_N^{n+1} \end{bmatrix}^{T^i}$  until reach the desired convergence.

## Drained Split

In this scheme, the sequential approximation is obtained by first solving the elliptic problem (deformation equation) and then the parabolic problem (flow equation). The pressure variation is frozen during the solution of the elliptic problem, the form of the operator is represented by:

$$\left\{ \begin{array}{l} \mathcal{A}_{dr}^e : a_u(\mathbf{u}_N^{n+1}, \phi_{Nu}) - b_u(p_N^n, \phi_{Nu}) + c_u(\phi_{Nu}) - f_u(\phi_{Nu}) = 0 \quad \delta p_N^{n+1} = 0 \\ \mathcal{A}_{dr}^p : a_p(p_N^{n+1}, \phi_{Np}) + b_p(\mathbf{u}_N^{n+1}, \phi_{Np}) + c_p(p_N^{n+1}, \phi_{Np}) - f_p(\phi_{Np}) = 0 \quad \boldsymbol{\epsilon}_N^{n+1} \end{array} \right. \quad (3.34)$$

In terms of system of equations 3.33:

$$\begin{bmatrix} A & -B^T \\ B & F \end{bmatrix} \begin{bmatrix} \delta \mathbf{u}_{\mathcal{N}}^{n+1} \\ \delta p_{\mathcal{N}}^{n+1} \end{bmatrix}^i = \begin{bmatrix} A & 0 \\ B & F \end{bmatrix} \begin{bmatrix} \delta \mathbf{u}_{\mathcal{N}}^{n+1} \\ \delta p_{\mathcal{N}}^{n+1} \end{bmatrix}^i - \begin{bmatrix} 0 & B^T \\ 0 & 0 \end{bmatrix} \begin{bmatrix} \delta \mathbf{u}_{\mathcal{N}}^{n+1} \\ \delta p_{\mathcal{N}}^{n+1} \end{bmatrix}^i \quad (3.35)$$

In this scheme, the first step is solved  $A\delta \mathbf{u}_{\mathcal{N}}^{n+1} = -R^e$  subject to  $\delta p_{\mathcal{N}}^{n+1} = 0$ , and then  $F\delta p_{\mathcal{N}}^{n+1} = -R^p - B\delta \mathbf{u}_{\mathcal{N}}^{n+1}$ . In this operation, physically the fluid can flow while the elliptic problem is solved.

In this way the drained method, sequentially solves the system 3.35 obtaining  $\begin{bmatrix} \mathbf{u}_{\mathcal{N}}^{n+1} & p_{\mathcal{N}}^{n+1} \end{bmatrix}^T$  until reach the desired convergence.

## Undrained Split

Unlike 3.2.1 the pressure predictor scheme is different. In this case, a zero variation of the total fluid content is imposed  $\delta\phi^* B_f^{-1}$ , thus the operator is:

$$\left\{ \begin{array}{l} \mathcal{A}_{udr}^e : a_u(\mathbf{u}_{\mathcal{N}}^{n+1}, \phi_{\mathcal{N}u}) - b_u(p_{\mathcal{N}}^{n+1/2}, \phi_{\mathcal{N}u}) + c_u(\phi_{\mathcal{N}u}) - f_u(\phi_{\mathcal{N}u}) = 0 \delta\phi^* B_f^{-1} = 0 \\ \mathcal{A}_{udr}^p : a_p(p_{\mathcal{N}}^{n+1}, \phi_{\mathcal{N}p}) + b_p(\mathbf{u}_{\mathcal{N}}^{n+1}, \phi_{\mathcal{N}p}) + c_p(p_{\mathcal{N}}^{n+1}, \phi_{\mathcal{N}p}) - f_p(\phi_{\mathcal{N}p}) = 0 \epsilon_{\mathcal{N}}^{n+1} \end{array} \right. \quad (3.36)$$

This strategy allows the pressure to change locally during the solution of the elliptic problem, by using the following expression:

$$p^{1+1/2} = p^n - \alpha S_e^{-1} (\epsilon_v^{n+1} - \epsilon_v^n) \quad (3.37)$$

The equation system is represented by:

$$\begin{bmatrix} A & -B^T \\ B & F \end{bmatrix} \begin{bmatrix} \delta \mathbf{u}_{\mathcal{N}}^{n+1} \\ \delta p_{\mathcal{N}}^{n+1} \end{bmatrix}^i = \begin{bmatrix} A + B^T Q^{-1} B & 0 \\ B & F \end{bmatrix} \begin{bmatrix} \delta \mathbf{u}_{\mathcal{N}}^{n+1} \\ \delta p_{\mathcal{N}}^{n+1} \end{bmatrix}^i - \begin{bmatrix} B^T Q^{-1} B & B^T \\ 0 & 0 \end{bmatrix} \begin{bmatrix} \delta \mathbf{u}_{\mathcal{N}}^{n+1} \\ \delta p_{\mathcal{N}}^{n+1} \end{bmatrix}^i \quad (3.38)$$

It is important to emphasize that the undrained condition is  $Q\delta p_{\mathcal{N}}^{n+1} + B\delta \mathbf{u}_{\mathcal{N}}^{n+1} = 0$ , which implies that  $(A + B^T Q^{-1} B) \delta \mathbf{u}_{\mathcal{N}}^{n+1} = -R^e$  during the elliptic step, the parabolic step is exactly the same as the drained split 3.2.1.

In this way, the undrained sequentially solves the system 3.38 obtaining  $\begin{bmatrix} \mathbf{u}_{\mathcal{N}}^{n+1} & p_{\mathcal{N}}^{n+1} \end{bmatrix}^T$  until reach the desired convergence.

## Fixed Strain Split

Unlike the previous splits, the parabolic problem is solved first. The operator is represented by:

$$\begin{cases} \begin{aligned} & \left[ \begin{array}{c} \mathbf{u}_{\mathcal{N}}^n \\ p_{\mathcal{N}}^n \end{array} \right] \xrightarrow{A_{ss}^p} \left[ \begin{array}{c} \mathbf{u}_{\mathcal{N}}^{n+1/2} \\ p_{\mathcal{N}}^{n+1} \end{array} \right] \xrightarrow{A_{ss}^e} \left[ \begin{array}{c} \mathbf{u}_{\mathcal{N}}^{n+1} \\ p_{\mathcal{N}}^{n+1} \end{array} \right] \\ & \mathcal{A}_{ss}^p : a_p(p_{\mathcal{N}}^{n+1}, \phi_{\mathcal{N}p}) + b_p(\mathbf{u}_{\mathcal{N}}^{n+1/2}, \phi_{\mathcal{N}p}) + c_p(p_{\mathcal{N}}^{n+1}, \phi_{\mathcal{N}p}) - f_p(\phi_{\mathcal{N}p}) = 0 \quad \delta \boldsymbol{\epsilon}_{\mathcal{N}}^{n+1} = 0 \\ & \mathcal{A}_{ss}^e : a_u(\mathbf{u}_{\mathcal{N}}^{n+1}, \phi_{\mathcal{N}u}) - b_u(p_{\mathcal{N}}^{n+1}, \phi_{\mathcal{N}u}) + c_u(\phi_{\mathcal{N}u}) - f_u(\phi_{\mathcal{N}u}) = 0 \quad p_{\mathcal{N}}^{n+1} \end{aligned} \end{cases} \quad (3.39)$$

In this case  $\delta \boldsymbol{\epsilon}_{\mathcal{N}}^{n+1} = 0$ , or in other terms  $\boldsymbol{\epsilon}_{\mathcal{N}}^{n+1/2} = \boldsymbol{\epsilon}_{\mathcal{N}}^n$ , thus the volumetric deformation in the parabolic term is calculated explicitly.

The equation system is represented by:

$$\left[ \begin{array}{cc} A & -B^T \\ B & F \end{array} \right] \left[ \begin{array}{c} \delta \mathbf{u}_{\mathcal{N}}^{n+1} \\ \delta p_{\mathcal{N}}^{n+1} \end{array} \right]^i = \left[ \begin{array}{cc} A & -B^T \\ 0 & F \end{array} \right] \left[ \begin{array}{c} \delta \mathbf{u}_{\mathcal{N}}^{n+1} \\ \delta p_{\mathcal{N}}^{n+1} \end{array} \right]^i - \left[ \begin{array}{cc} 0 & 0 \\ -B & 0 \end{array} \right] \left[ \begin{array}{c} \delta \mathbf{u}_{\mathcal{N}}^{n+1} \\ \delta p_{\mathcal{N}}^{n+1} \end{array} \right]^i \quad (3.40)$$

Solving the parabolic step first through  $F \delta p_{\mathcal{N}}^{n+1} = -R^p$ , while the variation in the deformation field is null i.e.  $B \delta \mathbf{u}_{\mathcal{N}}^{n+1} = 0$ . Then, the elliptic problem becomes  $A \delta \mathbf{u}_{\mathcal{N}}^{n+1} = -R^e + B^T \delta p_{\mathcal{N}}^{n+1}$ .

**Remark: Settari1998** emphasizes that the properties are dained for the elliptic problem and the pressures act as volumetric loads inside the poroelastic medium.

Sequentially, the system 3.40 is solved obtaining  $\left[ \begin{array}{c} \mathbf{u}_{\mathcal{N}}^{n+1} \\ p_{\mathcal{N}}^{n+1} \end{array} \right]^{T,i}$  until reach the desired convergence.

## Fixed Stress Split

In this case, the parabolic problem is solved by freezing the variation of the volumetric stress  $\delta \sigma_v = 0$ . Thus, the volumetric term  $\frac{\alpha}{K_{dr}} (\sigma_v - \sigma_{v0})$  of equation 3.11 is calculated explicitly. The operator is represented by:

$$\begin{cases} \begin{aligned} & \left[ \begin{array}{c} \mathbf{u}_{\mathcal{N}}^n \\ p_{\mathcal{N}}^n \end{array} \right] \xrightarrow{A_{fss}^p} \left[ \begin{array}{c} \mathbf{u}_{\mathcal{N}}^{n+1/2} \\ p_{\mathcal{N}}^{n+1} \end{array} \right] \xrightarrow{A_{fss}^e} \left[ \begin{array}{c} \mathbf{u}_{\mathcal{N}}^{n+1} \\ p_{\mathcal{N}}^{n+1} \end{array} \right] \\ & \mathcal{A}_{ss}^p : a_p(p_{\mathcal{N}}^{n+1}, \phi_{\mathcal{N}p}) + b_p(\mathbf{u}_{\mathcal{N}}^{n+1/2}, \phi_{\mathcal{N}p}) + c_p(p_{\mathcal{N}}^{n+1}, \phi_{\mathcal{N}p}) - f_p(\phi_{\mathcal{N}p}) = 0 \quad \delta \boldsymbol{\sigma}_{v\mathcal{N}}^{n+1} = 0 \\ & \mathcal{A}_{ss}^e : a_u(\mathbf{u}_{\mathcal{N}}^{n+1}, \phi_{\mathcal{N}u}) - b_u(p_{\mathcal{N}}^{n+1}, \phi_{\mathcal{N}u}) + c_u(\phi_{\mathcal{N}u}) - f_u(\phi_{\mathcal{N}u}) = 0 \quad p_{\mathcal{N}}^{n+1} \end{aligned} \end{cases} \quad (3.41)$$

The condition for fixed stress is  $-B \mathbf{u}_{\mathcal{N}}^{n+1} + BA^{-1}B^T p_{\mathcal{N}}^{n+1} = 0$ . Thus, in terms of the equivalent system of equations:

$$\left[ \begin{array}{cc} A & -B^T \\ B & F \end{array} \right] \left[ \begin{array}{c} \delta \mathbf{u}_{\mathcal{N}}^{n+1} \\ \delta p_{\mathcal{N}}^{n+1} \end{array} \right]^i = \left[ \begin{array}{cc} A & -B^T \\ 0 & F + BA^{-1}B^T \end{array} \right] \left[ \begin{array}{c} \delta \mathbf{u}_{\mathcal{N}}^{n+1} \\ \delta p_{\mathcal{N}}^{n+1} \end{array} \right]^i - \left[ \begin{array}{cc} 0 & 0 \\ -B & BA^{-1}B^T \end{array} \right] \left[ \begin{array}{c} \delta \mathbf{u}_{\mathcal{N}}^{n+1} \\ \delta p_{\mathcal{N}}^{n+1} \end{array} \right]^i \quad (3.42)$$

In this scheme, the parabolic problem becomes  $(F + BA^{-1}B^T) \delta p_{\mathcal{N}}^{n+1} = -R^p$ , inserting the term  $\frac{\alpha}{K_{dr}} (\sigma_v - \sigma_{v0})$  locally in each element, it is guaranteed that the variation of the volumetric stress is zero. Thus, within the solution of the parabolic step the product  $BA^{-1}B^T$  is not required. The elliptic step is exactly the same as in the previous step.

Sequentially, the fixed stress method solves the system 3.42, obtaining  $\begin{bmatrix} \mathbf{u}_{\mathcal{N}}^{n+1} & p_{\mathcal{N}}^{n+1} \end{bmatrix}^T$  until reach the desired convergence.

The fixed stress scheme for the mixed formulation 3.25 is described in a similar way but with the following modification:

$$\left\{ \begin{array}{l} \mathcal{A}_{ss}^p : \begin{aligned} a_q(\mathbf{q}_{\mathcal{N}}^{n+1}, \boldsymbol{\phi}_{\mathcal{N}q}) - b_q(p_{\mathcal{N}}^{n+1}, \boldsymbol{\phi}_{\mathcal{N}q}) - c_q(\boldsymbol{\phi}_{\mathcal{N}q}) + f_q(\boldsymbol{\phi}_{\mathcal{N}q}) &= 0 \\ -b_p(\mathbf{q}_{\mathcal{N}}^{n+1}, \boldsymbol{\phi}_p) - c_p(p_{\mathcal{N}}^{n+1}, \boldsymbol{\phi}_{\mathcal{N}p}) - c_u(\mathbf{u}_{\mathcal{N}}^{n+1}, \boldsymbol{\phi}_{\mathcal{N}p}) &= 0 \\ a_u(\mathbf{u}_{\mathcal{N}}^{n+1}, \boldsymbol{\phi}_{\mathcal{N}u}) - b_u(p_{\mathcal{N}}^{n+1}, \boldsymbol{\phi}_{\mathcal{N}u}) + c_u(\boldsymbol{\phi}_{\mathcal{N}u}) - f_u(\boldsymbol{\phi}_{\mathcal{N}u}) & \end{aligned} \end{array} \right. \begin{array}{l} \delta \boldsymbol{\sigma}_{v\mathcal{N}}^{n+1} = 0 \\ p_{\mathcal{N}}^{n+1} \end{array} \quad (3.43)$$

**Remark:** Kim2011c perfom a Von Neumann stability analysis of the sequential or staggered schemes described above, and report that drained and undrained splits are conditionally stable, whereas the fixed strain and fixed stress schemes are unconditionally stable. In addition, the authors report that the fixed stress scheme has better convergence properties than the fixed strain. For all above and for robustness, in this research is desired implementations based on unconditionally stable strategies and for better convergence properties the fixed stress split is implemented.

### 3.2.2 Implementation for the Fixed Stress Split

The sequential algorithm 3.1 approximates the time-space evolution of  $\begin{bmatrix} \mathbf{u}_{\mathcal{N}}^{n+1} & \mathbf{q}_{\mathcal{N}}^{n+1} & p_{\mathcal{N}}^{n+1} \end{bmatrix}^T$  for a time step with size  $\Delta t$ . In addition, for a given state  $\begin{bmatrix} \mathbf{u}_{\mathcal{N}}^n & \mathbf{q}_{\mathcal{N}}^n & p_{\mathcal{N}}^n \end{bmatrix}^T$  are performed  $m_{ss}$  fixed stress iterations whether the process does not converge within given tolerances  $\epsilon_p$  and  $\epsilon_e$ , for parabolic and elliptic steps, respectively.

Two examples are introduced in order to verify the implementation of the operators 3.41 and 3.43 using the algorithm 3.1. The purpose of this verification is to show that the algorithm given by the fixed stress split, generates the same results as the fully coupled scheme 3.30. Subsequently, these results are used as reference in the procedure of detailed reduction of the subsection 3.2.5.

### 3.2.3 Consolidation benchmark problem

A simple one-dimensional problem with known solution is approximate. The problem can be found in Murad1992 it represents a porous column with a fixed and impermeable wall on three sides. On top a load  $\boldsymbol{\sigma}_0$  is suddenly applied and the fluid is free to drain. Column length is  $L$  [m].

---

**Algorithm 3.1** Algorithm using Fixed Stress Split 3.41 (CG case) or 3.43 (Mixed case).

---

**Require:**  $\mathbf{K}_0$ ,  $\phi_0$ , poromechanic parameters:  $\lambda$ ,  $\mu$ ,  $\lambda_u$ ,  $\mu_u$ ,  $\alpha$  and control parameters:  $m_{ss}$ ,  $\epsilon_e$  and  $\epsilon_p$

**Ensure:**  $\begin{bmatrix} \mathbf{u}_{\mathcal{N}}^{n+1} & \mathbf{q}_{\mathcal{N}}^{n+1} & p_{\mathcal{N}}^{n+1} \end{bmatrix}^T$  over all time steps  $\Delta t_n$

Set initial data:  $\mathbf{u}_{\mathcal{N}}^0$  and  $p_{\mathcal{N}}^0$  from  $\nu \approx 0.5$

**for**  $n \in \{0, \dots, n_t\}$  **do**

    At given state  $\begin{bmatrix} \mathbf{u}_{\mathcal{N}}^n & \mathbf{q}_{\mathcal{N}}^n & p_{\mathcal{N}}^n \end{bmatrix}^T$

$\begin{bmatrix} \mathbf{u}_{\mathcal{N}0}^n & \mathbf{q}_{\mathcal{N}0}^n & p_{\mathcal{N}0}^n \end{bmatrix}^T \rightarrow \begin{bmatrix} \mathbf{u}_{\mathcal{N}}^n & \mathbf{q}_{\mathcal{N}}^n & p_{\mathcal{N}}^n \end{bmatrix}^T$

**for** fixed stress iteration  $k \in \{1, \dots, m_{ss}\}$  **do**

        Compute  $\mathcal{A}_{ss}^p$  and transfer  $p_{\mathcal{N}k}^{n+1}$  to elliptic structure (Parabolic step)

        Compute  $\mathcal{A}_{ss}^e$  and transfer  $\mathbf{u}_{\mathcal{N}k}^{n+1}$  to parabolic structure (Elliptic step)

**if**  $\|\mathbf{u}_{\mathcal{N}k}^{n+1} - \mathbf{u}_{\mathcal{N}k-1}^{n+1}\| \leq \epsilon_e$  **and**  $\|p_{\mathcal{N}k}^{n+1} - p_{\mathcal{N}k-1}^{n+1}\| \leq \epsilon_p$  **then**

            Set  $\begin{bmatrix} \mathbf{u}_{\mathcal{N}}^n & \mathbf{q}_{\mathcal{N}}^n & p_{\mathcal{N}}^n \end{bmatrix}^T = \begin{bmatrix} \mathbf{u}_{\mathcal{N}k}^{n+1} & \mathbf{q}_{\mathcal{N}k}^{n+1} & p_{\mathcal{N}k}^{n+1} \end{bmatrix}^T$

$n \rightarrow n + 1$

            Stop fixed stress iteration

**end if**

**end for**

**end for**

---

The boundary and initial conditions are  $\mathbf{u}(\mathbf{x}, 0) = \mathbf{u}_0 = 0$  and  $p(\mathbf{x}, 0) = p_0 = \boldsymbol{\sigma}_0$ . The figure 3.1 shows the physical setting of the problem. The equation 3.44 documents the analytical solution.

$$\begin{aligned}
 p_D &= \sum_{k=0}^{\inf} \frac{2}{M} \sin(M y_D) \exp(-M^2 t_D) \\
 \mathbf{u}_{yD} &= 1 - y_D - \sum_{k=0}^{\inf} \frac{2}{M^2} \cos(M y_D) \exp(-M^2 t_D) \\
 M &= \frac{1}{2} \pi (2k + 1) \\
 y_D &= \frac{y}{L} \\
 t_D &= \frac{(\lambda + 2\mu) \kappa t}{\eta L^2}
 \end{aligned} \tag{3.44}$$

Property	Value
Domain dimensions	$L = 1 \text{ [m]}$
Permeability	$\kappa = 1 \times 10^{-10} \text{ [m]}$
Viscosity	$\eta = 0.01 \text{ [Pa s]}$
Load	$\sigma_0 = -1000 \text{ [Pa]}$
Pressure	$p_D = 0$
Time	$t_f = 10, \Delta t = 1 \times 10^{-3} \text{ [s]}$
Element type	quadrilateral
First lamé	$\lambda = 8.333 \text{ [kPa]}$
Second lamé	$\mu = 12.5 \text{ [kPa]}$
First lamé $\nu = 0.4999$	$\lambda = 4.99933 \text{ [MPa]}$
Second lamé $\nu = 0.4999$	$\mu = 10.0007 \text{ [kPa]}$

Table 3.1: Input data for the column problem. Quase-incompresible solid-fluid structure response  $\text{tr}(\boldsymbol{\sigma}^*) = -p_0$  is forced by setting ( $\nu = 0.4999$ ) .

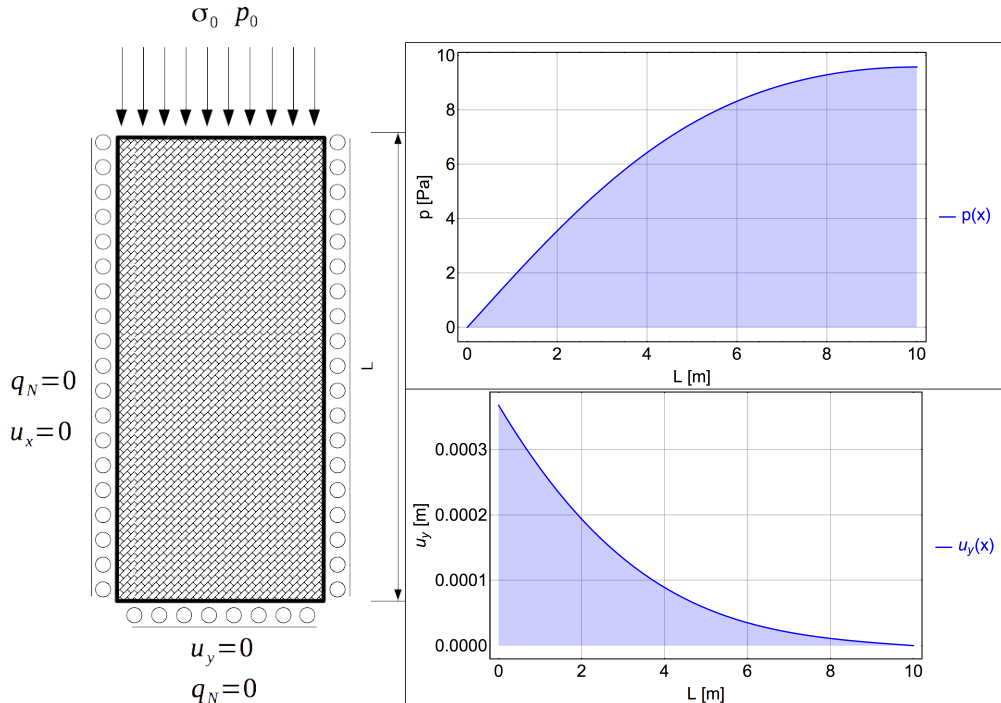


Figure 3.1: Boundary conditions for the column problem (left). Analytical solution at  $t = 10 \text{ [s]}$  (right), with  $n = 1000$  terms.

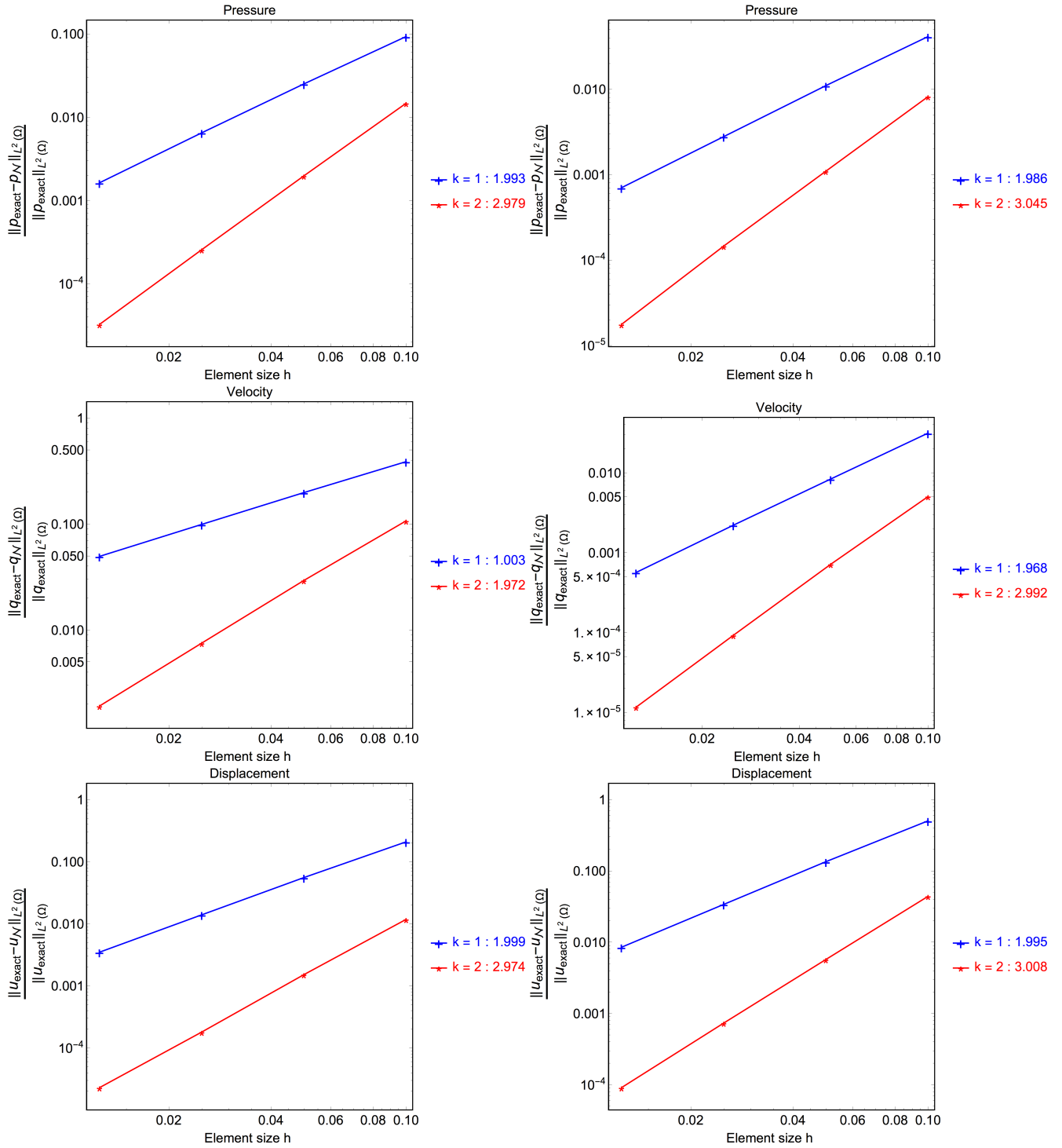


Figure 3.2:  $L^2(\Omega)$  error plots for  $k = \{1, 2\}$ , left correspond for operator 3.41, right for operator 3.43. Analytical solution at  $t = 10$  [s], with  $n = 1000$  terms.

$$e_{\mathcal{N}}(p) = \frac{\|p - p_{\mathcal{N}}\|_{L^2(\Omega)}}{\|p\|_{L^2(\Omega)}} ; \quad e_{\mathcal{N}}(\mathbf{q}) = \frac{\|\mathbf{q} - \mathbf{q}_{\mathcal{N}}\|_{L^2(\Omega)}}{\|\mathbf{q}\|_{L^2(\Omega)}}; \quad e_{\mathcal{N}}(\mathbf{u}) = \frac{\|\mathbf{u} - \mathbf{u}_{\mathcal{N}}\|_{L^2(\Omega)}}{\|\mathbf{u}\|_{L^2(\Omega)}} \quad (3.45)$$

Relative Errors 3.45 are computed for the case defined by the input data in table 3.1. The figures 3.2 show relative error curves for the approximation, using CG (see subsection 3.2) and for the mixed formulation (see subsection 3.2). In order to observe the approximation properties of the spatial scheme, it is used the polynomial orders  $k = \{1, 2\}$ , and the parameters are fixed to  $\epsilon_p = \epsilon_e = 1 \times 10^{-10}$  and  $\Delta t = 1.0 \times 10^{-6}$  [s].  $\Delta t$  is small enough to decrease the error in the separation defined by the algorithm 3.1 and in the temporal discretization. As it is expected, the approximation of the velocity using a mixed setting of type I (see chapter 2), it has one order greater than the approximation of CG for the fluid equation, and it is local conservative vector field. For the deformation equation, the pressure approximation error dominates the displacements error, which for  $k = 1$ , it has quadratic functions and therefore the resulting approximation order, is only the same of the pressure. The figure 3.3 shows an snapshot at  $t = 10$  [s] with  $k = 1$ , the partition is shown with red gridlines, the pressure of the column under deformation is shown on a color map, the change in volume is increased 10 times to make the consolidation more evident in relation to the initial state (black outline). Graphically, the velocity  $\mathbf{q}$  shows a higher approximation compared to an approximation by CG (blue points) for the flow equation.

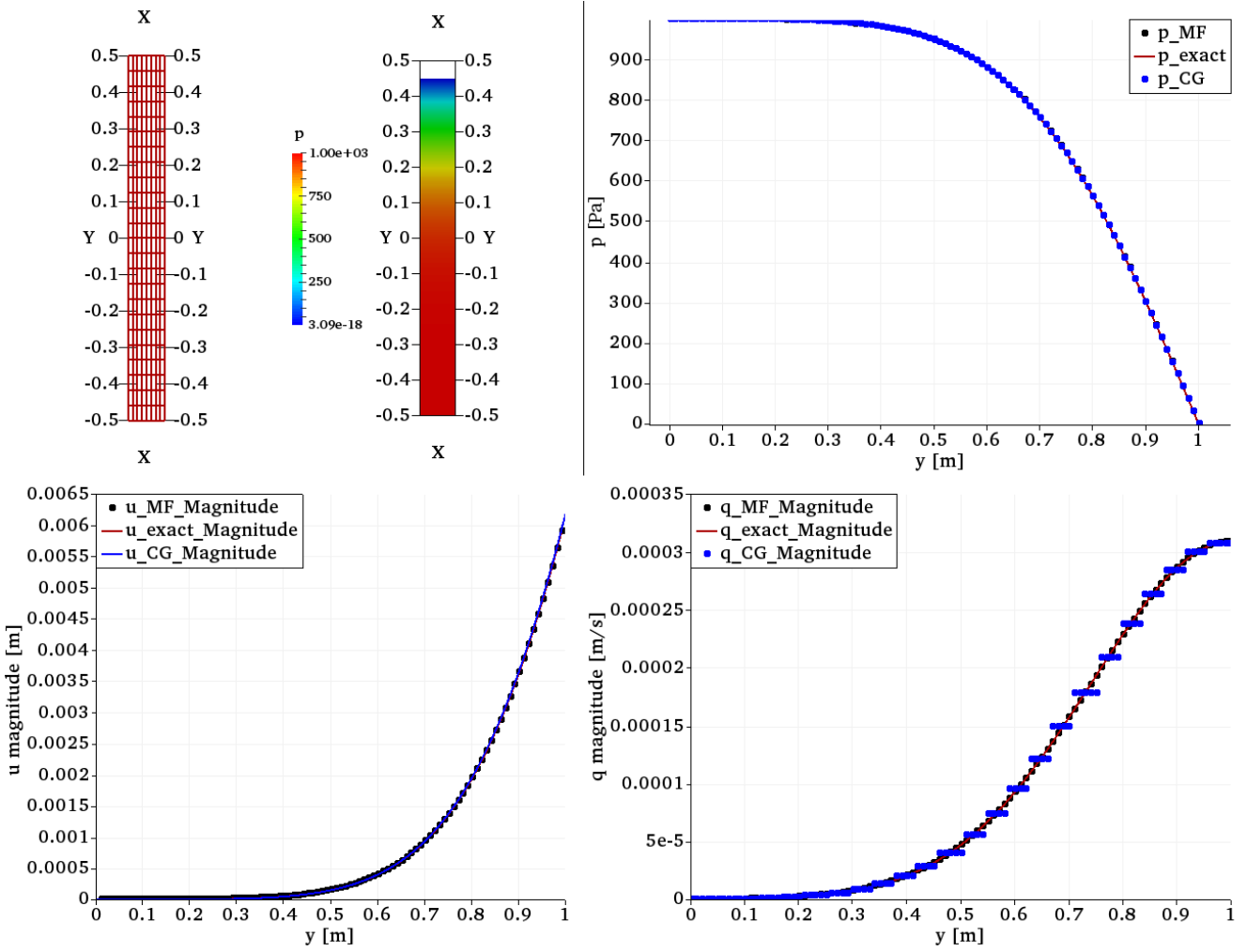


Figure 3.3: Snapshot for approximations with  $k = 1$  (blue dots Continuous Galerkin) and (black dots Mixed formulation of Type I). Plot over line  $l = \{\{0, 0.5\}, \{0, -0.5\}\}$ .

### 3.2.4 Footing problem

The following problem is introduced to verify the approximations of the sequential method implementation in a 2D configuration. Taking advantage of the symmetry, half of the domain is being used. The physical configuration is presented in the figure 3.4. The problem approximates the behavior of a porous medium (soil) suddenly subjected to a load  $\sigma_0$  over the first  $a$  [m] on the top boundary, the soil under localized consolidation, allows the fluid free to drain on the same boundary.

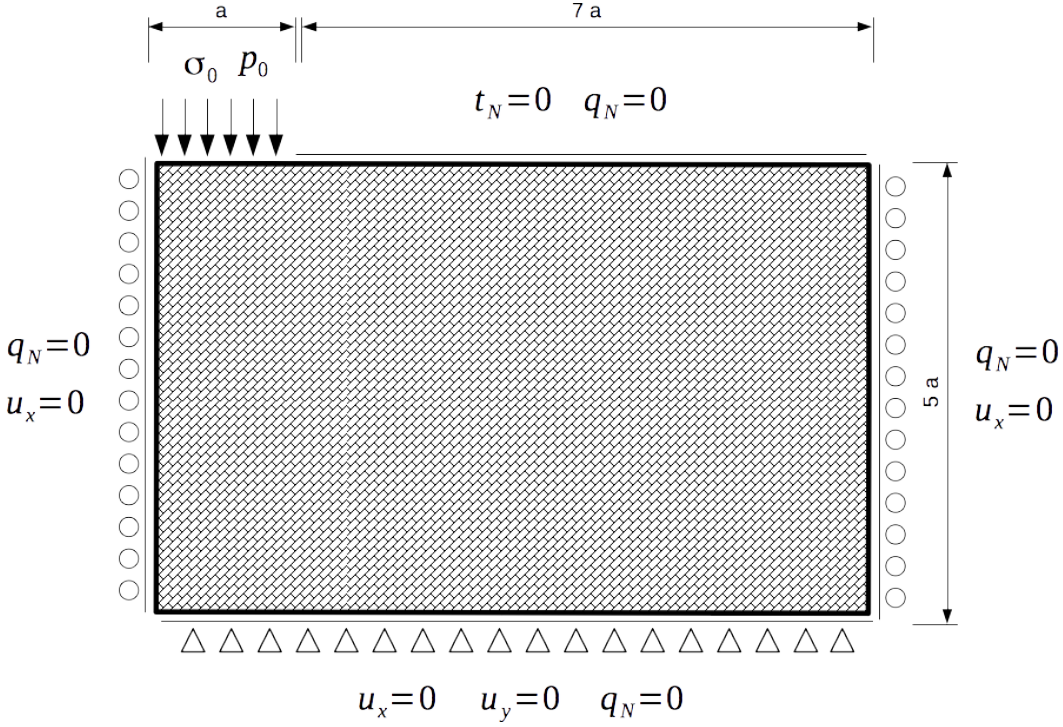


Figure 3.4: Boundary conditions for the footing problem.

Property	Value
Domain dimensions	$a = 1 \text{ [m]}$
Permeability	$\kappa = 1 \times 10^{-10} \text{ [m]}$
Viscosity	$\eta = 0.01 \text{ [Pa s]}$
Load	$\sigma_0 = -1000 \text{ [Pa]}$
Pressure	$p_D = 0$
Time	$t_f = 10, \Delta t = 1 \text{ [s]}$
Element type	triangle
First lamé	$\lambda = 8.333 \text{ [kPa]}$
Second lamé	$\mu = 12.5 \text{ [kPa]}$
First lamé $\nu = 0.4999$	$\lambda = 4.99933 \text{ [MPa]}$
Second lamé $\nu = 0.4999$	$\mu = 10.0007 \text{ [kPa]}$

Table 3.2: Input data for the footing problem. Quase-incompressible solid-fluid structure response  $tr(\boldsymbol{\sigma}^*) = -p_0$  is forced by setting ( $\nu = 0.4999$ ) .

The figures show two sanpshots of the approximation by the operator 3.41 and 3.43, with the respective pressure and velocity maps on the deformed configuration at  $t = 10 \text{ [s]}$ . The pressure profiles correspond to those ones reported in **Korsawe2006** ( figure 6), showing the consistency of the approximation in a purely 2D case over an unstructured mesh. Due to the balance of the spaces in the mixed configuration, once again, it is expected the same approximation properties for

pressure and velocity. The figure 3.5 documents the partition being used, as well as is expected, the approximations of the displacements are very similar, because the elliptic component is equal in the operators 3.41 and 3.43. So because the pressure approximation order is equal, the approximation order of  $\mathbf{u}$  for the two operators is the same. This feature allows to state that, from any surrogate model of  $\mathbf{u}$  will be expected the same error effect in both operators.

Figure 3.5 also shows a color map for the stress  $\sigma_{yy}$  associated with mixed discretization of type I.

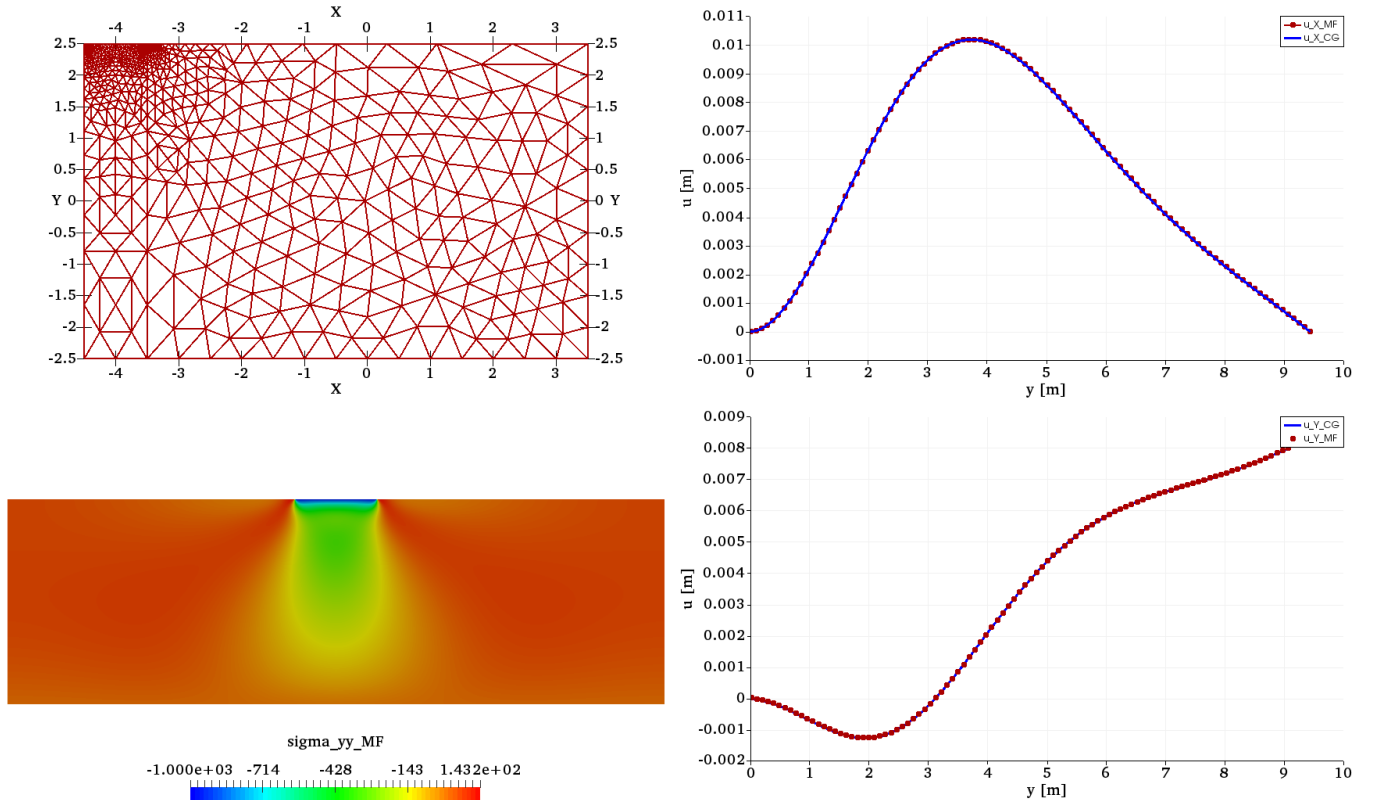
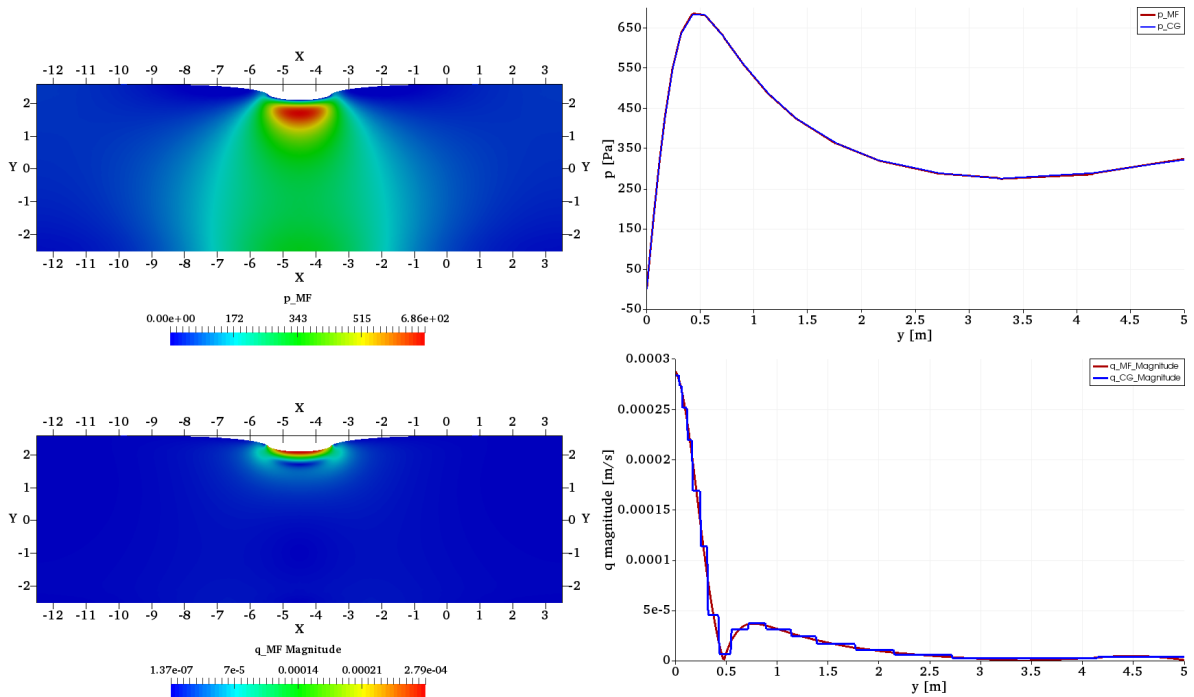
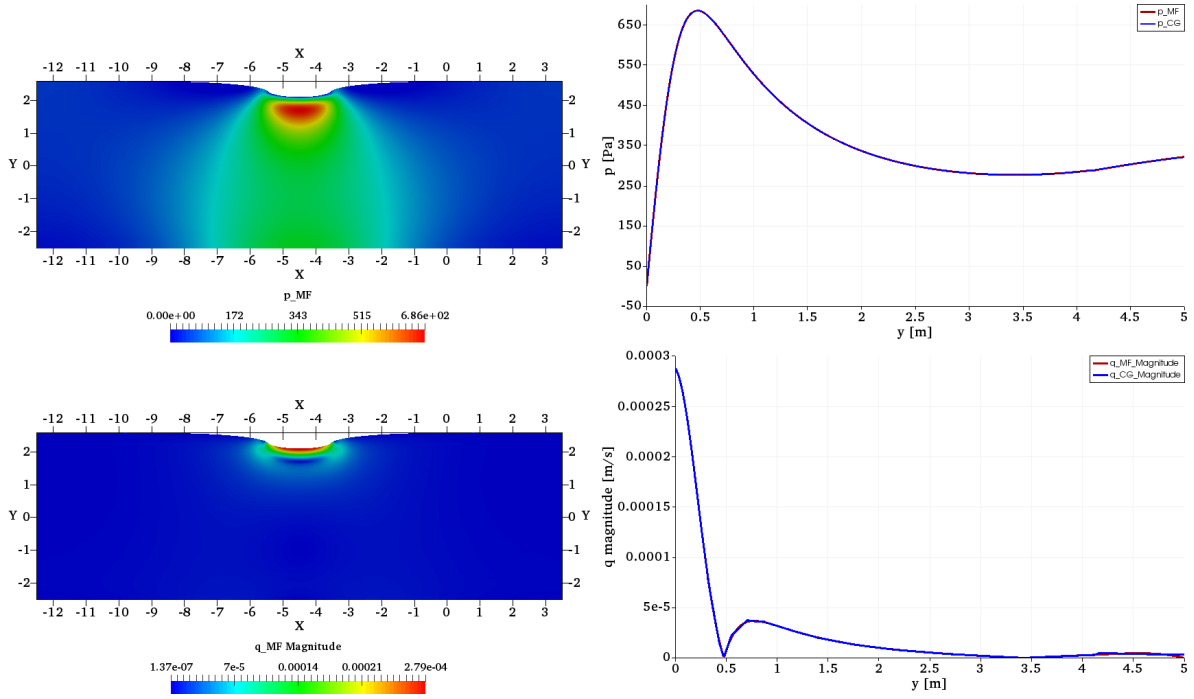


Figure 3.5: Snapshot for approximations of displacements associated to discretization of flow equation (blue Continuous Galerkin) and (red dots Mixed formulation of Type I). Right top partition, Right bottom color map of  $\sigma_{yy}$ . Profiles rendered over line  $l = \{(-4.5, 0), (-4.5, -5)\}$ .

Figure 3.6, on the left, shows pressure and flow contours on the deformed configuration augmented to 10 times, the apporoximation is computed using the mixed formulation applied on the fluid. In the left, the figure 3.6 presents, several graphs of the pressure and flow approximated by the two formulations for order  $k = \{1, 2\}$ , these comparative graphs document the consistency of the two approximations in the same two-dimensional configuration. The flux and pressure profiles are rendered plotting the quantities over the line  $l = \{(-4.5, 0), (-4.5, -5)\}$  at  $t = 10$  [s].



(a) Footing problem approximation with  $k = 1$ .



(b) Footing problem approximation with  $k = 2$ .

Figure 3.6: Snapshot for approximations (blue Continuous Galerkin) and (red Mixed formulation of Type I). Plot over line  $l = \{(-4.5, 0), (-4.5, -5)\}$ .

### 3.2.5 Empirical reduction strategy

A geomechanical configuration of the reservoir is presented in figure 3.7. In this configuration, the reservoir is modeled as a large poroelastic inclusion within a pure elastic medium (the sideburden rocks).

In conventional simulations, the discretization of the sideburden rocks represent a costly computational load, mainly because a large elasticity system at each step of time must be solved as the pressure evolves. A simulation of reservoirs with geomechanical coupling is still considered an expensive process.

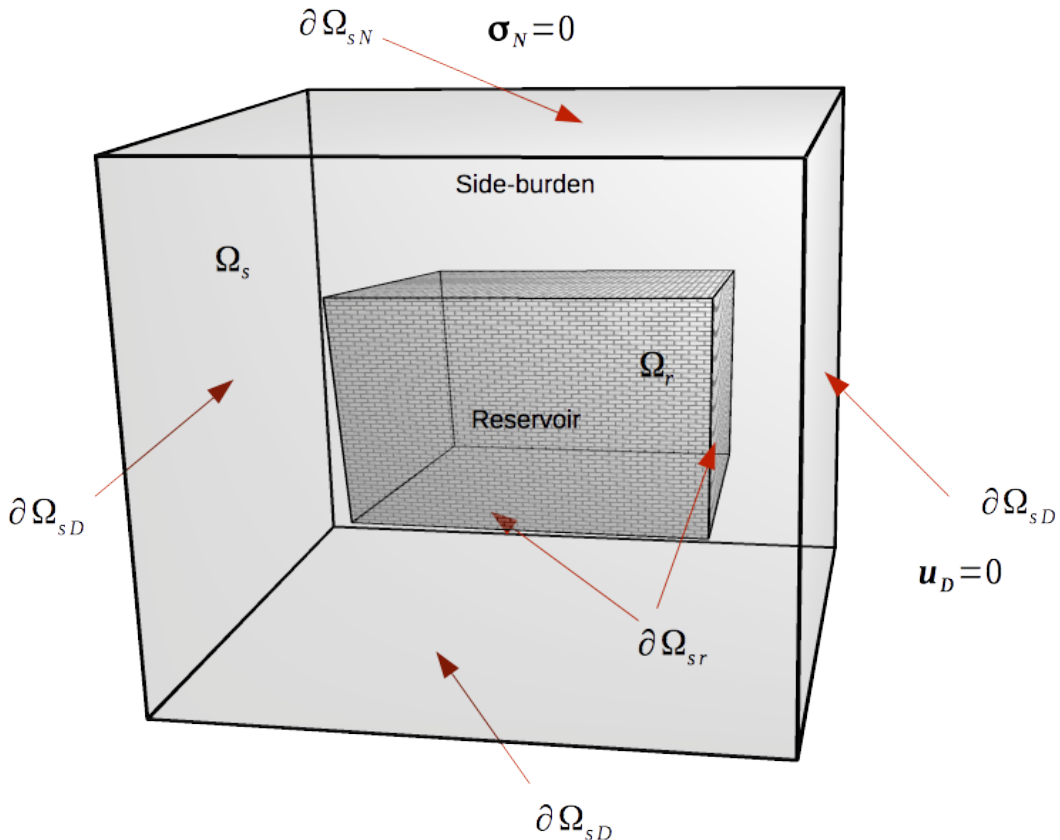


Figure 3.7: Reservoir  $\Omega_r$  and side-burden  $\Omega_s$  regions for a typical deformation.

The need to reduce the poromechanic problem is motivated by:

- The numerical approximation of sideburden rocks deformation, requires the mesh of a large computational domain, taking great computational costs.
- In the sense of reservoir simulation, it prioritizes the simulations of multiphase flow without neglecting the geomechanic coupling.
- It represents a suitable way to consider full coupling, but an excellent alternative in staggered schemes.

The objective of this study is the approximation inside the reservoir, but considering the correction of the rock deformation and the side burden effects. In addition, knowing that  $\mathbf{u}_N$  is a big computational burden, it is intentionally replaced by an approximation  $\mathbf{u}_M$  that captures the rock deformation, based on an empirical reduction strategy. The key idea is: In each element  $K$ , the elastic deformation can be computed as a linear combination of the global elastic solution  $\mathbf{u}_M$ . The global solutions are computed as an elastic response to constant pressures, that act on a partition  $\Gamma_h$ . This concept naturally leads to an offline/online strategy for the simulation of the poroelastic deformation and is documented in the next sections.

## Offline Split

Offline separation is divided into two main parts:

- A methodology for the definition of the pressure fields acting in the poroelastic environment  $\Omega_r$ , as is shown in figure 3.7.
- The calculation of  $M$  approximations of a linear symmetric operator that defines the reduction used in the online split procedure.

For the definition of the pressures, the methodology adopted is based on a constant function by parts on the computational domain defined as:

$$p_i(\mathbf{x}) = \begin{cases} c & \text{if } \mathbf{x} \in K_{gi} \\ 0 & \text{if } \mathbf{x} \notin K_{gi} \end{cases} \quad (3.46)$$

where  $K_{gi}$  represents a group or set of elements belonging to the partition  $\Gamma_h$ .

**Remark:** It is important to point out that the zero pressure field  $p_0 = 0$  characterizes the drained limit, and it must be included in the set of selected pressure fields.

### Methodology of selection of the pressure fields

The selection methodology is purely based on geometrical concepts as shown in figure 3.8. Once the domain geometry is meshed, it is overlaid over a cartesian mesh of blocks  $\{n_x, n_y, n_z\}$  of size  $\{\delta x, \delta y, \delta z\}$ , on which the grouping rule is defined as: for a given element  $K_{ci}$  of the cartesian mesh, the element  $K_j \in K_{gi}$  if  $\mathbf{x}_c \in K_{ci}$ , where  $\mathbf{x}_c$  is the centroid of  $K_j$ . In the figure 3.8, the blue region represented the selected group of elements in the partition  $\Gamma_h$  that belong to the  $K_{ci}$ , element outlined by color green.

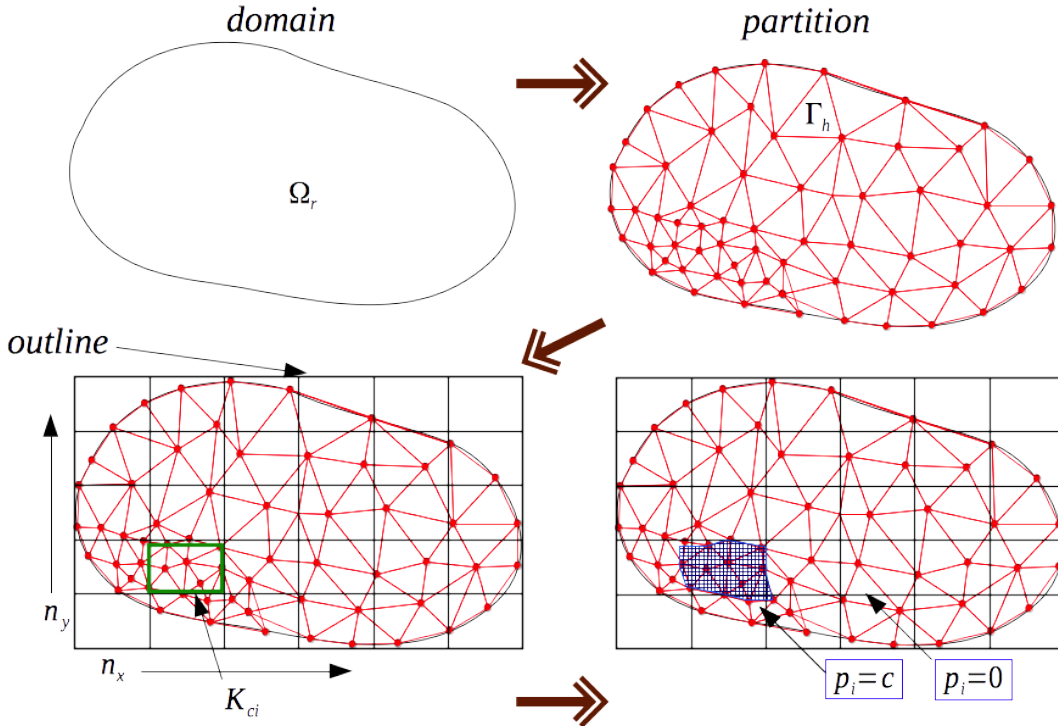


Figure 3.8: Process for selection of elements where the pressure field  $p_i$  is applied.

For each element group  $K_{gi}$ , the solution  $\mathbf{u}_i(p_i(\mathbf{x}))$  is associated with a discrete weak problem, that results from taking only the equation related to the elliptic counter part of 3.24.

The discrete problem is find  $\mathbf{u}_{i\mathcal{N}}$  such that:

$$a_u(\mathbf{u}_{i\mathcal{N}}, \phi_{\mathcal{N}u}) - b_u(p_i(\mathbf{x}), \phi_{\mathcal{N}u}) + c_u(\phi_{\mathcal{N}u}) - f_u(\phi_{\mathcal{N}u}) = 0 \quad (3.47)$$

for all  $\phi_{\mathcal{N}u} \in V_{\mathcal{N}}$ .

In addition, it is important to point out that  $\theta_a^q(\mathbf{p}) = 1$  and  $\theta_f^q(\mathbf{p}) = 1$ , because the elastic parameters are constant and homogeneous, resulting in the independency the parameters in relation to the bilinear operators of 3.47, but with a clear dependency in the load force  $f$ . Also, another kind of reduction can be explored by the affine dependency of the lamé parameters in the bilinear forms, but this is left for future works. Since the problem is linear, the associated global matrix is decomposed once, and each base function of the reduced model is obtained through the coefficients associated with each solution  $\mathbf{u}_{i\mathcal{N}}(p_i(\mathbf{x}))$ .

## Online Split

The online part is calculated by modifying the problems 3.24 and 3.29 resulting in:

For the standard formulation GC, given  $(\mathbf{u}_{\mathcal{M}}^n, p_{\mathcal{N}}^n)$  find  $(\mathbf{u}_{\mathcal{M}}^{n+1}, p_{\mathcal{N}}^{n+1})$  such that:

$$\begin{aligned} a_u(\mathbf{u}_{\mathcal{M}}^{n+1}, \phi_{\mathcal{M}u}) - b_u(p_{\mathcal{N}}^{n+1}, \phi_{\mathcal{M}u}) + c_u(\phi_{\mathcal{M}u}) - f_u(\phi_{\mathcal{M}u}) &= 0 \\ a_p(p_{\mathcal{N}}^{n+1}, \phi_{\mathcal{N}p}) + b_p(\mathbf{u}_{\mathcal{N}}^{n+1}, \phi_{\mathcal{N}p}) + c_p(p_{\mathcal{N}}^{n+1}, \phi_{\mathcal{N}p}) - f_p(\phi_{\mathcal{N}p}) &= 0 \end{aligned} \quad (3.48)$$

for all  $\phi_{\mathcal{M}u} \in V_{\mathcal{M}}$ , and  $\phi_{\mathcal{N}p} \in V_{\mathcal{N}}$ .

for the mixed formulation, given  $(\mathbf{u}_{\mathcal{M}}^n, p_{\mathcal{N}}^n)$  find  $(\mathbf{u}_{\mathcal{M}}^{n+1}, \mathbf{q}_{\mathcal{N}}^{n+1}, p_{\mathcal{N}}^{n+1})$  such that:

$$\begin{aligned} a_u(\mathbf{u}_{\mathcal{M}}^{n+1}, \phi_{\mathcal{M}u}) - b_u(p_{\mathcal{N}}^{n+1}, \phi_{\mathcal{M}u}) + c_u(\phi_{\mathcal{M}u}) - f_u(\phi_{\mathcal{M}u}) &= 0 \\ a_q(\mathbf{q}_{\mathcal{N}}^{n+1}, \phi_{\mathcal{N}q}) - b_q(p_{\mathcal{N}}^{n+1}, \phi_{\mathcal{N}q}) + c_q(\phi_{\mathcal{N}q}) - f_q(\phi_{\mathcal{N}q}) &= 0 \\ -b_p(\mathbf{q}_{\mathcal{N}}^{n+1}, \phi_p) - c_p(p_{\mathcal{N}}^{n+1}, \phi_{\mathcal{N}p}) &= 0 \end{aligned} \quad (3.49)$$

for all  $\phi_{\mathcal{M}u} \in V_{\mathcal{M}}$ ,  $\phi_{\mathcal{N}q} \in W_{\mathcal{N}}$  and  $\phi_{\mathcal{N}p} \in Z_{\mathcal{N}}$ .

## Application of the reduction procedure

In this section are revisited the problems described in the sub sections 3.2.3 and 3.2.4, approximating the solution with the same mathematical structure, but this time using the reduction procedure on the elliptic operator.

Defining the error ratio:

$$r_e = \frac{e_{\mathcal{M}}}{e_{\mathcal{N}}} \quad (3.50)$$

where  $1 \leq r_e$

in terms of degree of freedom the reduction percent is:

$$r_{\mathcal{M}} = 100 \cdot \left(1 - \frac{\mathcal{M}}{\mathcal{N}}\right) \quad (3.51)$$

An error graph that relates  $r_e$  with  $r_{\mathcal{M}}$ , shows the amount of reduced bases needed to achieve a precision similar to the full-order problem, i.e.  $r_{\mathcal{M}}$  such that  $r_e \approx 1$ .

In this section the offline and online stages are executed for a given partition (reference), which the number of bases  $\mathcal{M}$  is increased to observe the consistency of the reduction process, i.e. as the number of bases increases the error decreases.

### 3.2.6 RB approximation for consolidation problem

The figures 3.10 show the evolution of the error ratio, using reduced bases instead of the full order elliptic operator. The table 3.3 shows the parameters used for the generation of the following graphs.

For both 3.41 and 3.43, the consolidation problem is approximated, and it is demonstrated that:

- For linear and quadratic orders, the process converges close to the precision of the approximated solution with the full order operator, i.e. black line where  $r_e = 1$ .
- With  $\mathcal{M} = 40$  is obtained a reliable approximation with  $k = \{1, 2\}$ . In case of  $k = 2$  curves they tend to have a more substantial reduction.
- It is evident that using the reduction procedure, the spatial approximation properties of the full order problem are deteriorated. However, with a sufficient number of reduced bases the scheme recovers the full order operator and its properties.

Property	Value
Domain dimensions	$L = 1$ [m]
Permeability	$\kappa = 1 \times 10^{-10}$ [m]
Viscosity	$\eta = 0.01$ [Pa s]
Load	$\sigma_0 = -1000$ [Pa]
Pressure	$p_D = 0$
Time	$t_f = 10, \Delta t = 1 \times 10^{-3}$ [s]
Element type	quadrilateral
$k = 1$ elliptic DoF	$\mathcal{N}_e = 1458$
$k = 2$ elliptic DoF	$\mathcal{N}_e = 3146$
First lamé	$\lambda = 8.333$ [kPa]
Second lamé	$\mu = 12.5$ [kPa]
First lamé $\nu = 0.4999$	$\lambda = 4.99933$ [MPa]
Second lamé $\nu = 0.4999$	$\mu = 10.0007$ [kPa]

Table 3.3: Input data for the column problem. Quase-incompresible solid-fluid structure response  $tr(\boldsymbol{\sigma}^*) = -p_0$  is forced by setting ( $\nu = 0.4999$ ) .

- The figure 3.9 shows an instant with the approximation RB with  $\mathcal{M} = 40$ . Graphically, the reduction shows a good adjustment compared with the analytical solution.
- The graphics, of the figure 3.10 are not conclusive for the certification of the reduce basis procedure, but show the potential of the reduction proposed in this investigation.

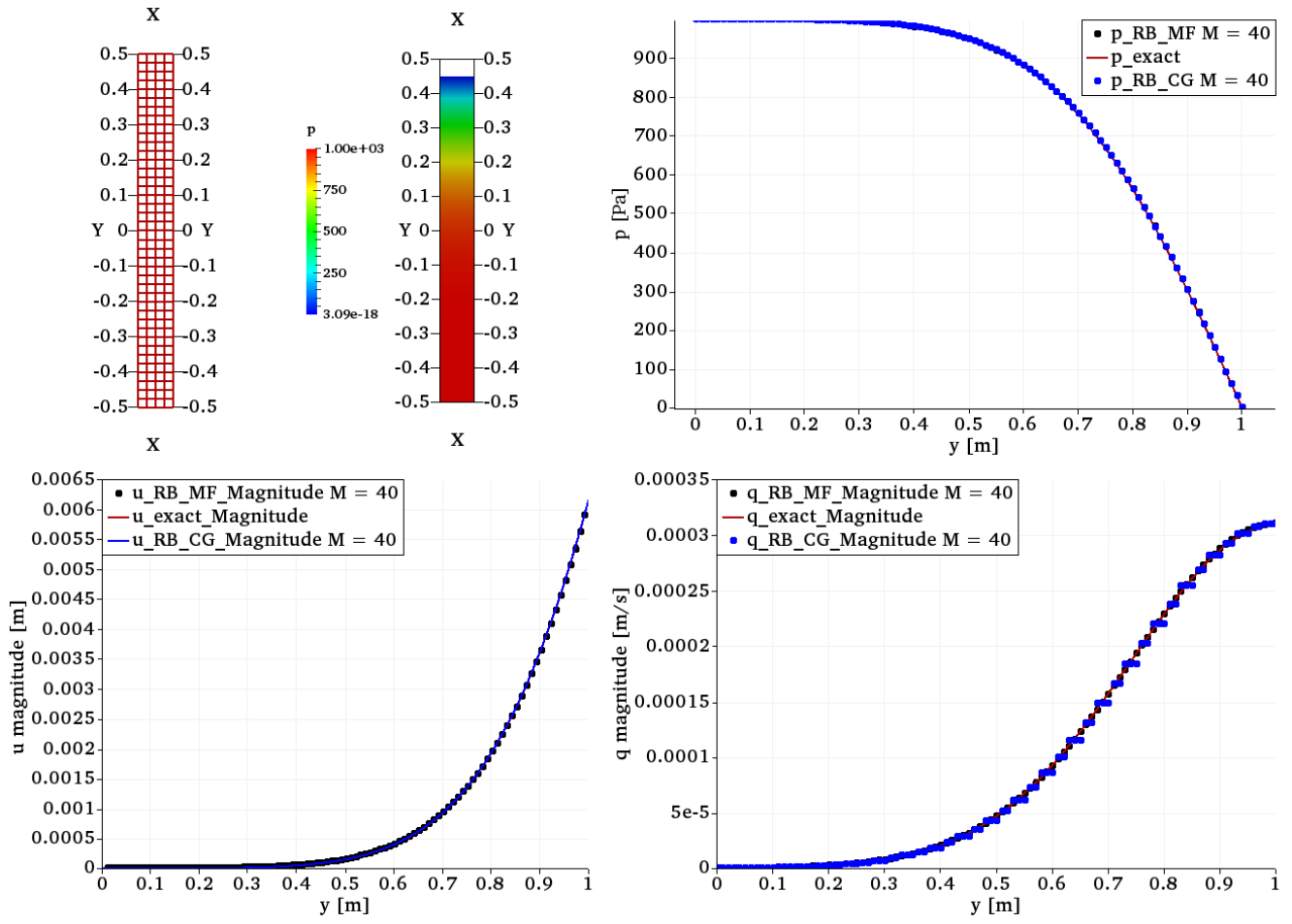


Figure 3.9: Snapshot for RB approximations with  $k = 1$  and  $\mathcal{M} = 40$ , (blue dots Continuous Galerkin) and (black dots Mixed formulation of Type I). Plot over line  $l = \{\{0, 0.5\}, \{0, -0.5\}\}$ .

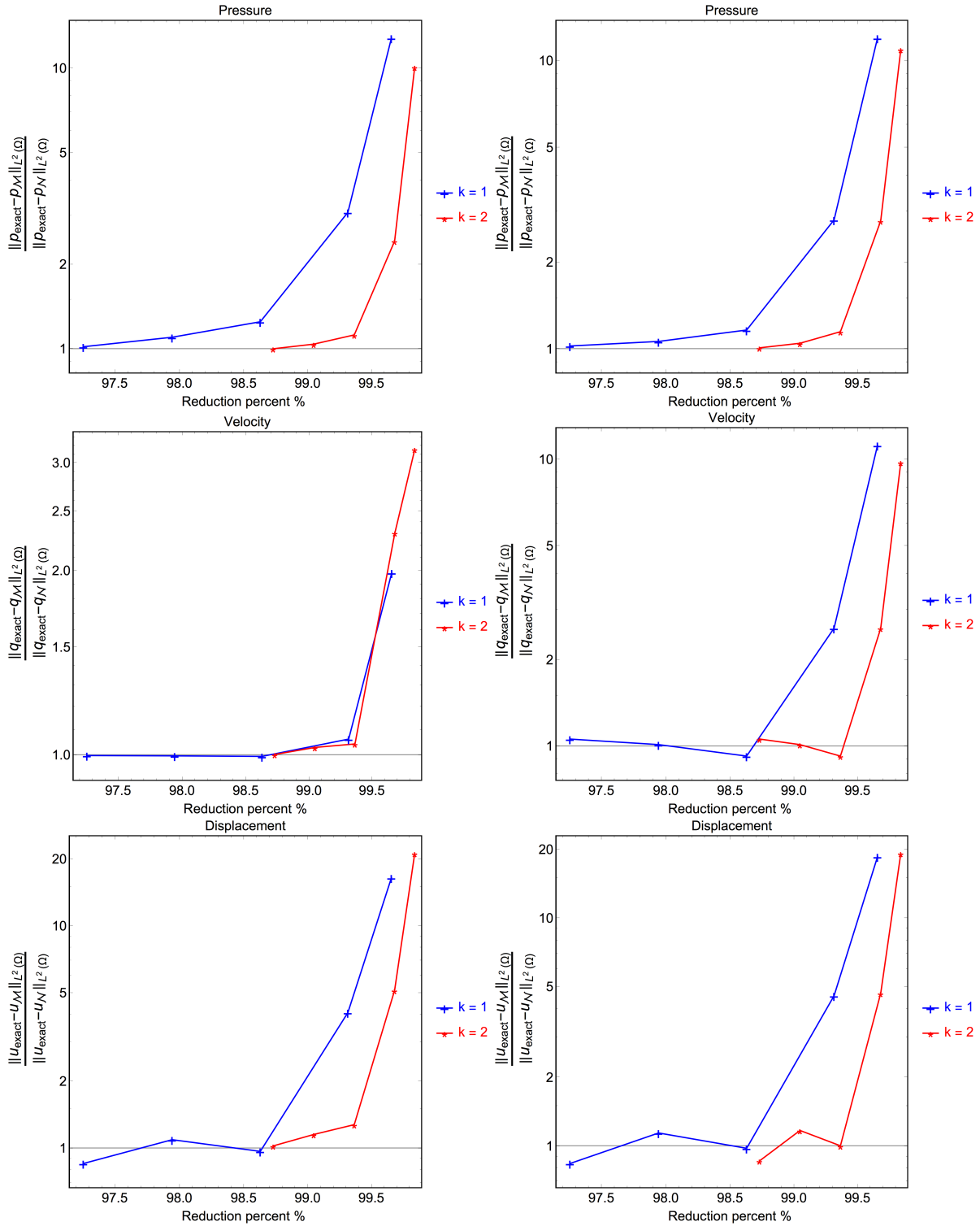


Figure 3.10: Error ratio for flow equation left (CG) and right (MF Tipe I).  $\mathbf{u}_N$  is replaced by the RB approximation  $\mathbf{u}_M$ .

### 3.2.7 RB approximation for the footing problem

In the absence of an analytical solution, the exact solution can be replaced by a problem of high order and considerable refinement  $h$ , with the aim of obtain graphs, with a similar meaning to those of the figure 3.10. Shortly, it is only shown an instant of the approximations RB with the full order approximation. Used the data in the table 3.2 with the same partition shown in the figure 3.5 and  $k = 1$  elliptic DoF  $\mathcal{N}_e = 4194$ .

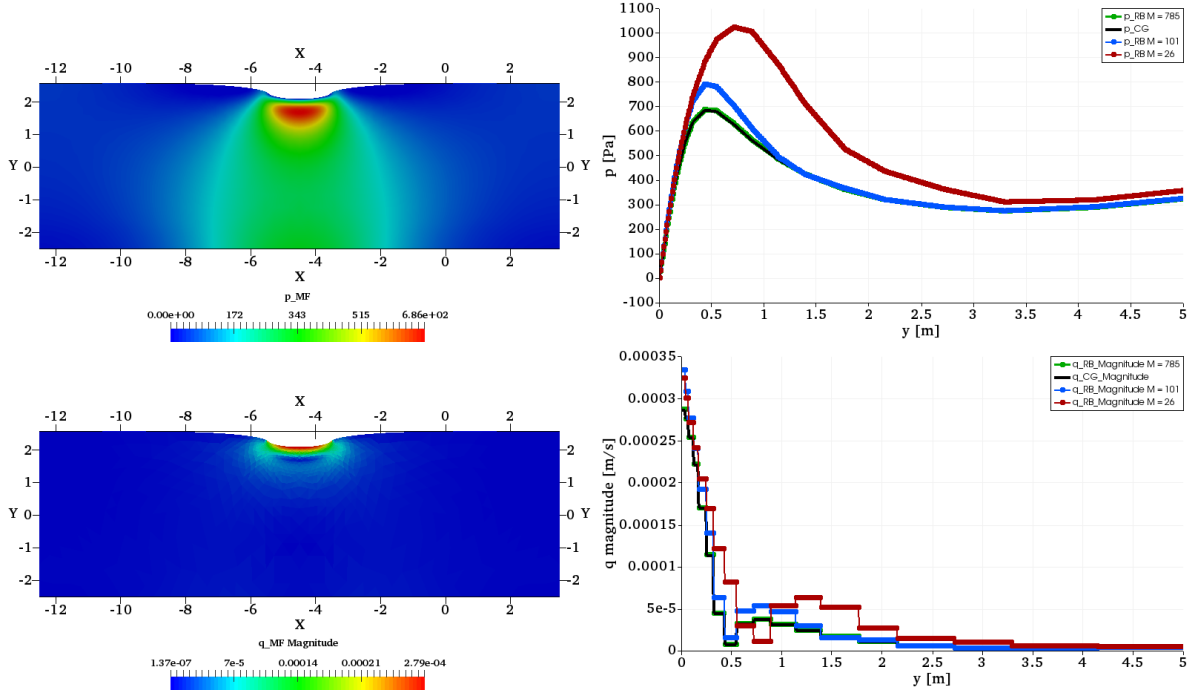
In the figure 3.11a and 3.11b are shown different approximations with different approximations by reduced bases, as the bases increase the approximation recovers the operator of complete order. Additionally, color maps are shown for approximation with  $\mathcal{M} = 101$ , Capturing the characteristics of the deformation at  $t = 10$  [s], after the application of the load. The reference partition has 784 triangular elements, and the approximation is intentionally shown when  $\mathcal{M}$  is equal to the number of volumetric elements plus one (i.e.  $r_{\mathcal{M}} \approx 81$ ). In this case, there is no quantitative difference between the reduction and the full order approximation.

**Remark:** When creating as many bases as elements in the mesh, it is obtained a better approximation, as is shown in the figures 3.9, 3.10 and 3.11. Thus, if the mesh is asymptotically zero, the reduction process can be reinterpreted to a green function that returns the poro-elastic response, to an application of a load, that asymptotically becomes a punctual load.

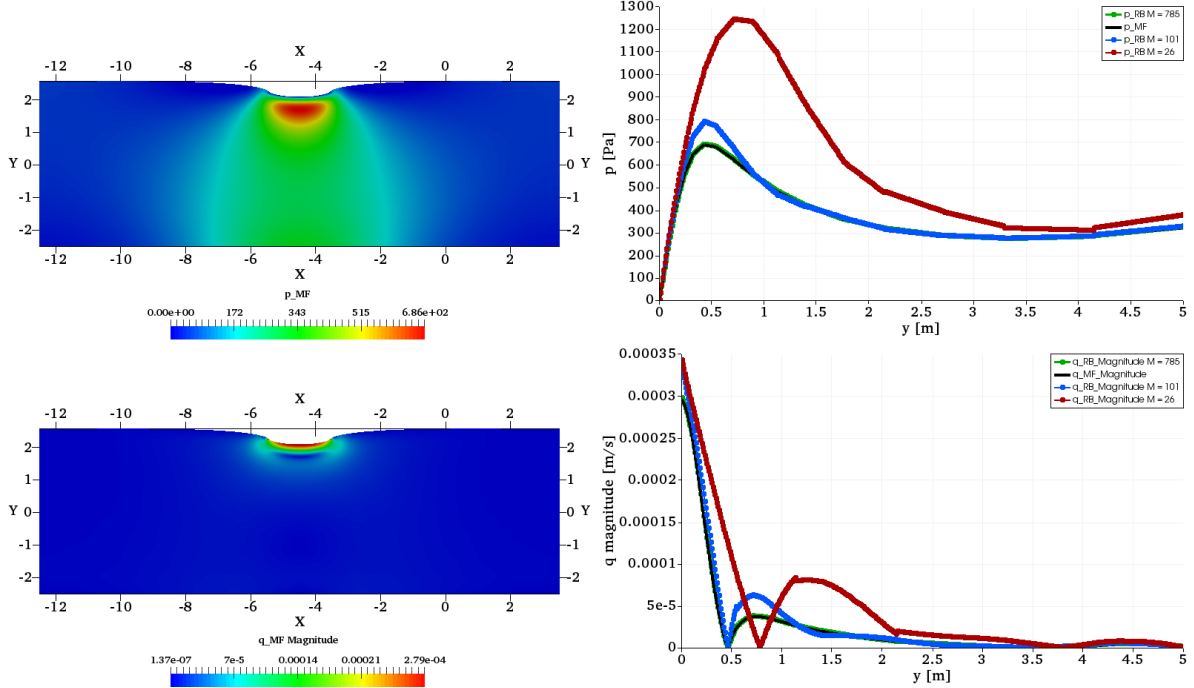
## Conclusions

This chapter documents the contribution of this research to the development of reduced order models applied to the approximation of poroelastic problems. The main conclusions of this chapter are:

- In this research, it is shown in terms of convergence rates that the scheme segregated by fixed split, could be equivalent to solve the problem completely coupled.
- The reduction strategy is suitable and verified.
- The reduced base is a good way of consider the complete coupling with a reduced number of degrees of freedom. However, it can be used under the separation by fixed split, in order to have greater efficiency in the execution of the online part for the reduction strategy.
- Since the construction of the base functions is built on constant pressures and  $H^1(\Omega)$  for  $\mathbf{u}_{\mathcal{M}}$ , this reduction process can be used for either continuous CG or mixed MF approaches of the flow equation. Any workflow based on  $H^1(\Omega)$  approximation for  $\mathbf{u}$  is a candidate for this reduction strategy.
- It is well known the mathematical equivalence between linear poroelasticity and thermoelasticity, being physical systems of different nature, share the same mathematical description in terms of dimensionless forms. Thus, naturally the reduction process detailed above, can be used in the case of strain induced by thermal changes.



(a) Footing problem approximation with CG + RB.



(b) Footing problem approximation with MF + RB.

Figure 3.11: Snapshot for RB approximations with  $\mathcal{M} = \{26, 101, 785\}$ . Plot over line  $l = \{\{0, 0\}, \{0, -5\}\}$ .

# Chapter 4

## A Multiscale Method

The rapid growth of the computing capacity, makes the approach of multiphysics detailed models with multiscale characteristics feasible. There is a considerable interest in the calculation of multiscale solutions in different engineering problems, like composite materials, porous media, turbulent flows, etc. In reservoir engineering, the accuracy of a reservoir simulation is dominated by the simulation of the multiscale characteristics of the geological models (**Aarnes2004**).

To understand the role of the multiscale characteristics of rocks, the reservoir models, must be able to master and model the multiscale characteristics of the equations of a blackoil model, or even the characteristics of the elliptic kernel, that is embedded in the equations for flow inside porous media, for instance the stationary case. For reservoir engineers, the accuracy of a multiphase simulation in porous media is fundamental for the correct prediction of the performance and the evaluation of the best strategy for the exploitation of an oil field. The heterogeneities of the rocks make the development of high precision models difficult, for two main reasons; first, the heterogeneity of the rocks are understood as properties randomly distributed and second, because the flow has characteristics of multiple scales.

In order to overcome these difficulties, a variant of the multiscale approach of **Paredes2013**; **Harder2013** was adopted in this work. In this variant, a mixed method is applied with precision, being controlled through the resolution of the mesh and solving the elliptic problem with variable coefficients, that comes from any porous medium.

The method is based on the construction of basis functions, that incorporate the local properties of the PDE coefficients. Like several fine-coarse approaches, this method incorporates the effects of fine scales to calculate velocities and pressures in a coarse resolution, to later calculate detailed velocity fields, which are suitable for the approximation of convection dominated problems. The method is locally conservative at any scale, and takes into account radial flows. It does not need complicated source/sink well models near the wellbore region, and global / local upscaling procedures. The accuracy of the method is demonstrated through 3D simulations in a monophasic case. The computational implementation of this technology is supported by the *Neopz* library (**Neopz**).

# Contents

---

4.1	A mixed multiscale method	77
4.1.1	Reinterpreting MHM	78
4.1.2	Multiscale Process	80
4.1.3	Downscaling operator	83
4.1.4	Upscaling operator	83
4.1.5	MHM- $H$ ( $\text{div}$ ) implementation	85
4.2	Application of the multiscale method	86
4.2.1	Examples of MHM- $H$ ( $\text{div}$ ) approximations	86
4.3	Conclusions	92

---

## 4.1 A mixed multiscale method

The discussion begins with a description of a new family of multiscale finite element methodologies so-called Multiscale Hybrid-Mixed (MHM), that was introduced by **Paredes2013; Harder2013**. The essential characteristics of this method can be summarized as follows:

- An upscaling/downscaling strategy is embedded within the mathematical infrastructure.
- The pressure field is composed of a collection of functions, that satisfy local elliptic problems with boundary conditions of the Neumann type. This elliptic operations depend on the multiscale nature of the problem data, the values of the lagrange multipliers, and the mean pressure of each domain belonging to the coarse scale.
- The continuity of the pressure is satisfied in a weak sense, but the formulation naturally induces, through the hybrid variable, the strong continuity of normal flows between the internal interfaces of the macro elements.
- The method provides a postprocessing cycle, which results in a vector field with continuous normal components. The vector field comes from the normal fluxes at the boundary value problems, that are defined inside macro domains or elements in the coarse scale.
- Mass conservation is obtained in the macroscopic sense, but not limited to it.
- The methodology has high parallel content.
- In terms of degrees of freedom, the method represents a dimensional reduction of a mixed 3D problem on the fine scale, to a 2D problem at the borders of each macro element.

### 4.1.1 Reinterpreting MHM

The MHM approximations are determined by the extension of polynomial fluxes, defined at the interfaces between the macro elements. In addition, the extension of the fluxes is computed using  $H^1(\Omega)$ . However, the vector field of this numerical approximation, has the disadvantage, that the vector field is inappropriate for convection dominated problems, because the field is not conservative.

In this research, a different approximation is introduced for the same boundary value problem, or in other words the MHM- $H(\text{div})$  method corresponding to the Darcy problem. Instead of using a  $H^1(\Omega)$  approximation for the extension of the internal fluxes, a mixed finite element approximation of  $H(\text{div})$  is used. The main differences between MHM and MHM- $H(\text{div})$  are:

- (i) A polynomial flow by parts is defined at the interfaces between the coarse elements. In this case, the interface fluxes do not have the Lagrange multiplier function; instead it uses degree of freedom restraints to couple a collection of elliptical problems, on each coarse element by condensing all the fine data on interface fluxes.
- (ii) The extension of the coarse fluxes into the micro elements is carried out by solving the elliptic problem embedded in the macro elements.

In this contribution an approximation of the global mixed problem is calculated differently to **Paredes2013** In the sense that an  $H(\text{div}, \Omega)$  is used for the extension of the fluxes of a composite mesh of internal interfaces over the micro elements, and projecting the macro fluxes on the micro fluxes to force the necessary continuity. The use of  $H(\text{div}, \Omega)$  is primarily motivated to obtain locally conservative vectors at the finest scales, which are required without the need for an extra computational cycle dedicated to the reconstruction of the desired fluxes. MHM- $H(\text{div})$  is composed mainly of two operations:

- (i) Upscaling operator: This operation is based mainly on fine scale data for the construction of fluxes in the coarse scale problem. Its main function is the restriction of the fine scale fluxes to the coarse scale fluxes.
- (ii) Downscaling operator: Given the fluxes in the coarse problem, this operator extends the solution over the fine scales.

During the multiscale process, the upscaling and downscaling operators are executed sequentially, but in just one step, generating an approximation of the global mixed operator over the fine scales.

Let consider  $\partial\Omega = \partial\Omega_D \cup \partial\Omega_N$  as the boundary of  $\Omega$ , where  $D$  is the boundary with Dirichlet data and  $N$  is the boundary with Neumann data. Also with the partition  $\Gamma_h$  of  $\Omega$ , it induced a set of sides:  $\partial\Gamma_h = \{\partial K : K \in \Gamma_h\}$ , a set of sides with Dirichlet data  $\zeta_D = \{\partial K \cap \Gamma_D : \partial K \in \partial\Gamma_h\}$ ; a set of sides with Neumann data  $\zeta_N = \{\partial K \cap \Gamma_N : \partial K \in \partial\Gamma_h\}$ ; a set of external sides  $\zeta_\Gamma = \zeta_D \cup \zeta_N$ ; and a set of internal sides  $\zeta_{skeleton} = \{\partial K_1 \cap \partial K_2 : \partial K_1, \partial K_2 \in \partial\Gamma_h\}$ .

Within the desired multiscale process, it is also necessary to define a partition  $\Gamma_h^K$  which is composed of micro elements of  $K$ , that are not conforming to  $\zeta_{skeleton}$  as shown in the figure 4.1.

It is important to note that the partitions  $\Gamma_h^K$  correspond to very fine discretizations, such that they capture the scales of interest. In the case of the reservoir simulations, these scales are the geocellular models of porosity  $\phi(\mathbf{x})$  and permeability  $\mathbf{K}(\mathbf{x})$ .

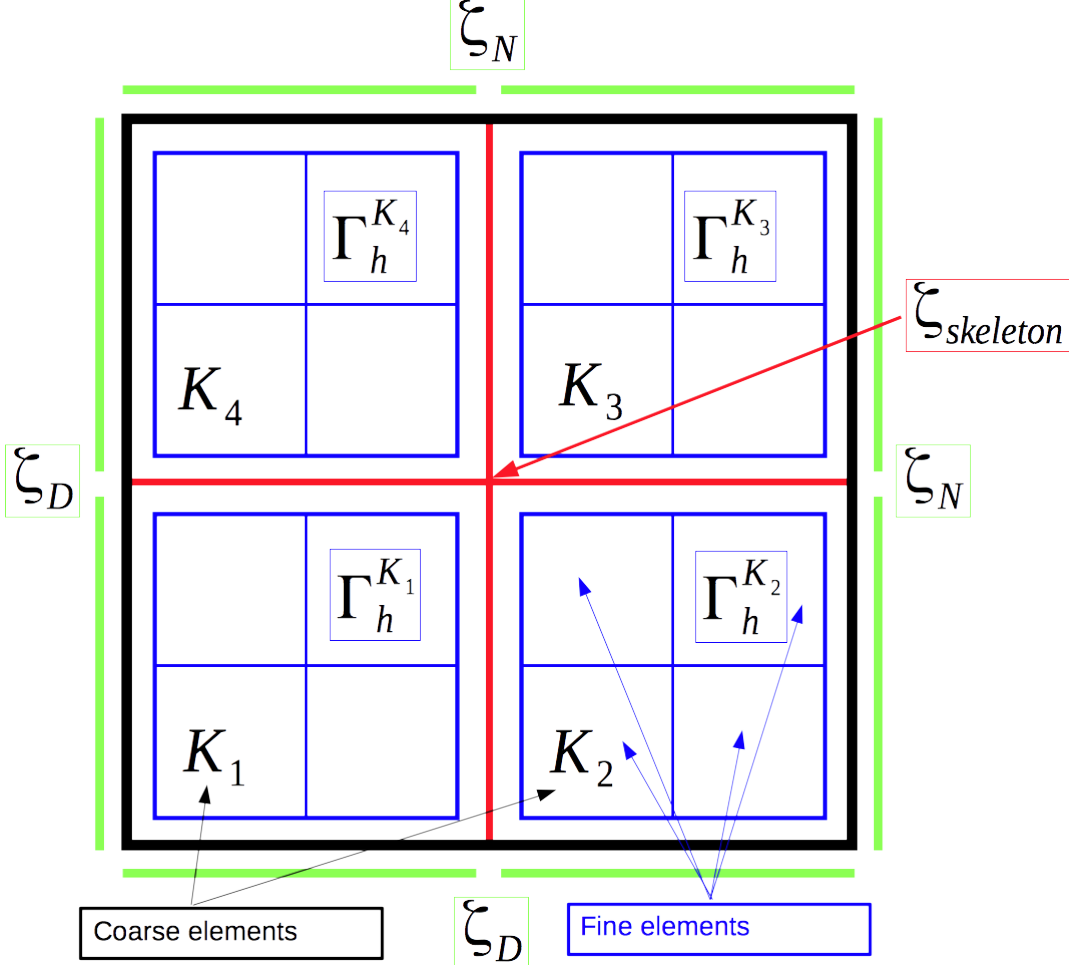


Figure 4.1: MHM- $H$  ( $div$ ) partition and subpartitions defined over  $\Omega$ .

In addition, the problem of Darcy is revisited and modified with a source term  $f$  in its mixed form:

$$\begin{aligned}
 \left( \mathbf{K} \frac{B_f^{-1}}{\eta} \right)^{-1} \mathbf{q} + \nabla p &= 0 \quad x \in \Omega \\
 div(\mathbf{q}) &= f \quad x \in \Omega \\
 p &= p_D \quad s \in \partial\Omega_D \\
 \mathbf{q} \cdot \mathbf{n} &= q_N \quad s \in \partial\Omega_N
 \end{aligned} \tag{4.1}$$

The weak statement of the continuous problem is to find  $(\mathbf{q}, p) \in H(\text{div}, \Omega) \times L^2(\Omega)$  such that:

$$\begin{aligned} \int_{\Omega} \left( \mathbf{K} \frac{B_f^{-1}}{\eta} \right)^{-1} \mathbf{q} \cdot \phi_q \, dV + \int_{\partial\Omega} p_D \phi_q \cdot \mathbf{n} \, dS - \int_{\Omega} p \text{div}(\phi_q) \, dV &= 0 \\ \int_{\Omega} \text{div}(\mathbf{q}) \phi_p \, dV - \int_{\Omega} f \phi_p \, dV &= 0 \end{aligned} \quad (4.2)$$

for all  $\phi_q \in W$  and  $\phi_p \in Z$ .

The discrete form of the weak statement is to find  $(\mathbf{q}_{\mathcal{N}}, p_{\mathcal{N}}) \in W_{\mathcal{N}} \times Z_{\mathcal{N}}$  such that

$$\begin{aligned} \int_{\Omega} \left( \mathbf{K} \frac{B_f^{-1}}{\eta} \right)^{-1} \mathbf{q}_{\mathcal{N}} \cdot \phi_{\mathcal{N}q} \, dV + \int_{\partial\Omega} p_D \phi_{\mathcal{N}q} \cdot \mathbf{n} \, dS - \int_{\Omega} p_{\mathcal{N}} \text{div}(\phi_{\mathcal{N}q}) \, dV &= 0 \\ \int_{\Omega} \text{div}(\mathbf{q}_{\mathcal{N}}) \phi_{\mathcal{N}p} \, dV - \int_{\Omega} f \phi_{\mathcal{N}p} \, dV &= 0 \end{aligned} \quad (4.3)$$

for all  $\phi_{\mathcal{N}q} \in W_{\mathcal{N}}$  and  $\phi_{\mathcal{N}p} \in Z_{\mathcal{N}}$ .

#### 4.1.2 Multiscale Process

The basis of the multiscale process is the mixed formulation of Darcy's problem. The multiscale approach exploits the structure of the mixed form, to get the approximation of  $(\mathbf{q}_{\mathcal{N}}, p_{\mathcal{N}})$  and decomposing the solution in terms of:

1. A set of fluxes that reside on the skeleton  $\zeta_{\text{skeleton}}$ .
2. A set of elliptic problems that are completely independent and computed on each macro element  $K \in \Gamma_h$ .
3. A set of constant functions by parts, associated to the partition  $\Gamma_h$ , that are necessary for solving the elliptic problems embedded in each macro element  $K$ .
4. The pressure is a field with weak continuity.
5. The strong continuity of the fluxes between the micro elements is achieved through the restriction of these normal fluxes, to the piecewise polynomial fluxes defined on the skeleton  $\zeta_{\text{skeleton}}$ .

The conditions 4 and 5 are inherent to the global mixed problem 4.3 defined at the finest scale being required. The techniques MHM and MHM-H ( $\text{div}$ ) share the same approximation properties and they have similar characteristics:

- (i) Both are stable in a family of  $K$  elements of type  $\Lambda(\partial K) \times V_c$ . Where  $V_c$  represents a space of constant pressures and  $\Lambda(\partial K)$  represents a normal fluxes space, in which they maintain the local flux continuity over the partition  $\Gamma_h$ .
- (ii) The construction of the base functions over  $\zeta_{\text{skeleton}}$ , naturally incorporates the finest scale through an operator named *upscaling*.

- (iii) The extention of fluxes  $\zeta_{\text{skelton}}$  over the fine scale fluxes is acomplished through a *downscaling* operation. This operator directly generates the velocity approximation of the global problem  $\mathbf{q}_{\mathcal{N}}$ , as well as the pressure field  $p_{\mathcal{N}}$ .

To introduce the notion of a multiscale approximation, it is necessary two kind of approximations, one coarse which incorporates the fine scale, and one fine which is embedded on the coarse one. This scale coupling is achieved, using two operators called upscaling and downscaling; such operators couple a pair of discretizations on two scales (macro and micro elements) as shown in figure 4.2. The following discussion similarly applies for all element topologies except pyramids.

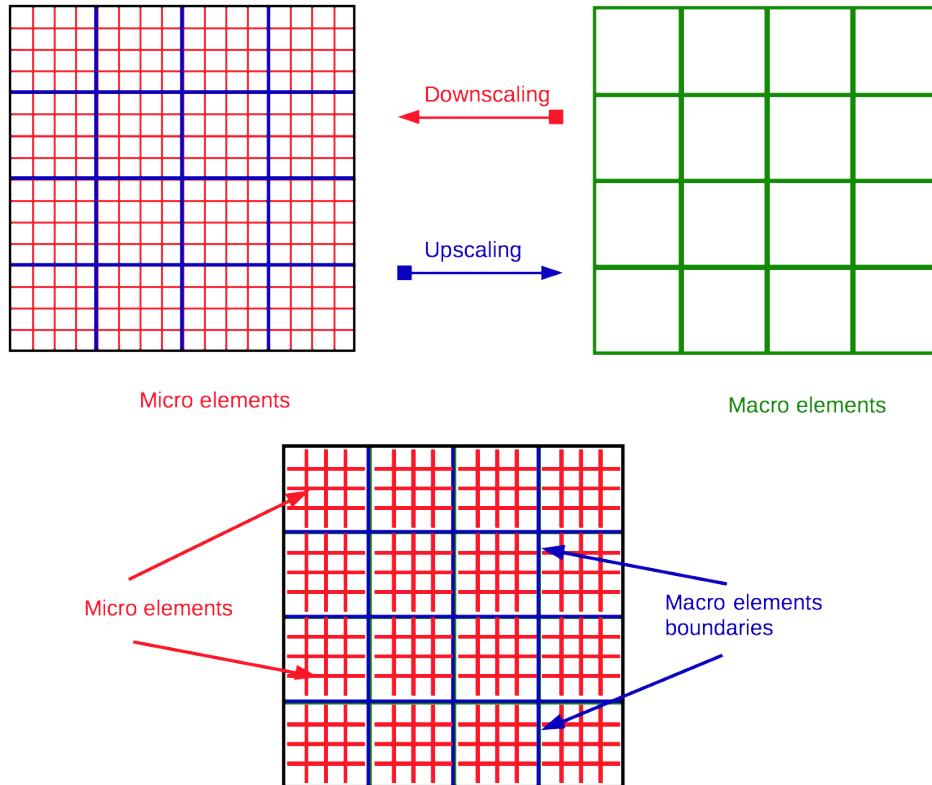


Figure 4.2: Downscaling and upscaling multiscale operators and MHM- $H$  ( $\text{div}$ ) variables separation.

Figure 4.3 represents a mesh of squares, where it is desired to approach the full-order operator  $(\mathbf{q}_{\mathcal{N}}, p_{\mathcal{N}})$  by a collection of local problems that are embedded, within each  $K \in \Gamma_h^l$ ; where  $l$  is the resolution level of the coarse scale in relation to the fine scale. From figure 4.3, it should be observed that in the desired multiscale process for a level resolution  $l = 3$ , the calculated approximation must be equal to the full-order operator.

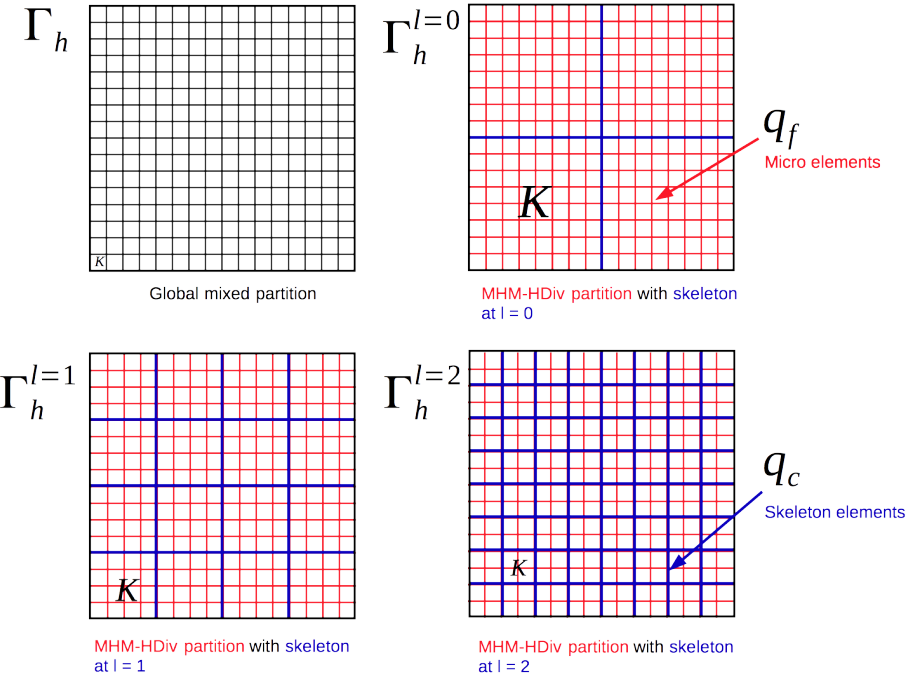


Figure 4.3: Downscaling and upscaling multiscale operators and MHM- $H$  ( $\text{div}$ ) variables separation.

## A local problem

The figure 4.3 presents the decomposition of the global problem, into local problems defined on each element  $K \in \Gamma_h$ .

The following local problem is defined as follows:

$$\begin{aligned}
 \left( \mathbf{K} \frac{B_f^{-1}}{\eta} \right)^{-1} \mathbf{q} + \nabla p &= 0 \quad x \in K \\
 \text{div}(\mathbf{q}) &= f \quad x \in K \\
 p &= p_D \text{ on } \partial K \in \zeta_D \\
 \mathbf{q} \cdot \mathbf{n} &= q_N \text{ on } \partial K \in \zeta_N \\
 \mathbf{q} \cdot \mathbf{n} &= q_{N_{inner}} \text{ on } \partial K \in \zeta_{\text{skeleton}}
 \end{aligned} \tag{4.4}$$

The continuous problem is find  $(\mathbf{q}, p) |_K \in H(\text{div}, K) \times L^2(K)$  such that:

$$\begin{aligned}
 \int_K \left( \mathbf{K} \frac{B_f^{-1}}{\eta} \right)^{-1} \mathbf{q} \cdot \boldsymbol{\phi}_q \, dV + \int_{\partial K} p_D \boldsymbol{\phi}_q \cdot \mathbf{n} \, dS - \int_K p \text{div}(\boldsymbol{\phi}_q) \, dV &= 0 \\
 \int_K \text{div}(\mathbf{q}) \phi_p \, dV - \int_K f \phi_p \, dV &= 0
 \end{aligned} \tag{4.5}$$

for all  $\boldsymbol{\phi}_q \in W$  and  $\phi_p \in Z$ .

In its discrete form the local problem is to find  $(\mathbf{q}_N, p_N) |_K \in W_N \times Z_N$  such that:

$$\begin{aligned} \int_K \left( \mathbf{K} \frac{B_f^{-1}}{\eta} \right)^{-1} \mathbf{q}_N \cdot \phi_{Nq} dV + \int_{\partial K} p_D \phi_{Nq} \cdot \mathbf{n} dS - \int_K p_N \operatorname{div}(\phi_{Nq}) dV &= 0 \\ \int_K \operatorname{div}(\mathbf{q}_N) \phi_{Np} dV - \int_K f \phi_{Np} dV &= 0 \end{aligned} \quad (4.6)$$

for all  $\phi_{Nq} \in W_N$  and  $\phi_{Np} \in Z_N$ .

When  $\zeta_D = \emptyset$  it is immediate that the local problem 4.6 is ill possed.

#### 4.1.3 Downscaling operator

To covert the local problem into well possed problem, the following local variables are introduced,  $p_K$  and  $f_K$  corresponding to a constant pressure, and a distributed flow defined over  $K$ . Thus, with this new variables the problem 4.6 is well possed and becomes:

Given  $q_{N_{inner}}$  on  $\partial K \in \zeta_{skeleton}$  and  $p_K$  on  $K$ , find  $(\mathbf{q}_N, p_N, f_K) |_K \in W_N \times Z_N \times V_c$  such that

$$\mathcal{A}_{downscaling}^K = \begin{cases} \int_K \left( \mathbf{K} \frac{B_f^{-1}}{\eta} \right)^{-1} \mathbf{q}_N \cdot \phi_{Nq} dV + \int_{\partial K} p_D \phi_{Nq} \cdot \mathbf{n} dS - \int_K p_N \operatorname{div}(\phi_{Nq}) dV &= 0 \\ \int_K \operatorname{div}(\mathbf{q}_N) \phi_{Np} dV + \int_K f_K \phi_{Np} dV - \int_K f \phi_{Np} dV &= 0 \\ \int_K f_K \phi_c dV &= 0 \\ \int_K (p_N - p_K) \phi_c dV &= 0 \end{cases} \quad (4.7)$$

with boundary conditions:

$$\begin{aligned} p &= p_D \text{ on } \partial K \in \zeta_D \\ \mathbf{q} \cdot \mathbf{n} &= q_N \text{ on } \partial K \in \zeta_N \\ \mathbf{q} \cdot \mathbf{n} &= q_{N_{inner}} \text{ on } \partial K \in \zeta_{skeleton} \end{aligned} \quad (4.8)$$

for all  $\phi_{Nq} \in W_N$ ,  $\phi_{Np} \in Z_N$  and  $\phi_c \in V_c$ .

The local problem 4.7 represents the downscaling operator that extends the fluxes  $q_{N_{inner}}$  over each subpartition  $\Gamma_h^K$ .

#### 4.1.4 Upscaling operator

The goal is to calculate the data  $q_{N_{inner}}$  on  $\partial K \in \zeta_{skeleton}$  and  $p_K$  for all  $K \in \Gamma_h$ . In order to obtain a strong continuity between each macro element  $K$ :

$$\mathbf{q}_{N_l} \cdot \mathbf{n}|_{\partial K_1} + \mathbf{q}_{N_l} \cdot \mathbf{n}|_{\partial K_2} = 0 \quad (4.9)$$

and between each micro element  $K_f \in \Gamma_h^K$ :

$$\mathbf{q}_N \cdot \mathbf{n}|_{\partial K_{f1}} + \mathbf{q}_N \cdot \mathbf{n}|_{\partial K_{f2}} = 0 \quad (4.10)$$

The following variables are introduced: the resolution level  $l$ , which is associated with the problem on the coarse scale; the coarse normal fluxes  $q_c^l = \mathbf{q}_{\mathcal{N}_l} \cdot \mathbf{n}|_{\partial K}$ ; and the fine normal fluxes  $q_f = \mathbf{q}_{\mathcal{N}} \cdot \mathbf{n}|_{\partial K_f}$ . The multiscale coupling is given by the restraints on  $q_f$  such that  $q_c^l = q_f$ . The space associated with  $q_c^l$ , is a space resulting from the trace of the functions  $W \in H(\text{div}, K)$  on the boundary  $\partial K$ , and it is defined as:

$$\Lambda(\partial K) = \{\mathbf{v} \in W : \mathbf{v}|_F \cdot \mathbf{n}, \forall F \in \partial K \cap \zeta_{\text{skeleton}}\} \quad (4.11)$$

When  $q_f$  is replaced with  $q_c^l$ , an error is induced in the approximation of  $(\mathbf{q}_{\mathcal{N}}, p_{\mathcal{N}})$ , obtaining an approximated solution  $(\mathbf{q}_{\mathcal{N}_l}, p_{\mathcal{N}_l}) \approx (\mathbf{q}_{\mathcal{N}}, p_{\mathcal{N}})$ . Increasing the resolution level the induced error is reduced  $l$ . The figure 4.4 shows how the fine fluxes on the boundary  $\partial K_f$ , are restricted to a coarse fluxes on the boundary  $\partial K$ .

The assembly of local problems defined by  $\mathcal{A}_{\text{downscaling}}^K$ , creates the coupling necessary to determine the values of  $q_c^l$  and  $p_K$ , making the assembly local problems equivalent to the original statement, and giving the necessary data  $q_c^l = q_{N_{\text{inner}}}$  on  $\partial K \in \zeta_{\text{skeleton}}$  and  $p_K$ . All internal degrees of freedom, with the exception of  $p_K$ , can be condensed on the boundary fluxes  $q_c^l$ .

**Condensation** Reusing the static condensation, the global problem resulting from the assembly of each local problem  $\mathcal{A}_{\text{downscaling}}^K$ , is reduced to a problem of smaller dimension in terms of the coarse fluxes  $q_c$ , and the constant pressures  $p_K$ . Thus, the matrix representation of the discrete global problem is expressed in the following form:

$$\begin{pmatrix} \mathbf{K}_{ff} & \mathbf{K}_{fc} \\ \mathbf{K}_{cf} & \mathbf{K}_{cc} \end{pmatrix} \begin{pmatrix} \alpha_{\mathcal{N}_l}^f \\ \alpha_{\mathcal{N}_l}^c \end{pmatrix} - \begin{pmatrix} \mathbf{F}_f \\ \mathbf{F}_c \end{pmatrix} = 0 \quad (4.12)$$

$$\alpha_{\mathcal{N}_l}^f = \mathbf{K}_{ff}^{-1} (\mathbf{F}_f - \mathbf{K}_{fc} \cdot \alpha_{\mathcal{N}_l}^c) \quad (4.13)$$

$$\begin{aligned} (\mathbf{K}_{cc} - \mathbf{K}_{cf} \mathbf{K}_{ff}^{-1} \mathbf{K}_{fc}) \alpha_{\mathcal{N}_l}^c - (\mathbf{F}_c - \mathbf{K}_{cf} \mathbf{K}_{ff}^{-1} \mathbf{F}_f) &= 0 \\ \bar{\mathbf{K}} \alpha_{\mathcal{N}_l}^c - \bar{\mathbf{F}} &= 0 \end{aligned} \quad (4.14)$$

The static condensation eliminates the internal degrees of freedom  $\alpha_{\mathcal{N}_l}^f = \{\mathbf{q}, p, f_K\}$  4.13, to obtain a condensed system in terms of  $\alpha_{\mathcal{N}_l}^c = \{p_K, q_c\}$  4.14.

Then, the upscaling operator  $\mathcal{A}_{\text{upscaling}}$  is generated through:

- (i) The sum over all the elements  $K$  of the coarse partition  $\Gamma_h$ .
- (ii) The static condensation of fine degrees of freedom on the coarse degrees of freedom  $\alpha_{\mathcal{N}_l}^c = \{p_K, q_c\}$ .

$$\mathcal{A}_{\text{upscaling}} = \begin{cases} \sum_{K \in \Gamma_h} \mathcal{A}_{\text{downscaling}}^K &= 0 \\ \bar{\mathbf{K}} \alpha_{\mathcal{N}_l}^c - \bar{\mathbf{F}} &= 0 \end{cases} \quad (4.15)$$

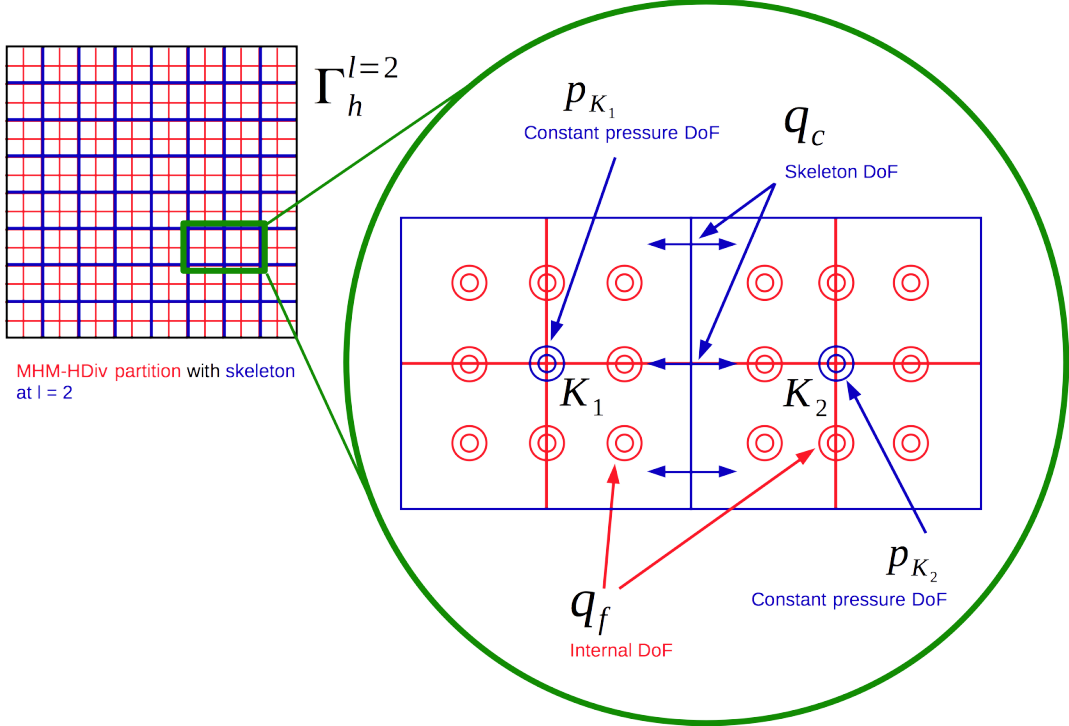


Figure 4.4: Fine fluxes restricted to coarse fluxes.

**Remark:** A fundamental difference between MHM- $H(\text{div})$  and MHM, is that the Neumann boundary condition is strongly imposed for local problems, i.e. the fluxes at the finest scale are restricted to the fluxes over the coarse scale interfaces. This whole process is accomplished in a very similar manner of the constrained functions, commonly used in hp-adaptive meshes, such as is presented in **Devloo2016**

#### 4.1.5 MHM- $H(\text{div})$ implementation

Several characteristics of *Neopz* were crucial to make the timely development of the MHM- $H(\text{div})$  possible:

- (i) Elements that form a macro element  $K$  were grouped into an object of type TPZSubCompMesh. This object was developed to implement the sub-structuring of the finest elements and to group them into macro elements. It also provides facilities for static condensation that characterize the upscaling operator 4.15.
- (ii) Restrictions between fine scale fluxes over those defined in  $\zeta_{\text{skeleton}}$ , are implemented through methods already developed for hp refinements.
- (iii) Once the constraints are calculated, the object substructures TPZSubCompMesh naturally implements the static condensation, that make MHM- $H(\text{div})$  a computationally efficient.

---

**Algorithm 4.1** MHM- $H$  ( $\text{div}$ ) process.

---

**Require:**  $\mathbf{K}_0, \phi_0, l$

**Ensure:**  $\begin{bmatrix} \mathbf{q}_{\mathcal{N}_l} & p_{\mathcal{N}_l} \end{bmatrix}^T$

for each element  $K \in \Gamma_h$  do

    Condense fine scale data using  $\mathcal{A}_{\text{upscale}}$  over  $\zeta_{\text{skeleton}}$ , fluxes  $\mathbf{q}_c$  and pressures  $p_K$

end for

    Solve the condensed coarse scale problem over  $\Gamma_h$

    for each element  $K \in \Gamma_h$  do

        Extend coarse scale problem using  $\mathcal{A}_{\text{downscale}}^K$  over  $K$  data

    end for

Return  $\begin{bmatrix} \mathbf{q}_{\mathcal{N}_l} & p_{\mathcal{N}_l} \end{bmatrix}^T = \begin{bmatrix} \delta\mathbf{q}_{\mathcal{N}_l} & \delta p_{\mathcal{N}_l} \end{bmatrix}^T$

---

The algorithm 4.1 execute the MHM- $H$  ( $\text{div}$ ) process for the linear problem 4.1 and returns an approximation  $(\mathbf{q}_{\mathcal{N}_l}, p_{\mathcal{N}_l}) \approx (\mathbf{q}_{\mathcal{N}}, p_{\mathcal{N}})$ . The process is performed in three substeps:

1. On the collection of elements defined in each subdomain  $K$ , a process of static condensation is applied performing the upscaling effect.
2. At the end of the upscaling operator process, it is obtained a reduction of the dimension problem and a linear system of equations in terms of  $(q_c, p_K)$ .
3. Once the data  $(q_c, p_K)$  is computed over the partition  $\Gamma_h$ , the extension of the fluxes is carried through the downscaling operator on each element  $K$ .

The capabilities in dealing with domains with different resolutions  $l$ , are demonstrated by the problems documented in the next subsections.

## 4.2 Application of the multiscale method

Revisiting the problem approximated with the linear mesh of the chapter 2, and using graphs similar to those presented in the chapter 3, it is shown that the MHM- $H$  ( $\text{div}$ ) approximates the global operator. Basically, the 3D problem is reduced to a 2D problem by means of static condensation. This 2D problem is defined on  $\{\zeta_{\text{skeleton}}, \zeta_D, \zeta_N\}$ , in other words, the method is a dimensional reduction. When the 2D problem corresponds to the resolution level of the finest problem, the same approximation is recovered in the sense of  $L^2(\Omega)$ , i.e.  $(\mathbf{q}_{\mathcal{N}_l}, p_{\mathcal{N}_l}) = (\mathbf{q}_{\mathcal{N}}, p_{\mathcal{N}})$ .

### 4.2.1 Examples of MHM- $H$ ( $\text{div}$ ) approximations

In this section, the Thiem-Dupoit problem is revisited 2.40 with the configuration presented in the chapter 2, and another configuration with a high oscillatory permeability tensor.

## Steady state radial flow

The figure 4.5 shows a plot over line of the MHM- $H$  ( $\text{div}$ ) approximations 4.3 with three different levels of mesh coarsening  $l = \{0, 1, 2\}$ , and the mesh associated with the global operator using the data in table 4.1. The number of total DoF  $\mathcal{N}$  and the condensed system DoF  $\mathcal{N}_{l=\text{ref}}$  are presented for each partition in table 4.2.

Property	Value
Reservoir dimensions	$h = 10 \text{ m}; r_w = 0.2 \text{ m}; r_o = 50 \text{ m}$
Permeability	$\kappa = 1 \times 10^{-13} \text{ m}$
Viscosity	$\eta = 0.01 \text{ Pa s}$
External pressure	$p_o = 25 \times 10^6 \text{ Pa}$
Flow rate	$Q = 0.01 \text{ m}^3 \text{s}^{-1}$

Table 4.1: Input data for MHM- $H$  ( $\text{div}$ ) approximation of the steady-state radial flow.

Topology	DoF
$K_H$	$\mathcal{N} = 71904; \mathcal{N}_{l=\text{ref}} = 3616$
$K_P$	$\mathcal{N} = 266624; \mathcal{N}_{l=\text{ref}} = 22048$
$K_T$	$\mathcal{N} = 634848; \mathcal{N}_{l=\text{ref}} = 40056$

Table 4.2: DoF data for MHM- $H$  ( $\text{div}$ ) approximation of the steady-state radial flow.

The figure 4.6 presents the approximation for each resolution of the MHM- $H$  ( $\text{div}$ ) outputs using the algorithm 4.1. The figure shows that for meshes composed of elements  $K_H$  (Hexahedrons),  $K_P$  (Prisms), and  $K_T$  (Tetrahedrons), the mixed global operator error is recovered when  $\frac{e_{\mathcal{N}_l}}{e_{\mathcal{N}_{l=\text{ref}}}} = 1$ .

The horizontal axis reflects the ratio of degrees of freedom of the multiscale process with resolution  $\mathcal{N}_l$  to the finest multiscale process resolution  $\mathcal{N}_{l=\text{ref}}$ . This graph shows that the MHM- $H$  ( $\text{div}$ ) technique induces an error in the approximation  $(\mathbf{q}_{\mathcal{N}_l}, p_{\mathcal{N}_l})$  of  $(\mathbf{q}_{\mathcal{N}}, p_{\mathcal{N}})$ , whose precision is controlled by the resolution of the coarse scale  $l$ , reaching the approximation of the finest scale  $(\mathbf{q}_{\mathcal{N}}, p_{\mathcal{N}})$  which is represented by the black line.

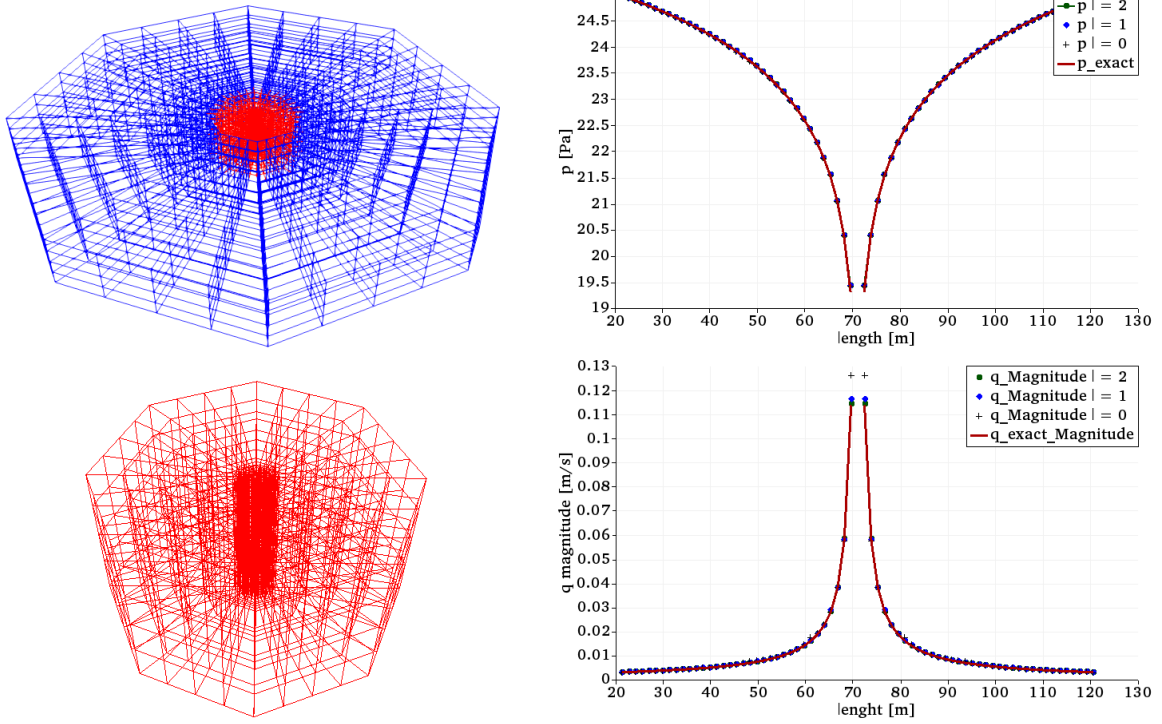


Figure 4.5: Multiscale approximations of Thiem solution, with different levels  $l = \{0, 1, 2\}$ . Left top geometric mesh with linear mappings, left bottom zoom on the wellbore region. Right plots over  $line = \{-50, -50, 0\}, \{50, 50, 0\}\}$ .

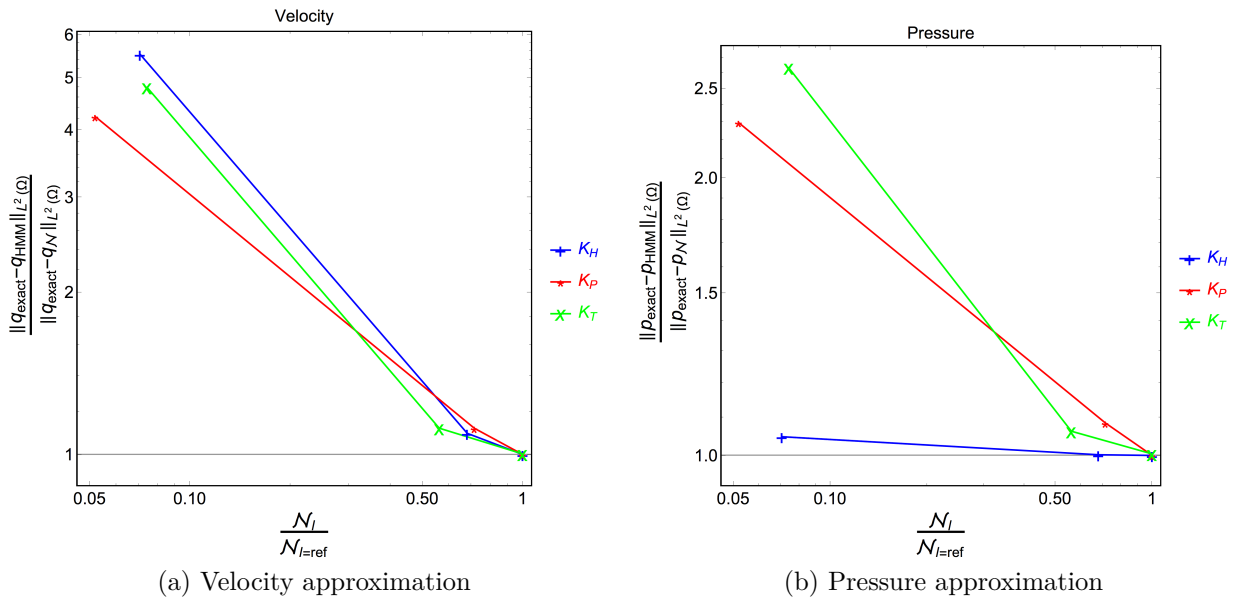


Figure 4.6: Error plots for MHM-H ( $div$ ) approximations of global mixed Thiem-Dupuit solution.

## Steady state radial flow with highly oscillatory permeability

The capability of MHM- $H$  ( $\text{div}$ ) technique is shown in a case represented by the data stated in the table 4.1, with permeability  $\mathbf{K}(\mathbf{x})$  [ $\text{m}^2$ ]:

$$\mathbf{K}(\mathbf{x}) = 1 \times 10^{-13} \begin{bmatrix} k_x & 0 & 0 \\ 0 & k_y & 0 \\ 0 & 0 & k_z \end{bmatrix} \quad (4.16)$$

where each component is highly oscillatory (see figure 4.11):

$$\begin{aligned} k_x &= 100 \frac{2 + 1.8 \sin\left(\frac{20\pi xy}{500}\right)}{2 + 1.8 \sin\left(\frac{20\pi y}{\epsilon}\right)} \\ k_y &= \frac{2 + 1.8 \sin\left(\frac{20\pi xy}{500}\right)}{2 + 1.8 \sin\left(\frac{20\pi x}{500}\right)} \\ k_z &= \frac{2 + 1.8 \sin\left(\frac{20\pi z^2}{500}\right)}{2 + 1.8 \sin\left(\frac{20\pi z}{500}\right)} \end{aligned} \quad (4.17)$$

The results shown are presented only for meshes with elements  $K_H$ . The figure 4.7 on the right side shows the partition of the skeleton  $\zeta_{\text{skeleton}}$  with level  $l = 0$  (color cyan); in its bottom right part, a zoom is shown on the well region, where the partition being used (red lines) and the outline of the macro element  $K$  is rendered in black color; at its upper and lower right side, two comparative graphs for pressure and velocity are shown, respectively. These figures display that for each resolution of  $\Gamma_h$  with  $l = \{0, 1, 2\}$  is obtained  $\{\mathbf{q}_{\mathcal{N}_l}, p_{\mathcal{N}_l}\} \approx \{\mathbf{q}_{\mathcal{N}}, p_{\mathcal{N}}\}$ , as well as increasing the resolution to  $l = 2$  is achieved  $\{\mathbf{q}_{\mathcal{N}_l}, p_{\mathcal{N}_l}\} = \{\mathbf{q}_{\mathcal{N}}, p_{\mathcal{N}}\}$ .

In the figures 4.8, 4.9 and 4.10 some color maps are shown for pressure and the velocity magnitude at different resolutions  $l = \{0, 1, 2\}$  of  $\Gamma_h$ , where pressure maps made for  $l = 0$  can reasonably capture the strong variation in pressure and velocity, mainly induced by the factor 100 in 4.17. This example shows the potential of the multiscale technique in the approximation of highly oscillatory permeability fields.

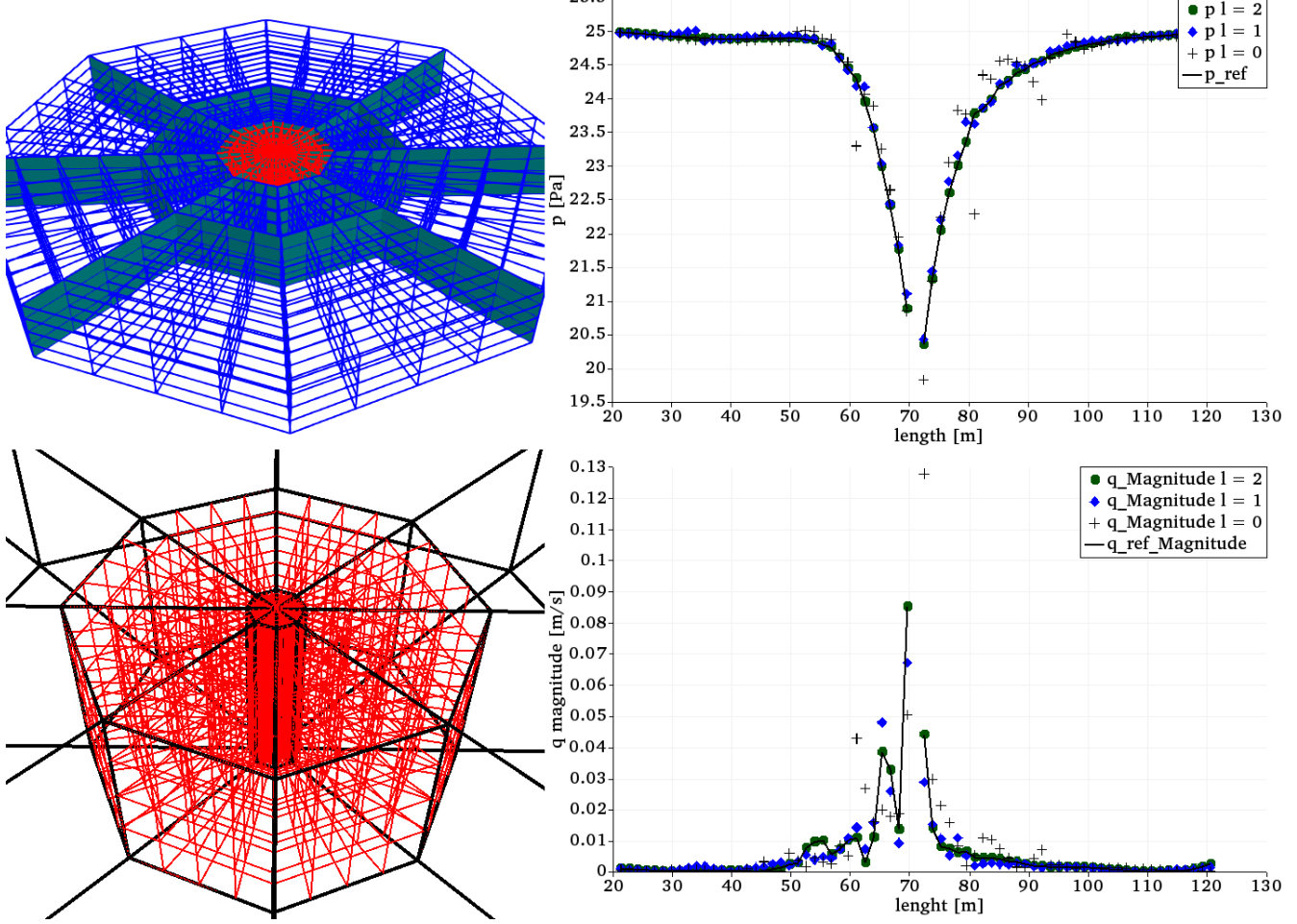


Figure 4.7: Multiscale approximations of Thiem setting with oscillatory permeability, and different levels  $l = \{0, 1, 2\}$ . Left top geometric mesh with linear mappings (skeleton mesh in  $\zeta_{\text{skeleton}}$  for  $l = 0$ ), left bottom zoom on the wellbore region with skeleton mesh  $\zeta_{\text{skeleton}}$  black wireframe for  $l = 0$ ). Right plots over  $line = \{\{-50, -50, 0\}, \{50, 50, 0\}\}$  of the pressure and flux respectively.

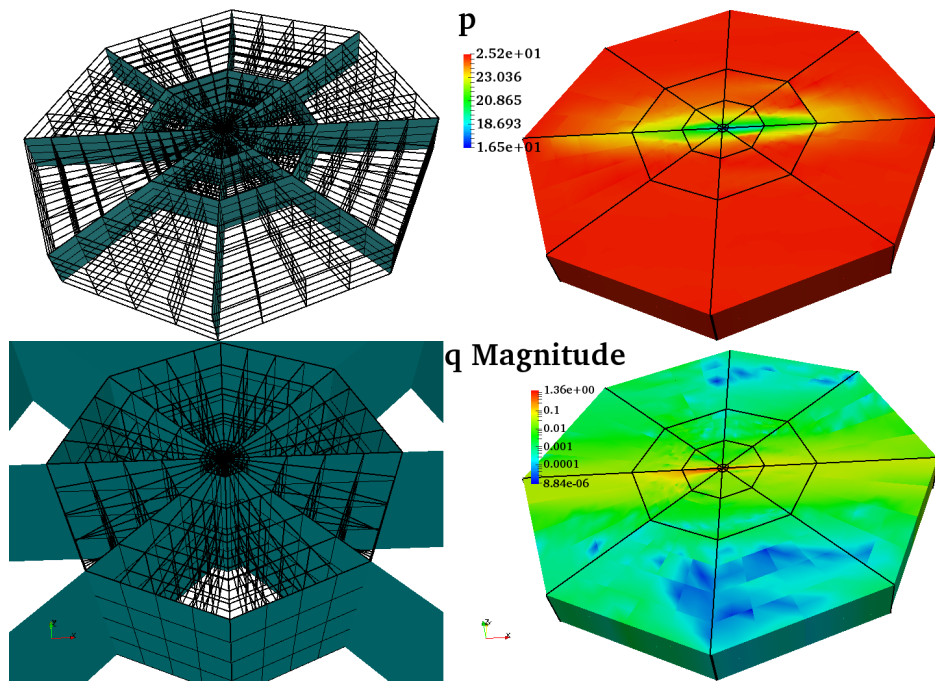


Figure 4.8: Multiscale approximations over Thiem problem setting with oscillatory permeability at  $l = 0$ .

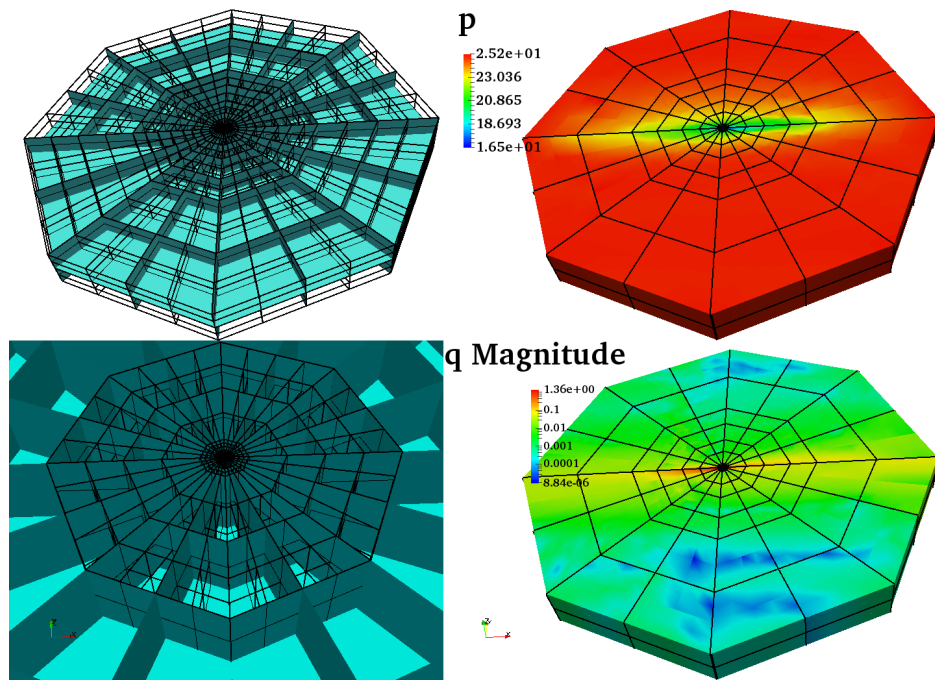


Figure 4.9: Multiscale approximations over Thiem problem setting with oscillatory permeability at  $l = 1$ .

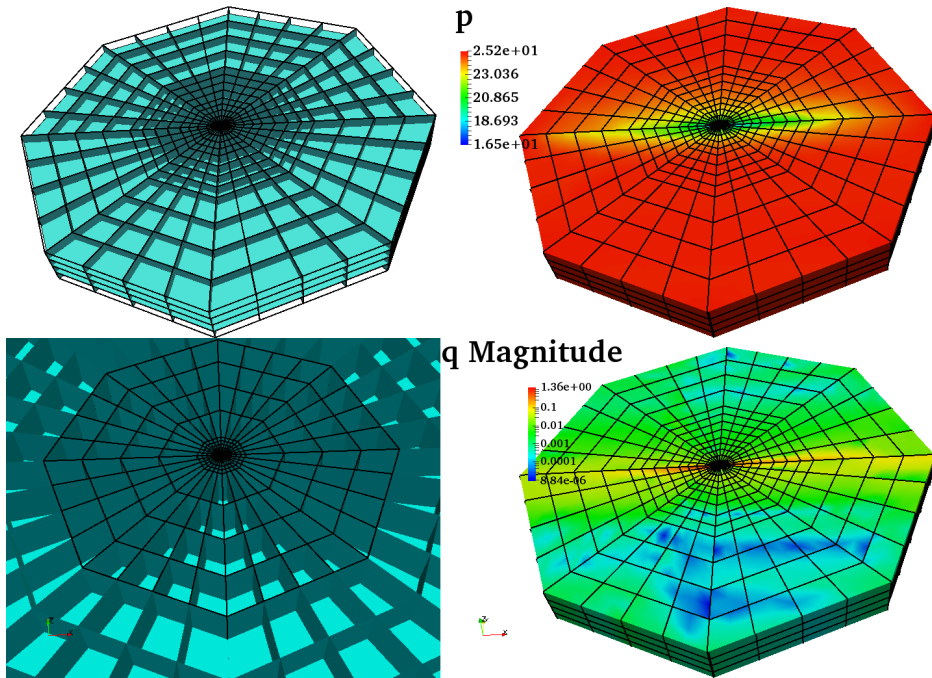


Figure 4.10: Multiscale approximations over Thiem problem setting with oscillatory permeability at  $l = 2$ .

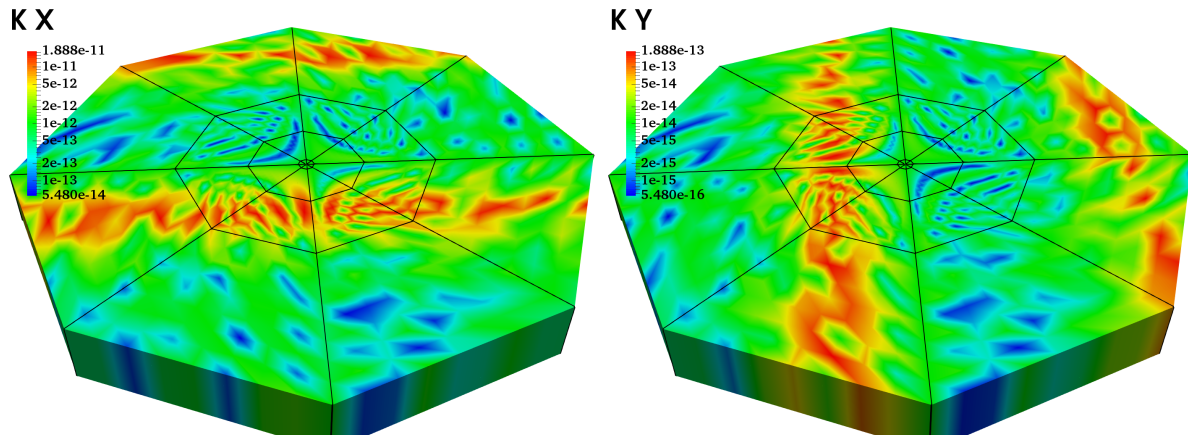


Figure 4.11: Color maps of  $k_x$  and  $k_y$ , the functions are rendered in log scale over the partition with resolution level  $l = 0$ .

### 4.3 Conclusions

The multiscale method outlined in this chapter represents a robust and precise technique to approximate problems with oscillatory coefficients.

- (i) The error graphs show that the MHM- $H$  ( $\text{div}$ ) method is verified, and the level of resolution coarse 1 controls the quality of the approximation, recovering the global mixed operator when 1 is equal to the finest scale. For the case of steady radial flow, the approximation of the Thiem-Dupuit solution, the global mixed operator is recovered in meshes with elements  $K_H$ ,  $K_P$  and  $K_T$ , verifying the implementation in all 3D topologies of the library with the exception of the pyramidal topology. These checks enable to strengthen and test the routines, in order to give reliability to any *Neopz* implementation.
- (ii) The method produces conservative fluxes inside each macro domain, that can be used for convection dominated problems (e.g. the case of tracer injection into a porous medium).
- (iii) The technique shows its robustness in the case of oscillatory coefficients, by incorporating fine scales effects in very coarse elements.
- (iv) The MHM- $H$  ( $\text{div}$ ) process shares similarities with the mixed version of MHM technique described in **Paredes2013**

## **Part II**

# **Geomechanics multi-phase reservoir modelling**

# Chapter 5

## Strong Formulation

In this section is introduced the mathematical model for multiphase flow description coupled with geomechanics. The theory of Biot incorporates the mathematical description of two phenomena with a strong coupling. In this chapter, a detailed development of the model is made, several comments and remarks are given, as well as a summary of the equations for the triphasic and biphasic case.

### Contents

---

5.1	Historical Note on Linear Poroelasticity . . . . .	96
5.2	Linear Poroelasticity . . . . .	96
5.2.1	Equilibrium Equation . . . . .	96
5.2.2	Constitutive Model for Rock Deformation . . . . .	96
5.3	Conservation of Mass for Fluid Flow in a Deformable Medium . . . . .	97
5.3.1	Mass conservation for multiphase flow . . . . .	98
5.3.2	Mass conservation considering the deformation of the solid phase . . . . .	98
5.3.3	Summary of the mathematical model . . . . .	99
5.4	Constitutive laws of the blackoil model . . . . .	100
5.5	Poroelasticity in a multiphase context . . . . .	101
5.6	Weighted pressure formulation . . . . .	102
5.7	Condensed form of the conservation laws and constitutive equations . . . . .	102
5.7.1	Three phase model: water oil gas system . . . . .	103
5.7.2	Two phase model: water oil system . . . . .	104
5.8	Conclusions . . . . .	105

---

## 5.1 Historical Note on Linear Poroelasticity

Many sedimentary rocks show a reversible behavior in a regime of small deformations (**Turcotte2014**). The Biot's poroelasticity theory can be applied in a regime of small deformations, to quantify the deformation of the rock and its interaction with the flow of fluids. There are several sources in the literature, that exhaustively describe this phenomena, such as (**Timoshenko2001; Wang2002; Coussy2005**). In all the discussion, displacement, stresses, deformations, pressures, are not defined relative to an initial state, unless this is specified by the variation  $\delta x = x - x^0$ .

The first work in the description of the fluid-solid coupling in a deformable medium, is attributed to **Terzaghi1943**. Its main contribution was the concept of effective stress for a one dimensional system with an incompressible rock matrix (see chapter 3). The concept of effective stress has been widely used in the study of subsidence and its related problems. Later, Biot generalized this concept in three dimensions, based on the continuum theory, in his subsequent works, **Biot1941a; Biot1941b; Biot1955; Biot1956a; Biot1956b** extended the theory for more complex cases with anisotropy and nonlinearity in the material under deformation.

The Biot's consolidation theory, consists essentially of a set of conservation equations and constitutive relations, for a representative rock element which is fully saturated. The principle of Biot's poroelasticity is described in the following subsections.

## 5.2 Linear Poroelasticity

### 5.2.1 Equilibrium Equation

$$\operatorname{div}(\boldsymbol{\sigma}^* - \boldsymbol{\sigma}^{0*}) + \mathbf{b} = 0 \quad (5.1)$$

where  $\boldsymbol{\sigma}^*$  [Pa] is the total Cauchy stress tensor,  $\mathbf{b}$  [ $\text{N m}^{-3}$ ] is the body force term, that is composed for the porosity  $\phi$ , saturations  $s_\beta$ , fluid densities  $\rho_\beta$  [ $\text{kg m}^{-3}$ ], rock densities  $\rho_r$  [ $\text{kg m}^{-3}$ ], and the gravity vector  $\mathbf{g}$  [ $\text{m s}^{-2}$ ]. The body ficer term is defined as:

$$\mathbf{b} = (\rho_r(1-\phi) + \phi(\rho_w s_w + \rho_o s_o + \rho_g s_g)) \mathbf{g} \quad (5.2)$$

The subscript  $\beta = \{w, o, g\}$  means water, oil and gas respectively.

### 5.2.2 Constitutive Model for Rock Deformation

Introducing effective stress  $\boldsymbol{\sigma}$  [Pa] :

$$\boldsymbol{\sigma}^* - \boldsymbol{\sigma}^{0*} = \boldsymbol{\sigma} - \boldsymbol{\sigma}^0 - \alpha(p - p^0) I \quad (5.3)$$

$\boldsymbol{\sigma}^*$  is decomposed 5.3 in two contributions, the stress acting on the rock structure and the stress caused by the expansion or contraction of the fluid. The last one only influences the hydrostatic

component of the stress tensor. The effective stress  $\sigma$  is related to deformation through:

$$\sigma = 2\mu\epsilon(\mathbf{u}) + \lambda \operatorname{tr}(\epsilon(\mathbf{u})) I \quad (5.4)$$

where  $\lambda$  [Pa] and  $\mu$  [Pa] are the first and second lamé parameters. Assuming small deformations

$$\epsilon(\mathbf{u}) = \frac{1}{2} (\nabla \mathbf{u} + \nabla^T \mathbf{u}) \quad (5.5)$$

## 5.3 Conservation of Mass for Fluid Flow in a Deformable Medium

In the literature there are many revisions and reinterpretations of Biot's consolidation theory, such as **Geertsma1957**; **Rice1976**; **Rudnicki1986**; **Bear1990**; **Lewis1998**; **Coussy2005**. In particular the work of **Bear1990**; **Lewis1998**; **Coussy2005** seem to be most relevant. In the following the equations for three phase model flow with blackoil properties described by **Lewis1998** is reviewed.

### Coupled equations for a blackoil model

The blackoil model can be interpreted as a simplified case of a compositional model, to describe the multiphase flow with mass interchange between phases: water, oil and gas, and two oil and gas components. The oil component is defined as the oil produced at surface conditions, and the gas component is defined as the gas produced at separation conditions.

### Model considerations

The model is subject to the following considerations:

- (i) Isothermal process.
- (ii) Dominant convective mass fluxes.
- (iii) There is no chemical reaction, adsorption and precipitation.
- (iv) Fluid flow is characterized by Darcy's law.
- (v) Injection and production wells are treated as boundary conditions.
- (vi) The permeability is diagonal.
- (vii) Viscosity is an exclusive function of pressure.
- (viii) The formation of the reservoir is slightly compressible.

In addition, the water component is assumed to be immiscible with the other two hydrocarbon components. The gas components are assumed to be soluble in oil but usually not in water. It may be described as follows:

Phase	water	oil	gas
Component	$m_w$	$m_o$	$m_g$
water	$\frac{m_{ww}}{m_w} = 1$	$\frac{m_{ww}}{m_o} = 0$	$\frac{m_{ww}}{m_g} = 0$
oil	$\frac{m_{ow}}{m_w} = 0$	$\frac{m_{oo}}{m_o}$	$\frac{m_{og}}{m_g} = 0$
gas	$\frac{m_{gw}}{m_w} = 0$	$\frac{m_{go}}{m_o}$	$\frac{m_{gg}}{m_g} = 1$
total concentration	1	1	1

Table 5.1: Phase interaction matrix for three-phase flow.  $m$  means fluid mass.

Phase	water	oil
Component	$m_w$	$m_o$
water	$\frac{m_{ww}}{m_w} = 1$	$\frac{m_{ww}}{m_o} = 0$
oil	$\frac{m_{ow}}{m_w} = 0$	$\frac{m_{oo}}{m_o} = 1$
total concentration	1	1

Table 5.2: Phase interaction matrix for two-phase flow.  $m$  means fluid mass

### 5.3.1 Mass conservation for multiphase flow

$$\frac{\partial (\phi s_w^*)}{\partial t} + \operatorname{div}(\phi s_w^* \mathbf{v}_{fw}) = 0 \quad (5.6)$$

$$\frac{\partial (\phi s_o^*)}{\partial t} + \operatorname{div}(\phi s_o^* \mathbf{v}_{fo}) = 0 \quad (5.7)$$

$$\frac{\partial (\phi s_g^*)}{\partial t} + \operatorname{div}\left(\phi (s_g^* \mathbf{v}_{fg} + s_o^* R_{so} \mathbf{v}_{fo})\right) = 0 \quad (5.8)$$

### 5.3.2 Mass conservation considering the deformation of the solid phase

$$\frac{\partial ((1 - \phi) \rho_s)}{\partial t} + \operatorname{div}((1 - \phi) \rho_s \mathbf{v}_s) = 0 \quad (5.9)$$

Darcy's law:

$$\bar{\mathbf{v}}_\beta = -\mathbf{K} \frac{k_{r\beta}}{\eta_\beta B_\beta} (\nabla p_\beta - \rho_\beta \mathbf{g}) \quad (5.10)$$

Where,  $B_\beta$  is the fluid formation volume factor of the phase  $\beta$ ,  $\mathbf{v}_{f\beta}$  [ $\text{m s}^{-1}$ ] is the intrinsic fluid velocity,  $\mathbf{v}_s$  [ $\text{m s}^{-1}$ ] is the solid velocity,  $\bar{\mathbf{v}}_\beta$  [ $\text{m s}^{-1}$ ] is the Darcy velocity,  $\eta_\beta$  is the fluid dynamic viscosity [Pa s],  $\mathbf{K}$  [ $\text{m}^2$ ] is the absolute permeability,  $k_{r\beta}$  is the relative permeability,  $R_{so}$  is the gas oil solution ratio,  $s_\beta^*$  are fluid concentrations. The fluid concentrations are related to the fluid saturations as follow:

$$s_w^* = \frac{s_w}{B_w}; s_o^* = \frac{s_o}{B_o} s_g^* = \frac{s_g}{B_g} + R_{so} \frac{s_o}{B_o} \quad (5.11)$$

These relations have an important simplification in the operations and segregated schemes defined in the following chapter 6. Another characteristic is that, once the conditions at surface are specified, the balance of injected and produced fluids can be determined, by volumes corrections from surface conditions.

Through several physical considerations inside the model, a coupling described entirely by the porous volume change is reached. This derivation is detailed in the appendix A, and through it the following equations of the poroelastic blackoil model are obtained:

$$\frac{\partial (s_\beta^* (\phi^0 + \alpha \delta \operatorname{div}(\mathbf{u}) + S_\epsilon \delta p))}{\partial t} + \operatorname{div}(\bar{\mathbf{v}}_\beta) = 0 \quad (5.12)$$

The following is a variation of 5.12, which is commonly used in the simulation by sequential operators:

$$\phi^* \frac{\partial (s_\beta^*)}{\partial t} + s_\beta^* (c_b - (1 + \phi^0) c_s) \frac{\partial (\delta p)}{\partial t} + s_\beta^* (c_b - c_s) \frac{\partial (\delta \sigma_v)}{\partial t} + \operatorname{div}(\bar{\mathbf{v}}_\beta) = 0 \quad (5.13)$$

The above equations are based on variations of the porous volume, so it is expected that the influence of stress or deformations is only through the volumetric components.

Inside the term  $\operatorname{div}(\bar{\mathbf{v}}_\beta)$  exists, another kind of coupling related to the rock permeability. There are laboratory studies, that report changes in porosity in rocks with relative compressibility, these changes imply alterations in absolute permeability. Some references on this subject are **Morita1992; Gutierrez1998; Osorio1999**

A primitive approach for this coupling, is to perform a sequencial steps with simple models, such as Garman-Kozeny, a relationship that is commonly used in sedimentary basin simulators. Other models of stress-dependent permeability can be found in **Morita1992**

The focus of this work is to consider just the coupling of the porous volume, thus the permeability coupling is proposed as future work.

### 5.3.3 Summary of the mathematical model

Below are presented the characteristics associated with a poromechanic simulation (**Osorio1999**):

- (i) The multicomponent nature of the reservoir fluids, requires the correct description of the fluid and the solid component. As is customary in macroscopic modeling, conservation laws and constitutive relationships are used for the derivations. In this research, the conservation of linear momentum, mass conservation, linear poroelasticity and Darcy's law as conservation and constitutive laws are the basis of the implementation.
- (ii) The simulation of the reservoir depletion in terms of deformations, affects the deformation of the sideburden and reservoir rocks, in a coupled way. The consideration of sideburden rocks, implies in an increase of the computational domain, because it is necessary to model a domain that represents the deformation of these rocks whose extension must be large enough to avoid the effects of the far field boundaries. This reason motivates the use of a reduced model introduced in chapter 3.

In this research, the simulation of the geomechanical coupling is carried out through the interaction of different physical phenomena with overlapping materials. For simplicity, the rock materials are the same, inside and outside of the reservoir. These reservoir and the sideburden rocks are modeled as slightly compressible elastic material.

## 5.4 Constitutive laws of the blackoil model

The state variables are  $p$ , the concentrations  $s_\beta^*$  and velocities  $\bar{\mathbf{v}}_\beta$ . The pore pressure is equal to the phase pressures by the fact of neglecting capillary pressure effects.

The mass conservation:

$$\frac{\partial (s_w^* \phi^*)}{\partial t} + \operatorname{div} (\bar{\mathbf{v}}_w) = 0 \quad (5.14)$$

$$\frac{\partial (s_o^* \phi^*)}{\partial t} + \operatorname{div} (\bar{\mathbf{v}}_o) = 0 \quad (5.15)$$

$$\frac{\partial (s_g^* \phi^*)}{\partial t} + \operatorname{div} (\bar{\mathbf{v}}_g) = 0 \quad (5.16)$$

With the restrictions

$$0 \leq s_\beta^* \text{ and } s_w + s_o + s_g = 1 \quad (5.17)$$

Darcy's velocities:

$$\bar{\mathbf{v}}_w = -\mathbf{K} \frac{k_{rw}}{\eta_w B_w} (\nabla p - \rho_w \mathbf{g}) \quad (5.18)$$

$$\bar{\mathbf{v}}_o = -\mathbf{K} \frac{k_{ro}}{\eta_o B_o} (\nabla p - \rho_o \mathbf{g}) \quad (5.19)$$

$$\bar{\mathbf{v}}_g = -\mathbf{K} \frac{k_{rg}}{\eta_g B_g} (\nabla p - \rho_g \mathbf{g}) + R_{so} \bar{\mathbf{v}}_o \quad (5.20)$$

for a oil/gas system  $R_{so} = \frac{s_g^*}{s_o^*}$ .

Initial conditions:

$$\begin{cases} p = p^0 \\ s_w = s_w^0 \\ s_o = s_o^0 \\ R_{so} = R_{so}^0 \end{cases} \quad (5.21)$$

Boundary conditions

$$\begin{cases} \bar{\mathbf{v}}_w \cdot \mathbf{n} = 0 \\ \bar{\mathbf{v}}_o \cdot \mathbf{n} = 0 \quad \text{on } \partial\Omega_N \\ \bar{\mathbf{v}}_g \cdot \mathbf{n} = 0 \\ \begin{cases} p = p_{aquifer} \\ s_w = s_w \text{ in} \end{cases} \quad \text{on } \partial\Omega_{aquifer} \\ \begin{cases} p = p_{inj} \\ s_w = s_w \text{ in} \end{cases} \quad \text{on } \partial\Omega_{inj} \\ p = p_{prod} \quad \text{on } \partial\Omega_{prod} \end{cases} \quad (5.22)$$

## 5.5 Poroelasticity in a multiphase context

The state variable is the displacements  $\mathbf{u}$ . The problem of poroelasticity is defined by the following equations subject to initial and boundary conditions.

$$\operatorname{div}(\boldsymbol{\sigma} - \boldsymbol{\sigma}^0 - \alpha(p - p^0)) + \mathbf{b} = 0 \quad (5.23)$$

where

$$\mathbf{b} = (\rho_r(1 - \phi) + \phi(\rho_w s_w + \rho_o s_o + \rho_g s_g)) \mathbf{g} \quad (5.24)$$

$$\boldsymbol{\sigma} = 2\mu\boldsymbol{\epsilon}(\mathbf{u}) + \lambda \operatorname{tr}(\boldsymbol{\epsilon}(\mathbf{u})) I \quad (5.25)$$

Initial conditions:

$$\begin{aligned} \sigma &= \sigma^0 \\ p &= p^0 \end{aligned} \quad (5.26)$$

Boundary conditions:

$$\begin{cases} \mathbf{u} = 0 & \text{on } \partial\Omega_D \\ \boldsymbol{\sigma} \cdot \mathbf{n} = \mathbf{t} & \text{on } \partial\Omega_N \end{cases} \quad (5.27)$$

## 5.6 Weighted pressure formulation

In order to decrease the state variables and rewrite the equations in the more appropriate mathematical form. The formulation presented by **Chen2000** is chosen for the mixed representation of flow equations, by the following steps:

- (i) Sum of the equations 5.14, 5.15 and 5.16, commonly referred as a pressure equation, leads to total velocity  $\mathbf{q} = \bar{\mathbf{v}}_w + \bar{\mathbf{v}}_o + \bar{\mathbf{v}}_g$ .
- (ii) Sum of Darcy's velocities 5.18, 5.19 and 5.20, motivates the definition of fractional flow and gravitational segregation terms.

**Remark:** It is important to note, that in the absence of capillary pressure, only an equivalent pressure exists and therefore the pressures of each phase of the system are equal to  $p$ .

$$\frac{\partial (\phi^* (s_w^* + s_o^* + s_g^*))}{\partial t} + \operatorname{div}(\mathbf{q}) = 0 \quad (5.28)$$

$$\mathbf{q} = -\mathbf{K}\lambda (\nabla p - G_\lambda) \quad (5.29)$$

$$G_\lambda = \sum_{\beta} f_{\beta} \rho_{\beta} \mathbf{g} \quad (5.30)$$

$$\lambda_w = \frac{k_{rw}}{\eta_w B_w}; \quad \lambda_o = \frac{(1 + R_{so}) k_{ro}}{\eta_o B_o}; \quad \lambda_g = \frac{k_{rg}}{\eta_g B_g} \quad \lambda = \sum_{\beta} \lambda_{\beta} \quad (5.31)$$

$$f_{\beta} = \frac{\lambda_{\beta}}{\lambda} \quad (5.32)$$

## 5.7 Condensed form of the conservation laws and constitutive equations

Next, the equations are arranged in a more appropriate form for the formulation of sequential algorithms.

### 5.7.1 Three phase model: water oil gas system

Thus, the strong problem with the respective boundary conditions is to find  $(\mathbf{u}, \mathbf{q}, p, s_w^*, s_o^*)$  such that:

$$\mathcal{A}_e = \left\{ \operatorname{div} \left( 2\mu\boldsymbol{\epsilon}(\mathbf{u}) + \lambda \operatorname{tr}(\boldsymbol{\epsilon}(\mathbf{u})) I - \boldsymbol{\sigma}^0 - \alpha(p - p^0) \right) + \mathbf{b} = 0 \right. \quad (5.33)$$

corresponding to computing the displacements

$$\mathcal{A}_p = \begin{cases} (\mathbf{K}\lambda)^{-1}\mathbf{q} + \nabla p - G_\lambda &= 0 \\ \frac{\partial(\phi^*(s_w^* + s_o^* + s_g^*))}{\partial t} + \operatorname{div}(\mathbf{q}) &= 0 \end{cases} \quad (5.34)$$

corresponding to computing the fluxes and pressures respectively

$$\mathcal{A}_h = \begin{cases} \frac{\partial(\phi^* s_w^*)}{\partial t} + \operatorname{div}(f_w \mathbf{q} + f_w f_o \mathbf{q}_{Gwo} + f_w f_g \mathbf{q}_{Gwg}) &= 0 \\ \frac{\partial(\phi^* s_o^*)}{\partial t} + \operatorname{div}\left(\frac{1}{1+R_{so}}(f_o \mathbf{q} + f_o f_w \mathbf{q}_{Gow} + f_o f_g \mathbf{q}_{Gog})\right) &= 0 \end{cases} \quad (5.35)$$

corresponding to computing the transport of water and oil respectively

Once more, with some abuse of mathematical notation, we denote 5.33, 5.34 and 5.35, as operators representing the elliptic, parabolic and hyperbolic components of the poroelastic blackoil model. These operators are subject to the following initial conditions: 5.26 , 5.21; and boundary conditions: 5.27 and 5.22.

To close the model, the following functional relations and dependencies are presented in the table 5.3.

Operator	Symbol	Expression
$\mathcal{A}_e$	$\mathbf{b}(\mathbf{u}, p, s_\beta^*)$	$(\rho_r(1 - \phi) + \phi(\rho_w s_w + \rho_o s_o + \rho_g s_g)) \mathbf{g} \phi \rightarrow \text{A.25}$
$\mathcal{A}_p \& \mathcal{A}_h$	$G_\lambda(p, s_\beta^*)$	$\sum_\beta f_\beta \rho_\beta \mathbf{g}$
	$s_g^*(p, s_\beta^*)$	$\frac{1}{B_g} (1 - s_w^* B_w + (1 - B_g R_{so}) s_o^* B_o) \rightarrow \{0 \leq s_\beta^* \ 0 < B_\beta\}$
	$\lambda_w(p, s_w^*)$	$\frac{k_{rw}}{\eta_w B_w}$
	$\lambda_o(p, s_o^*)$	$\frac{k_{ro}}{\eta_o B_o}$
	$\lambda_g(p, s_g^*)$	$\frac{k_{rg}}{\eta_g B_g}$
	$f_\beta(p, s_\beta^*)$	$\frac{\lambda_\beta}{\lambda}$
	$\mathbf{q}_{G\beta\gamma}(p, s_\beta^*)$	$\mathbf{K}\lambda(\rho_\beta - \rho_\gamma)\mathbf{g}$
Standard variables		
Variety of 5.18	$\bar{\mathbf{v}}_w$	$f_w \mathbf{q} + f_w f_o \mathbf{q}_{Gwo} + f_w f_g \mathbf{q}_{Gwg}$
Variety of 5.19	$\bar{\mathbf{v}}_o$	$\frac{1}{1 + R_{so}} (f_o \mathbf{q} + f_o f_w \mathbf{q}_{Gow} + f_o f_g \mathbf{q}_{Gog})$
Variety of 5.20	$\bar{\mathbf{v}}_g$	$\left(f_g + \frac{R_{so} f_o}{1 + R_{so}}\right) \mathbf{q} + f_g f_w \mathbf{q}_{Ggw} + f_g f_o \mathbf{q}_{Ggo}$
Variety of 5.11	$s_w(p, s_w^*)$	$s_w^* B_w = s_w^* \frac{\rho_{wstd}}{\rho_w}$
	$s_o(p, s_o^*)$	$s_o^* B_o = s_o^* \frac{\rho_{ostd}}{\rho_o}$
	$s_g(p, s_\beta^*)$	$s_g^* B_g - s_o^* B_o R_{so} B_g = s_g^* \frac{\rho_{gstd}}{\rho_g} - s_o^* \frac{\rho_{ostd}}{\rho_o} R_{so} \frac{\rho_{gstd}}{\rho_g}$

Table 5.3: Closure relationships for the operators 5.33, 5.34 and 5.35. The subscript *sdt* means standard or surface conditions, and  $\beta = \{w, o, g\}$ .

### 5.7.2 Two phase model: water oil system

Thus, the strong problem with the respective initial and boundary conditions, is to find  $(\mathbf{u}, \mathbf{q}, p, s_w^*)$  such that:

$$\mathcal{A}_e = \left\{ \operatorname{div} \left( 2\mu \boldsymbol{\epsilon}(\mathbf{u}) + \lambda \operatorname{tr}(\boldsymbol{\epsilon}(\mathbf{u})) I - \boldsymbol{\sigma}^0 - \alpha(p - p^0) \right) + \mathbf{b} = 0 \right. \quad (5.36)$$

corresponding to the displacements

$$\mathcal{A}_p = \begin{cases} (\mathbf{K}\lambda)^{-1} \mathbf{q} + \nabla p - G_\lambda &= 0 \\ \frac{\partial (\phi^*(s_w^* + s_o^*))}{\partial t} + \operatorname{div}(\mathbf{q}) &= 0 \end{cases} \quad (5.37)$$

corresponding to the flux and pressure variables respectively

$$\mathcal{A}_h = \left\{ \frac{\partial(\phi^* s_w^*)}{\partial t} + \operatorname{div}(f_w \mathbf{q} + f_w f_o \mathbf{q}_{Gwo} + f_w f_g \mathbf{q}_{Gwg}) \right. = 0 \quad (5.38)$$

corresponding to the transport of the water phase

To close the model the following functional relations and dependencies are presented in the table 5.4.

Operator	Symbol	Expression
$\mathcal{A}_e$	$\mathbf{b}(\mathbf{u}, p, s_\beta^*)$	$(\rho_r(1-\phi) + \phi(\rho_w s_w + \rho_o s_o)) \mathbf{g}$ $\phi \rightarrow \text{A.25}$
$\mathcal{A}_p$ & $\mathcal{A}_h$	$G_\lambda(p, s_\beta^*)$	$\sum_\beta f_\beta \rho_\beta \mathbf{g}$
	$s_o^*(p, s_w^*)$	$\frac{1}{B_o}(1 - s_w^* B_w) \rightarrow \{0 \leq s_\beta^* \leq B_\beta\}$
	$\lambda_w(p, s_w^*)$	$\frac{k_{rw}}{\eta_w B_w}$
	$\lambda_o(p, s_o^*)$	$\frac{k_{ro}}{\eta_o B_o}$
	$f_\beta(p, s_\beta^*)$	$\frac{\lambda_\beta}{\lambda}$
	$\mathbf{q}_{G\beta\gamma}(p, s_\beta^*)$	$\mathbf{K}\lambda(\rho_\beta - \rho_\gamma)\mathbf{g}$
Standard variables		
Variety of 5.18	$\bar{\mathbf{v}}_w$	$f_w \mathbf{q} + f_w f_o \mathbf{q}_{Gwo}$
Variety of 5.19	$\bar{\mathbf{v}}_o$	$f_o \mathbf{q} + f_o f_w \mathbf{q}_{Gow}$
Variety of 5.11	$s_w(p, s_w^*)$	$s_w^* B_w = s_w^* \frac{\rho_{wstd}}{\rho_w}$
	$s_o(p, s_o^*)$	$s_o^* B_o = s_o^* \frac{\rho_{ostd}}{\rho_o}$

Table 5.4: Closure relationships for the operators 5.36, 5.37 and 5.38. The subscript *sdt* means standard or surface conditions, and  $\beta = \{o, w\}$ .

## 5.8 Conclusions

During the sequence of equations described in this chapter, is possible to conclude:

- (i) The poroelastic coupling in a blackoil model has a similar form as the single-phase flow model.
- (ii) In the poroelastic blackoil model, it is possible to identify elliptic, parabolic and hyperbolic components, relating to the problems of deformation, total mass conservation and transport of the concentrations, respectively.
- (iii) The model written in a separate form, it has a natural shape for the idealization of sequential methods, to obtain with greater efficiency approximated solutions of the fully coupled operator.

# Chapter 6

## Finite Element Reservoir Modelling

A finite element discretization of the coupled equations presented in chapter 5 is delineated in this chapter. A sequential scheme for the solution of the elliptic, parabolic and hyperbolic components of the multiphase system is briefly described in terms of: the base reduction technique of chapter 3, the multiscale technique of chapter 4 and a first order upwind scheme for the saturation equations. In order to simplify notation, the documented method refers to a water oil system documented in table 5.4.

### Contents

---

6.1	Weak Formulation	106
6.2	Nested sequencial method (NSM)	109
6.2.1	Sequential method for multiphase equations	110
6.2.2	Solving the multiphase equations	110
6.2.3	Solving the geomechanical coupling	111
6.2.4	Transfer Interfaces	112
6.3	Conclusions	113

---

### 6.1 Weak Formulation

Starting from the strong formulation presented in the chapter 5 for the biphasic case, the temporal derivatives are treated by an implicit Euler scheme and regarding the spatial dimension a finite element discretization is used. The weak statements corresponding to the operators  $\mathcal{A}_e$ ,

$\mathcal{A}_p$  and  $\mathcal{A}_h$  are:

$$\begin{aligned}
& \int_{\Omega} (2\mu\epsilon + \lambda \operatorname{tr}(\boldsymbol{\epsilon}) \mathbf{I}) \cdot \nabla (\boldsymbol{\phi}_u) \, dV - \int_{\partial\Omega_N} \mathbf{t} \cdot \boldsymbol{\phi}_u \, dS - \int_{\Omega} (\alpha p \mathbf{I}) \cdot \nabla (\boldsymbol{\phi}_u) \, dV + \\
& \quad \int_{\Omega} \rho_r(s_w^*, p) \mathbf{g} \cdot \boldsymbol{\phi}_u \, dV = 0 \\
& \int_{\Omega} (\mathbf{K} \lambda(s_w^*, p))^{-1} \mathbf{q} \cdot \boldsymbol{\phi}_q \, dV + \int_{\partial\Omega_D} p_D \boldsymbol{\phi}_q \cdot \mathbf{n} \, dS - \int_{\Omega} p \operatorname{div}(\boldsymbol{\phi}_q) \, dV + \\
& \quad - \int_{\Omega} G_\lambda(s_w^*, p) \cdot \boldsymbol{\phi}_q \, dV = 0 \tag{6.1} \\
& - \int_{\Omega} \frac{(\phi^*(s_w^* + s_o^*))^{n+1} - (\phi^*(s_w^* + s_o^*))^n}{\Delta t} \phi_p \, dV - \int_{\Omega} \operatorname{div}(\mathbf{q}) \phi_p \, dV = 0 \\
& \int_{\Omega} \frac{(\phi^* s_w^*)^{n+1} - (\phi^* s_w^*)^n}{\Delta t} \, dV + \int_{\partial\Omega_{inj/prod}} f_w(s_{w,in/out}^*) \mathbf{q} \cdot \mathbf{n} \, dS + \\
& \quad \sum_K \int_{\partial K} (f_w(s_w^*) \mathbf{q} + f_w f_o(s_w^*) \mathbf{q}_{Gwo}) \cdot \mathbf{n} \, dS = 0
\end{aligned}$$

Subject to the respective initial and boundary conditions (see chapter 5).

For simplicity  $s = s_w^*$  is used. In short, the weak problem is find  $(\mathbf{u}, \mathbf{q}, p, s) \in H^1(\Omega)^d \times H(\operatorname{div}, \Omega) \times L^2(\Omega) \times L^2(\Omega)$  such that:

$$\begin{aligned}
a_u(\mathbf{u}, \boldsymbol{\phi}_u) - b_u(p, \boldsymbol{\phi}_u) + c_u(p, s, \boldsymbol{\phi}_u) - f_u(\boldsymbol{\phi}_u) &= 0 \\
a_q(\mathbf{q}, p, s, \boldsymbol{\phi}_q) - b_q(p, \boldsymbol{\phi}_q) - c_q(p, s, \boldsymbol{\phi}_q) + f_q(\boldsymbol{\phi}_q) &= 0 \tag{6.2} \\
- b_p(\mathbf{q}, \phi_p) - c_p(p, s, \phi_p) - c_u(\mathbf{u}, s, \phi_p) &= 0 \\
d_s(\mathbf{q}, s, 1) + d_q(\mathbf{q}, 1) + d_p(p, s, 1) + d_u(\mathbf{u}, s, 1) &= 0
\end{aligned}$$

for all  $\boldsymbol{\phi}_u \in H^1(\Omega)^d$ ,  $\boldsymbol{\phi}_q \in H(\operatorname{div}, \Omega)$  y  $\phi_p \in L^2(\Omega)$ . Where the forms have the following integral expressions:

$$\begin{aligned}
a_u(\mathbf{u}, \boldsymbol{\phi}_u) &= \int_{\Omega} (2\mu\epsilon + \lambda \operatorname{tr}(\boldsymbol{\epsilon}) \mathbf{I}) \cdot \nabla (\boldsymbol{\phi}_u) \, dV \\
b_u(p, \boldsymbol{\phi}_u) &= \int_{\Omega} (\alpha p \mathbf{I}) \cdot \nabla (\boldsymbol{\phi}_u) \, dV \\
c_u(p, s, \boldsymbol{\phi}_u) &= \int_{\Omega} \rho_r \mathbf{g} \cdot \boldsymbol{\phi}_u \, dV \\
f_u(\boldsymbol{\phi}_u) &= \int_{\partial\Omega_N} \mathbf{t} \cdot \boldsymbol{\phi}_u \, dS \tag{6.3}
\end{aligned}$$

$$\begin{aligned}
a_q(\mathbf{q}, p, s, \boldsymbol{\phi}_q) &= \int_{\Omega} (\mathbf{K}\lambda(s, p))^{-1} \eta B_f \mathbf{q} \cdot \boldsymbol{\phi}_q \, dV \\
b_q(p, \boldsymbol{\phi}_q) &= \int_{\Omega} p \operatorname{div}(\boldsymbol{\phi}_q) \, dV \\
c_q(p, s, \boldsymbol{\phi}_q) &= \int_{\Omega} G_{\lambda}(s, p) \cdot \boldsymbol{\phi}_q \, dV \\
f_q(\boldsymbol{\phi}_q) &= \int_{\partial\Omega_D} p_D \boldsymbol{\phi}_q \cdot \mathbf{n} \, dS
\end{aligned} \tag{6.4}$$

$$\begin{aligned}
c_u(\mathbf{u}, s, \phi_p) &= \int_{\Omega} \frac{\alpha}{K_{dr}} \frac{(\sigma_v(s_w^* + s_o^*))^{n+1} - (\sigma_v^0(s_w^* + s_o^*))^n}{\Delta t} \phi_p \, dV \\
c_p(s, p, \phi_p) &= \int_{\Omega} \left( S_e + \frac{\alpha^2}{K_{dr}} \right) \frac{(p(s_w^* + s_o^*))^{n+1} - (p^0(s_w^* + s_o^*))^n}{\Delta t} \phi_p \, dV
\end{aligned}$$

$$\begin{aligned}
d_s(\mathbf{q}, s, 1) &= \sum_K \int_{\partial K} (f_w(s_w^*) \mathbf{q} + f_w f_o(s_w^*) \mathbf{q}_{Gwo}) \cdot \mathbf{n} \, dS \\
d_q(\mathbf{q}, 1) &= \int_{\partial\Omega_{inj}} f_w(s_{w_{in}}^*) \mathbf{q} \cdot \mathbf{n} \, dS + \int_{\partial\Omega_{prod}} f_w(s_{w_{out}}^*) \mathbf{q} \cdot \mathbf{n} \, dS \\
d_p(p, s, 1) &= \int_{\Omega} \left( S_e + \frac{\alpha^2}{K_{dr}} \right) \frac{(p s_w^*)^{n+1} - (p^0 s_w^*)^n}{\Delta t} \, dV \\
d_u(\mathbf{u}, s, 1) &= \int_{\Omega} \frac{\alpha}{K_{dr}} \frac{(\sigma_v s_w^*)^{n+1} - (\sigma_v^0 s_w^*)^n}{\Delta t} \, dV
\end{aligned} \tag{6.5}$$

**Remark:** The system composed of 6.3, 6.4 and 6.5, which represent the poroselastic multiphasic system are a nonlinear non-symmetric system of equations with strong coupling.

the discrete problem is find  $(\mathbf{u}_{\mathcal{N}}^{n+1}, \mathbf{q}_{\mathcal{N}}^{n+1}, p_{\mathcal{N}}^{n+1}, s_{\mathcal{N}}^{n+1})$  for a given  $(\mathbf{u}_{\mathcal{N}}^n, p_{\mathcal{N}}^n, s_{\mathcal{N}}^n)$ , such that:

$$\begin{aligned}
a_u(\mathbf{u}_{\mathcal{N}}^{n+1}, \boldsymbol{\phi}_u) - b_u(p_{\mathcal{N}}^{n+1}, \boldsymbol{\phi}_u) + c_u(p_{\mathcal{N}}^{n+1}, s_{\mathcal{N}}^{n+1}, \boldsymbol{\phi}_u) - f_u(\boldsymbol{\phi}_u) &= 0 \\
a_q(\mathbf{q}_{\mathcal{N}}^{n+1}, p_{\mathcal{N}}^{n+1}, s_{\mathcal{N}}^{n+1}, \boldsymbol{\phi}_q) - b_q(p_{\mathcal{N}}^{n+1}, \boldsymbol{\phi}_q) - c_q(p_{\mathcal{N}}^{n+1}, s_{\mathcal{N}}^{n+1}, \boldsymbol{\phi}_q) + f_q(\boldsymbol{\phi}_q) &= 0 \\
-b_p(\mathbf{q}_{\mathcal{N}}^{n+1}, \phi_p) - c_p(p_{\mathcal{N}}^{n+1}, s_{\mathcal{N}}^{n+1}, \phi_p) - c_u(\mathbf{u}_{\mathcal{N}}^{n+1}, s_{\mathcal{N}}^{n+1}, \phi_p) &= 0 \\
d_s(\mathbf{q}_{\mathcal{N}}^{n+1}, s_{\mathcal{N}}^{n+1}, 1) + d_q(\mathbf{q}_{\mathcal{N}}^{n+1}, 1) + d_p(p_{\mathcal{N}}^{n+1}, s_{\mathcal{N}}^{n+1}, 1) + d_u(\mathbf{u}_{\mathcal{N}}^{n+1}, s_{\mathcal{N}}^{n+1}, 1) &= 0
\end{aligned} \tag{6.6}$$

for all  $\boldsymbol{\phi}_{\mathcal{N}u} \in V_{\mathcal{N}}$ ,  $\boldsymbol{\phi}_{\mathcal{N}q} \in W_{\mathcal{N}}$  and  $\phi_{\mathcal{N}p} \in Z_{\mathcal{N}}$ .

The use of a fully implicit discretization, to solve the nonlinear system associated with 6.1, is predominant in commercial simulators, and is adopted here. The discrete system 6.6 is linearized and then solved using a direct solver. In the case of Eclipse (Schlumberger simulator) a nested factorization is employed (**Kumar2010**) as a direct solver. In order to get more efficiency in large problems, it is common to replace the direct solver with an iterative solver preconditioned using the restricted pressure equation see **Wallis1983**. In this research greater efficiency is obtained by using a sequential method based on the parabolic and hyperbolic components of the multiphase equations.

## 6.2 Nested sequential method (NSM)

There exists a great variety of sequential methods for the resolution of the discrete problem 6.6, these varieties of numerical schemes are based on the choice of different state variables and their manipulations in temporal space discretizations. Perhaps the most used and classic sequential approximation is the IMPES method, which solves the parabolic component by implicitly freezing, the velocities and pressures are subsequently used for the explicit updating of the volumetric saturations, this method suffers from instabilities due to the explicit scheme in saturations. A method with better stability is obtained treating saturations implicitly (**Watts1986**).

There are several strategies for the formulation of fully implicit sequential methods, aided to solve the equations associated with the black oil model. Nevertheless during the development of this research, it was experienced that a robust and efficient implementation depends on numerous inconspicuous details as: The right choice of state variables, numerical treatment the gravitational fluxes depending on the state variables selection, CFL restrictions and time step cutting when implicit-explicit approach is used, treatment of the wells as sources or boundaries, and in the linearization process the use a complete Jacobian or incomplete Jacobian.

Next, the proposed sequential method is described, which is inspired on **Watts1986** **Watts1986** describes a sequential implicit formulation of the compositional reservoir flow, but is no clear the way that the separated mathematical components are coupled. In this research, the sequential method uses interfaces that couple the operators  $\mathcal{A}_p$  and  $\mathcal{A}_h$ . These interfaces are based on volume average quantities.

In this research, for the pressure and flux equations, the secant method is used for the solution of non-linear parts, it increases the the number of iterations, but allow to computed a simetric approximation of the Jacobian matrix, which is decomposed once per time step cycle. For transport component the Newton-Raphson method is used.

For the coupling of the elasticity operator  $\mathcal{A}_e$ , is used the fixed stress split, described in chapter 3. Thus, the nested sequential method (NSM) is given by the execution of the method coupling  $\mathcal{A}_p$  and  $\mathcal{A}_h$  within each fixed-stress iteration that couples  $\mathcal{A}_e$ .

The discrete operators  $\mathcal{A}_{e\mathcal{N}}$ ,  $\mathcal{A}_{p\mathcal{N}}$  y  $\mathcal{A}_{h\mathcal{N}}$  from 6.6 are rewritten as follows:

$$\mathcal{A}_{e\mathcal{N}} = \left\{ a_u (\mathbf{u}_{\mathcal{N}}^{n+1}, \boldsymbol{\phi}_u) - b_u (p_{\mathcal{N}}^{n+1}, \boldsymbol{\phi}_u) + c_u (p_{\mathcal{N}}^{n+1}, s_{\mathcal{N}}^{n+1}, \boldsymbol{\phi}_u) - f_u (\boldsymbol{\phi}_u) = 0 \right. \quad (6.7)$$

$$\mathcal{A}_{p\mathcal{N}} = \begin{cases} a_q (\mathbf{q}_{\mathcal{N}}^{n+1}, p_{\mathcal{N}}^{n+1}, s_{\mathcal{N}}^{n+1}, \boldsymbol{\phi}_q) - b_q (p_{\mathcal{N}}^{n+1}, \boldsymbol{\phi}_q) - c_q (p_{\mathcal{N}}^{n+1}, s_{\mathcal{N}}^{n+1}, \boldsymbol{\phi}_q) + f_q (\boldsymbol{\phi}_q) = 0 \\ -b_p (\mathbf{q}_{\mathcal{N}}^{n+1}, \boldsymbol{\phi}_p) - c_p (p_{\mathcal{N}}^{n+1}, s_{\mathcal{N}}^{n+1}, \boldsymbol{\phi}_p) - c_u (\mathbf{u}_{\mathcal{N}}^{n+1}, s_{\mathcal{N}}^{n+1}, \boldsymbol{\phi}_p) = 0 \end{cases} \quad (6.8)$$

$$\mathcal{A}_{h\mathcal{N}} = \left\{ d_s (\mathbf{q}_{\mathcal{N}}^{n+1}, s_{\mathcal{N}}^{n+1}, 1) + d_q (\mathbf{q}_{\mathcal{N}}^{n+1}, 1) + d_p (p_{\mathcal{N}}^{n+1}, s_{\mathcal{N}}^{n+1}, 1) + d_u (\mathbf{u}_{\mathcal{N}}^{n+1}, s_{\mathcal{N}}^{n+1}, 1) = 0 \right. \quad (6.9)$$

### 6.2.1 Sequential method for multiphase equations

The parabolic component 6.8 is solved by the MHM-*H* (*div*) method or, alternatively, using the mixed formulation for comparison purposes. The algorithm of the multiscale process is modified, in order to obtain the corrections instead of the variable itself, because the equations are linearized and approximated using the secant method at the given step  $\Delta t$ .

Once the pressure and velocity field are converged, the transport problem represented by the operator 6.9 is approximated applying a first-order upwind method described by (Brenier1991), in this method both, velocities, diffusion  $\mathbf{q}$  and gravitational  $\mathbf{q}_{Gwo}$  are considered (see table 5.3 and 5.4). During the solution of the operator 6.9, water conservation is implicitly solved, allowing the use of relatively large time steps. This results in increased robustness in the implementation with the price of diffuse saturations profiles. After the saturations are updated the system is ready for the next iteration.

### 6.2.2 Solving the multiphase equations

Both the 6.8 operator and the 6.9 operator are nonlinear and are strongly coupled, and must be resolved iteratively. As was state above, in the case of the 6.8 operator, the secant method is used, and in the case of saturation transport, the Newton-Raphson Method is used. Thus, for a given time step and  $(\mathbf{q}_{\mathcal{N}}^n, p_{\mathcal{N}}^n, s_{\mathcal{N}}^n)$ , the algorithm of the solution of  $(\mathbf{q}_{\mathcal{N}}^{n+1}, p_{\mathcal{N}}^{n+1}, s_{\mathcal{N}}^{n+1})$  is given as follows:

1. Starting from  $\{\mathbf{q}_{\mathcal{N}}^n, p_{\mathcal{N}}^n, s_{\mathcal{N}}^n\}$  initial estimates are obtained for  $\{\mathbf{q}_{k\mathcal{N}}^{n+1}, p_{k\mathcal{N}}^{n+1}, s_{l\mathcal{N}}^{n+1}\}$ .

2. Initialize two iteration counters  $k$  and  $l$  for the solution of 6.8 and 6.9, respectively.
3. Solve the 6.8 operator and update the velocity and pressure, using a transfer interface  $A_{p-p}$  until the norms of the residues  $R_{p\mathcal{N}}$  associated with  $\mathcal{A}_{p\mathcal{N}}$   $\|R_p\| < \epsilon_{p1}$  and  $\|\{\mathbf{q}_{k\mathcal{N}}^{n+1}, p_{k\mathcal{N}}^{n+1}\} - \{\mathbf{q}_{k+1\mathcal{N}}^{n+1}, p_{k+1\mathcal{N}}^{n+1}\}\| < \epsilon_{p2}$
4. Using a transfer interface  $A_{p-h}$ , the pressure and velocity fields are inserted into the discrete operator  $\mathcal{A}_{h\mathcal{N}}$ .
5. Solve the 6.8 operator and update the saturations, using a transfer interface  $A_{h-h}$ , until the residues  $R_{h\mathcal{N}}$  associated with  $\mathcal{A}_{h\mathcal{N}}$   $\|R_h\| < \epsilon_{h1}$  and  $\|\{s_{l\mathcal{N}}^{n+1}\} - \{s_{l+1\mathcal{N}}^{n+1}\}\| < \epsilon_{h2}$ .
6. Using a transfer interface  $A_{h-p}$ , the saturations are inserted into the discrete operator  $\mathcal{A}_{p\mathcal{N}}$ .
7. Finally, if  $\|R_p\| + \|R_h\| < \epsilon_{T1}$  and  $\|\{\mathbf{q}_{k\mathcal{N}}^{n+1}, p_{k\mathcal{N}}^{n+1}, s_{l\mathcal{N}}^{n+1}\} - \{\mathbf{q}_{k+1\mathcal{N}}^{n+1}, p_{k+1\mathcal{N}}^{n+1}, s_{l+1\mathcal{N}}^{n+1}\}\| < \epsilon_{T2}$ , all the variables are updated  $\{\mathbf{q}_{\mathcal{N}}^{n+1}, p_{\mathcal{N}}^{n+1}, s_{\mathcal{N}}^{n+1}\} = \{\mathbf{q}_{k+1\mathcal{N}}^{n+1}, p_{k+1\mathcal{N}}^{n+1}, s_{l+1\mathcal{N}}^{n+1}\}$ . Otherwise return to second step.

### 6.2.3 Solving the geomechanical coupling

The elasticity equation 6.7 is solved using the reduced basis technique. The CG formulation was also implemented for evaluating of the precision of the reduced basis. In an analogous way to the sequential scheme by fixed stress, the monophasic operator is replaced by the sequential method, previously described, giving the nested form of the following algorithmic steps, for the solution of  $(\mathbf{u}_{\mathcal{N}}^{n+1}, \mathbf{q}_{\mathcal{N}}^{n+1}, p_{\mathcal{N}}^{n+1}, s_{\mathcal{N}}^{n+1})$  on a given time step  $\Delta t$ :

1. Initialize the iterations counter by fixed stress  $m$  (for simplicity, suffix  $ss$  is left out), for the solution of the operator 6.7. Also from  $\{\mathbf{u}_{\mathcal{N}}^n, \mathbf{q}_{\mathcal{N}}^n, p_{\mathcal{N}}^n, s_{\mathcal{N}}^n\}$  The initial estimates are obtained  $\{\mathbf{u}_{m\mathcal{N}}^{n+1}, \mathbf{q}_{k\mathcal{N}}^{n+1}, p_{k\mathcal{N}}^{n+1}, s_{l\mathcal{N}}^{n+1}\}$ .
2. Initialize two iteration counters  $k$  and  $l$  for the solution of 6.8 and 6.9, respectively.
3. Solve the 6.8 operator and update the velocity and pressure, using a transfer interface  $A_{p-p}$  until: the residues  $R_{p\mathcal{N}}$  associated with  $\mathcal{A}_{p\mathcal{N}}$  satisfy  $\|R_p\| < \epsilon_{p1}$  and  $\|\{\mathbf{q}_{k\mathcal{N}}^{n+1}, p_{k\mathcal{N}}^{n+1}\} - \{\mathbf{q}_{k+1\mathcal{N}}^{n+1}, p_{k+1\mathcal{N}}^{n+1}\}\| < \epsilon_{p2}$
4. Using a transfer interface  $A_{p-h}$ , the pressure and velocity fields are inserted into the discrete operator  $\mathcal{A}_{h\mathcal{N}}$ .
5. Solve the 6.9 operator and update the saturations, using a transfer interface  $A_{h-h}$ , until the residues  $R_{h\mathcal{N}}$  associated with  $\mathcal{A}_{h\mathcal{N}}$  satisfy  $\|R_h\| < \epsilon_{h1}$  and  $\|\{s_{l\mathcal{N}}^{n+1}\} - \{s_{l+1\mathcal{N}}^{n+1}\}\| < \epsilon_{h2}$ .
6. Using a transfer interface  $A_{h-p}$ ,  $A_{h-e}$ , the saturations are inserted in the discrete operators  $\mathcal{A}_{p\mathcal{N}}$  and  $\mathcal{A}_{e\mathcal{N}}$ . The transfer interface  $A_{p-e}$  Inserts the pressure field into the discrete operator  $\mathcal{A}_{e\mathcal{N}}$ .

- (a) Solve the operator 6.7 and updating the displacements through a transfer interface  $A_{e-e}$  until the residue  $R_{eN}$  associated to  $\mathcal{A}_{eN}$  be  $\|R_e\| < \epsilon_{e1}$  and  $\|\{\mathbf{u}_{mN}^{n+1}\} - \{\mathbf{u}_{m+1N}^{n+1}\}\| < \epsilon_{e2}$ .
  - (b) Using transfer interfaces  $A_{e-p}$  and  $A_{e-h}$ , the displacements and their gradients are inserted into the discrete operators  $\mathcal{A}_{pN}$  and  $\mathcal{A}_{hN}$ , respectively.
  - (c)  $m \rightarrow m + 1$
7. Finally, if  $\|R_e\| + \|R_p\| + \|R_h\| < \epsilon_{T1}$  and  $\|\{\mathbf{u}_{mN}^{n+1}, \mathbf{q}_{kN}^{n+1}, p_{kN}^{n+1}, s_{lN}^{n+1}\} - \{\mathbf{u}_{m+1N}^{n+1}, \mathbf{q}_{k+1N}^{n+1}, p_{k+1N}^{n+1}, s_{l+1N}^{n+1}\}\| < \epsilon_{T2}$ , the variables are updated  $\{\mathbf{u}_N^{n+1}, \mathbf{q}_N^{n+1}, p_N^{n+1}, s_N^{n+1}\} = \{\mathbf{u}_{m+1N}^{n+1}, \mathbf{q}_{k+1N}^{n+1}, p_{k+1N}^{n+1}, s_{l+1N}^{n+1}\}$ . Otherwise return to second outer step.

#### 6.2.4 Transfer Interfaces

Nine different transfer interfaces are used during the nested sequential solution of the poroelastic multiphasic equations. The transfer of information becomes a critical point in terms of efficiency. An approximation for finite elements requires numerical integration; thus, the operations given by the forms 6.3, 6.4 and 6.5 must be executed quickly.

To deal with this problem we take advantage of the fact that linear combinations of each state variable  $\{\mathbf{u}_N^{n+1}, \mathbf{q}_N^{n+1}, p_N^{n+1}, s_N^{n+1}\}$  admit the following matrix representation:

$$\vec{v}_N = A \alpha_{vN} \quad (6.10)$$

Where  $A$  is an application, which contains base functions, evaluated at each integration point in the properly indexed mesh. This linear application has dimensions number of global integration points by number of degrees of freedom, i.e.  $n \times N$ ,  $\alpha_{vN}$  are the multiplier coefficients associated with the variable, and  $\vec{v}$  represents a vector containing the finite element solution evaluated at each indexed integration point, i.e.  $v_N(\mathbf{x}_i)$ . Thus, for the correct transfer of the necessary values between each operator, there must be a system of indexation of integration points, a system to store previous states of the variables (memory) as well as other information necessary for the calculation of the forms 6.3, 6.4 and 6.5.  $A_{ij}$  represents the group of necessary linear applications, to transfer the information of the operator  $\mathcal{A}_{iN}$  to the operator  $\mathcal{A}_{jN}$ . The table 6.1 represents the relationship matrix of each transfer operation, necessary for the execution of the NSM.

origin\target	$\mathcal{A}_{eN}$	$\mathcal{A}_{pN}$	$\mathcal{A}_{hN}$
$\mathcal{A}_{eN}$	$A_{e-e}$	$A_{e-p}$	$A_{e-h}$
$\mathcal{A}_{pN}$	$A_{p-e}$	$A_{p-p}$	$A_{p-h}$
$\mathcal{A}_{hN}$	$A_{h-e}$	$A_{h-p}$	$A_{h-h}$

Table 6.1: Matrix relation for the transfer interfaces.

Through the series of calculations given by the NSM, its approximations and properties must be verified, in order to have correct solutions in complex problems, these verifications are given in chapter 7.

## 6.3 Conclusions

During the sequence of equations described in this chapter, is possible to conclude:

- (i) The sequential approach allows that each component of the model can be implemented by separate, or even by use simulators, that are already implemented. The coupling are given by the necessary corresponding interfaces. This idea, lends to a modular program design, and provides a physical interpretation that can be very helpful in the understanding of model behavior.
- (ii) The sequential nested method described in this chapter, involves conservative solutions for each time step, and take advantages of the model written in a separate components.

# **Part III**

## **An advance reservoir simulator**

# Chapter 7

## Advanced Reservoir Simulator

As an anthology, several finite element technologies described in the previous sections, have been incorporated into a home-made reservoir simulator coupled with geomechanics, called iMRS (innovative Multiscale Reservoir Simulator). For reasons of simplicity, a detailed description of the algorithms and procedures involved in the development of the simulator is avoided. The main scope of this chapter, is to show its potential to treat large problems (hundred of thousands degrees of freedom). At first a sequence of checks are presented and then we present a set of three-dimensional simulations.

### Contents

---

7.1	A multiscale geomechanic reservoir simulator . . . . .	116
7.1.1	Geometry description . . . . .	116
7.1.2	Spatial properties . . . . .	117
7.1.3	Well Model . . . . .	118
7.1.4	Something about the implementation . . . . .	119
7.2	Numerical verification . . . . .	121
7.2.1	Homogeneous pressure change of a poroelastic inclusion . . . . .	121
7.2.2	Single phase water injection . . . . .	126
7.2.3	Injection of a passive tracer . . . . .	131
7.2.4	Water injection in an oil-water system . . . . .	134
7.3	Reservoir simulations . . . . .	139
7.3.1	Injection of linear tracer in 3D reservoir . . . . .	139
7.3.2	Reduced geomechanic 3D simulation . . . . .	147
7.3.3	Water injection in an oil water system in 3D . . . . .	152
7.4	Conclusions . . . . .	154

---

## 7.1 A multiscale geomechanic reservoir simulator

In this section the main components of the iMRS are described with a very brief review on some details about the implementation.

### 7.1.1 Geometry description

In this investigation, the reservoir is considered to be a computational domain  $\Omega_r \in \mathbf{R}^d$  with  $d = \{2, 3\}$ , and with outer boundary  $\partial\Omega_r$ , from which the oil and water fluids are extracted by a finite number  $k$  of small domains  $\Omega_{w1}, \dots, \Omega_{wk}$  within  $\Omega_r$ , which represent the injection or production wells,  $w = \{i, p\}$  respectively. These domains  $\Omega_{wk}$ , can be imagined as small circles when  $d = 2$  and small cylinders with spherical bases  $d = 3$ , with any orientation and inclination, a third kind of domains  $\Omega_{wr1}, \dots, \Omega_{wrk}$ , represents the wellbore region, these domains surround  $\Omega_{wk}$ , can be imagined as small circles bigger than  $\Omega_{wk}$  in  $d = 2$  and small ellipsoids with major axis oriented with wellbore axis wrapping  $\Omega_{wk}$  in  $d = 3$ . In either case the wellbore is denoted by  $\Omega_{wk}$  with contour  $\partial\Omega_{wk}$ , and the wellbore region denoted by  $\Omega_{wrk}$  with contour  $\partial\Omega_{wrk}$ . Once  $\partial\Omega_{wrk}$  has been defined it becomes part of the inner contour of  $\Omega_r$ , and  $\partial\Omega_{wk}$  becomes part of the inner contour of  $\Omega_{wrk}$  closing the volume. When the geomechanical problem is considered, the volume  $\Omega_s$  is incorporated to represents the side burden rocks with outer boundary  $\partial\Omega_s$ . The figures 7.1 and 7.2 show two types of geometric representations of the reservoir in the two dimensional case (7.1) and in the three dimensional case (figure 7.2).

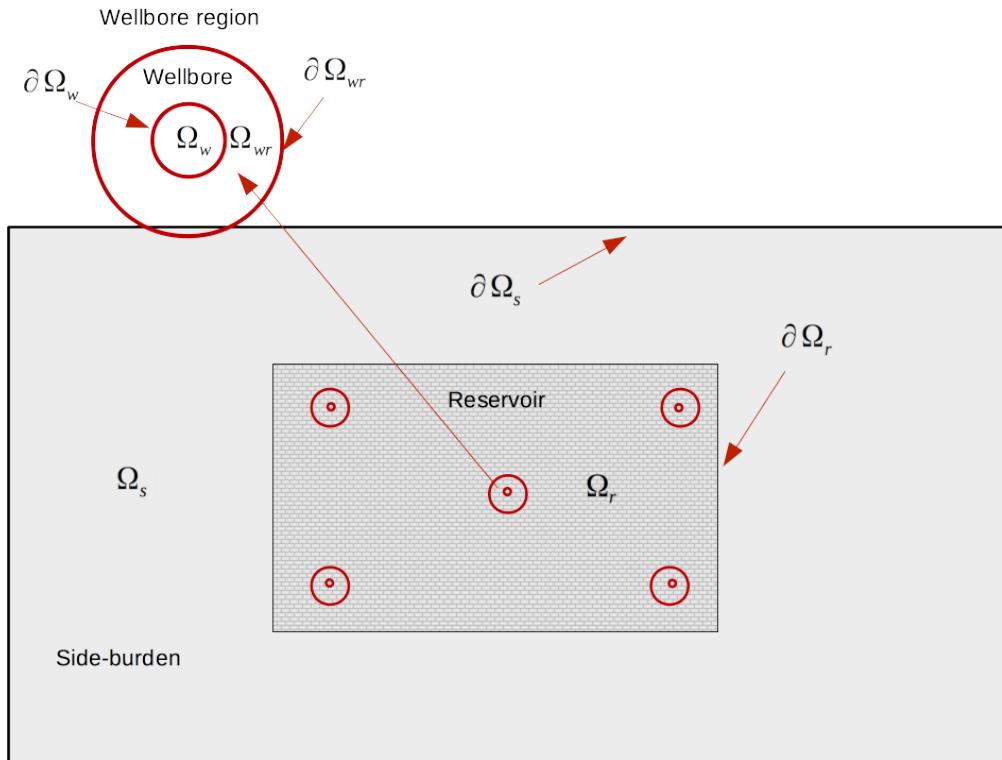


Figure 7.1: 2D reservoir, wellbore, wellbore region, side-burden, and boundaries representation.

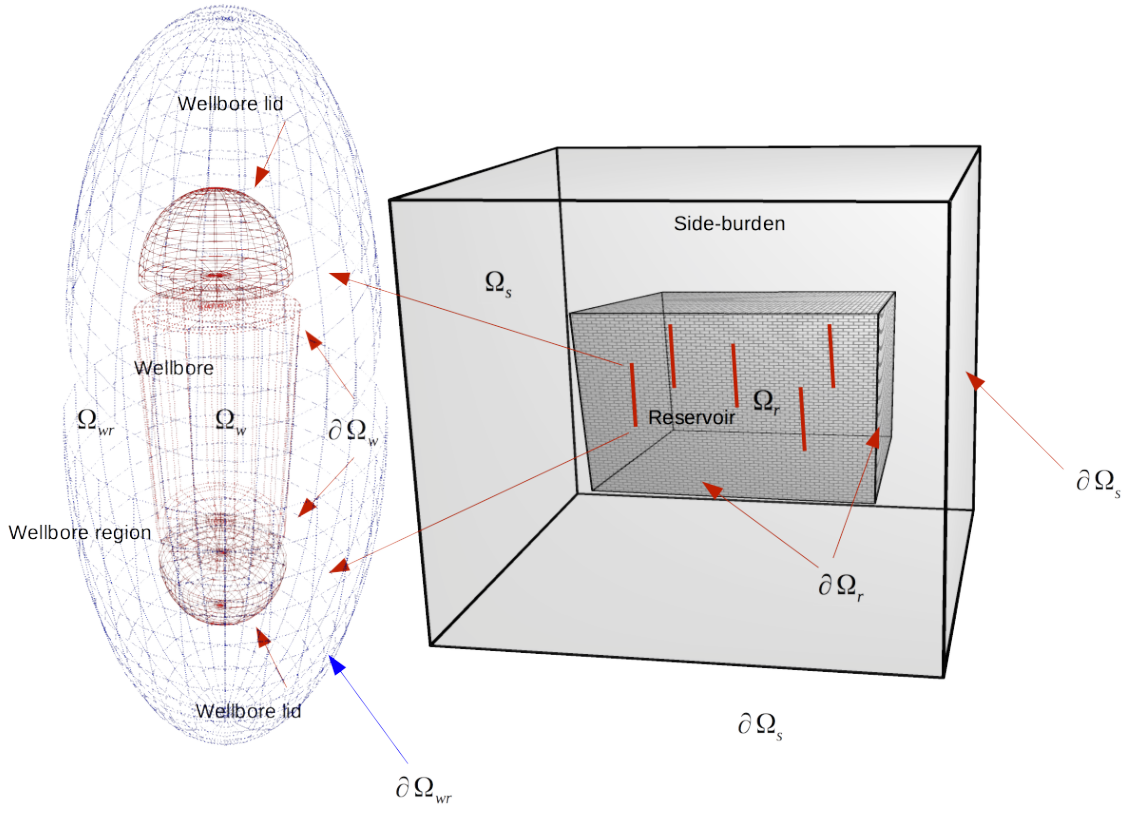


Figure 7.2: 3D reservoir, wellbore, wellbore region, side-burden, and boundaries representation.

For the simulation of complex geological geometries, the use of a mesh generator is required. In this research Gmsh is used. Gmsh is a mesh generator commonly used in engineering. Gmsh is integrated with iMRS for the rapid generation of meshes. A Gmsh oriented script with CAD support was developed for the generation of the geometry according to the figures 7.1 and 7.2.

### 7.1.2 Spatial properties

The generation of a field of geological properties is carried out through a stochastic process, which represents a study to be constructed. In order to pass the generation of a stochastic process, a method for the transfer of spatial properties to integration points fields available on the web was implemented. The procedure for transfer is defined as follows:

It is evident that the execution of the algorithm 7.1, becomes expensive as the number of pixels in the rasterization increases. However, the execution of the same is performed only once, during the initialization of the transfer applications introduced in the chapter 6. The figure 7.3 (upper right) shows a section of the spatial porosity data from the comparative case 10 of the SPE, where the first 40, 60, 60 blocks already rasterized and provided at <http://www.spe.org/web/>

---

**Algorithm 7.1** Spatial property transfer.

**Require:**  $\mathbf{K}$  and  $\phi$  number of blocks in  $n_i, n_j, n_k$  directions

**Ensure:**  $\mathbf{K}$  and  $\phi$  over mesh integration points

Rasterized  $\mathbf{K}$  and  $\phi$  over all blocks

**for all** Integration points **do**

    Find the block that contains the integration point

    Insert properties to integration point memory

**end for**

---

[csp/datasets/set02.htm](#), the figure 7.3 (upper left) shows a tetrahedron partition embedded in the raster map, through the algorithm 7.1 are obtained the figures 7.3 (lower) for porosity (left) and permeability in  $\mathbf{z}$  (right).

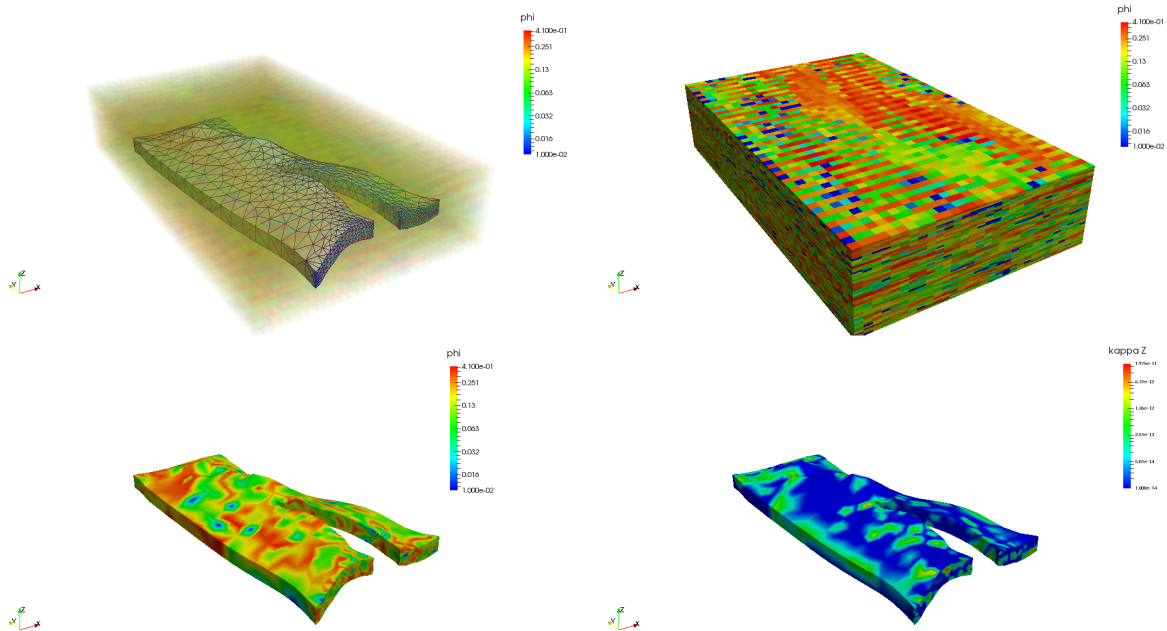


Figure 7.3: Discretization of finite elements embedded within a rasterization of a section of the SPE case. Properties transferred to the geometric representation after the use of the algorithm 7.1.

For the cases shown in this chapter with heterogeneous permeability tensor and porosity. A map of permeabilities and porosities is extracted from case number 10 of the SPE was used as a source for the generation of heterogeneous results.

### 7.1.3 Well Model

In iMRS wells are not treated as source terms, but rather as internal contours of the wellbore regions  $\partial\Omega_{wk}$ . In these regions  $\partial\Omega_{wk}$  only represent injection or production of fluids. Each well is

represented by a circle (2D) or cylinder with spherical terminals (3D), as is shown in figure 7.2. In the 3D case, wells can assume any inclination and orientation, and the spherical terminals have zero flow conditions (for the flow problem). For the deformation problem the boundary condition is the pressure of the wellbore applied as normal force to the rock.

### 7.1.4 Something about the implementation

In **Neopz** the object-oriented paradigm is the pillar for the separation of different modules, which are described by numerous classes with well-defined directives and purposes. For more details about the library refer to **Devloo2009; Forti2010; Farias2014**. The simulator iMRS is supported entirely by **Neopz**. iMRS follows an object-oriented phylosophy, and its implementation is based on a series of properly structured classes, which are briefly described below.

## Class structure

The class structure aims to facilitate the control of the different simulation models. As documented, several finite element technologies are combined with different approximation spaces. Therefore overlapping multiphysics meshes are used. For the execution of finite elements discretizations inside the sequential method described previously several classes are dedicated to some specific tasks:

- (i) Geometry;
- (ii) Material properties;
- (iii) Approximation spaces;
- (iv) Weak formulations;
- (v) Finite element analysis;

Each class has its proper interface and attributes. They are be described in this section.

## Geometry

**TRMGmshReader:** This class implements the reader of a Gmsh \*.msh file and return a TPZGeoMesh neopz object which represents the geometry, it is unique, and shared between all the classes that are related with geometric information and approximation space generation.

## Material Properties

**TRMSimulationData:** Class structure that stores all the simulation data with respect to numeric controls and input parameters.

**TRMWaterPhase:** Class structure to store the data related to the water phase.

**TRMOilPhase:** Class structure to store the data related to the oil phase.

**TRMPetrophysicsProperties:** Class structure to store data related to the petrophysical properties of the rock.

**TRMSpatialPropertiesMap:** Class structure dedicated to execute the procedure for transfer the spatial properties with the aim to allow permeability variation with respect to  $\mathbf{x}$ . Using materials with memory structures, it the spatial dependency of the permeability, porosity, and poroelastic parameters are precomputed and stored as an attribute of each integration point.

## Approximation spaces

**TRMSpaceOdissey:** This class constructs the approximation space objects in accordance to the elliptic, parabolic and hyperbolic operator. It implements the construction of MHM- $H$  ( $div$ ) conforming spaces (see chapter 4) for the parabolic operator, and the implement the offline procedure for computing the reduced order model for the elliptic operator (see chapter 3).

## Weak formulations

The following classes define the weak formulation using sequential method with the information transfers operators described in Chapter 6.

**TRMBiotPoroelasticity:** This class implements the weak formulation of the Maurice Biot linear poroelasticity for the elliptic operator  $\mathcal{A}_e$ .

**TRMMixedDarcy:** This class implements the mixed weak formulation for the parabolic operator  $\mathcal{A}_p$ .

**TRMPHaseTransport:** This class implements the convective transport of each phase described by the hyperbolic operator  $\mathcal{A}_h$ .

## Finite element analysis

**TRMGeomechanicsAnalysis:** This class implements the approximation of the elastic response represented by  $\mathcal{A}_{e\mathcal{N}}$ , or in the case of the reduced basis (RB) procedure  $\mathcal{A}_{e\mathcal{M}}$  (see chapter 3).

**TRMFluxPressureAnalysis:** This class implements the procedure for updating the flux and pressure for a given saturation over one time step, by solving  $\mathcal{A}_{p\mathcal{N}_t}$ .

**TRMTransportAnalysis:** This class implements the procedure for updating saturations of the different phase at one time step, by solving  $\mathcal{A}_{h\mathcal{N}}$ .

**TRMSegregatedAnalysis:** This class implements the nested sequential method (NSM) (see Chapter 6).

**TRMBuildTransfers:** This class implements the information transfer required for the NSM method (see chapter 6).

**TRMOchestra:** This class implements the creation of the analysis objects and manages the interaction between the different analyses processes, time step control and reporting times for postprocessing purposes. It execute the initial static problem and the evolutionary problem. The main purposes of this class is the execution of the simulation with the given directives defined by **TRMSimulationData** class.

## 7.2 Numerical verification

In this section, different physical situations are introduced in a 2D context, where different problems that arise from certain simplifications are solved. These physical configurations have the objective of verifying the consistent approximation of the operators  $\mathcal{A}_{eN}$ ,  $\mathcal{A}_{pN}$  y  $\mathcal{A}_{hN}$ , both separately and coupled by the nested sequential method NSM. Due to the amount of coding required for error calculation, in this section the verifications are restricted only to graphical comparisons and quantitative verifications. The calculation of convergence rates of the different problems is left as a future task.

### 7.2.1 Homogeneous pressure change of a poroelastic inclusion

An inclusion is defined as a sub domain  $\Omega_r$  in a domain  $\Omega_s$ , where a field of deformations referred as eigenstrains  $\boldsymbol{\epsilon}(\mathbf{x})$  (see Soltanzadeh2009; Mura2013) are given within  $\Omega_r$  and zero in  $\Omega_s - \Omega_r$ , this field of deformations can be treated as internal deformations, which could be caused by different mechanisms, including poroelasticity, elastoplasticity and thermal changes in a body not bounded by external forces or surface constraints. The elasticity modulus associated with of materials of  $\Omega_r$  and  $\Omega_s - \Omega_r$  are the same (i.e. there is no property contrast). The resulting domain is called the elastic matrix (the side burden rocks). In his acknowledged papers on this subject, Eshelby1957 showed that the problem of inclusion is equivalent to solving the equations of elasticity for a homogeneous body with a known distribution of force. For such bodies, the elasticity equations are solved using Green elastic functions (Soltanzadeh2009).

The Green's function of  $\mathbf{G}(\mathbf{x}, \mathbf{x}')$  returns the magnitude of the displacements in the direction  $\mathbf{x}_i$  in a point  $\mathbf{x}$ , when a unit force is applied in the direction  $\mathbf{x}_j$  at a point  $\mathbf{x}'$ . In an elastic medium under plane strain conditions within a halfspace. In the method of the Green's functions for the displacements  $\mathbf{u}$  and the stress  $\boldsymbol{\sigma}$ , due to the eigenstrains  $\boldsymbol{\epsilon}(\mathbf{x})$  are given as:

$$\mathbf{u} = \oint_{\Omega_r} C_{jlmn} \boldsymbol{\epsilon}_{mn}^*(\mathbf{x}') \mathbf{G}_{ij,l}(\mathbf{x} - \mathbf{x}') d\mathbf{x}' \quad (7.1)$$

$$\boldsymbol{\epsilon} = -\frac{1}{2} \oint_{\Omega_r} C_{jlmn} \boldsymbol{\epsilon}_{mn}^*(\mathbf{x}') \{ \mathbf{G}_{ik,lj}(\mathbf{x} - \mathbf{x}') + \mathbf{G}_{jk,li}(\mathbf{x} - \mathbf{x}') \} d\mathbf{x}' \quad (7.2)$$

$$\boldsymbol{\sigma} = -C_{ijkl} \oint_{\Omega_r} C_{pqmn} \boldsymbol{\epsilon}_{mn}^*(\mathbf{x}') \mathbf{G}_{kp,ql}(\mathbf{x} - \mathbf{x}') d\mathbf{x}' + \boldsymbol{\epsilon}_{kl}^*(\mathbf{x}') \quad (7.3)$$

where  $\boldsymbol{\epsilon}^*(\mathbf{x}) = 0$  for  $\mathbf{x} \in \Omega_s - \Omega_r$ , and  $C_{ijkl} = \lambda\delta_{ij}\delta_{kl} + 2\mu(\delta_{ik}\delta_{jl} + \delta_{il}\delta_{jk})$ .

Some quantities must be continuous in the boundary interface  $\partial\Omega_r$ , in this case the displacements and the normal stresses between  $\Omega_r$  and  $\Omega_s - \Omega_r$  must be continuous, as follows:

$$\delta\mathbf{u}|_{\partial\Omega_r} = \mathbf{u}_{out} - \mathbf{u}_{in} = 0 \quad (7.4)$$

$$\delta\boldsymbol{\sigma}|_{\partial\Omega_r} \cdot \mathbf{n} = \{\boldsymbol{\sigma}_{out} - \boldsymbol{\sigma}_{in}\} \cdot \mathbf{n} = 0 \quad (7.5)$$

Eshelby showed that, for an ellipsoidal inclusion within a complete space, the deformations and stresses are uniform for all interior points. In the case of expansion eigenstrain, in other words those referred by the tendency of inclusion to expand or contract isotropically, as in the case of poroelasticity or thermoelasticity, i.e.  $\boldsymbol{\epsilon}^*(\mathbf{x}) = \boldsymbol{\epsilon}^C(\mathbf{x})I$ , so the equations 7.1, 7.2 and 7.3 are reduced to:

$$\mathbf{u} = -(2\mu + 3\lambda) \oint_{\Omega_r} \boldsymbol{\epsilon}^C(\mathbf{x}) \mathbf{G}_{ij,l}^D(\mathbf{x} - \mathbf{x}') d\mathbf{x}' \quad (7.6)$$

$$\boldsymbol{\epsilon} = -\frac{1}{2}(2\mu + 3\lambda) \oint_{\Omega_r} \boldsymbol{\epsilon}^C(\mathbf{x}') \left\{ \mathbf{G}_{ik,lj}(\mathbf{x} - \mathbf{x}') + \mathbf{G}_{jk,li}(\mathbf{x} - \mathbf{x}') \right\} d\mathbf{x}' \quad (7.7)$$

$$\boldsymbol{\sigma} = -(2\mu + 3\lambda) \oint_{\Omega_r} \boldsymbol{\epsilon}^C(\mathbf{x}') \mathbf{G}_{ij}^S(\mathbf{x}, \mathbf{x}') d\mathbf{x}' + \boldsymbol{\sigma}^*(\mathbf{x}') \quad (7.8)$$

where  $\boldsymbol{\sigma}^*(\mathbf{x}') = (2\mu + 3\lambda)\delta_{ij}\boldsymbol{\epsilon}^C(\mathbf{x})$ , is the eigenstress at the point  $\mathbf{x}$ ,  $\mathbf{G}_i^D(\mathbf{x} - \mathbf{x}') = \mathbf{G}_{ij,l}(\mathbf{x} - \mathbf{x}')$  and  $\mathbf{G}_{ij}^S(\mathbf{x}, \mathbf{x}') = \mu \left\{ \mathbf{G}_{ip,pj}(\mathbf{x} - \mathbf{x}') + \mathbf{G}_{jp,pi}(\mathbf{x} - \mathbf{x}') + \lambda\mathbf{G}_{kp,pk}(\mathbf{x} - \mathbf{x}') \right\} \delta_{ij}$  respectively are the functions of influence by dilation (**Segall1985; Soltanzadeh2009**).

With all the above, it is possible to consider a reservoir as a poroelastic inclusion when there is no contrast between the mechanical properties of the rocks, and the eigenstrains are defined by dilatational deformations that could be caused by changes in the pore pressure  $\delta p$  temperature  $\delta T$  inside the reservoir. The values of dilatation deformation by change of pore pressure are:

$$\boldsymbol{\epsilon}^C(\mathbf{x})I = \frac{1}{3} \left( \frac{\alpha\delta p(\mathbf{x})}{K_{dr}} \right) = \frac{\alpha\delta p(\mathbf{x})}{(2\mu + 3\lambda)} \quad (7.9)$$

The treatment of a reservoir as a poroelastic inclusion requires the consideration that there is no change in the pore pressure in the burial rocks implying that there is no flows from aquifers, there is no heat transfer and completely drained conditions occur (long times of production). The integral kernel derived from the theory of inclusions allows to compute the stress state for any closed geometry in two dimensions.

**Remark:** The link between the equations 7.1, 7.2 and 7.3 and the reduction strategy of the Chapter 3, becomes evident when considering a reservoir as a poroelastic inclusion under the definitions given by 7.9, where  $\delta p(\mathbf{x})$  comes from any kind of analytical or numerical source. In this research, the strains are approximated by a continuous function space, that strongly satisfies 7.4 by the construction of the space associated with the strong statement, and weakly 7.5 when considering the weak formulation.

Based on the above, we introduce the following physical problem in which we seek to obtain the evolution of the poromechanic response, pressure, velocity, and the saturation fields. The physical configuration consists of a rectangular reservoir embedded in a purely elastic matrix, this reservoir is drained by a well in the center, and has pressure maintenance provided by two injector wells on the flanks. The Figure 7.4, shows the physical configuration and the boundary conditions.

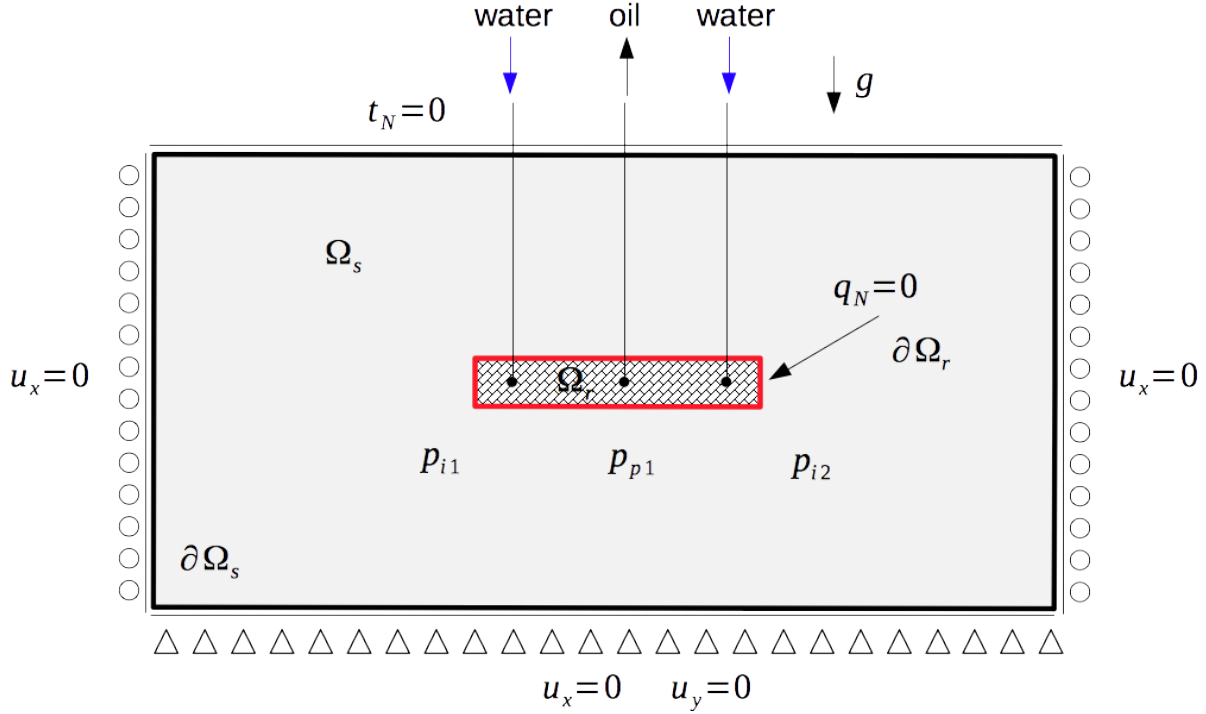


Figure 7.4: Physical setting of an oil-water reservoir under injection and side burden boundary conditions.

For the verification of the elliptical operator the modified  $\mathcal{A}_{e\mathcal{N}}$  is invoked as follows:

$$\mathcal{A}_{e\mathcal{N}} = \left\{ a_u(\mathbf{u}_\mathcal{N}, \boldsymbol{\phi}_u) - b_u(p_c, \boldsymbol{\phi}_u) + c_u(s_{wc}, \boldsymbol{\phi}_u) - f_u(\boldsymbol{\phi}_u) = 0 \right. \quad (7.10)$$

where  $p_c$  and  $s_{wc}$  are given fields of pressure and constant saturation in relation to an initial state, satisfying  $\delta p = c$  and  $\delta s_w = 0$ .

By means of the decoupled operator 7.10 it is possible to approximate the inclusion theory of the mechanical response by applying a homogeneous pressure change  $\delta p = p_c - p^0$ .

## Offline split

The table 7.1 and the figure 7.5 show the data and the partition, respectively, which are used for the generation of the reduced bases. In the case of six global basis functions ( $\mathcal{M} = 6$ ), two functions are shown in figure 7.6, after applying the process of selection of constant pressures (see Chapter 3).

Property	Value
Side burden dimensions	$L_x = 20000$ [m] $L_y = 10000$ [m]
Reservoir dimensions	$L_x = 1000$ [m] $L_y = 100$ [m]
Pressure	$\delta p = 20$ [MPa]
Saturations	$s_w = 1$
First lamé	$\lambda = 2.30769$ [GPa]
Second lamé	$\mu = 1.53846$ [GPa]

Table 7.1: Input data for the homogeneous pressure change problem.

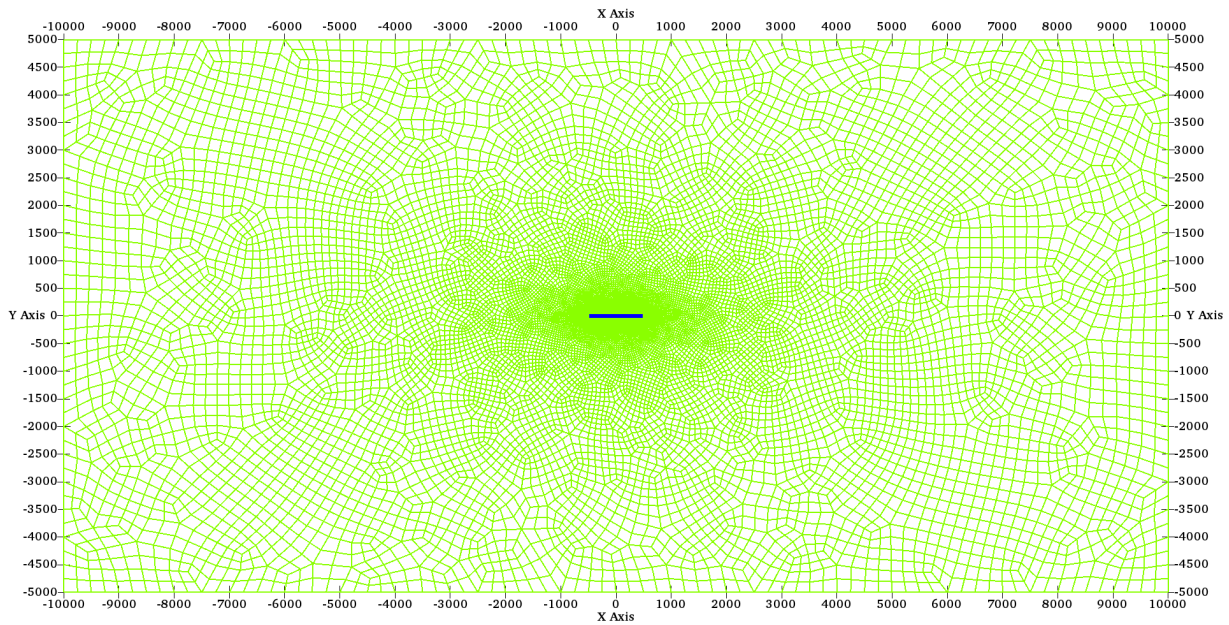


Figure 7.5: Geometric partition  $\Gamma_h$ . The blue region represent the rectangular reservoir.

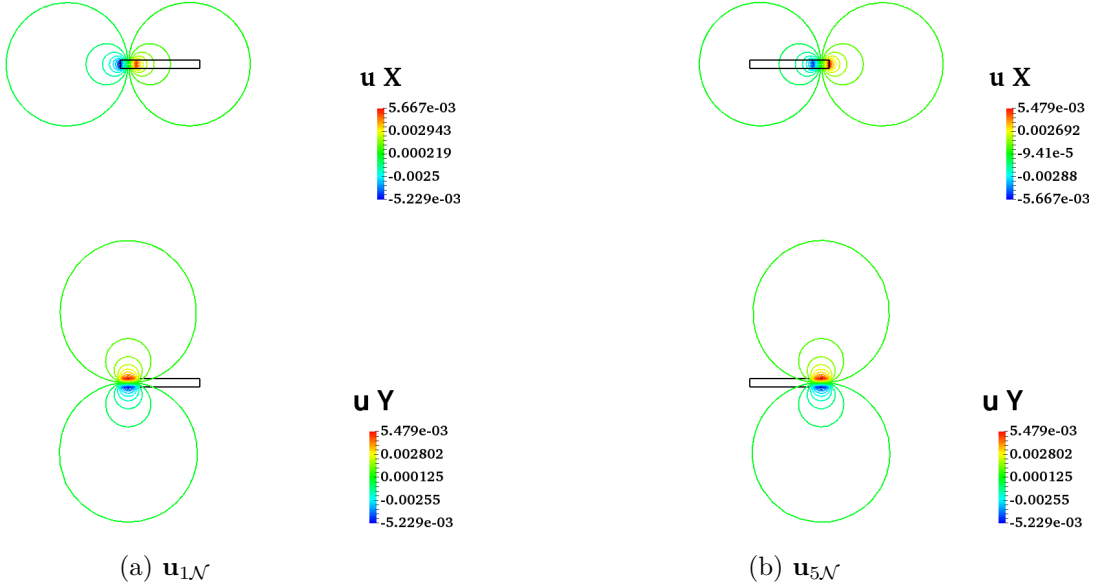


Figure 7.6: Sample of two RB functions for the case of  $\mathcal{M} = 6$ .

The functions rendered in figure 7.6, show the effect on the displacements of a homogeneous pressure change, applied inside a part of the reservoir. Note that the area influenced by the local pressure increase is bigger than the reservoir area. Its support extends into the area of the side burden rocks.

## Online split

In the figure 7.7 the solution of the displacements generated by a homogenous pressure change is shown and compared to the approximations of the solution of **Segall1985**

From the construction the reduced basis (RB) approximation it is evident that any number of basis functions  $\mathcal{M} \neq 0$  will correctly represent the constant pressure field. In order to verify this property two configurations with  $\mathcal{M} = \{6, 21\}$  are tested. They are shown in the figure 7.7, corroborating the correct implementation. The RB approximations substitute the full-order operator  $\mathcal{N} = 282358$  by a substantial reduction of the size of the approximation space. The shape functions generated by  $\mathcal{M} = \{6, 21\}$  are global functions that are combined in the sense of the operator  $\mathcal{A}_{e\mathcal{M}}$ .

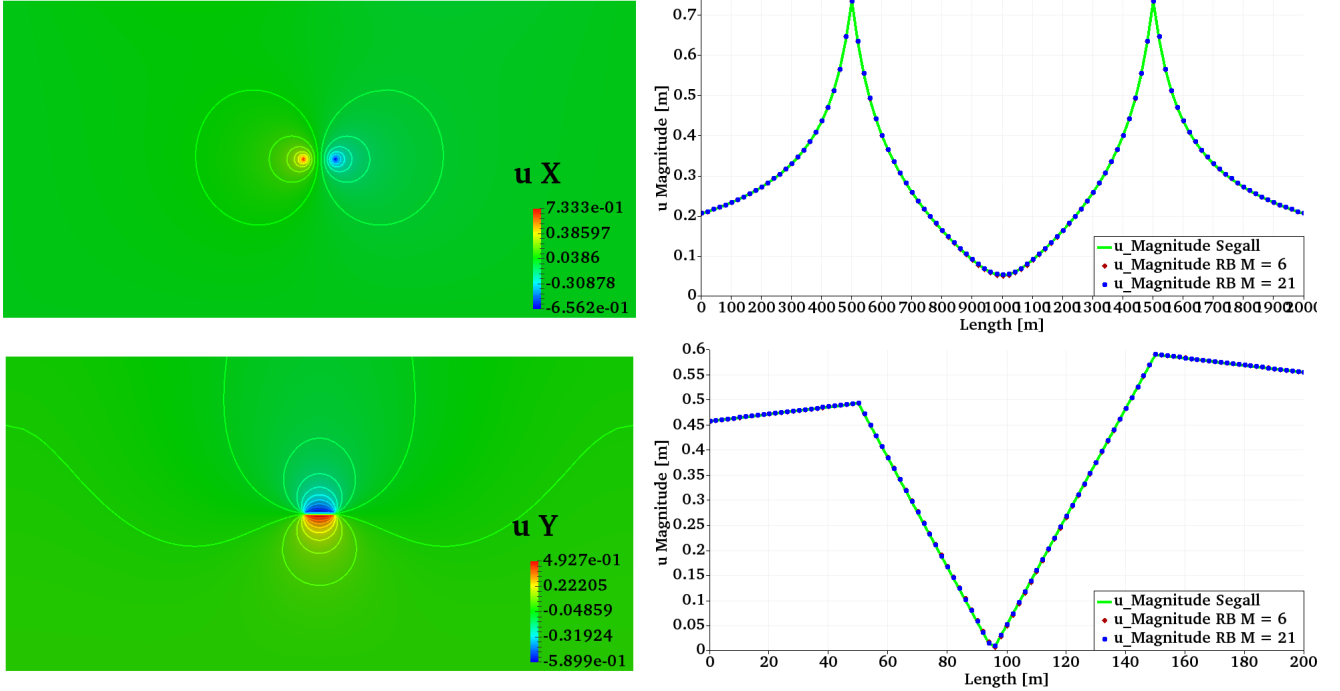


Figure 7.7: Contours and plots for RB approximation of the homogeneous pressure change. Top left shows contours of  $u_x$  for  $\mathcal{M} = 21$ . Bottom left shows contours of  $u_y$  for  $\mathcal{M} = 21$ . Top right shows plots over line  $\{\{-1000, 0\}, \{1000, 0\}\}$  of  $\|\mathbf{u}\|$  for  $\mathcal{M} = \{6, 21\}$  and **Segall1985** solution. Bottom right shows plots over line  $\{\{0, -100\}, \{0, 100\}\}$  of  $\|\mathbf{u}\|$  for  $\mathcal{M} = \{6, 21\}$  and **Segall1985** solution (Green line).

### 7.2.2 Single phase water injection

The objective of this section is to verify approximation operator  $\mathcal{A}_{p\mathcal{N}}$  by the technique MHM- $H(\text{div})$ , where the dependence of saturation transport on displacement is eliminated as follows:

$$\mathcal{A}_{p\mathcal{N}} = \begin{cases} a_q(\mathbf{q}_\mathcal{N}, p_\mathcal{N}, \phi_q) - b_q(p_\mathcal{N}, \phi_q) - c_q(p_\mathcal{N}, \phi_q) + f_q(\phi_q) = 0 \\ -b_p(\mathbf{q}_\mathcal{N}, \phi_p) - c_p(p_\mathcal{N}, \phi_p) = 0 \end{cases} \quad (7.11)$$

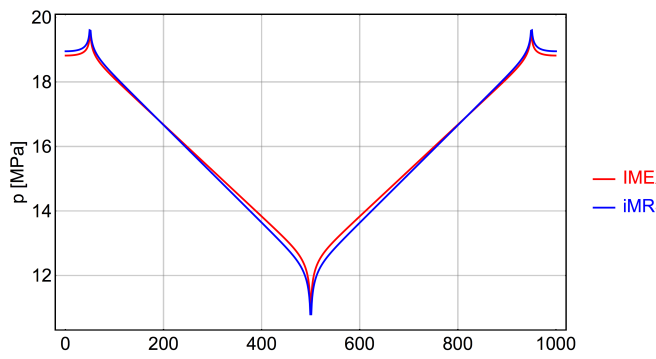
In this subsection the side burden domain is not considered. The aim is to verify the multiscale approximation in a steady state problem. The geometry is documented in Figure 7.4, and is represented by: the reservoir outlined in red; a producing well and two injectors with radius  $r_w$ ; and impervious boundaries. In order to compare with a reference, the same case is configured in the IMEX reservoir simulator, obtaining the pressure profiles of the figure 7.8. In the IMEX configuration a cartesian mesh of resolution  $ni = 1001$ ,  $nj = 101$  was used.

The difference between the profiles is due to the type of numerical scheme used by the simulators. The mixed approximation of iMRS has better convergence properties (the curves show a great similarity). The Dirichlet data of the prescribed pressure in the wells are reproduced,

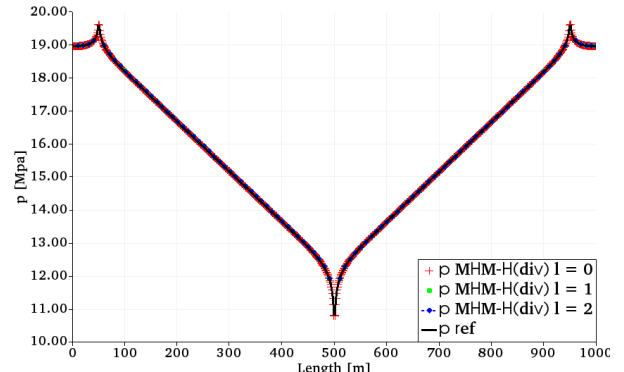
Property	Value
Reservoir dimensions	$L_x = 1000 \text{ [m]}$ $L_y = 100 \text{ [m]}$
Well radius	$r_w = 0.2 \text{ [m]}$
Production pressure	$p_p = 10 \text{ [MPa]}$
Injection pressure	$p_i = 20 \text{ [MPa]}$
Fluid viscosity	$\eta_f = 0.001 \text{ [Pa s]}$
Fluid density	$\rho_f = 1000 \text{ [kg m}^{-3}\text{]}$
Permeability	$\mathbf{K} = 1.0 \times 10^{-13} \mathbf{I} \text{ [m}^2\text{]}$
Relative permeabilities	$k_{rw} = s_w \text{ and } k_{rtracer} = 1 - s_w$
Porosity	$\phi = 0.25$

Table 7.2: Input data for the homogeneous pressure change problem.

and the logarithmic variation is properly captured. The simulation of iRMS represented by the blue curve is verified quantitatively and will be used as the reference for the following multiscale approximations.



(a) IMEX and iMRS pressure approximations.



(b) MHM- $H$  ( $\text{div}$ ) pressure approximations.

Figure 7.8: Approximation of reservoir pressure by iMRS and IMEX. The pressure profiles are rendered over the line  $\{-500, 0\}, \{500, 0\}$ .

From the skeleton mesh shown in the figure 7.9, the full order problem is approximated with MHM- $H$  ( $\text{div}$ ) meshes at levels  $l = \{0, 1, 2, 3\}$ , where  $l = 3$  represents the reference operator used for the approximation of the figure 7.8. The table 7.3 shows, the size of the linear equation system associated with each iMRS configuration. The figure 7.8b shows the different approximations of the full order operator showing a correct concordance. In terms of the linear condensed system, the multiscale approach uses very few degree of freedom, and consequently has much lower memory usage. It should be emphasized that the logarithmic variation of the pressure near the wells is captured even by the coarser level  $l = 0$  of the multiscale process.

Setting	DoF
$\mathcal{N}$	225152
$\mathcal{N}_0$	1348
$\mathcal{N}_1$	4740
$\mathcal{N}_2$	8740
$\mathcal{N}_3$	18532

Table 7.3: Condensed linear system of equations after MHM- $H$  ( $div$ ).

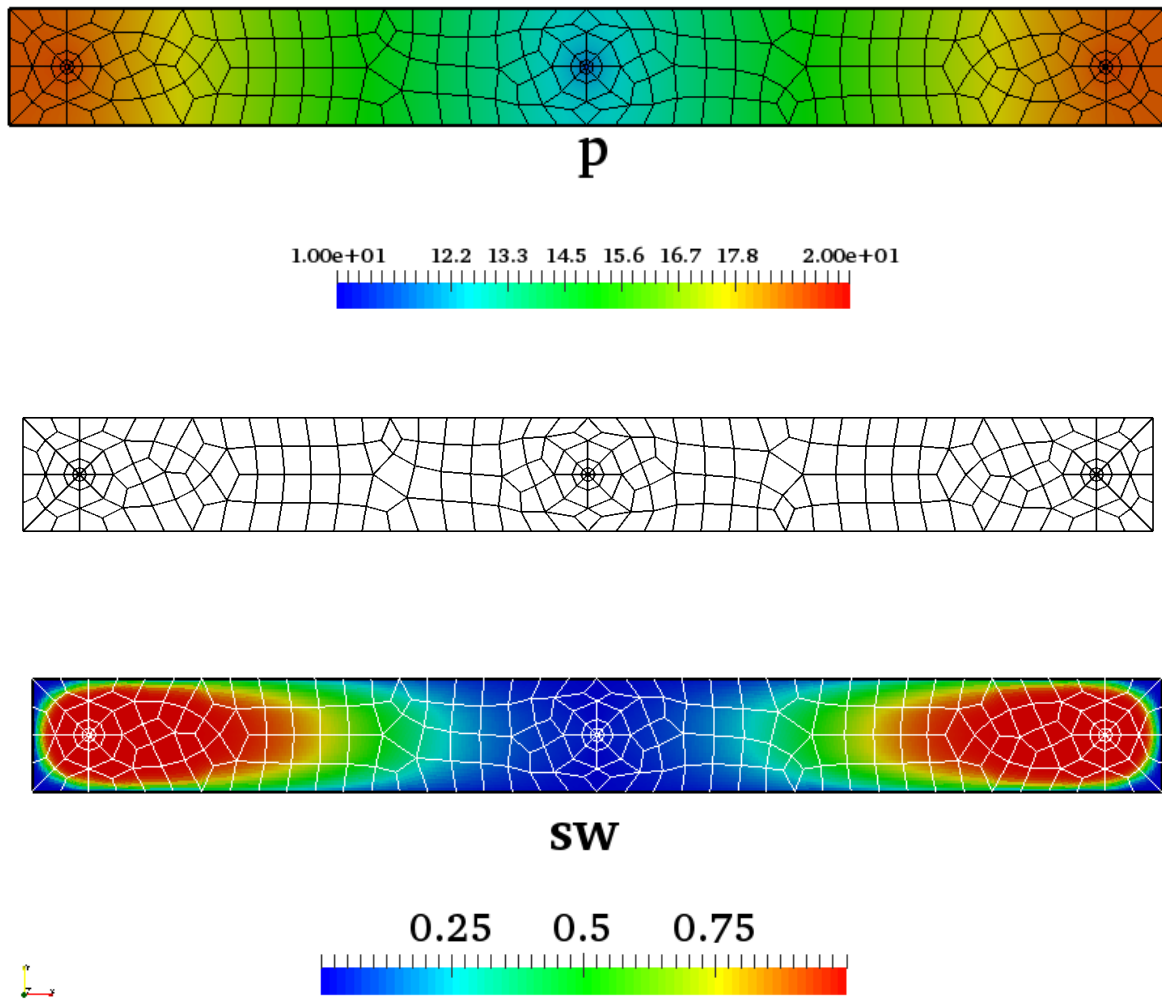


Figure 7.9: MHM- $H$  ( $div$ ) partition mesh with  $l = 0$ . Color maps of pressure and saturations at  $t = 500$  [d].

## Heterogeneous field

In this verification a field of heterogeneous permeabilities and porosities is introduced, described in section 7.1.2 and shown in the figure 7.10. This field must be properly captured, leaving the size of the micro elements as small as necessary to capture the variation of the property map. This process is shown in the figure 7.11, where a sequence of refinements on the micro elements are carried out, until they are small enough to completely capture the variation of properties. In Figure 7.11, an plot overline is shown, comparing the map transferred in refinements with level two and three, showing that level three is fine enough to capture the scale of the map, and the upscaling process is avoided since, upscaling and downscaling operators are naturally incorporated by the multiscale process described in chapter 4.

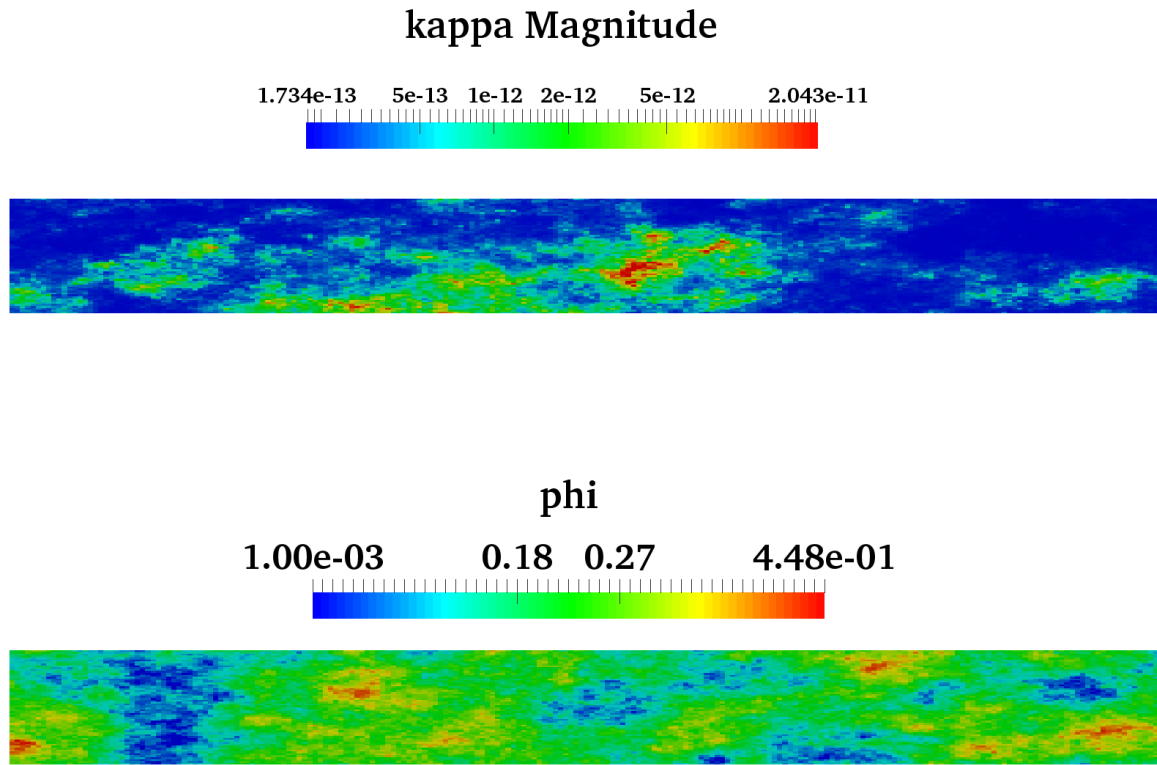
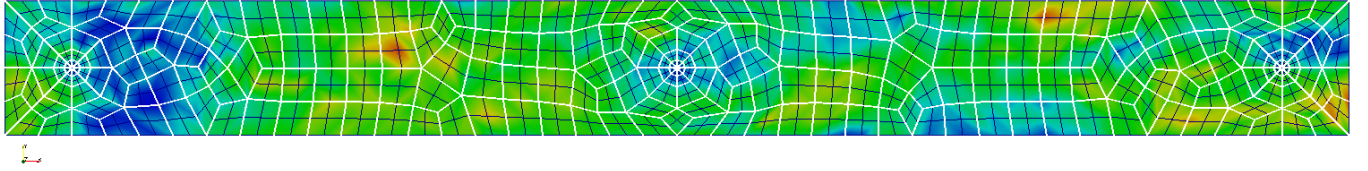
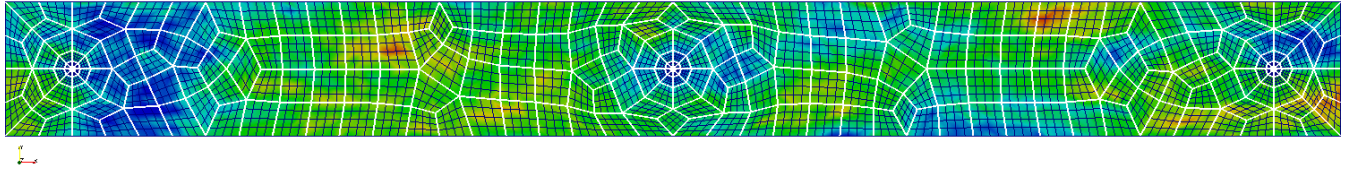


Figure 7.10: Natural logarithm of a field of permeability and 2D porosity, this field was extracted from the top layer of the 3D model of the SPE 10. The variance of log-permeability is  $\sigma_{\ln k}^2 = 5.49$ , which corresponds to a coefficient of variation  $CV = 2.97$ .

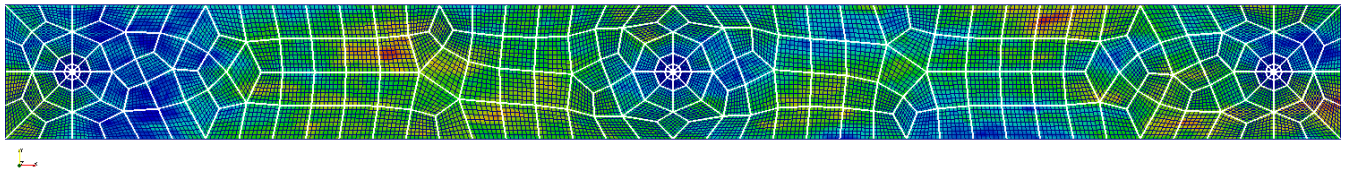
Micro elements at refinement level 1



Micro elements at refinement level 2



Micro elements at refinement level 3



Porosity from SPE data

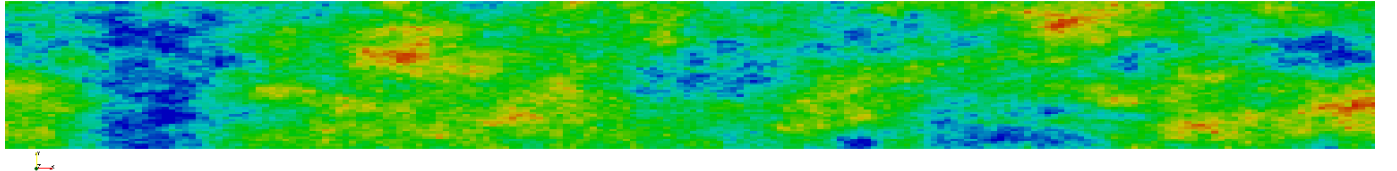


Figure 7.11: Examples of porosity transferred to MHM- $H$  ( $\text{div}$ ) meshes at three different levels. The white wire frame represents the skeleton mesh. Properties transmitted with the algorithm 7.1.

**Remark 1:** The figure 7.11 emphasizes that the multiscale method can be configured to capture the fine level of the properties of interest. Through the mesh adaptation in the wellbore regions, more degrees of freedom are concentrated and dedicated to capture the smaller scales, including those that come from the realization of a geological properties model.

**Remark 2:** The skeleton meshes used in this example are non-structured meshes, demonstrating the capability to very complex geometries.

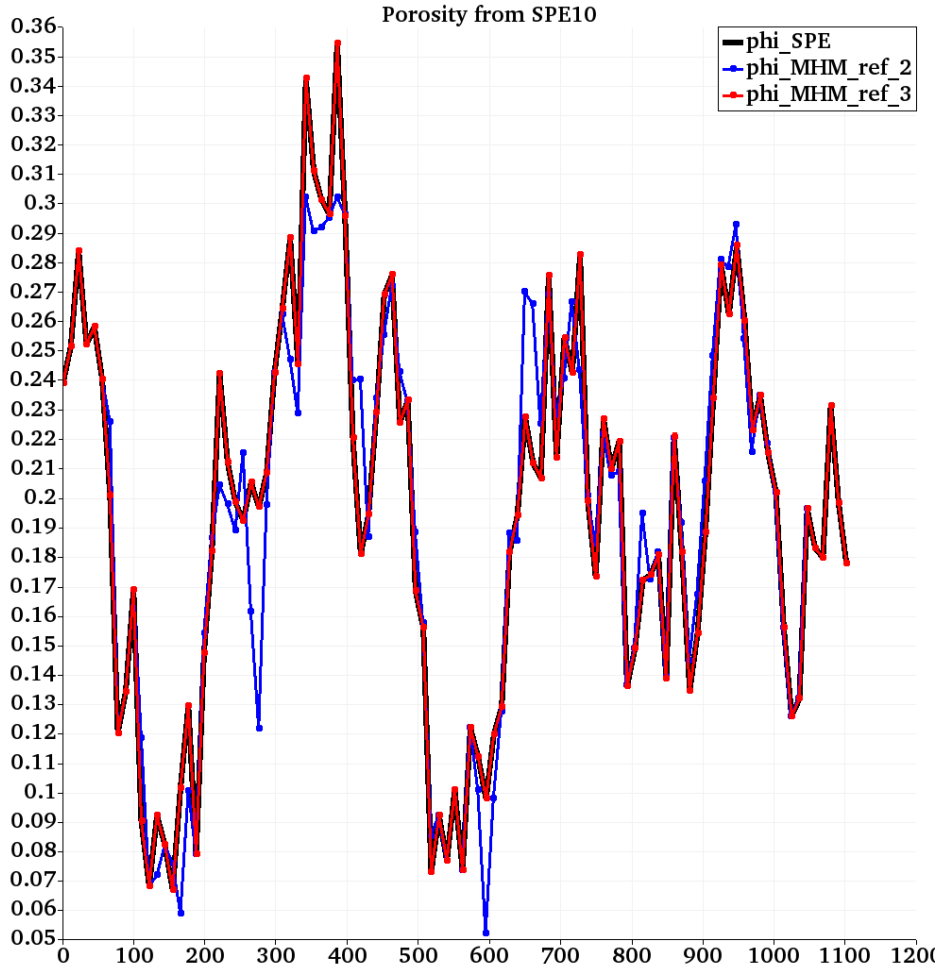


Figure 7.12: Plot over line  $l = \{\{-500, 0\}, \{500, 0\}\}$  of porosity transferred to the MHM- $H$  ( $\text{div}$ ) meshes at level 2 and 3. The black line represents the SPE porosity.

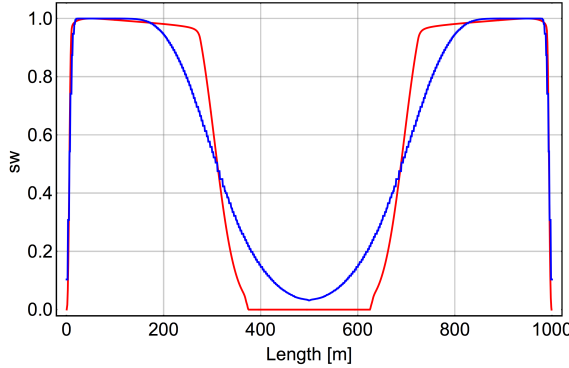
### 7.2.3 Injection of a passive tracer

In this section, a version of the operator  $\mathcal{A}_{h\mathcal{N}}$  is used, decoupled from the displacements and pressure. The velocity  $\mathbf{q}_{\mathcal{N}_l}$  is a given and is the solution from the multiscale approximations of the previous section in different levels of coarse resolution  $l$ , as follows:

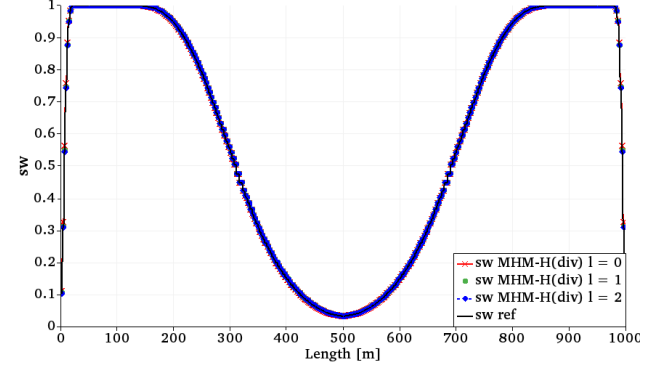
$$\mathcal{A}_{h\mathcal{N}} = \left\{ d_s(\mathbf{q}_{\mathcal{N}_l}, s_{\mathcal{N}}, 1) + d_q(\mathbf{q}_{\mathcal{N}_l}, 1) + d_p(s_{\mathcal{N}}, 1) = 0 \right. \quad (7.12)$$

It is important to note that for this configuration, the physical setting corresponds to an incompressible fluid and an passive tracer corresponding to phases with linear relative permeabilities, as shown in the table 7.2. The approximate solution of equation 7.12 uses velocities from the mixed multiscale scheme. The solutions present little difference between the multilevel approximation, and the finer level or reference level (see figure 7.13b). The calculated velocity of the multilevel approximation possess the same local conservation properties as the mixed global operator. The

figure 7.13a compares the IMEX solution with the iMRS solution, in which it is observed that due to the purely implicit nature of the iMRS scheme, the saturation profile is more diffusive when compared to the IMEX profile saturations. This does not invalidate the results, but it does motivate the incorporation of less diffusive schemes in the transport, which is left for future work.



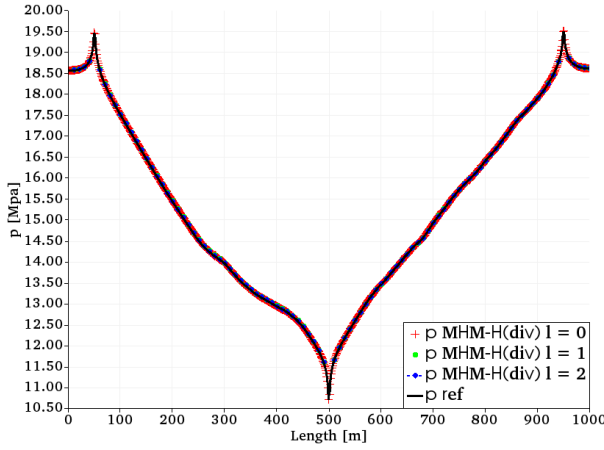
(a) IMEX and iMRS saturation approximations.



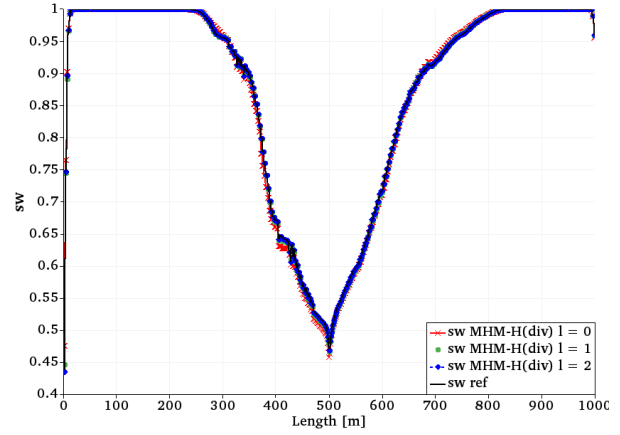
(b) MHM-H (*div*) saturations approximations at  $t = 500$  [d].

Figure 7.13: Approximation of reservoir pressure by iMRS and IMEX. The pressure profiles are rendered over the line  $\{(-500, 0), (500, 0)\}$ .

## Heterogeneous field



(a) MHM-H (*div*) pressure approximations.



(b) MHM-H (*div*) saturations approximations at  $t = 500$  [d].

Figure 7.14: Approximation of reservoir pressure and saturations with SPE10 properties. The profiles are rendered over the line  $\{(-500, 0), (500, 0)\}$ .

The figures 7.14a and 7.14b show that the coarser approximation with  $l = 0, 1$  manages to capture the effects of the finer scales without compromising the solution of the transport problem.

Another point to note is that through the separation of  $\Omega_{wr}$  and  $\Omega_r$  is used to capture the effects of small scales, in the regions near the wellbore where the pressure gradients tends to be higher (See figure 7.15). The figure 7.16 as well as the velocity in the reservoir domain can be well approximated at level  $l = 0$ . Through these examples it is possible to affirm that the implementation of the separated operators is consistent and verified.

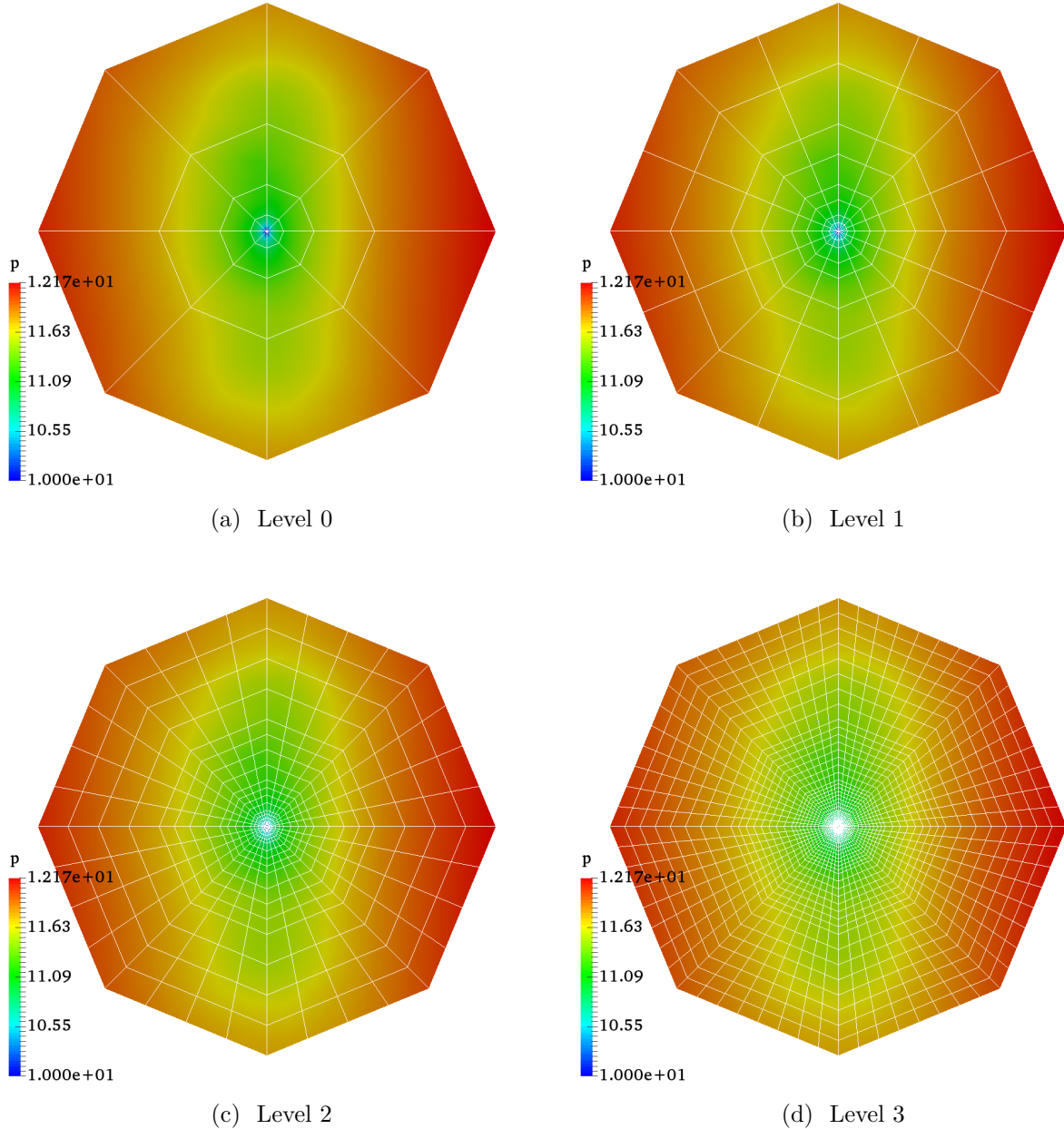


Figure 7.15: MHM- $H$  ( $div$ ) wellbore pressure approximations with SPE10 properties.

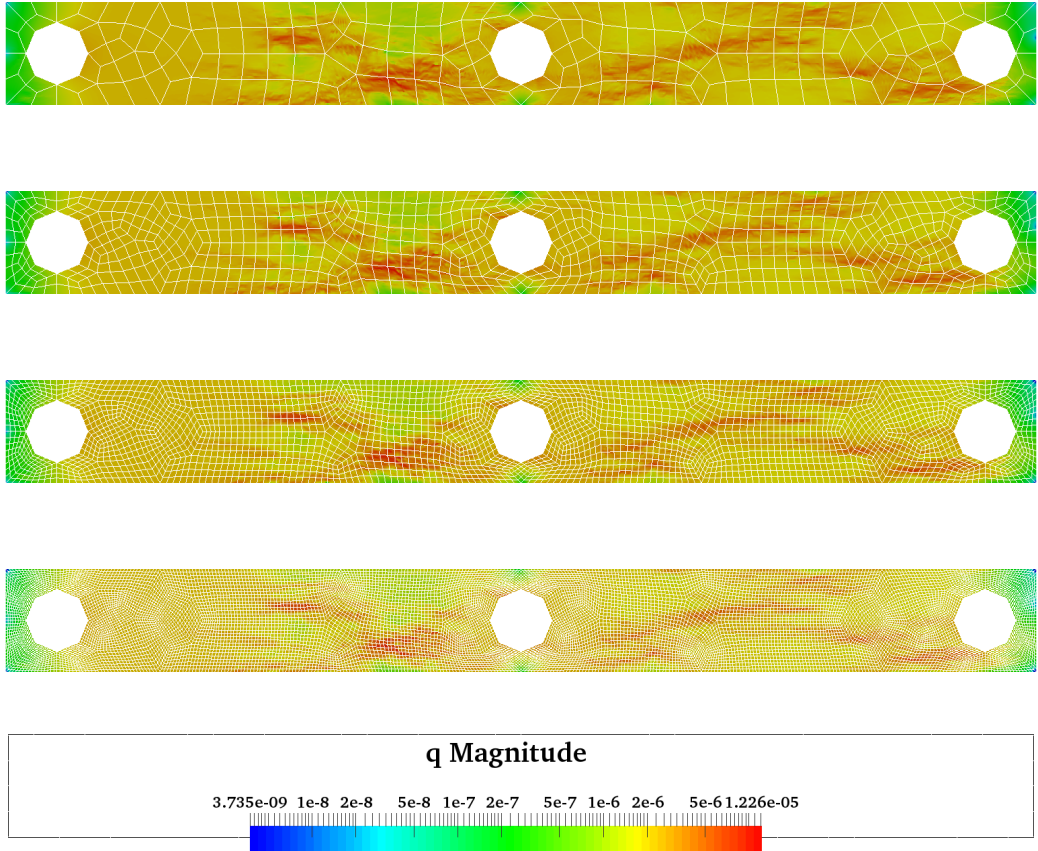


Figure 7.16: MHM- $H$  ( $\text{div}$ ) velocity on reservoir domain  $\Omega_r$ . Approximations with SPE10 properties.

#### 7.2.4 Water injection in an oil-water system

In this section the injection of water into a reservoir completely saturated with oil is verified, using the geomechanical configuration represented by figure 7.4, in conjunction with the data of the table 7.4, and the mechanical properties of the table 7.1.

In this case, to verify the consistency of the presented results, the same physical situation is simulated with the CMG STARS geomechanical simulator. The results are presented in comparative curves for two cases, one with linear relative permeabilities and the other with quadratic relative permeabilities, in order to show the consistency in the sequential scheme with nonlinearities. The figure 7.17 shows the type of refinement. The keywords used for the mesh generation and the definition of both, geomechanical and reservoir domain are presented as follows:

Property	Value
Reservoir dimensions	$L_x = 1000 \text{ [m]}$ $L_y = 50 \text{ [m]}$
Well radius	$r_w = 0.2 \text{ [m]}$
Production pressure	$p_p = 10 \text{ [MPa]}$
Injection pressure	$p_i = 20 \text{ [MPa]}$
Water viscosity	$\eta_w = 0.001 \text{ [Pa s]}$
Oil viscosity	$\eta_o = 0.005 \text{ [Pa s]}$
Water density incompressible	$\rho_w = 1000 \text{ [kg m}^{-3}]$
Oil density	$\rho_{o std} = 800 \text{ [kg m}^{-3}]$
Oil compressibility	$c_o = 1.45037 \times 10^{-9}$
Permeability	$\mathbf{K} = 1.0 \times 10^{-13} \mathbf{I} \text{ [m}^2]$
Linear relative permeabilities	$kr_w = s_w \text{ and } kr_o = 1 - s_w$
Quadratic relative permeabilities	$kr_w = s_w^2 \text{ and } kr_o = (1 - s_w)^2$
Time step	$\Delta t = 10 \text{ [d]}$
Number of reduced functions	$\mathcal{M} = 101$
MHM- $H$ ( $div$ ) level	$l = 0$
Initial porosity	$\phi^0 = 0.25$
Initial saturation	$s_w = 0.0$
Initial pressure	from undrained response

Table 7.4: Input data for the two phase no homogeneous pressure change problem.

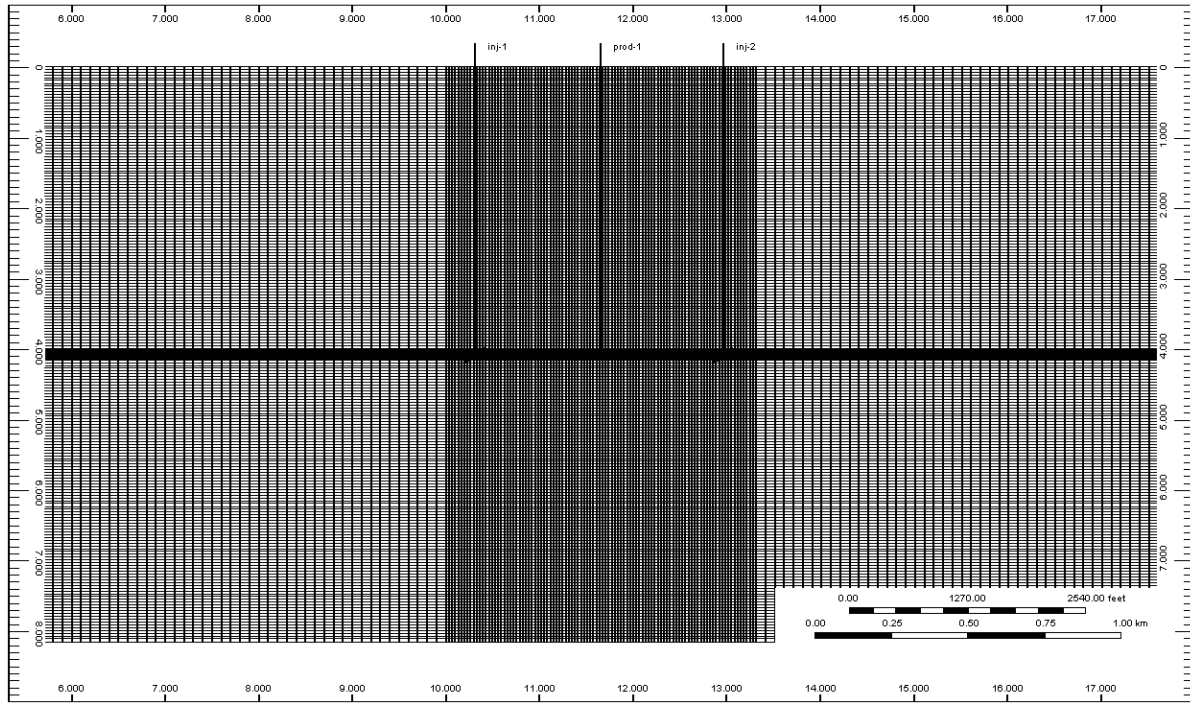


Figure 7.17: . Partition used in the STARS simulations.

```

*GRID *CART 1 301 221
*KDIR DOWN
*DI *IVAR 1*1.0
*DJ *JVAR 100*100.0 101*32.8084 100*100.0
*DK *KVAR 100*40.0 21*7.8095 100*40.0
*FLUIDHEAT *CON 0
*MOD 1 101:201 101:121 = 1

```

#### Case with linear relative permeabilities:

The figure 7.18 shows a plot over line  $l = \{\{-500, 0\}, \{500, 0\}\}$ , which represents the center of the reservoir. In relation to the pressure plot, it shows good agreement in the pressure field of the two simulators in reproducing the v form of the profile, limited by the conditions of the Dirichlet data in the wells. In relation to the saturation plot, a concordance in the effect of the viscosity ratio is shown, which is known as an unstable displacement, where the water breaks in the producer quickly, in relation to the case with viscosities ratio as  $\frac{\eta_o}{\eta_w} \approx 1$ . In relation to the displacements plots, they show good agreement in the center of the reservoir.

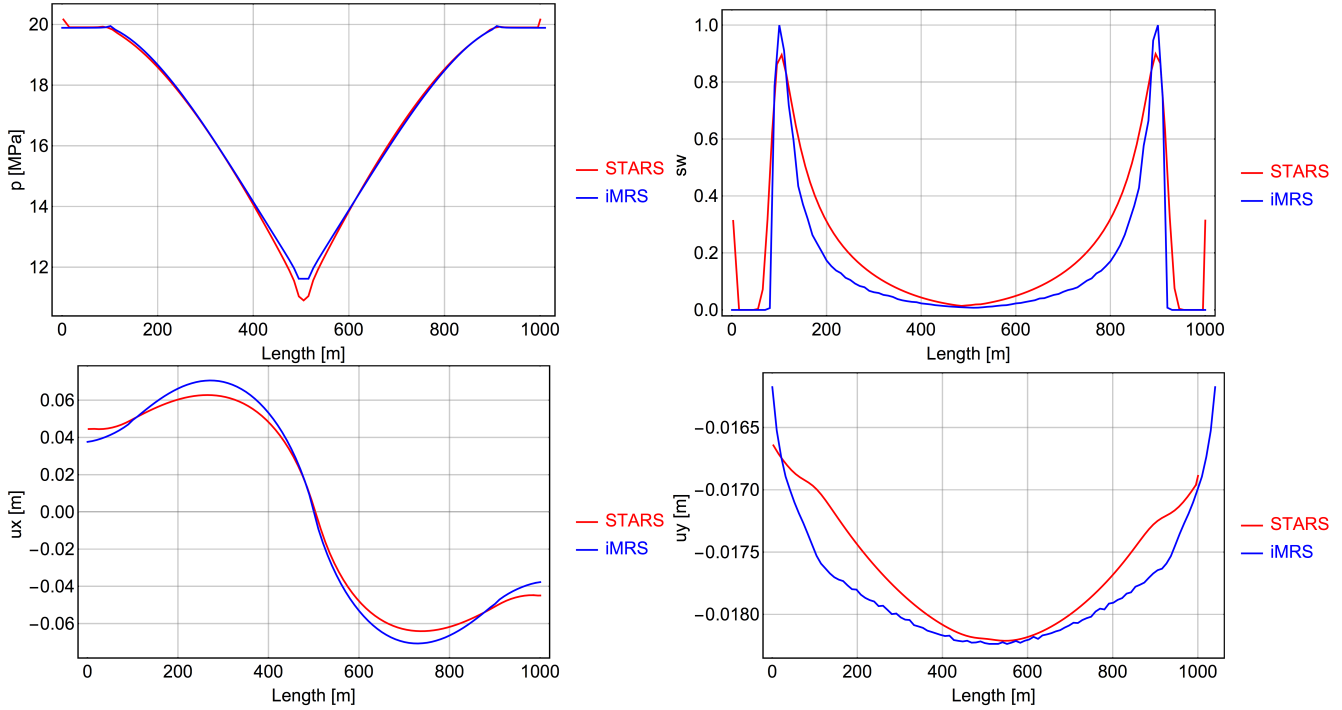


Figure 7.18: Comparison of variables  $(\mathbf{u}_M, p_{Ni}, s_{wN})$  at  $t = 250$  [d], the plot is rendered over the line  $l = \{(-500, 0), (500, 0)\}$ .

### Case with quadratic relative permeabilities:

The figure 7.19 shows the saturation and displacement color map  $u_x$  near the reservoir region. In relation to the constant pressure simulation shown in the figure 7.7, the contour of  $u_x$  ceases to have a circular form to have a shape that shows the effect of a non-homogeneous pressure distribution, induced by the conditions of pressure in the wells. The skeleton mesh associated with the multiscale approximation is shown in a white wire frame representation.

The figure 7.20 shows a plot over the line  $l = \{(-500, 0), (500, 0)\}$ , similar as the figure 7.18. The pressure plot shows the concordance of the pressure of the two simulators in reproducing the v form, but with a slight deformation due to the effect of quadratic relative permeability. In relation to the saturations, the effect of the quadratic relative permeability is clearly shown. It makes the water take longer to break into the producer well. The displacements shows good agreement between two simulators, and similarly to the pressure, it also presents a slight perturbation due the quadratic relative permeability. The quadratic relative permeabilities influences the transmisibilities, or in other words, the term  $(\mathbf{K}\lambda(p, s_w))^{-1}$  in the mixed formulation.

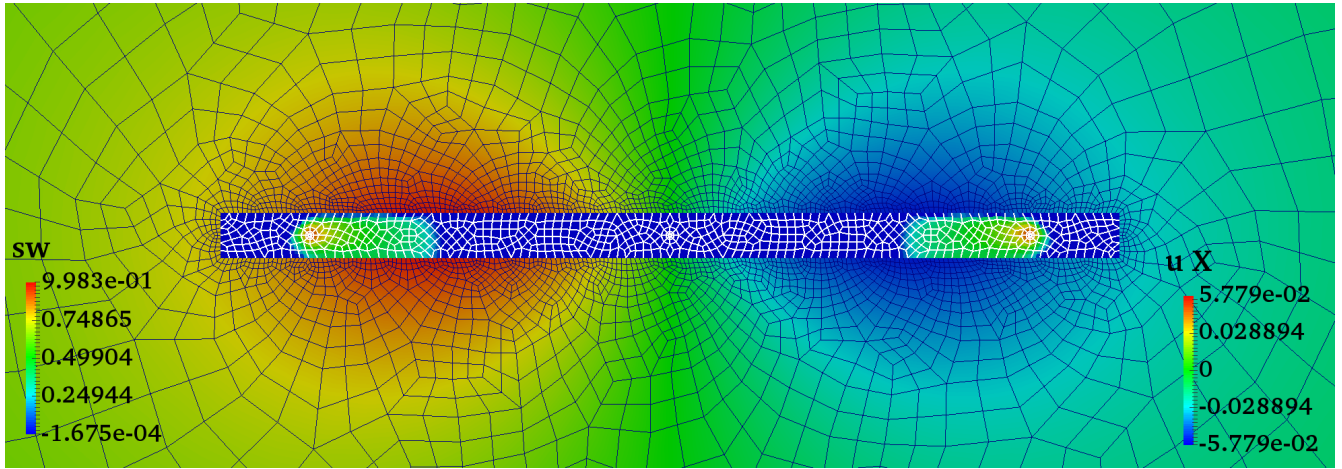


Figure 7.19: Color maps of variables  $\mathbf{u}_{x\mathcal{M}}, s_{w\mathcal{N}}$  at  $t = 250$  [d]. The black wire fram represents the multiscale mesh.

Figure 7.19, documents the superposition of domains to perform the multiphysical calculations, where the domain of the reservoir clearly overlaps the domain of the elastic matrix. This technology was developed inside the Neopz by **Farias2014** and is intensively used/tested here.

The saturation plot in figure 7.20 obtained by STARS is more diffusive because the STARS mesh is coarser than the iMRS mesh.

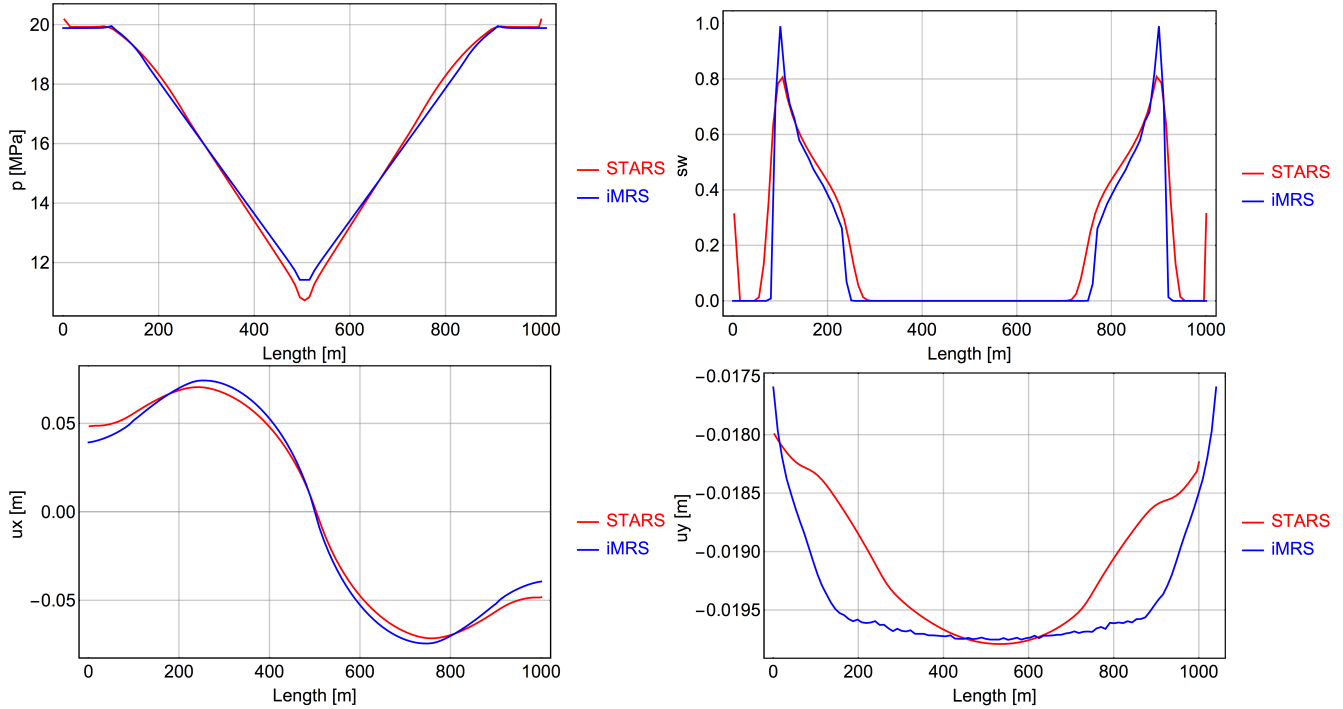


Figure 7.20: Comparison of variables  $(\mathbf{u}_{\mathcal{M}}, p_{\mathcal{N}_i}, s_{w\mathcal{N}})$  at  $t = 250$  [d], The plot is rendered over the line  $l = \{(-500, 0), (500, 0)\}$ .

In summary, the presented plots report the verification of the implementation of the technologies developed in this research: mixed formulations approximated by the MHM- $H(\text{div})$  multiscale method, base reductions and transport scheme. All of them are sequentially solved according as outlined in chapter 6. The differences between the obtained results and reference results are due to several reasons, starting from the type of mesh used, the type of discretization and the coupling scheme. The results represent the physical validity of the coupling of the elliptic, parabolic and hyperbolic operators.

## 7.3 Reservoir simulations

After verifying the approximations using 2D unstructured meshes, this section introduces a series of 3D simulations to show the capabilities of the simulator. It is important to emphasize that in relation to commercial software for reservoir simulation, the results shown here are not sophisticated in terms of the complexity of the constitutive models, but they contain the main components of most mathematical reservoir model. Through the results shown in this section the capability to treat problems with fairly complex geometries is demonstrated. Some of these geometries are difficult or impossible to deal with in commercial software, such as embedding a 3D well within a reservoir of arbitrary geometry with linear geometric description.

### 7.3.1 Injection of linear tracer in 3D reservoir

In this subsection the approximation of the passive tracer in a 3D setting is revisited with the objective to demonstrate the capabilities of the approximations in the 3D case.

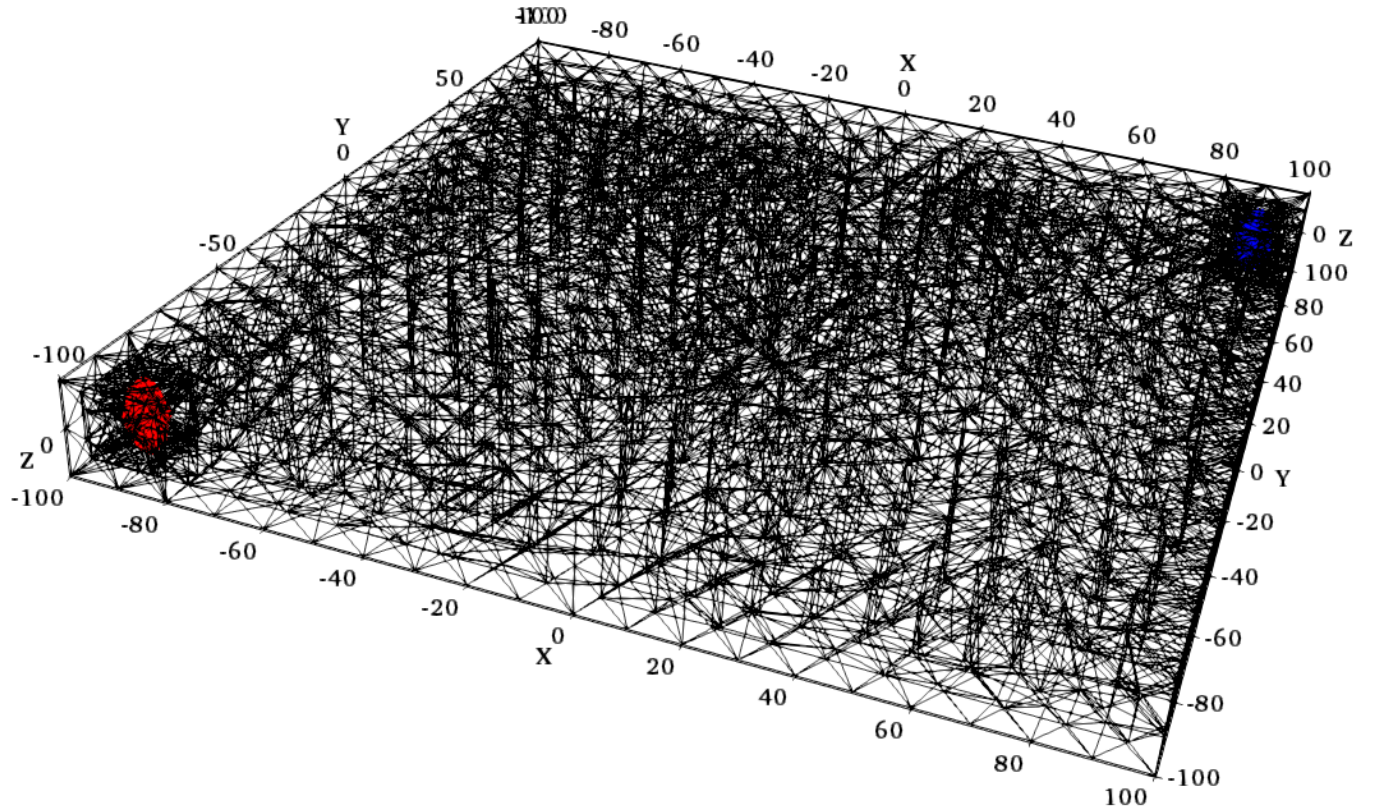


Figure 7.21: Partition of a rectangular 3D reservoir  $\Omega_r$ , ellipsoidal wellbore region  $\Omega_w$  and cylindrical wells  $\partial\Omega_w$ . The blue wellbore region is the producer.

Figure 7.21 shows the finite element partition, generated by the Gmsh script, following the schematic geometric directives of the figure 7.2. The blue and red regions represented the producer and injector wellbore regions respectively, they represent a cylindrical wellbore with spherical lids, with  $r_w = 0.1$ . This avoid the use of complicated well treatments such as regularized sources terms.

Property	Value
Reservoir dimensions	$L_x = 100$ [m] $L_y = 100$ [m] $L_z = 10$ [m]
well radius	$r_w = 0.1$ [m]
Production pressure	$p_p = 10$ [MPa]
Injection pressure	$p_i = 30$ [MPa]
Water viscosity	$\eta_w = 0.001$ [Pa s]
Water density incompressible	$\rho_w = 1000$ [kg m <sup>-3</sup> ]
First lamé	$\lambda = 5.76923$ [GPa]
Second lamé	$\mu = 3.84615$ [GPa]
Permeability	$\mathbf{K} = 1.0 \times 10^{-13} \mathbf{I}$ [m <sup>2</sup> ]
Linear relative permeabilities	$k r_w = s_w$ and $k r_{tracer} = 1 - s_w$
Time step	$\Delta t = 10$ [d]
Number of reduced functions	$\mathcal{M} = \{9, 63, 108\}$
MHM- $H$ ( <i>div</i> ) level	$l = 0$
Initial porosity	$\phi = 0.25$

Table 7.5: Input data for the linear trace on 3D reservoir.

Figures 7.22, show the velocity approximation for the full order problem. Stream lines as rendered from  $\mathbf{q}_N$ , define the trajectory of tracer particles, from the injector to the producer. For incompressible flow the magnitude of vorticity of field associated with  $\mathbf{q}_N$  is zero. The approximate field vector is mostly irrotational as should be expected from a conservative vector field (see figure 7.23). Isopotential contours are shown on the left of the figure 7.22. They have an inclination with respect to the  $z$  axis, due to the effect of gravity.

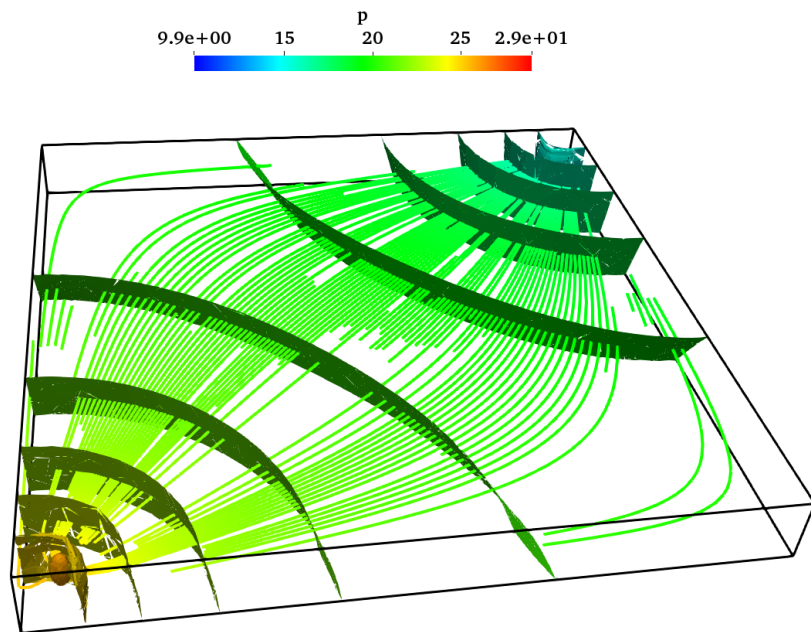


Figure 7.22: Stream lines from the velocity colored with pressure.

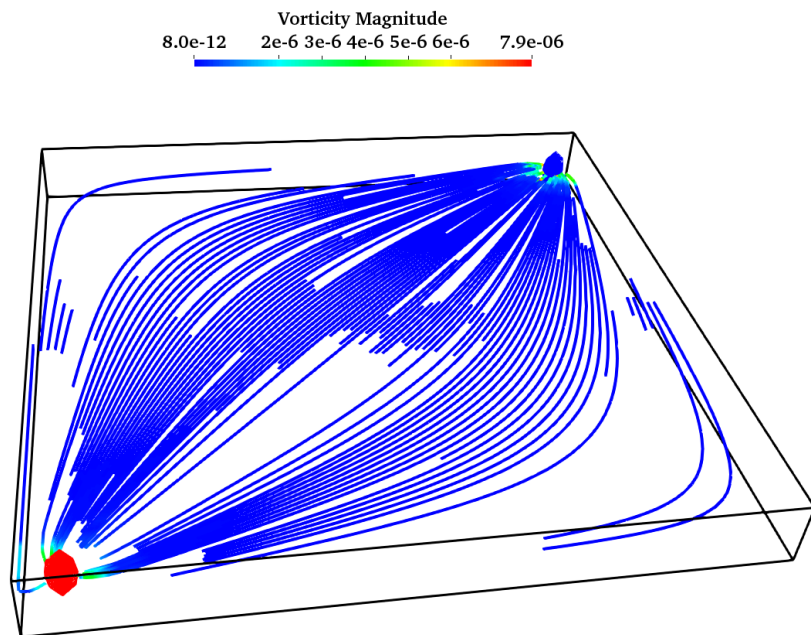


Figure 7.23: Stream lines from the velocity colored with vorticity magnitude (right). The blue wellbore region is the producer well.

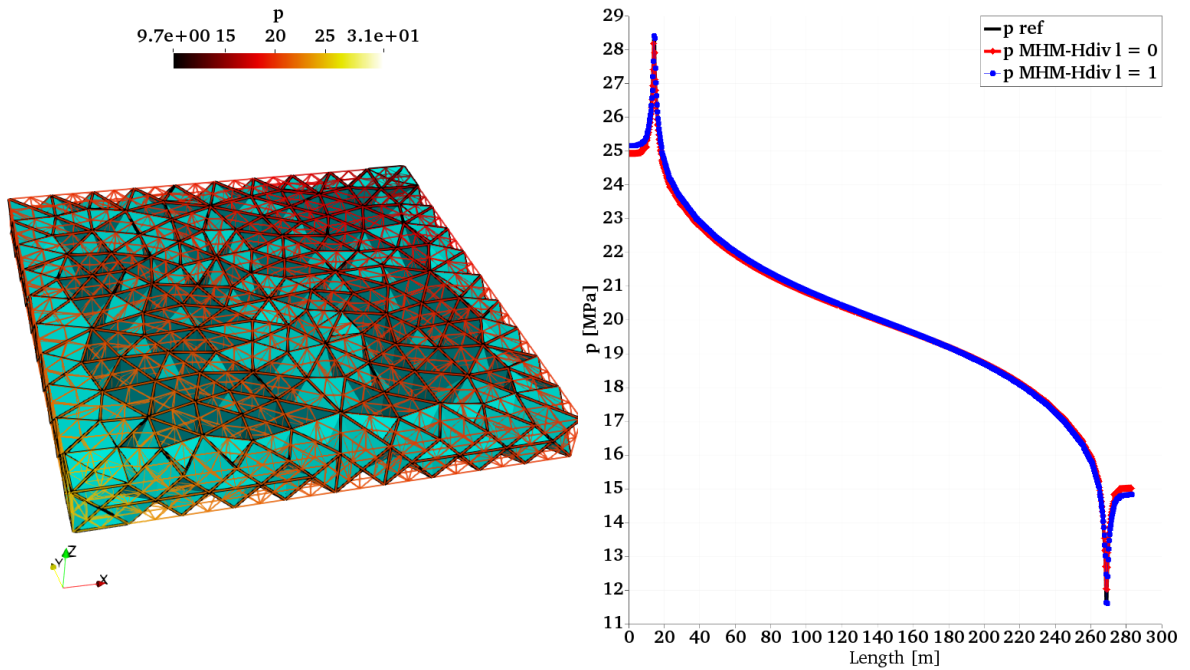


Figure 7.24: MHM- $H(\text{div})$  skeleton mesh and comparison of  $p_{\mathcal{N}_l}$  approximation of  $p_{\mathcal{N}}$ , plot over line  $l = \{\{-100, -100, 0\}, \{100, 100, 0\}\}$ .

Figure 7.24 shows approximations for pressure profiles over the line  $l = \{\{-100, -100, 0\}, \{100, 100, 0\}\}$ . The coarsest level  $l = 0$  already captures the pressure variation along the reservoir center.

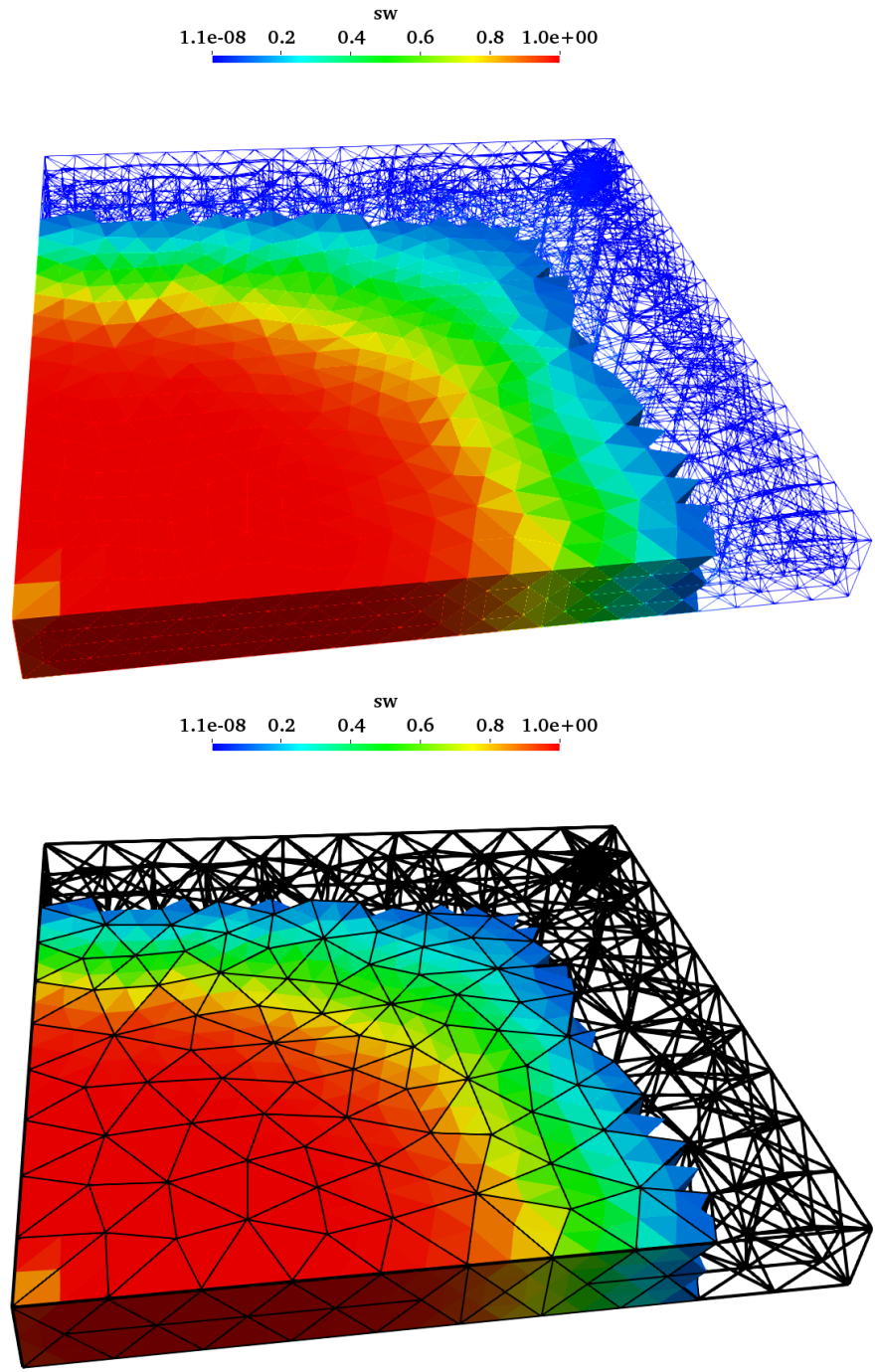


Figure 7.25: Tracer saturation at  $t = 100$  [d], transported with  $\mathbf{q}_{\mathcal{N}}$  (top) and computed with  $\mathbf{q}_{\mathcal{N}_i}$  (bottom).

Figure 7.25 shows the tracer saturation for the full order and the multiscale settings. The color maps of the saturations are very similar. The black wire frame representation of the bottom figure shows the macro element mesh being used.

## Heterogeneous field

In this subsection the approximation of a heterogeneous field of permeabilities is shown in the figure 7.26, with the same setting of the homogeneous case. The blue outline corresponds to the cartesian mesh, which contains the rasterized properties value with two layers in the vertical  $z$  direction; the red wire frame representation shows the micro element partition; the gray faces with blue edges, respresent the multiscale skeleton partition.

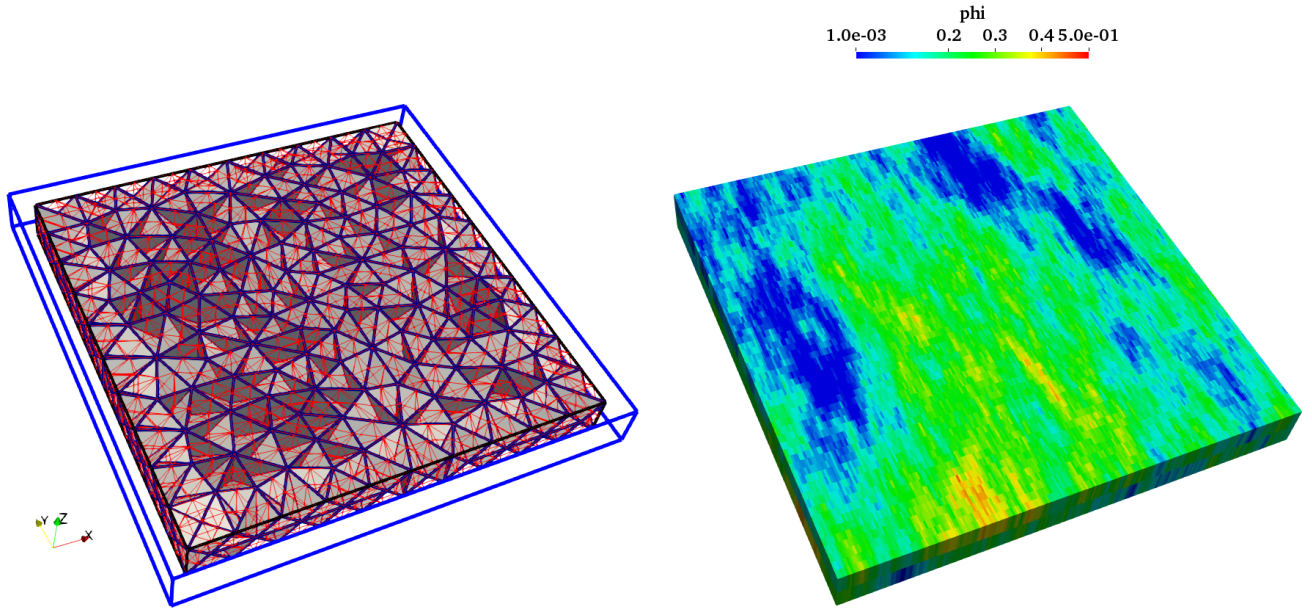


Figure 7.26: Multiscale mesh surrounded by the external cartesian mesh of properties, the cartesian mesh represented by blue outline (left). External mesh with used with rasterized porosity (right).

The spatial variation of properties, naturally results in a perturbation on velocity, and consequently modifies the pressure and saturation being transported. The velocity and pressure profile are shown in Figure 7.27. Figure 7.28 reports the saturations after  $t = 100$  [d] of tracer injection, at two different reservoir vertical levels; these levels result from the bisection of the geometry, using a plane which is perpendicular to the vertical  $z$  axis. The bottom and top saturation maps are on the left and right, respectively. They show that the effect of the spatial variation of permeability and porosity of the two layers being transferred to the finite element mesh, where the velocity magnitude favors the flow in the  $y$  direction.

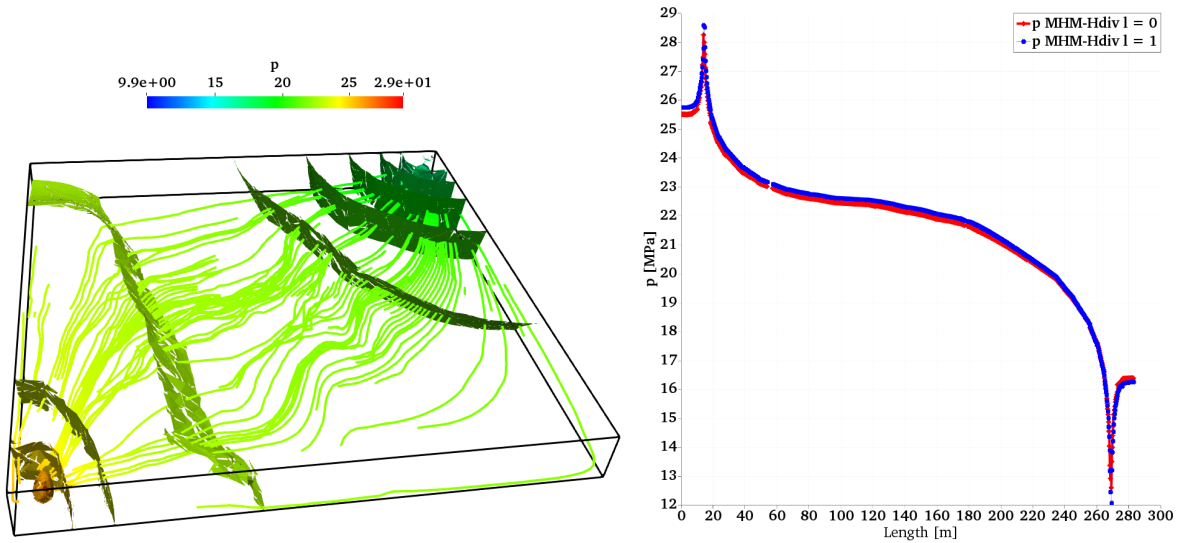


Figure 7.27: Stream lines from the velocity colored with pressure (left) and  $p_{N_i}$  approximation of  $p_N$ , plot over line  $l = \{(-100, -100, 0), (100, 100, 0)\}$  (right). The blue wellbore region is the producer.

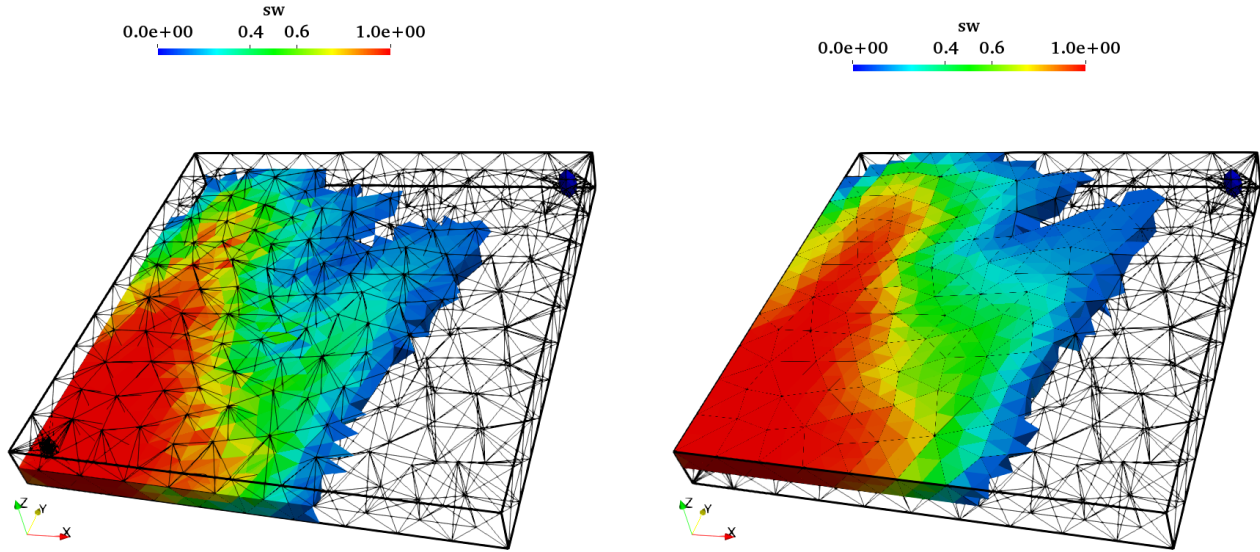


Figure 7.28: Water saturations at  $t = 100$  [d], computed with  $\mathbf{q}_{N_i}$ .

Figure 7.29 shows a comparison of the saturation at the producer wellbore region after  $t = 200$  [d] of tracer injection, the red wire frame representation shows the wellbore boundary mesh. It is important to point out the high level of detail, that the simulator provides.

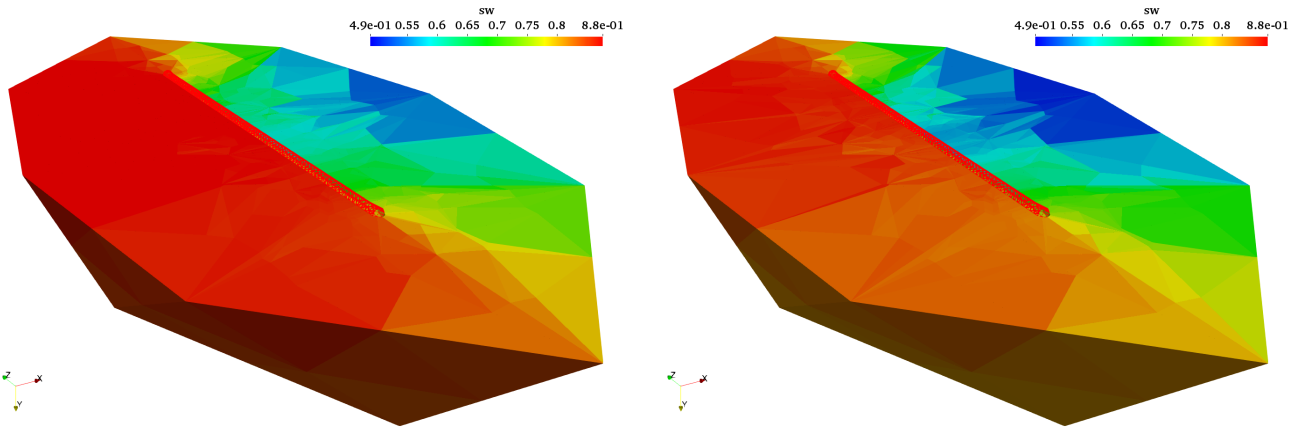


Figure 7.29: Saturation states at  $t = 200$  [d]. Left transport with  $\mathbf{q}_{\mathcal{N}_l}$  at  $l = 1$ , and right transport with  $\mathbf{q}_{\mathcal{N}_l}$  at  $l = 0$ .

**Remark:** Inspecting figure 7.26, where the red mesh represents the micro elements, these are clearly not small enough to capture the permeability variation of the reservoir. However, in the collection of elements of the partition used, inspecting again the radius of the producing well as  $r_w = 0.1$  [m], the small elements in the wellbore region (see figure 7.29) are much smaller than the rasterization size used for the spatial properties. This raises the idea of obtain multiscale approximations located just in the well regions  $\Omega_w$ , while random realizations inside the domain  $\Omega_r$  are constructed sequentially. This idea is left as further improvements and future research.

### 7.3.2 Reduced geomechanic 3D simulation

In this subsection, the effect of the approximation of the reservoir as a poroelastic hexagonal inclusion is shown. In this approach, the calculation of a reference solution  $(\mathbf{u}_{\mathcal{N}}, \mathbf{q}_{\mathcal{N}}, p_{\mathcal{N}}, s_{w\mathcal{N}})$  is out of our reach, because of the excessive need of computational memory. The mixed fluid approximation plus the displacement approximation, turns the computational burden prohibitive at the level of the fine partition. Instead of trying to solve the full order operator for the poroelasticity, the 3D partition associated to the elliptic operator (see figure 7.30) is replaced by the reduced order approach, turning the problem solvable.

#### Offline split

Figure 7.32, represent the vertical component contours are shown, corresponding to two different reduced base functions  $(\mathbf{u}_{1\mathcal{N}}, \mathbf{u}_{2\mathcal{N}})$ , for an approximation RB with  $\mathcal{M} = 9$ . As in the previous RB approximations these functions are calculated once during the offline process and are stored on disk, in the form of a matrix full of size  $\mathcal{N} \times \mathcal{M}$ . Figure 7.31 shows an illustrative Xcode report, for memory use with a maximum about 4.84 [Gb] during the offline phase. The offline process is associated with the geometric configuration of the figure 7.30.

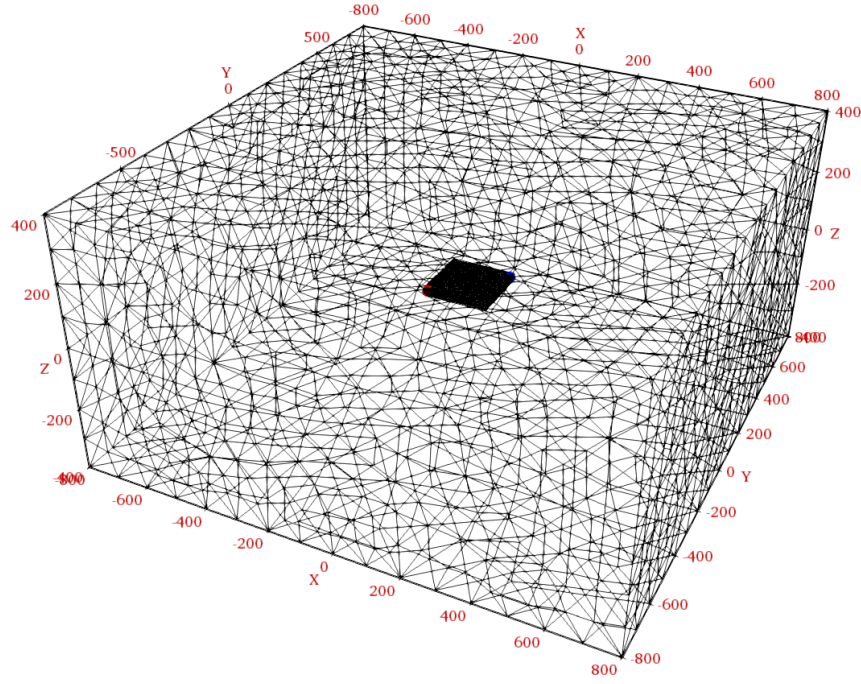


Figure 7.30: Partition of a rectangular 3D sideburden  $\Omega_s$ , reservoir  $\Omega_r$ , ellipsoidal wellbore region  $\Omega_w$  and cylindrical wells  $\partial\Omega_w$ . The blue wellbore region is the producer. For visualization purposes just the surface mesh is rendered.

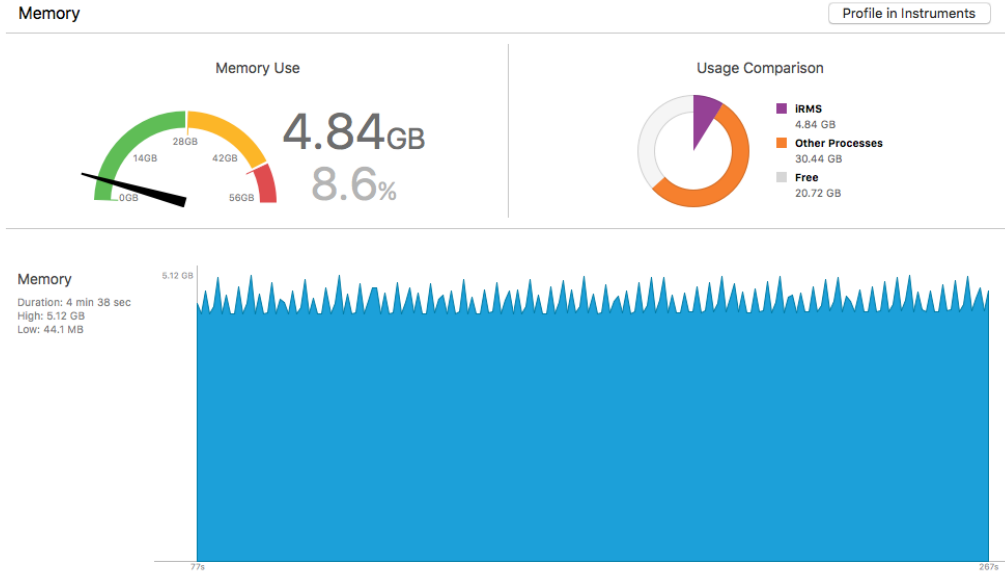


Figure 7.31: Memory consumption during the offline phase with  $\mathcal{N} = 218547$ ,  $\mathcal{M} = 108$ .

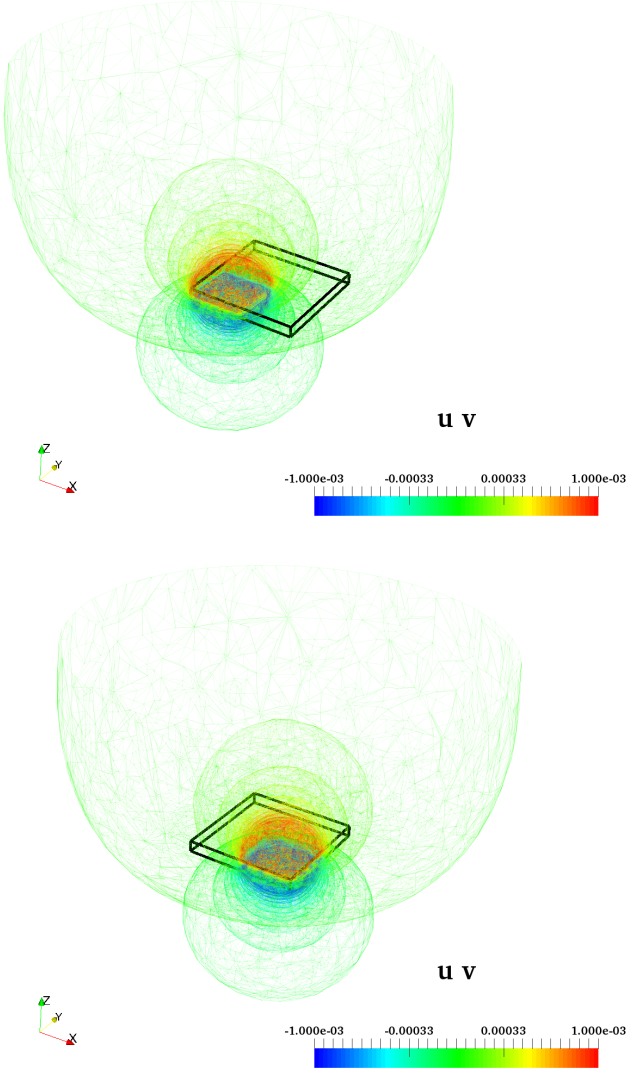


Figure 7.32: RB functions samples when  $\mathcal{M} = 9$ . Left  $\mathbf{u}_{1\mathcal{N}}$ , right  $\mathbf{u}_{2\mathcal{N}}$ .

### Online split

The use of an offline / online strategy shows the effective use of computational memory resources, by dividing memory consumption during the two stages: A first stage where only the reduced base functions  $\mathbf{u}_{i\mathcal{N}}$  with  $i = \{1 \dots \mathcal{M}\}$  are calculated, when only the definition of geometry and elastic properties are given; the second stage is responsible for executions where low consumption of memory is obtained, because the consideration of the side burden rocks does not increase dramatically the use of memory, when there is no geomechanical coupling. The effect of RB is strongly felt here, since the elastic calculations are replaced by functions with global support, which capture the dilation modes of the reservoir, in the sense of Green's functions.

Figure 7.33 shows three different configurations. The first two are related to the memory use for the RB approximatoin with  $\mathcal{M} = 63$  on left, and RB approximation with  $\mathcal{M} = 108$  on the right.

The use memory increases with  $\mathcal{M}$ , because the RB functions are composed by a full matrix with size  $\mathcal{N} \times \mathcal{M}$ , and for the case  $\mathcal{M} = 108$ , the approximate amount of memory is about 1.75 [Gb], but with  $\mathcal{N} = 218547$  and  $\mathcal{M} = 1000$  in 3D simulations, the amount of memory is about 16.28 [Gb]. The graph at the bottom center of figure 7.33 shows the memory use for the case of rigid rocks, i.e. the geomechanic effect is not considered, only the multiscale approach remains. In the current specifications of personal computers a memory comsumption of 6.95 [Gb] is acceptable for a full 3D geomechanic simulation, which means our 3D simulations can be run on a personal computer

The figure 7.34 shows the solution a 3D displacements color maps, for horizontal and vertical displacement components. Comparing the 3D solution with the plane strain 2D solution, the horizontal and vertical displacement approximations have similar shapes. It verifies the qualitative approximation for the geomechanic reduction using RB.

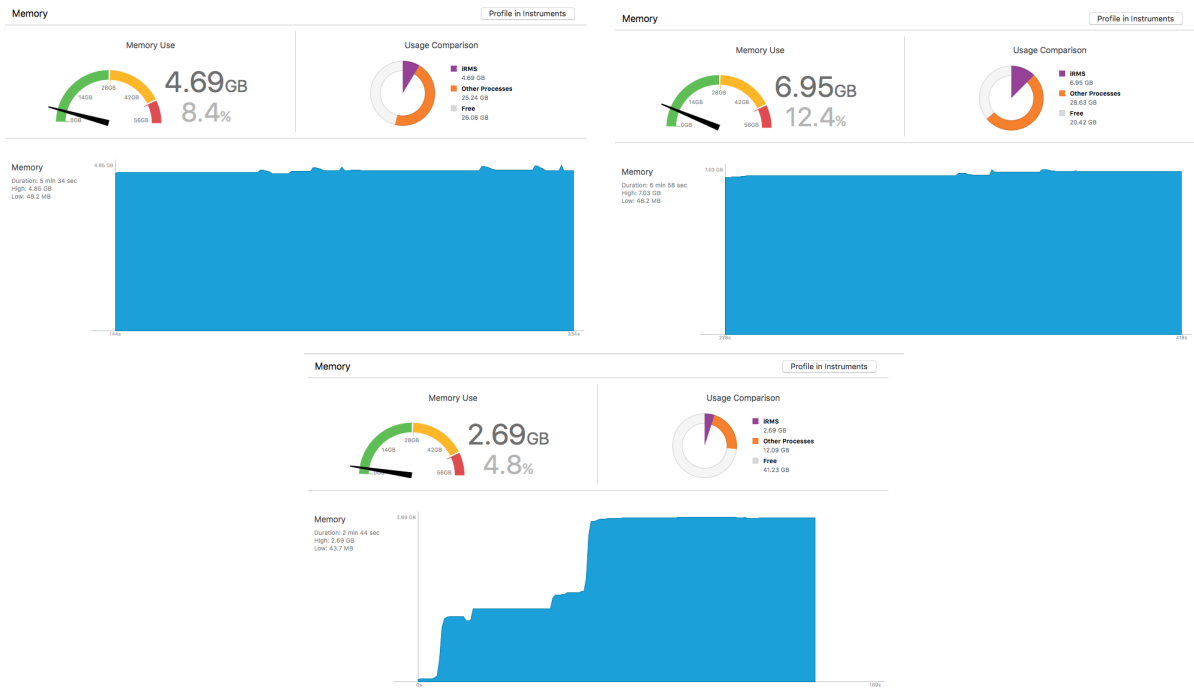


Figure 7.33: Memory consume for: Top online RB with  $\mathcal{M} = 63$  (Left), Top online RB with  $\mathcal{M} = 108$  (Right), and below rigid problem (not geomechanic effect). phase with  $\mathcal{N} = 218547$ .

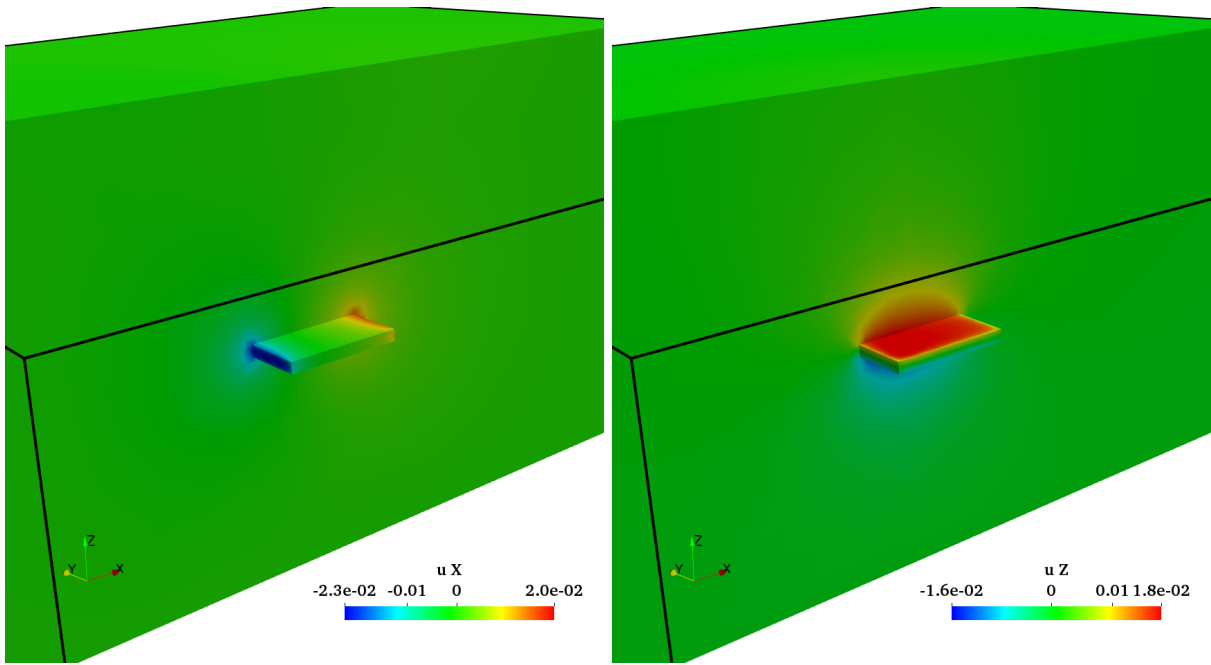


Figure 7.34: Color maps for displacements  $u_x$  and  $u_z$  with  $\mathcal{M} = 108$ .

In figure 7.35, the vertical displacements are shown in the top and the bottom of the reservoir.

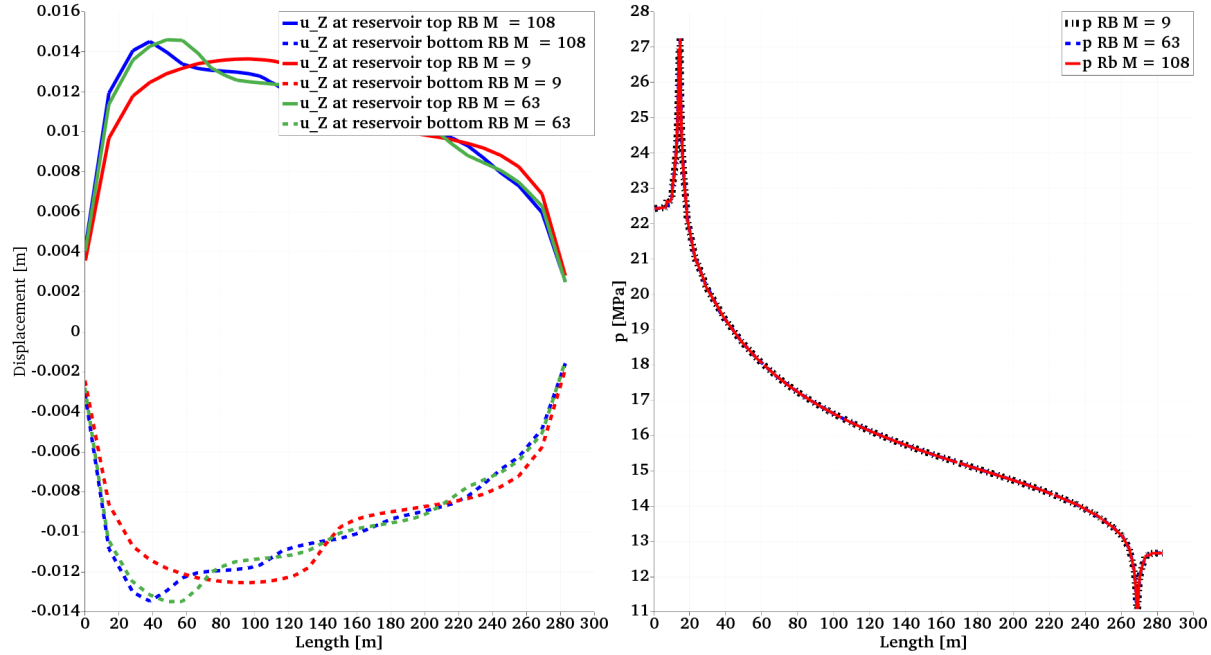


Figure 7.35: Reservoir expansion due to injection and saturations profile at  $t = 100$  [d]. Reservoir top plot over line  $l = \{(-100, -100, 10), (100, 100, 10)\}$  and reservoir bottom plot over line  $l = \{(-100, -100, -10), (100, 100, -10)\}$ .

The figure 7.35 shows a series of comparison plots for both, vertical displacement and pressure at  $t = 10$  [d]. For the displacements at reservoir top and bottom, along the line that connect the wells, this reports the RB approximation for  $\mathcal{M} = 9, 63$  and  $108$ ; when using  $\mathcal{M} = 108$  as references, the approximation is improved by increasing the number of reduced functions. For the case of the pressure, very small differences were observed, showing the priority given to the reservoir equations while the geomechanical deformation is considered.

Figure 7.36, show the effect of porosity change due to the injection at  $t = 10$  [d]. When the reservoir suffer injection the geomechanical effect increases the porosity and it delays the saturation transport because the pore volume is augmented. On the left, the color maps for displacements and saturations are shown, where the deformation was exaggerated 200 times to observe the reservoir volumetric dilatation in relation to the reference undeformed configuration.

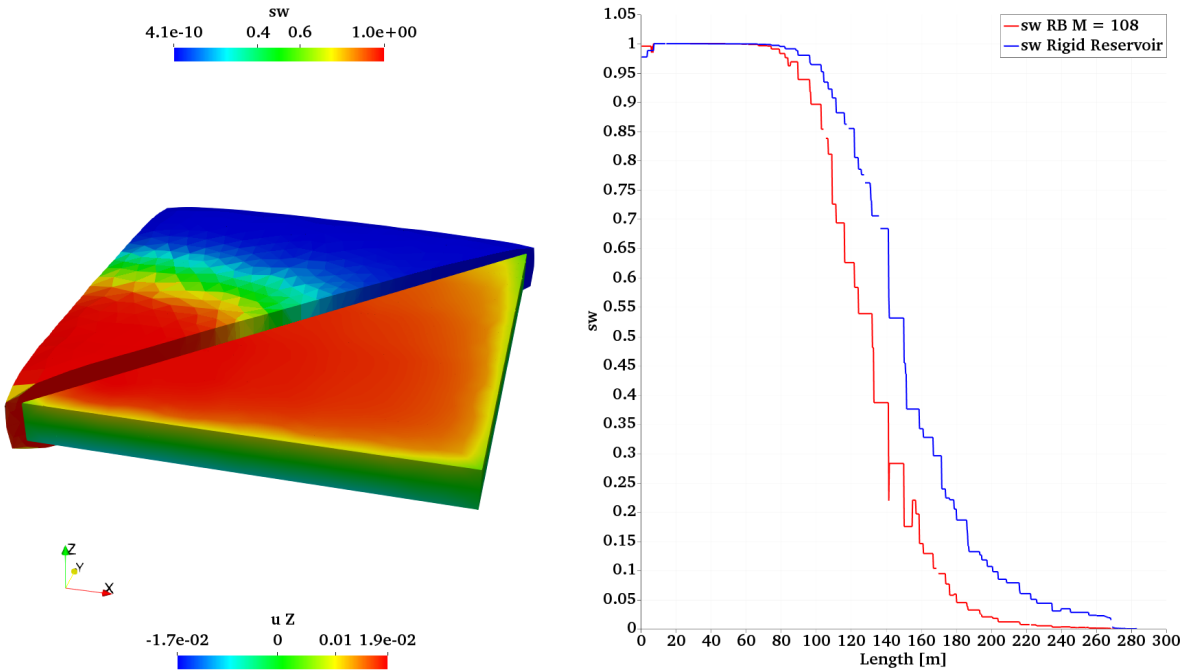


Figure 7.36: Vertical displacements at reservoir top and bottom, at  $t = 10$  [d]. Plot over line  $l = \{-100, -100, 0\}, \{100, 100, 0\}\}$ .

### 7.3.3 Water injection in an oil water system in 3D

Since in a two dimensional nonlinear configuration the sequential algorithm was verified and by the fact that the elliptical component associated with  $\mathcal{A}_e$  is linear, in both its complete  $\mathcal{A}_{eN}$  and its reduced version  $\mathcal{A}_{eM}$ , this subsection disregards the geomechanical coupling. The capabilities of the sequential algorithm without geomechanical coupling in a nonlinear 3D configuration is documented.

This subsection shows the injection of water into an oil water system using the data documented in the table 7.6. Emphasizing that the MHM-( $H(\text{div})$ ) technique is capable of treating non-linear problems, such as a lightly compressible flow subject to the effect of gravitational segregation of

the water-oil phases. Figure 7.37 shows the effect of gravity at  $t = 200$  [d] where it can be seen that the saturation  $s_w$  is higher at the bottom of the reservoir. In relation to the pressure the figure 7.37, shows the change of pressure from  $t = 200$  [d], to  $t = 1000$  [d] where after 700 [d] the volume is completely saturated with water by recovering the monophase solution from the previous problem.

Property	Value
Reservoir dimensions	$L_x = 100$ [m] $L_y = 100$ [m] $L_z = 10$ [m]
Well radius	$r_w = 0.1$ [m]
Production pressure	$p_p = 10$ [MPa]
Injection pressure	$p_i = 30$ [MPa]
Water viscosity	$\eta_w = 0.001$ [Pa s]
Oil viscosity	$\eta_o = 0.005$ [Pa s]
Water density incompressible	$\rho_w = 1000$ $\text{kg m}^{-3}$
Oil density	$\rho_o \text{ std} = 800$ $\text{kg m}^{-3}$
Oil compressibility	$c_o = 1.45037 \times 10^{-9}$
Permeability	$\mathbf{K} = 1.0 \times 10^{-13} \mathbf{I}$ [ $\text{m}^2$ ]
Linear relative permeabilities	$k r_w = s_w$ and $k r_{\text{tracer}} = 1 - s_w$
Time step	$\Delta t = 10$ [d]
MHM-H ( <i>div</i> ) level	$l = 0$
Porosity	$\phi = 0.25$
Initial saturation	$s_w^0 = 0.0$
Initial pressure	$p^0 = 30$ [MPa]

Table 7.6: Input data for the water injection on 3D reservoir.

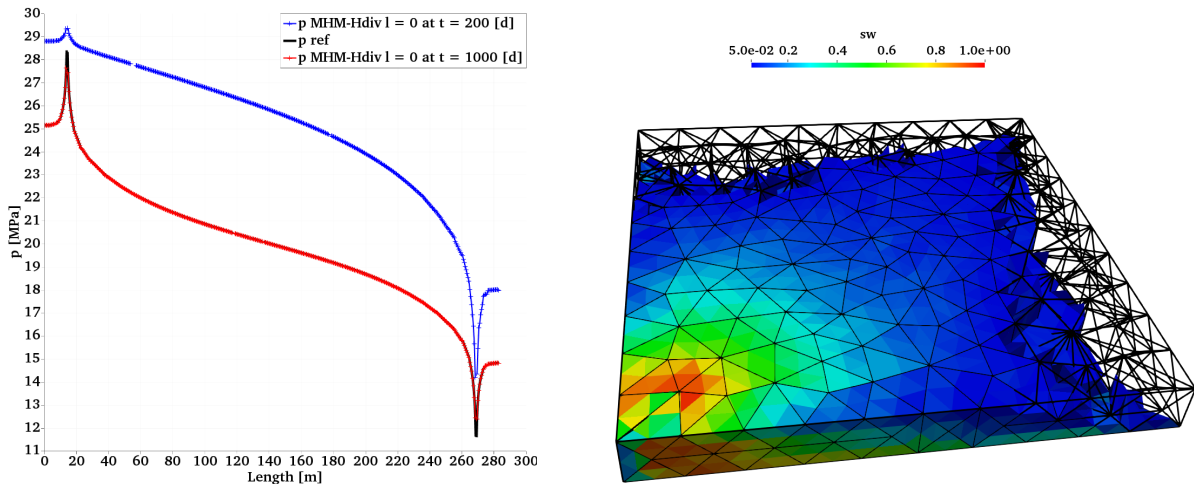


Figure 7.37: MHM-H (*div*) with  $l = 0$ . Left  $p_{N_i}$  evolution at  $t = 200$  [d] and  $t = 1000$  [d], plot over line  $l = \{-100, -100, 0\}, \{100, 100, 0\}\}$ . Right gravity effect on saturations at  $t = 200$  [d].

## 7.4 Conclusions

According to the results presented in this chapter, it is possible to conclude that:

1. In this chapter we present a reservoir simulator that incorporates several finite element technologies that are fully functional in Neopz and are used for the approximation of a water injection problems in a two-phase system where the geomechanical coupling is modeled by a reduced basis (RB) model and the fluid flow by a multiscale model MHM- $H(\text{div})$ . These techniques were reviewed and tested. Comparative graphs show the approximation potential of the two techniques, as well as the potential to enable large-scale discretizations using standard personal computers.
2. With a certain level of rigor, the simulations are presented within a physically possible framework, resulting in coherent and high quality approximations, in some cases the results are compared with commercial simulators of reservoirs with and without geomechanical coupling.
3. The sequential method described in the chapter 6, is applied to both 2D and 3D configurations. It successfully applied to the approximation of full-order operators in the case of  $\mathcal{A}_e$  using the proposed RB approach and  $\mathcal{A}_p$  using MHM- $H(\text{div})$  approximations.
4. The MHM- $H(\text{div})$  technique is verified through a series of 2D and 3D examples in geometries that provide a high level of details, especially in the wellbore region.

# Chapter 8

## Conclusions and outlook

In this document, a sequence of computational tools have been dedicated to the modeling and simulation of petroleum reservoirs, subject to mechanical deformation. The physics of the reservoir leads to strongly coupled nonlinear multiphysics model. The objective of model this physics was attained, through the integration of several computational tools in a simulation program. All the developments, from the point of view of approximation, rests on the pillar of the finite elements, and from the computational point of view, on the Neopz library. The use of the library resulted in both, advantages and bottlenecks; one of the main advantages in the development was the use of an object-oriented programming, a paradigm on which the library is supported. Thus, the reuse of code made possible to implement the proposed algorithms in an acceptable time. On the other hand, with respect to the three-dimensional executions, using Neopz has the disadvantage that 3D structures become quickly heavy and slow with the increase of the refinement level, hindering the process of optimization and fast execution.

## Contents

---

8.1 Conclusions . . . . .	155
8.2 Outlook . . . . .	157

---

### 8.1 Conclusions

Throughout the development of this document, conclusions are drawn and commented in each chapter. They are briefly revisited and discussed as follows:

## On finite element implementations:

The mathematical model based on the mixed formulation of the Darcy's equations, requires the use of  $H(\text{div})$  approximation spaces, mainly due to the need to obtain locally conservative vector fields. These are necessary for the simulation of convection dominated problems. This effort fits as a complement to the existing efforts in terms of 2D approximation spaces, already incorporated in the library. In this sense, the development given by this research, closed the cycle of 3D implementation of the spaces with two types of approximation space configurations  $\mathbf{P}_k^* P_k$  y  $\mathbf{P}_k^{**} P_{k+1}$ . These configurations were tested for arbitrary geometries with linear and nonlinear representations. Optimal convergence rates were obtained.

## On the reduced base:

The reduced base approach developed in this research, is inspired on the Green's functions, given by the theory of inclusions, and preserves the mathematical form of the original operators, which is a characteristic of projection based surrogated models. In addition, these projection based models are interesting from the point of view of programming. The verification was given through two implementations in the case of two-dimensional linear poroelasticity; first, in full continuous formulations  $(\mathbf{u}_{\mathcal{N}}, p_{\mathcal{N}})$ ; second, in a continuous with mixed formulations for the flow equation  $(\mathbf{u}_{\mathcal{N}}, \mathbf{q}_{\mathcal{N}}, p_{\mathcal{N}})$ . In the 3D case the reduced base, represents an efficient technique for the approximation of the full order operator  $\mathcal{N}$ . The novel process of reduction of the elastic component, results in a technique that is applicable in different physics, such as poroelasticity and thermoelasticity, since they share the same mathematical kernel. From the computational point of view, the offline-online strategy distributes computational effort and memory usage. Another aspect is that in modular programming, any reservoir simulator can be coupled with the reduction procedure, through the correct definition of information transfer interfaces.

## About the multiscale method:

In connection with the finite element approximation, its execution in 3D discretizations rapidly becomes prohibitive. The MHM- $H(\text{div})$  technique provides a way of approximating problems of order  $\mathcal{N}$  with order  $\mathcal{N}_l$  with  $\mathcal{N}_l \ll \mathcal{N}$ . It induces an error, that is controlled by the level of coarse scale  $l$ . In this investigation, the technique MHM- $H(\text{div})$  is conceptually a reinterpretation of the original MHM technique (**Paredes2013**); but differs by construction, because MHM- $H(\text{div})$  makes extensive use of  $H(\text{div})$  for the extension of the fluxes in the macro elements to the micro elements, and also extensively uses the static condensation to give a dimensional reduction effect, in terms of the degrees of freedom of the boundary and of the skeleton partition. In this research MHM- $H(\text{div})$  is implemented in 2D and 3D, and it is applied to the simulation of non-linear equations for a water-oil system.

## About the strong formulation:

The poroelastic formulation of the blackoil model shows that the geomechanical coupling occurs in a similar way to its single-phase version. Although in this case, the expressions were developed

for a biphasic system, the main mathematical components allow for the construction of more complex and sophisticated models, such as a three-phase or compositional ones. Thus, the approach for a biphasic nonlinear system provides a good starting point for the understanding, and definition of guidelines necessary for the correct approximation of multiscale coupling with geomechanics.

### **On the approximation by sequential methods:**

In terms of computational efficiency, feasibility and development time, the sequential methods offer the possibility of using appropriate techniques for multiphysics problems, allowing their decomposition in decoupled or partially coupled problems. The problems are weakly coupled through splitted methods and appropriate interfaces of information transfer. Such information transfers, in the context of the finite element formalism, are implemented as sparse matrix multiplications with the degrees of freedom associated with the information that needs to be transferred. The interface algorithm efficiency corresponds to the efficiency of a matrix vector multiplication.

The implementation developed in this work, uses a nested method to attain the solution of problems of order  $\mathcal{N}$ . This nested sequential method is applied to a geomechanical problem associated with the injection of water into a compressible water-oil system under deformation. Thus, the sequential method, in its modular form, allows the acceleration of simulations of both operators, the complete order operators as their approximated versions RB and MHM- $H$  (*div*), respectively. In this research RB and MHM- $H$  (*div*) methods, were applied to elasticity and fluid flow in 2D and 3D configurations.

### **On the reservoir simulator coupled with geomechanics:**

The development of iMRS was based on object-oriented programming philosophy adopted inherently in Neopz. It is possible to develop techniques that are devised for just one unique purpose; for instance, RB and MHM- $H$  (*div*) methods. This modular components, through their correct separation, can be integrated as in a symphony, where each instrumentalist plays its contribution in a complex piece of music. iMRS represents the master of a computational orchestra, that harmonizes and directs the modules, in order to couple them for the solution of a nonlinear multiphysics problem. This coupling is favored by the adopted sequential method.

As all algorithms are essentially centered on finite element formalism. The implementation possess high flexibility and precision, it is applicable to complex geometric configurations and uses efficient information transfer based on sparse matrix vector multiplications.

## **8.2 Outlook**

In this stage of conclusion, this project has several paths of extension which are outlined briefly:

- (i) The sequential method adopted here generated satisfactory results. However, it is necessary to verify the accuracy of the problem resolution with known analytic solutions. For example, the use of the tracer injection in a vertical well, provides a way to generate an analytic

solution of the tracer being transported. Thus, the sequential method could be verified in terms of approximation rates and number of sequential iterations.

- (ii) In this investigation, two-phase nonlinear problems are simulated. The implementation of a blackoil model is also desired for capture the effects of a compressible phase in the geomechanic coupling.
- (iii) The implementation in this investigation is deficient in terms of computational time, since the operations in the multiscale process are performed serially. Thus, in terms of the performance ratio, the implementation gets  $r_{per} \approx 1$ . But in terms of computational memory, the multiscale approximation is truly efficient. This point motivates the corresponding optimization of the multiscale process to decrease the computational times.
- (iv) The definition of regions near the well, proposes the idea to construct a deterministic multiscale approaches inside the well region, and stochastic approximation within the reservoir. This is due to the fact, that most reliable information in the petroleum exploitation process comes from small and localized regions ( logs and rock samples), which in terms of scale only covers just a small region of the complete reservoir volume. This suggest the idea that in a multiscale simulation, the well information is incorporated in a deterministic way, but the information of the reservoir is left to a stochastic process. In this way, the properties of the wellbore regions are preserved.
- (v) The process of base reduction is correctly verified in this research. In addition, its use in thermoelasticity is recommended. In steam injection simulations the elastic response can be again simulated by reduced order modeling.

During the development of this research, in terms of implementation within Neopz, were identified several points to be treated in the field of optimization, being the most relevant: the need of calculate the approximation error in parallel, allowing the rapid verification of numerical schemes especially in 3D; the generation of a graphic file which makes use of plain text files. These files contain data from finite element solutions, that are numerically calculated serially. Other point related to the library is the lack of documentation, which makes the development slow and not autonomous; for this reason, the writing of a documentation as a book is recommended, since this would not only increase the Neopz's users productivity, it would also make the benefits of using the library evident. At this point these advantages reveal themselves only after a slow and tortuous process.

# Appendix A

## Derivation of poroelastic black-oil equations

The velocities expressed in 5.6, 5.7, 5.8 and 5.9 correspond to flow in the interstices of the rock, and considering the solid as a reference phase, the following expression links  $(\mathbf{v}_{f\beta}, \mathbf{v}_s)$  to the Darcy's law:

$$\bar{\mathbf{v}}_\beta = \frac{\phi^* s_\beta}{B_\beta} (\mathbf{v}_{f\beta} - \mathbf{v}_s) \quad (\text{A.1})$$

Using the expression A.1 in the equations 5.6, 5.7 and 5.8 is obtained:

$$\frac{\partial(\phi s_w^*)}{\partial t} + \operatorname{div}(\bar{\mathbf{v}}_w) + \operatorname{div}(\phi s_w^* \mathbf{v}_s) = 0 \quad (\text{A.2})$$

$$\frac{\partial(\phi s_o^*)}{\partial t} + \operatorname{div}(\bar{\mathbf{v}}_o) + \operatorname{div}(\phi s_o^* \mathbf{v}_s) = 0 \quad (\text{A.3})$$

$$\frac{\partial(\phi s_g^*)}{\partial t} + \operatorname{div}(\bar{\mathbf{v}}_g + R_{so}\bar{\mathbf{v}}_o) + \operatorname{div}(\phi s_g^* \mathbf{v}_s) = 0 \quad (\text{A.4})$$

It is important to note that velocities  $(\bar{\mathbf{v}}_w, \bar{\mathbf{v}}_o)$  and  $(\bar{\mathbf{v}}_g + R_{so}\bar{\mathbf{v}}_o)$  are related to surface conditions. The coupling terms in the equations A.2, A.3 and A.4, are given by  $\phi$  and  $\mathbf{v}_s$ , where normally  $\mathbf{v}_s \ll \mathbf{v}_{f\beta}$  motivates to neglect  $\operatorname{div}(\phi s_w^* \mathbf{v}_s)$ ;  $\operatorname{div}(\phi s_o^* \mathbf{v}_s)$  from  $\operatorname{div}(\phi s_g^* \mathbf{v}_s)$  the equations A.2, A.3 and A.4. The reason for it, is that rock velocity is very slow in comparison with fluid velocity.

Rewriting A.2, A.3 and A.4, in a compact form:

$$\frac{\partial(\phi s_\beta^*)}{\partial t} + \operatorname{div}(\bar{\mathbf{v}}_\beta) + \operatorname{div}(\phi s_\beta^* \mathbf{v}_s) = 0 \quad (\text{A.5})$$

The rest of the discussion is oriented to find one expression, that replaces  $\operatorname{div}(\phi s_\beta^* \mathbf{v}_s)$  in terms of  $(\mathbf{u}, p)$ . To arrive at the final form of the equations, it is required the use of the material derivative

with respect to the velocity is used:

$$\frac{D(\cdot)}{Dt} = \frac{\partial(\cdot)}{\partial t} + \mathbf{v}_s \cdot \nabla(\cdot) = 0 \quad (\text{A.6})$$

Applying the chain rule in equations 5.9 and A.5:

$$\frac{\partial((1-\phi)\rho_s)}{\partial t} + \mathbf{v}_s \cdot \nabla((1-\phi)\rho_s) + (1-\phi)\rho_s \operatorname{div}(\mathbf{v}_s) = 0 \quad (\text{A.7})$$

$$\frac{\partial(\phi s_\beta^*)}{\partial t} + \operatorname{div}(\bar{\mathbf{v}}_\beta) + \mathbf{v}_s \cdot \nabla(\phi s_\beta^*) + \phi s_\beta^* \operatorname{div}(\mathbf{v}_s) = 0 \quad (\text{A.8})$$

Using A.6 in A.7 and A.8:

$$\frac{D((1-\phi)\rho_s)}{Dt} + (1-\phi)\rho_s \operatorname{div}(\mathbf{v}_s) = 0 \quad (\text{A.9})$$

$$\frac{D(\phi s_\beta^*)}{Dt} + \operatorname{div}(\bar{\mathbf{v}}_\beta) + \phi s_\beta^* \operatorname{div}(\mathbf{v}_s) = 0 \quad (\text{A.10})$$

The equation A.9 shows two important aspects: first,  $(1-\phi^*) = \frac{V_s}{V_b}$  is just a volume relation and second, by solving  $\operatorname{div}(\mathbf{v}_s)$  from A.9 is obtained a expression for the divergence of  $\mathbf{v}_s$ , as follows :

$$\operatorname{div}(\mathbf{v}_s) = -\frac{V_b}{\rho_s V_s} \frac{D\left(\frac{\rho_s \mathbf{v}_s}{V_b}\right)}{Dt} \quad (\text{A.11})$$

Considering a constant rock mass, i.e.  $\delta\rho_s V_s = 0$ .

$$\operatorname{div}(\mathbf{v}_s) = -\frac{1}{V_b} \frac{D(V_b)}{Dt} \quad (\text{A.12})$$

From the linear elastic theory, the volumetric strain  $\epsilon_v$  is defined as follow:

$$\epsilon_v = \operatorname{div}(\mathbf{u}) = \frac{\delta V_b}{V_b} \quad (\text{A.13})$$

Using A.13 in A.12 we obtain:

$$\operatorname{div}(\mathbf{v}_s) = \frac{D\epsilon_v}{Dt} = \frac{D(\operatorname{div}(\mathbf{u}))}{Dt} \quad (\text{A.14})$$

In this way, it can be more evident that the effects of the term  $\operatorname{div}(\mathbf{v}_s)$  are simply interpreted with volume changes, substituting A.14 in A.10 one obtains:

$$\frac{D(\phi s_\beta^*)}{Dt} + \operatorname{div}(\bar{\mathbf{v}}_\beta) + \phi s_\beta^* \frac{D\epsilon_v}{Dt} = 0 \quad (\text{A.15})$$

Adding and subtracting  $\epsilon_v \frac{D(\phi s_\beta^*)}{Dt}$  which is much smaller than  $\frac{D(\phi s_\beta^*)}{Dt}$  or:

$$\epsilon_v \frac{D(\phi s_\beta^*)}{Dt} \ll \frac{D(\phi s_\beta^*)}{Dt} \quad (\text{A.16})$$

$$\frac{D(\phi(1 + \epsilon_v) s_\beta^*)}{Dt} + \operatorname{div}(\bar{\mathbf{v}}_\beta) - \epsilon_v \frac{D(\phi s_\beta^*)}{Dt} = 0 \quad (\text{A.17})$$

Defining the total fluid content:

$$\phi^* = \phi(1 + \epsilon_v) \quad (\text{A.18})$$

Using the equation A.17 with  $\epsilon_v \frac{D(\phi^* s_\beta^*)}{Dt} \approx 0$  in A.17, it turns in a similar equation to one that model the uncoupled reservoir flow:

$$\frac{D(\phi^* s_\beta^*)}{Dt} + \operatorname{div}(\bar{\mathbf{v}}_\beta) = 0 \quad (\text{A.19})$$

For a regime of small deformations, the total volume  $V_b$  can be approximated by a linear function of  $\epsilon_v$ :

$$\frac{V_b}{V_b^0} = (1 + \epsilon_v) \quad (\text{A.20})$$

Taking into consideration A.20 in A.18, the total fluid content  $\phi^*$  is the change of porosity in relation to an initial state  $V_b^0$ :

$$\phi^* = \phi \frac{V_b}{V_b^0} = \frac{V_{\text{porous}}}{V_b} \quad (\text{A.21})$$

From A.21, it is important to note that:

- (i)  $\phi^* = \phi^0$  in the initial configuration.
- (ii)  $\phi^*$  is a function of volumetric deformations and pore pressure.
- (iii) In the conventional simulation  $\phi^* = \phi^0 (1 + c_r (p - p^0))$  is a function only of the pore pressure.

Following **Geertsma1957** the variation of porosity a deformed porous medium is approximated by:

$$\frac{\delta\phi}{\phi} = \left[ \frac{1}{\phi} \left( \frac{1}{K_b} - \frac{1}{K_s} \right) - \frac{1}{K_b} \right] (\delta\sigma_v + \delta p) \quad (\text{A.22})$$

$$\delta\sigma_v = \frac{3\lambda + 2\mu}{3} \delta\epsilon_v - \alpha \delta p = K_{dr} \delta\epsilon_v - \alpha \delta p \quad (\text{A.23})$$

where  $\sigma_v$  [Pa] is the volumetric stress,  $\alpha$  is the Biot's coefficient and it is associated with bulk modulus  $K_b$  y  $K_s$ .

$$\alpha = 1 - \frac{K_b}{K_s} \quad (\text{A.24})$$

Under the small deformations regime, the porosity can be approximated by:

$$\phi = \phi^0 + \left[ \left( \frac{1 - \phi^0}{K_b} - \frac{1}{K_s} \right) \right] (\delta\sigma_v + \delta p) \quad (\text{A.25})$$

Replacing A.25 in A.18 and neglecting terms of second order, is obtained:

$$\phi^* = \phi^0 + \left( c_b - (1 + \phi^0) c_s \right) \delta p + (c_b - c_s) \delta\sigma_v \quad (\text{A.26})$$

Or commonly in terms of  $\epsilon_v$  and  $p$ :

$$\phi^* = \phi^0 + \alpha \delta\epsilon_v + S_\epsilon \delta p \quad (\text{A.27})$$

$S_\epsilon$   $[\text{Pa}^{-1}]$  is the inverse of the Biot constant, defined as:

$$S_\epsilon = \frac{1}{M} = (1 - \alpha) (\alpha - \phi^0) c_b \quad (\text{A.28})$$

The inverse of the modules  $c_b = \frac{1}{K_b}$   $[\text{Pa}^{-1}]$  and  $c_s = \frac{1}{K_s}$   $[\text{Pa}^{-1}]$  can be interpreted as the bulk and solid compressibilities.

The expression A.28 shows that:

$$\phi^0 \leq \alpha \leq 1 \quad (\text{A.29})$$

If the solid is incompressible  $K_s \rightarrow \infty$ ,  $c_s \rightarrow 0$ , on the other hand  $\alpha = 1$  or  $\alpha = \phi^0$  implies  $S_\epsilon = 0$ .

Finally considering in the equation of mass balance  $\mathbf{v}_s \cdot \nabla (\phi^* s_\beta^*) \ll \frac{\partial (\phi^* s_\beta^*)}{\partial t}$ , then :

$$\frac{D (\phi^* s_\beta^*)}{Dt} \approx \frac{\partial (\phi^* s_\beta^*)}{\partial t} \quad (\text{A.30})$$

The physical consideration of A.30, implies that the medium under deformation is in steady state, in other words is a quase stationary approximation. The equations coupled with geomechanic coupling, become:

$$\frac{\partial (s_\beta^* (\phi^0 + \alpha \delta \operatorname{div} (\mathbf{u}) + S_\epsilon \delta p))}{\partial t} + \operatorname{div} (\bar{\mathbf{v}}_\beta) = 0 \quad (\text{A.31})$$

The following is a variation of A.31, which is commonly used in the simulation by sequential operators:

$$\phi^* \frac{\partial (s_\beta^*)}{\partial t} + s_\beta^* \left( c_b - (1 + \phi^0) c_s \right) \frac{\partial (\delta p)}{\partial t} + s_\beta^* (c_b - c_s) \frac{\partial (\delta\sigma_v)}{\partial t} + \operatorname{div} (\bar{\mathbf{v}}_\beta) = 0 \quad (\text{A.32})$$

